The " Turkana Grits ": Potential Hydrocarbon Reservoirs of the Northern and Central Kenya Rifts

George Muia

▶ **To cite this version:**

George Muia. The " Turkana Grits ": Potential Hydrocarbon Reservoirs of the Northern and Central Kenya Rifts . Applied geology. Université de Rennes 1, 2015. English. NNT : . tel-01379989

HAL Id: tel-01379989

https://insu.hal.science/tel-01379989

Submitted on 12 Oct 2016

HAL is a multi-disciplinary open access archive for the deposit and dissemination of scientific research documents, whether they are published or not. The documents may come from teaching and research institutions in France or abroad, or from public or private research centers.

L'archive ouverte pluridisciplinaire **HAL**, est destinée au dépôt et à la diffusion de documents scientifiques de niveau recherche, publiés ou non, émanant des établissements d'enseignement et de recherche français ou étrangers, des laboratoires publics ou privés.

THÈSE / UNIVERSITÉ DE RENNES 1
sous le sceau de l'Université Européenne de Bretagne

pour le grade de
DOCTEUR DE L'UNIVERSITÉ DE RENNES 1
Mention : Sciences de la Terre

Ecole Doctorale Sciences de la Matière

présentée par

George Muia

Préparée à l'unité de recherche UMR 6118
Géosciences Rennes
Observatoire des Sciences de l'Univers de Rennes

The "Turkana Grits": Potential Hydrocarbon Reservoirs of the Northern and Central Kenya Rifts

Thèse soutenue à Rennes
le 24/07/2015
devant le jury composé de :

Jean-Luc POTDEVIN
Professeur, Université de Lille 1 / rapporteur

Stéphane DUCROCQ
Directeur de Recherche,
CNRS-Université de Poitiers / rapporteur

Jean-Yves REYNAUD
Professeur, Université de Lille 1 / examinateur

Mathieu SCHUSTER
Chargé de Recherche, CNRS
Université de Strasbourg / examinateur

Peter R. COBBOLD
Directeur de Recherche Emérite, CNRS
Université de Rennes 1/ examinateur

Jean-Jacques TIERCELIN
Directeur de Recherche,
CNRS-Université de Rennes 1 / directeur de thèse

Erwan HALLOT
Maître de Conférences
Université de Rennes 1 / co-directeur de thèse

The “Turkana Grits”: Potential Hydrocarbon Reservoirs of the Northern and Central Kenya Rifts

Table of contents

Abstract 6

General Introduction 8

Chapter I 19

1. Introduction 28

2. Field study, sampling and analytical methods 33

3. Regional background of the Central and Northern Kenya Rifts 35

3.1. Physiography and climate of the Central and Northern Kenya Rifts 35

3.2. Geological outline of the Kerio and Baringo Basins 38

3.3. Geological outline of the North Kerio Basin 41

4. The Kimwarer Formation 43

4.1. Lithostratigraphy 43

4.1.1. The “Lower Kimwarer Formation” 45

4.1.2. The “Upper Kimwarer Formation” 52

4.2. Structural framework of the Kimwarer Formation at the scale of the Kerio Basin 52

4.2.1. Seismic interpretation 54

4.2.2. Correlation of seismic packages to stratigraphic column of the Kerio Basin 57

4.2.3. Geological evolution of the Kerio Basin 57

4.3. Chronostratigraphic setting of the Kimwarer Formation 59

4.3.1. Volcanic units associated with the Kimwarer Formation 59

4.3.2. Dynamics of emplacement of the different volcanic units 75

4.3.3. Stratigraphy and correlations 76

4.3.4. Chronological setting of the Kimwarer Formation 77

4.4. Facies analysis, depositional processes and environments of the Lower and Upper Kimwarer Formation 79

4.4.1. Distal fluvial channel lithofacies associations 79

4.4.2. Alluvial fan lithofacies association 79

4.4.3. Floodplain lithofacies association 80

4.5. Post-depositional evolution of the Kimwarer Formation of the Kimwarer Formation, “Lower” and “Upper” 80

4.5.1. Texture 81

4.5.2. Detrital minerals 81

4.5.2.1. Quartz 81

4.5.2.2. Feldspars 82

4.5.2.3. Other detrital elements 82

4.5.3. Authigenic minerals 82

4.5.3.1. Zone 1 (Hematite-rich) 82

4.5.3.2. Zone 2 (Calcite-rich) 85

4.5.3.3. Zone 3 (Kaolinite-rich) 85

4.6. Origin of authigenic cements associated with the Lower Kimwarer Formation 85

4.6.1. Hematite cementation 85

4.6.2. Carbonate cementation (calcite) 86

4.6.3. Kaolinite cementation 86

4.6.4. Chronology of main diagenetic events 86

4.7. Porosity 86

4.8. Discussion 89

4.8.1. Palaeogeographical and climatic reconstructions 89

4.8.2. Implications on the reservoir potential of the Kimwarer Formation 90

4.9. Conclusion 91

5. The Kamego Formation 93

5.1. Lithostratigraphy 93

5.2. Chronostratigraphic setting of the Kamego Formation 99

5.3. Facies analysis, depositional processes and environments of the Kamego Formation 104

5.3.1. Distal fluvial channel lithofacies association 104

5.3.2. Floodplain lithofacies association 104

5.4. Post-depositional evolution of the Kamego Formation 105

5.4.1. Texture 105

5.4.2. Detrital minerals 105

5.4.2.1. Monocrystalline quartz 107
5.4.2.2. Polycrystalline quartz 107
5.4.2.3. Feldspars 109
5.4.2.4. Other detrital components 109
5.4.3. Authigenic minerals 109
5.4.3.1. Zone 1 (Calcite-rich) 109
5.4.3.2. Zone 2 (Hematite-rich) 109
5.4.3.3. Chronology of main diagenetic events 109
5.4.4. Porosity 110
5.5. Discussion 110
5.6. Conclusion 111
6. The Loriu Formation 112
6.1. Lithostratigraphy 112
6.1.1. The Loriu Section 114
6.1.2. The Kangabeiye Section 119
6.2. Chronostratigraphic setting of the Loriu Sandstone 120
6.3. Facies analysis, depositional processes and environments of the Loriu Sandstone, Loriu Section 125
6.3.1. Texture 126
6.3.2. Detrital minerals 125
6.3.2.1. Polycrystalline quartz 126
6.3.2.2. Monocrystalline quartz 126
6.3.2.3. Feldspars 128
6.3.2.4. Lithics, accessory minerals and matrix 128
6.4. Post-depositional evolution of the Loriu Sandstone, Loriu Section 128
6.4.1. Matrix/authigenic components 128
6.4.1.1. Zone 1 (Hematite-rich) 128
6.4.1.2. Zone 2 (Carbonate-rich) 129
6.4.1.3. Zone 3 (Kaolinite-rich) 129
6.4.2. Chronology of diagenetic events 130
6.4.3. Porosity 130
6.5. Facies analysis, depositional processes and environments of the Kangabeiye Section 132
6.5.1. Texture 132
6.5.2. Detrital minerals 133
6.5.2.1. Monocrystalline quartz 133
6.5.2.2. Polycrystalline quartz 133
6.5.2.3. Feldspars 133
6.6.2.4. Lithics, accessory minerals and matrix 133
6.6. Post-depositional evolution of the Kangabeiye Section 135
6.6.1. Matrix/authigenic components 135
6.6.1.1. Zone 1 (Calcite-rich) 135
6.6.1.2. Zone 2 (Kaolinite-rich) 135
6.6.2. Chronology of main diagenetic events 135
6.6.3. Porosity 135
6.7. Discussion 137
6.8. Conclusion 139
7. Discussion 141
7.1. The Lokone Sandstone, Lokichar Basin: the best hydrocarbon reservoir in the Kenya Rift? 143
7.2. The Kimwarer Formation, Kerio Basin (Figs. 17 and 18b; Table 15) 146
7.2.1. Lithology and depositional environments 146
7.2.2. Chronology 146
7.2.3. Reservoir characterization 147
7.2.4. Lateral and vertical extension of reservoirs 147
7.3. The Kamego Formation, Baringo Basin (Figs. 38 and 39; Table 15) 148
7.3.1. Lithology and depositional environments 148
7.3.2. Chronology 148
7.3.3. Reservoir characterization 148
7.4. The Loriu Sandstone, North Kerio Basin (Figs. 46 and 47; Table 16) 149
7.4.1. Lithology and depositional environments 149
7.4.2. Chronology 149
7.4.3. Reservoir characterization 150
7.5. The “Turkana Grits”: Potential reservoirs in the Kenya Rift? 1(à

Conclusion 153

References 164

Appendix 174

Abstract

The Turkana Grits: Potential reservoirs of the Northern and Central Kenya Rifts.

Over two thirds of the world's giant oilfields are found in two principle tectonic regimes; continental passive margins and continental rifts. The preferential formation of hydrocarbons in rifts is attributed to the proximal juxtaposition of high grade, lacustrine source rock units with medium to high grade reservoir rocks - a consequence of both faulting and sedimentation in the resulting accommodation space, which in many cases may locally modify the prevailing climatic conditions. In one of such basins, the Lokichar Basin in the Kenyan Rift, over 600 million barrels of recoverable oil have been discovered. The principle reservoir unit in this basin is the Lokone Sandstone that belongs to a larger family of sandstones called the 'Turkana Grits', arkosic sandstones that are sandwiched between metamorphic basement and mid-Miocene volcanics. The hydrocarbon proclivity of the Lokone Sandstones as reservoir units motivated further study of the 'Turkana Grits', as potential hydrocarbon reservoirs.

In this work, three sedimentary formations, i.e. Kimwarer Formation, Kamego Formation and Loriu Sandstones, which have not been previously fully characterized from chronostratigraphic and sedimentological point of views were studied through detailed logging. Over 170 samples were collected to determine, detrital and authigenic components, the main cementation zones in the different outcrops, and, from lithofacies analysis, the depositional environments. Volcanic and intrusive samples were also characterized and used for 39Ar-40Ar dating.

Three superposed depositional environments were determined for the Kimwarer Formation, a distal fluvial channel, an alluvial fan and a floodplain depositional environment. The diagenetic study shows cements change from dominant hematite at the base to calcite within the middle zones and back to hematite towards the top of the Formation. These cementation episodes occur during early and relatively late diagenesis in low temperature conditions (<80 °C), under significant mechanical compaction. A minimum deposition age at ca. 18 Ma (Early Miocene – Burdigalian) has also been set for the Kimwarer Formation. The Kamego Formation evolves from fluvial to floodplain depositional environments and is dominantly cemented by hematite. Calcite cement is only noted in the lowermost 5m. A thin lava flow interbedded with the topmost sediments of the Kamego Formation gave a minimum deposition age of ca. 20 Ma for most of the sediments. The Loriu Sandstone is composed predominantly of fluvial channel deposits. The main cements are calcite, hematite and kaolinite clays. A cross-cutting dyke suggests a minimum deposition age of ca. 18.5Ma.

A final reservoir analysis of the Turkana Grits shows that while compaction and cementation are dominant agents of porosity reduction, the Turkana Grits are generally poor to moderately good reservoir units. The Lokone Sanstone has been proven to have sub-surface porosities ranging between 10 - 20% and permeabilities as high as 3 darcies (Africa Oil Corporation, 2011). For petrographic analyses, the Kimwarer Formation has been ranked as having the second best reservoir potential with porosities as high as 20% in some sections of its studied stratigraphy. The Kamego Formation also has good potential but is not as highly ranked owing to the huge component of volcanic material that have a greater propensity to diagenetic alteration. No good porosities were noted for the Loriu Sandstone and hence this formation has been ranked 5th amongst the Turkana Grits.

General Introduction

General introduction

As the era of cheap, easy to reach, abundantly available hydrocarbons comes to an end, progressively smaller petroleum resources are now being discovered in continually more challenging exploration targets and in more subtle trapping settings. Comparatively, the number of new discoveries has dropped steadily since the early 1990's and the hydrocarbon content of these new discoveries has been on the decline for the last four decades (Gao, 2012). This is despite the significant technological advances that have been made in the fields of engineering and geophysical prospecting, suggesting that the fundamental keys to success in hydrocarbon exploration are grounded in innovative play concepts determined by tectonic settings and consequent basin evolution.

Mann et al. (2003) noted that the 877 giant oil fields, which account for 67% of the total world hydrocarbon reserves, cluster in approximately 30% of the world's land surface. These oil fields can be segregated into six main tectonic depositional configurations: (1) continental passive margins fronting major ocean basins (304 giants); (2) continental rifts and overlying sag or steer's head basins (271 giants); (3) collisional margins produced by terminal collision between two continents (173 giants); (4) collisional margins produced by continental collision related to terrane accretion, arc collision, and/or shallow subduction (71 giants); (5) strike-slip margins (50 giants); (6) subduction margins not affected by major arc or continental collisions (8 giants) (Fig. 1). Of these tectonic regimes, continental passive margins and continental rifts are dominant; the two accounting for over two thirds of the total global hydrocarbon reserves (Perrodon, 1976; Mann et al., 2003). The dominance of these two tectonic regimes as the main hydrocarbon hotspots is attributed to a generic depositional preference that allows for the localized accumulation of high-grade source-rock units in either lacustrine or restricted marine setting and the proximal juxtaposition of medium to high grade reservoir units in the immediately overlying basin fill. In continental rift basins, this apparent excess of hydrocarbons exists despite the common tendency for these basins to have relatively poorer reservoir quality, which is a result of compositional immaturity owing to the proximal provenance zones of these sediments (Burke et al., 2003).

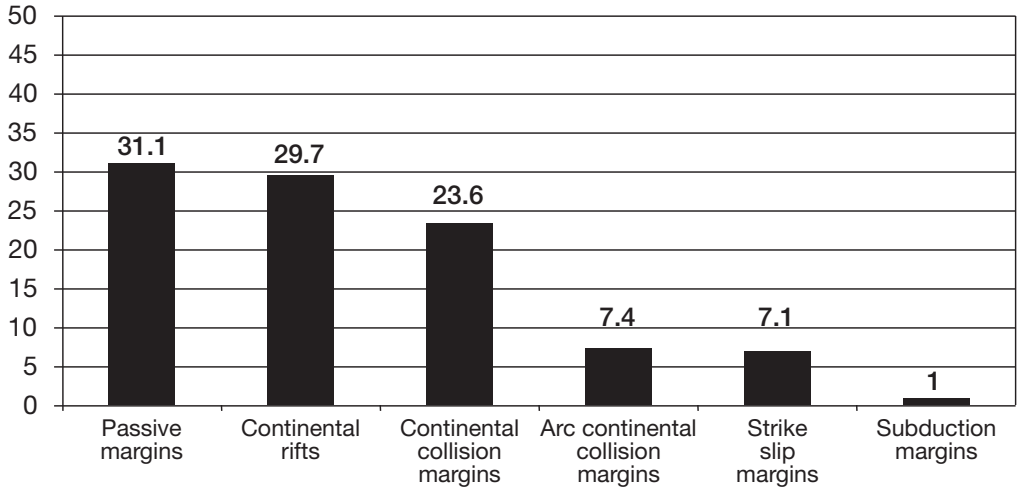

Fig. 1. *Histogram showing the distribution of giant oil fields as defined by the tectonic regimes in which they exist. A giant oil field is defined as a field containing proved reserves exceeding 500 million billion barrels (bbl). A giant gas field contains proved reserves of greater than 3 trillion cubic feet (tcf) (after Mann et al., 2003).*

Various workers have studied the development of continental rifts and subsequent basin fills (Bosworth et al., 1986; Lambiase and Bosworth, 1995; Morley, 1995; Morley et al., 1999; Corti, 2011). Continental rifting is generally preceded by crustal downwarping where sediments are held in sag-like depressions prior to lithospheric rupture (Baker and Wohlenberg, 1971; Crossley, 1979; Lambiase and Bosworth, 1995). Continental rupture then gives rise to elongate, 50-100 km long elementary basins (or sub-basins) that are separated along-strike by positive topographic features called 'accommodation zones' (sensu Lambiase and Bosworth, 1995). These sub-basins are in many cases asymmetrical with sediment accommodation space being formed closest to the active border faults. As the extension process continues, mechanically inefficient crustal detachments may coalesce along strike to form larger and more structurally efficient geometries to aid further crustal extension (Lambiase and Bosworth, 1995). This joining of faults results in the merging of sub-basins to form larger basins both in length and in depth, the latter being due to the combined effects of hanging wall subsidence and the isostatic readjustment of the footwall wall (Bosworth, 1985; Lambiase and Bosworth, 1995; Morley, 1995) (Fig. 2).

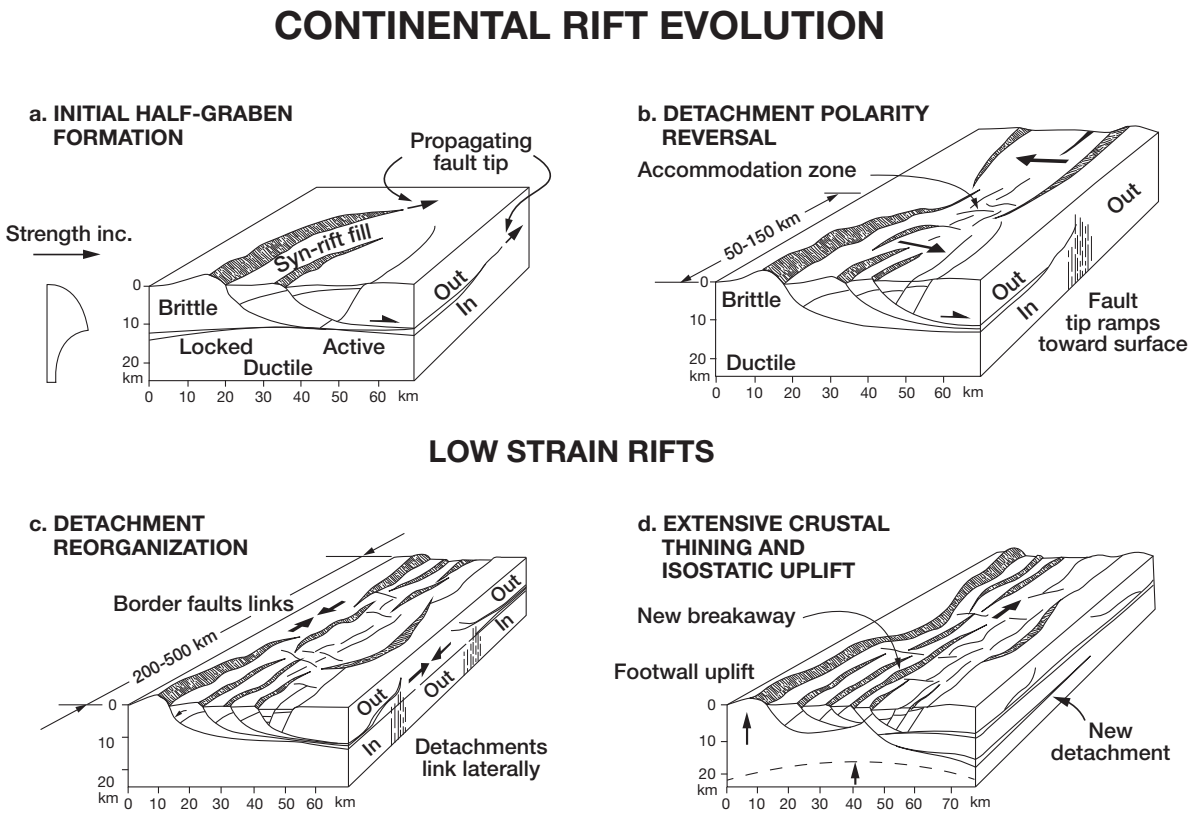

Fig. 2. *Continental rifts are initiated by: (a) Gentle sagging that develops into an asymmetrical half-graben owing to movement along a single detachment in the basement rock; (b) and (c) Additional detachments (which in many cases reflect pre-existing basement structures) develop both vertically and laterally and could coalesce to form a more effective fault system; (d) Crustal thinning leads to isostatic uplift and possible abandonment of existing detachments and creation of new detachment breakaways (modified from Lambiase and Bosworth, 1995).*

When such basins develop, their drainage becomes restricted and is cut-off from adjacent basins, the immediate consequence of which is termination of drainage flow within the basin (Gawthrope and Hurst., 1993; Gawthrope et al., 1994; Collier and Gawthrope., 1995; Lambiase and Bosworth, 1995) and the development

of deep lacustrine systems similar to modern Lake Albert, Lake Tanganyika or Lake Malawi amongst others (Coulter, 1963; Scholz and Rosendahl, 1988; Scholz et al., 1990; Tiercelin and Mondeguer, 1991; Morley, 1995; Scholz et al., 2003) (Fig. 2). Under these conditions, excellent quality source rock can develop, the formation of which is determined by organic matter productivity and preservation after sedimentation. Organic productivity is influenced by the availability of nutrients, solar input, water chemistry and temperature and the amount of wind energy to which the lacustrine systems are exposed. The quality of the eventual source-rock units is further dependent on the ingredients of the organic matter, i.e. whether the original input is derived predominantly from plant debris or from the endogenic production of algae and microbes, and whether this organic matter, once deposited, is diluted by exogenous inorganic matter such as chemical, biological and detrital sediments (Tissot and Welte, 1978; Demaison and Moore, 1980; Kelts, 1988; Lambiase, 1990). Preservation of the organic matter, which is by this time resting on the interface between the lake waters and the topmost basin sediments, is also determined by the water chemistry, the biosphere within the underlying sedimentary column, and the waters' mixing rates (Kelts, 1988; Talbot, 1988). Mixing can be induced by strong winds and waves although in many cases, due to the geometric configuration of continental rifts, the elevated rift shoulders offer basinal lacustrine systems wind protection, reducing the mixing effect of wind and waves that would dilute organic elements that have been deposited at depth (Katz, 1995). Organic matter preservation is also and most critically enhanced when the supply of oxygen is less than its demand, commonly as a result of the development of anoxic conditions at depth (Tissot et al., 1978).

Good to excellent reservoirs can also develop in continental rift settings. Generally, the main fault scarp and associated uplifted footwall shoulders act as topographic barriers that direct both internal and external drainage into the rift basin (Leeder and Gawthorpe, 1987; Leeder and Jackson, 1993). Depending on the rate of subsidence of the hanging wall, river systems in such settings could (with an increasing subsidence rate relative to sedimentation) give rise to: 1) thick fluvial packages that onlap the flexed margin; 2) stratal units that thicken into the hanging wall but converge at the flexural margin; and 3) axial or across-rift progradational strata (Peacock and Sanderson, 1991; Davison and Underhill, 2012) as is noted in the US Triassic palaeorifts as well as in the North Sea Rift (e.g. Tomasso et al., 2008; Davison and Underhill, 2012). Good to excellent reservoir units can result from any of these basin infill configurations.

Eighty Years of Oil Exploration in Central and Eastern Africa

Such continental rift systems exist in Africa and within which great success in oil and gas exploration is currently being witnessed (Fig. 3) (Ramberg and Neumann, 1984; Rosendahl, 1987; Morley et al., 1999; Burke et al., 2003; Corti, 2011). In Eastern and Central Africa, these rifts are represented by: 1) the NW-SE trending Central African Rift System (CARS) that formed during the break up and separation of South America and Africa in the Cretaceous times (Browne et al., 1985; Binks and Fairhead, 1991; Guiraud et al., 2005); and 2) the N-S trending, Tertiary East African Rift System (EARS) (Baker and Wohlenberg, 1971; Baker et al., 1972) (Fig. 3a). Petroleum exploration in East Africa was initially related to the wavering interest of international oil companies that was largely dictated by prevailing regional and global trends in the oil industry. Oil and gas exploration in Eastern Africa started more than eight decades ago after geological mapping of the eastern flanks of the Albertine Graben (EARS, western branch) in the early 1920s that resulted in the identification of 52 oil seeps which pointed to the existence of good source and reservoir rock units within the basin (Wayland, 1925). In the late thirties through to the mid-fifties, working petroleum units were further highlighted through the drilling of shallow stratigraphic wells. A total of 22 wells were drilled on the western and southern shores of Lake Albert and included the Butiaba Waki B-1 well drilled in 1938 by the African-European Investment Company which was the first to demonstrate the excellent source and reservoir potential of the Kaiso and Kisegi Formations (PEPD, 2014).

Recent work has confirmed fourteen hydrocarbon seeps on the eastern flanks of the Albertine Graben which are from north to south: 3 – Butiaba area; 3 – Kibiro area; 5 (oil), 1 (gas) – Kaiso-Tonya area, and 2 – Semliki Basin on the southern shores of Lake Albert. The presence of these hydrocarbon seepages confirmed the presence of laterally extensive, operational petroleum systems with mature source rocks, which have generated and expelled oil (PEPD, 2014) (Fig. 4). The exploratory work of the 1920's to 50's was followed by a period of lackluster oil prospecting that lasted almost six decades and which was only reignited by the 1973 oil embargo placed by the Organization of Arab Petroleum Exporting Countries (OAPEC) against Canada, Japan, Netherlands, the United Kingdom and the United States.

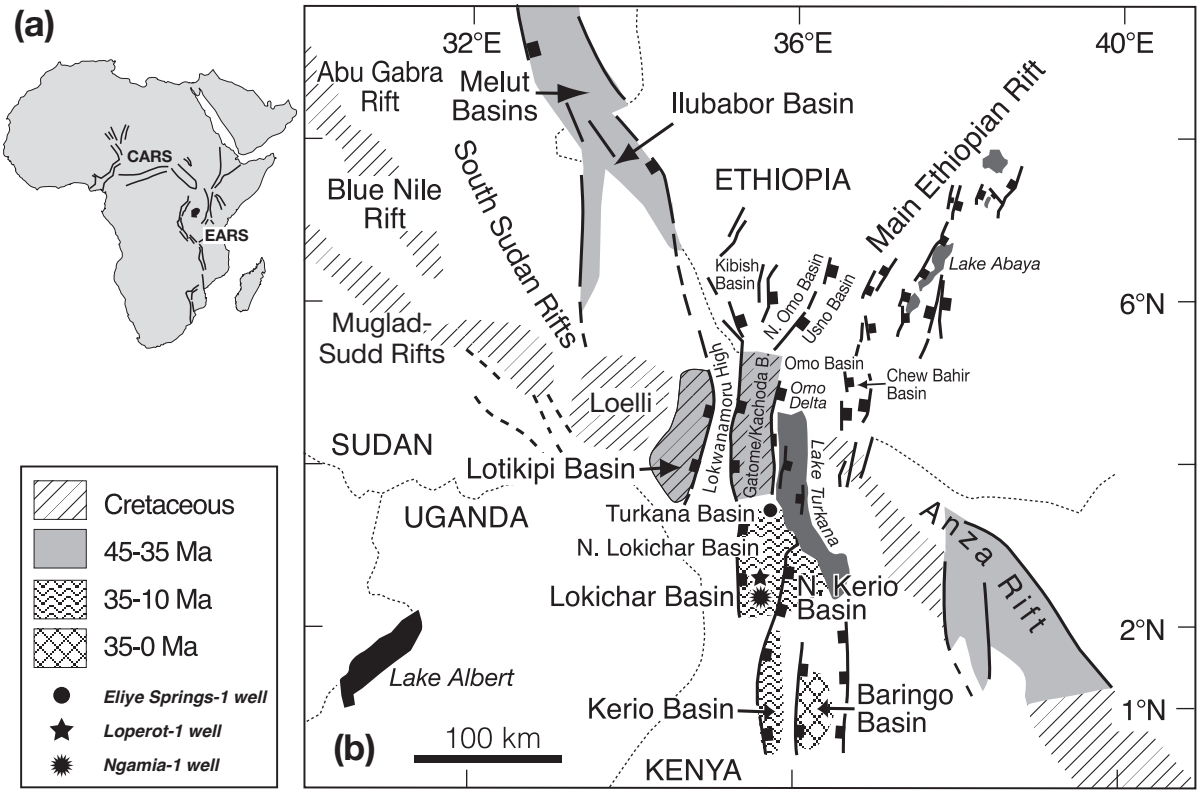

Fig. 3. *(a) The Central African (CARS) and East African (EARS) Rift Systems. (b) Map showing the distribution of Cretaceous-Paleogene to Neogene rift basins in Southern Sudan (CARS) and Northern-Central Kenya (EARS). In the northwest region of Kenya, the Lotikipi and Gatome Basins are described as Cretaceous?-Paleogene age synformal basins that are on trend with the south Sudan basins. In the Northern Kenya Rift are the Cretaceous?-Paleogene to Neogene old Lokichar, North Kerio, North Lokichar and Turkana Basins. More than 10 exploration wells have been drilled since the 90s, two in 1992: Eliye Springs-1, which was dry, was drilled in the Turkana Basin (indicated by a black dot). The Loperot-1 well, which had good oil shows, was drilled in the Lokichar Basin. Between 2012 and 2014, ten additional wells have been drilled in the Lokichar and South Lokichar Basins (Blocks 10BB and 13T), all of them targeting Tertiary play types and all except the Emong-1 well encountering significant payzones (Africa Oil Corporation, 2014). The two Loperot-1 and Ngamia-1 exploration wells are indicated by black star. To the south, in the Central Kenya Rift, are the poorly studied Kerio and Baringo Basins (modified from Morley et al., 1992; Tiercelin et al., 2004; Thuo, 2009; Tiercelin et al., 2012b). Seismic acquisition has been conducted in the Kerio Basin (Block 12A) (520 km of 2D seismic), and one exploration well, named Lekep-A, is planned for drilling in 2015.*

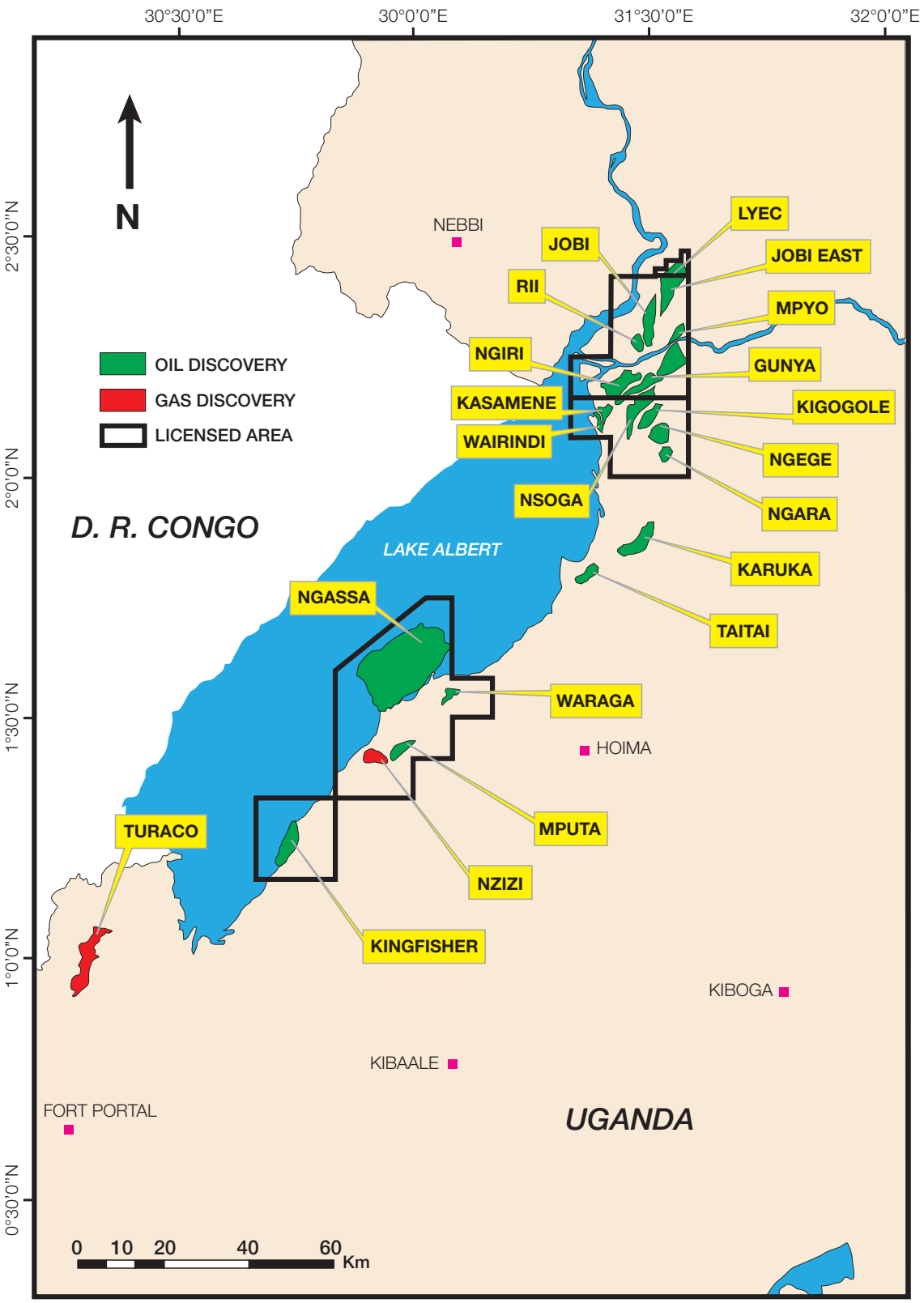

Fig. 4. *Map showing 21 oil (green) and 2 gas (red) discoveries in Uganda's Albertine Graben (PEPD, 2014).*

In 1974, the American oil giant, Chevron Overseas Inc. (Chevron) recorded the first exploration success on the north-western extreme of the Central African Fault Zone (CAFZ) in Sudan, after drilling the Bashayir-1 and Suakin-1 exploration wells in Block 15, 120 km from Port Sudan (Beydoun and Sikander, 1992). Chevron estimated possible production of over 50 MMSCFD (50 million cubic feet per day) and 1000 bbl/d of gas condensate (1000 barrels per day), which at the time was not commercially viable. Focus was then shifted to the then poorly known Muglad Basin located in the Sudanese Central African Rift System (CARS) (Fig. 3b). Exploration work started in 1975 with a 516,000 km2 concessionary award to Chevron from the Sudanese Government (Browne et al., 1985; Schull, 1988). Prior to this work, the basins in South Sudan were considered to be shallow intracratonic sags in which few hundred metres of Cretaceous, Tertiary and Quaternary sedimentary rocks had accumulated. Exploratory drilling started in 1977 and a year later, in 1978, the first oil shows were recorded in Unity-1 well (2nd well to be drilled by Chevron). However it was in the fifth well, named Abu Gabra-1, that was drilled in August 1979 that oil flowed, catapulting the sub-basins of the Muglad Basin to the category of world-class oil-producing provinces (Schull, 1988) with over 900 million barrels of recoverable reserves (Paul et al., 2003) entrapped in thick non-marine, clastic sequences representing lacustrine, floodplain, fluvial and alluvial environments of Jurassic? - Cretaceous and Tertiary age (Schull, 1988).

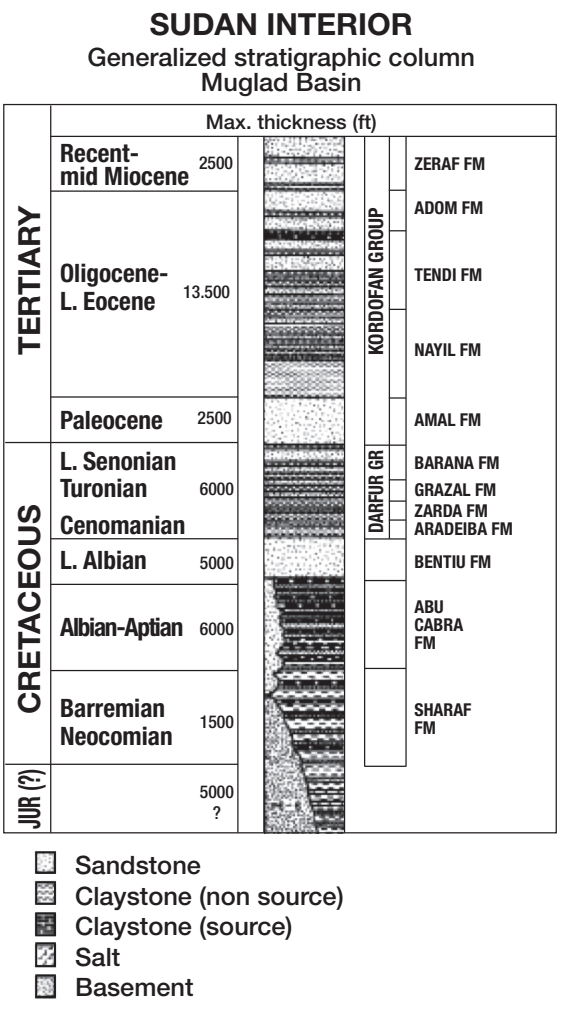

Fig. 5. *Generalized lithostratigraphic column based on collated data from 86 wells drilled in the Muglad Basin, South Sudan (after Schull, 1988).*

The geochemical tests of the dark grey lacustrine claystone and shales of the early rift phase (Neocomian-Albian) that are emplaced above the Precambrian Basement in the Muglad Basin demonstrated that the predominant organic constituent of these source rocks is algal with limited amounts of terrestrial plant debris, with TOC (Total Organic Carbon) values ranging from 1-5% with a mean average of 1.3% (Schull, 1988). Considering the homogeneity of the shale (claystone) units, deposition probably occurred in distal zones of a stratified lake, far from zones of clastic influx (Schull, 1988). The reservoir characters within the Muglad Basin are typical of many continental rift basins with variations between fluvial channel, lacustrine delta-plain and delta-front depositional environments. From Schull's (1988) generalised stratigraphic column (Fig. 5), that is based on the collation of data from 86 wells drilled in the Muglad Basin, good reservoir rocks are noted in the Bentiu Formation (1520-m thick - Lower Albian-Cenomanian), and the Aradeiba Formation (180-m thick - Turonian), both of which represent proximal alluvial fan environments. The Amal Formation (762-m thick – Paleocene), which is a predominantly fluvial sequence, has also been determined to be a good reservoir unit (Schull, 1988). The Bentiu Formation, which exhibits porosities (ϕ) between 10-20% is composed of dominantly conglomeratic to coarse-grained massive sandstones that are intercalated with finer sediments and few coal beds while the Aradeiba Formation (ϕ = 20-25%), is composed of conglomeratic units at the base and grey shales and siltstones interbedded with sandstone units. The Amal Formation (ϕ = 30-40%) consists mainly of carbonaceous claystones but with some interbedded, poorly consolidated,

medium to very coarse-grained sandstones (Abdalla et al., 2001). Within the basin, reservoir quality decreases: 1) with depth (as a result of compaction, quartz overgrowths and other diagenetic changes); 2) with decreasing grain size (coarser-grained alluvial and fluvial sandstones are better reservoirs); and 3) with increasing amounts of feldspars and lithic grains (due to feldspathic overgrowths and cementation) (Schull, 1988).

The Northern and Central Kenya Rifts: Emerging Exploration Provinces

Driven by this staggering success in South Sudan, a consortium of oil companies commissioned a reflection seismic study of the East African Rift System dubbed PROJECT PROBE (Proto-Rifts and Ocean Basin Evolution) that was coordinated by the Duke University (USA). The aim of the project was to establish if deep rift structures such as the oil rich basins found in South Sudan could exist below the larger lakes of the East African region (Rosendahl, 1987; Rosendahl et al., 1986, 1988, 1992). This project was conducted on Lake Malawi (Ebinger et al., 1984, 1987) and Lake Tanganyika (Burgess, 1985; Burgess et al., 1988; Lezzar, 1996; Lezzar et al., 1997), the two largest lakes of the western branch of the EARS, and on Lake Turkana, which is the largest lake of the eastern branch of the EARS (Dunkelman et al., 1988, 1989). The successful mapping of deep rift basins beneath these lakes spurred on the first industrial seismic campaign in the East Africa by Amoco Kenya Petroleum Company (AKPC) who proceeded to collect additional seismic and gravity data west and southwest of Lake Turkana. It was this seismic acquisition campaign that led to the discovery of a string of Cretaceous?-Paleogene to middle Miocene age, deep (5-7 km), N-S oriented half-grabens within the northern segment of the Kenya Rift, which include the Lokichar, North Kerio, North Lokichar, Lothidok and Turkana Basins (Morley et al., 1999; Vincens et al., 2006; Ducrocq et al., 2010). Two additional basins, Gatome (6-km deep) and Lotikipi (4-km deep) were also discovered in the extreme NW of Kenya through the same seismic data acquisition campaign (Wescott et al., 1999; Desprès, 2008) (Fig. 3b).

The confirmation of viable sedimentary depocentres in the Northern Kenya Rift from this geophysical data acquisition campaign led to the drilling in 1992 of the first two exploration wells in the Kenya Rift: The Eliye Springs-1 well, and the Loperot-1 well (Fig. 3b). The Eliye Springs-1 well was drilled in the middle Miocene Turkana Basin (Morley et al., 1999) and was dry. The Loperot-1 well was drilled in the Eocene-middle Miocene Lokichar Basin and despite good hydrocarbon shows, only yielded about 10 litres of waxy crude oil (Morley et al., 1999). This exploration well was nonetheless instrumental in constraining the Lokichar Basin's subsurface lithology, complementing the reflection seismic data, and outlining the presence of moderate to good quality reservoir rocks: the Lokone Sandstone, and the Auwerwer Sandstone (Fig. 6a) (Morley et al., 1999; Tiercelin et al., 2004, 2012). The Lokone Sandstone (>1100-m thick in the Loperot-1 well) (Morley, 1999) is represented by basement-derived pebbly sandstones and minor conglomerates deposited in a majorly fluvial/deltaic depositional environment punctuated by transgressive lacustrine phases. The formation has porosities ranging between 10-20%. Above it is the Auwerwer Sandstone (>620-m thick), formed by 5-10 m thick alternating beds of coarse to pebbly sandstones, which fine up to 3-6 m thick massive siltstones to fine sandstones, representing braided fluvial to marginal lacustrine units that exhibits porosities between 1-15% (Tiercelin et al., 2004). Petrological study of both the Lokone and Auwerwer Sandstones show a basement source although a shift to a more volcanic constitution (>50% of the detrital minerals) is noted within the Auwerwer Sandstone (Morley, 1999; Tiercelin et al., 2004, 2012b). This can be attributed to a change in sediment provenance zone from a predominantly metamorphic basement source area to a volcanic-rich provenance zone, which could potentially be associated with the emplacement of the Miocene Samburu Basalts (ca. 23-14 Ma) that are largely represented on the eastern part of the CKR (Chapman and Brook, 1978; Tiercelin et al., 2004; Tiercelin et al., 2012b). Diagenetic changes in the Lokone and Auwerwer Sandstones that have an impact on the reservoir porosity and permeability of these

sandstones include calcite precipitation by Na/Ca-rich fluids related to the dissolution of the overlying Auwerwer Basalts (dated ca. 12.5-10.7 Ma) (Morley et al., 1999; Tiercelin et al., 2004), quartzitic and feldspathic overgrowths, development of carbonate cements, zeolites and authigenic clays. The cements and clays are generally grain rimming and pore-filling with kaolinite acting as the major grain replacive mineral (Morley et al., 1995; Tiercelin et al., 2004; Thuo, 2009; Tiercelin et al., 2012b).

In the Lokichar Basin, the Lokone Sandstone contains two thick black shale units – the Lokone Shale Member (drilled between 920 m and 1385 m depth in the Loperot-1 well), and the Loperot Shale Member (2325-2950 m depth in the same well) (Morley et al., 1995, 1999; Talbot et al., 2004; Tiercelin et al., 2004; Thuo, 2009; Tiercelin et al., 2012b) (Fig. 6). Where they outcrop, these shale units have generally low TOC levels (<1%). Nonetheless, in the Loperot-1 well, values of up to 17% were noted in the sidewall core samples collected (Morley et al., 1999). This high source-rock potential was further confirmed by pyrolysis tests that recorded excellent source quality with up to 10 mg HCgm-1 oil potential. Maturity levels provided by Rock Eval Tmax ranged between 438-452°C for the Lokone Shale Member, and 463-478 °C for the Loperot Shale Member (Tissot and Welte, 1978; Talbot et al., 2004). Palynofacies analyses performed on cleaned cuttings from the two 'black shale' intervals demonstrated that the organic facies is dominated by amorphous organic matter accompanied by fungal remains, multicellular algae, Botryococcus spp., Pediastrum spp. and cysts of Prasinophycean algae indicative of a quite large and deep freshwater depositional environment (Talbot et al., 2004).

Palynological data from the Loperot-1 well give an age of Paleogene to middle Miocene for the Lokone Sandstone (Morley et al., 1999; Talbot et al., 2004). During the Paleogene to mid-Miocene times when the Lokichar paleolake was in existence, the regional landscape of the Lokichar Basin was characterized by a semi-deciduous forest and humid woodland similar to the modern Guineo-Congolian rainforest with rainfall exceeding 1000 mm/year and a well-defined dry season (Vincens et al., 2006) that supported a flourishing faunal assemblage as evidenced by the discovery of a rich late Oligocene (27-28 Ma) reptilian and mammalian fauna at the Lokone Horst site (Ducrocq et al., 2010; Marivaux et al., 2010; Ducrocq et al., 2011; Leakey et al., 2011; Marivaux et al., 2012).

The Lokone Sandstone and the Lower Auwerwer Sandstone are considered to be part of the "Turkana Grits" that were described by Murray-Hughes (1933) in reference to a series of hundreds of metres thick, immature arkosic sandstones resting on an eroded and locally faulted surface of basement rocks and which are overlain by volcanics of presumably Miocene age at several places in the northern and central segments of the rift (Fig. 7). These sediments were believed to mark the onset of tectonism in the Kenya Rift (e.g. Arambourg, 1935; Fuchs, 1939; Arambourg and Wolf, 1969; Wescott et al., 1993). Mainly due to the absence of palaeontological interest in the "Turkana Grits" (with the exception of the Lokone and Auwerwer Sandstones in the Lokichar Basin, and the base of the Lapur Sandstone (e.g. Sertich et al., 2005, 2006; Rasmussen and Gutiérrez, 2009; Ducrocq et al., 2010; Leakey et al., 2011; O'Connor et al., 2011), these formations have been intentionally ignored, resulting in a largely enigmatic history of several sedimentary basins of the Northern and Central Kenya Rifts. The "Turkana Grits" are, from the northwestern end of the Kenya Rift to the central segment (Figs. 7 and 8):

- The Lapur Sandstone outcrops widely at the extreme northwest end of Lake Turkana (Thuo, 2009; Tiercelin et al., 2012a);
- The Muruanachok Sandstone outcrops to the west of the central Lake Turkana region (Walsh and Dodson, 1969; Wescott et al., 1993; Morley et al., 1999; Thuo, 2009);
- The Lokone Sandstone and the Lower Auwerwer Sandstone belong to the Lokichar Basin, located to the immediate west of central-southern Lake Turkana (Boschetto et al., 1992; Morley et al., 1992; Morley et al., 1999; Tiercelin et al., 2012b);
- The Mount Porr Sandstone, also known as the Sera Iltomia Formation, outcrops widely on the southeast end of Lake Turkana (Savage and Williamson, 1978; Williamson and Savage, 1986; Tiercelin et al., 2004);
- The Loriu Sandstone (or Lariu Sandstone) outcrops on the southwest end of Lake Turkana (Wescott et al., 1993);

- The Kimwarer and Kamego Formations belong to the Kerio Basin, and the Baringo Basin (Central Kenya Rift), respectively (Lippard, 1973; Chapman and Brook, 1978; Chapman et al., 1978; Renaut et al., 1999; Tiercelin et al., 2004).

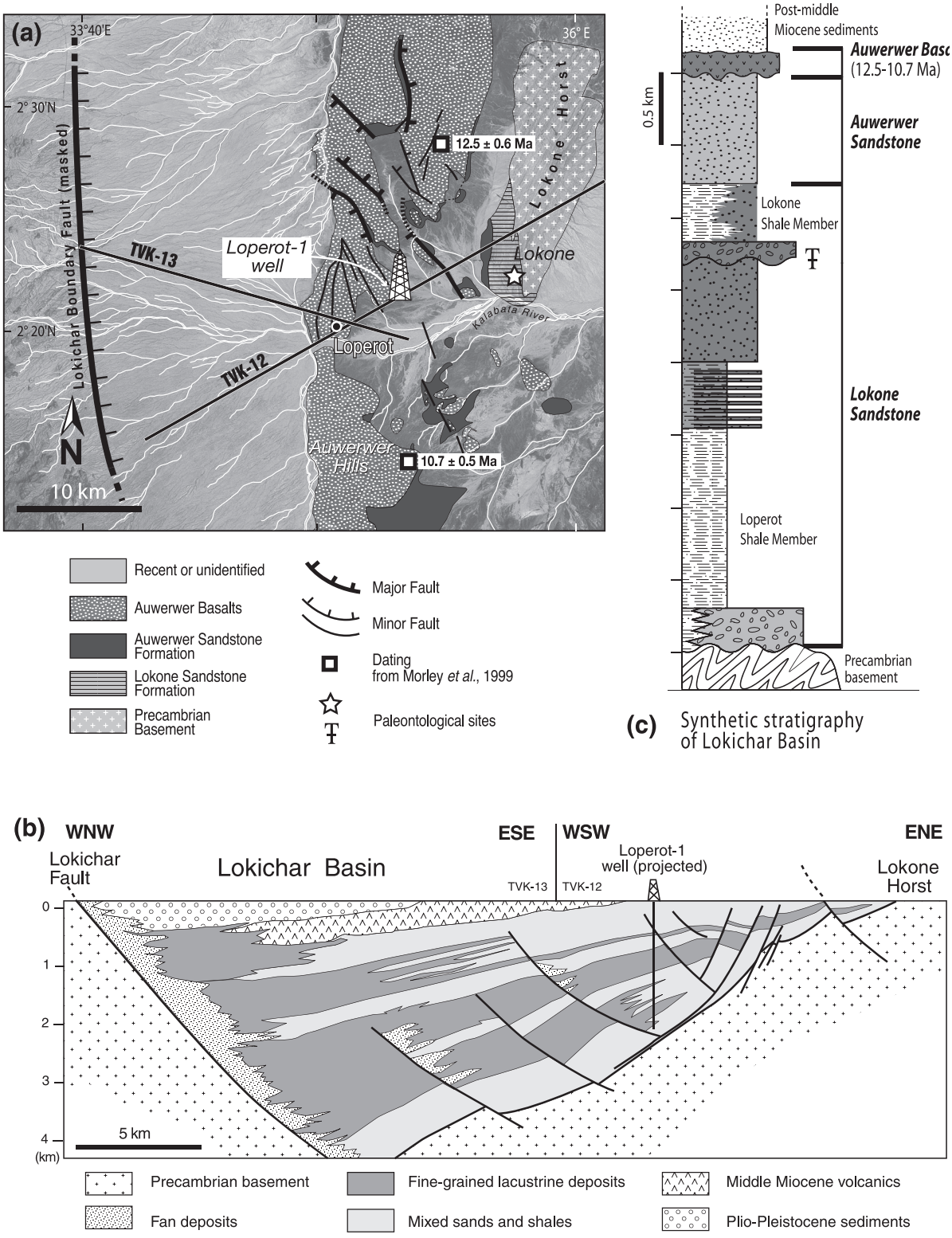

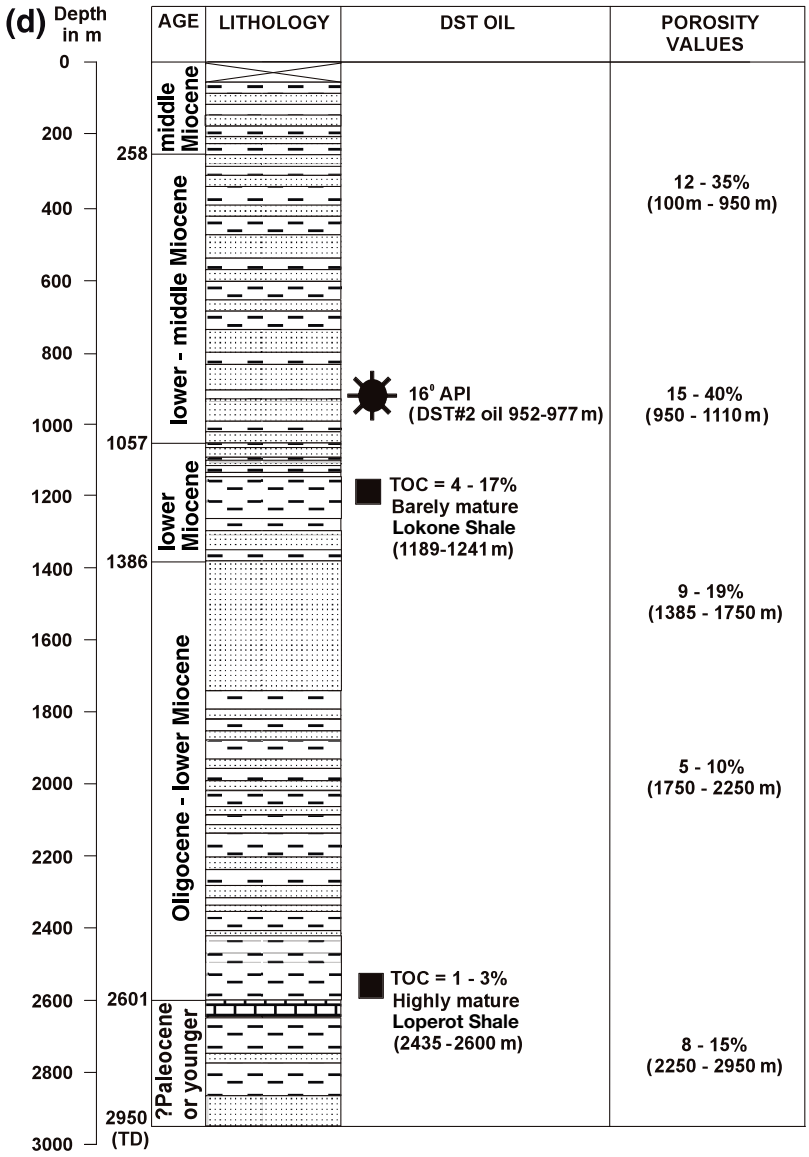

Fig. 6. *(a) Location of the Loperot-1 exploration well and lines TVK 12 and TVK 13. The star shows the location of the discovery of the Oligocene aged verterbrate discovery on the flanks of the Lokone Horst (b) Composite dip cross-section across the Lokichar Basin derived from reflection seismic data - Lines TVK 12 and TVK 13 (modified from Morley et al., 1999, (c) Synthetic lithotratigraphic log, showing the vertical distribution of potential source and reservoir rocks (Loperot and Lokone Shales and Lokone and Auwerwer Sandstone respectively) in the Lokichar Basin. (d) Lithological log of the Loperot 1 well (2950 m) with total organic carbon values of the different source rocks and porosity values of the reservoir rocks. The best source rocks are between ~ 1050 m and 1386 m. Porosity decreases with depth mainly due to compaction (redrawn from Maende et al., 2000).*

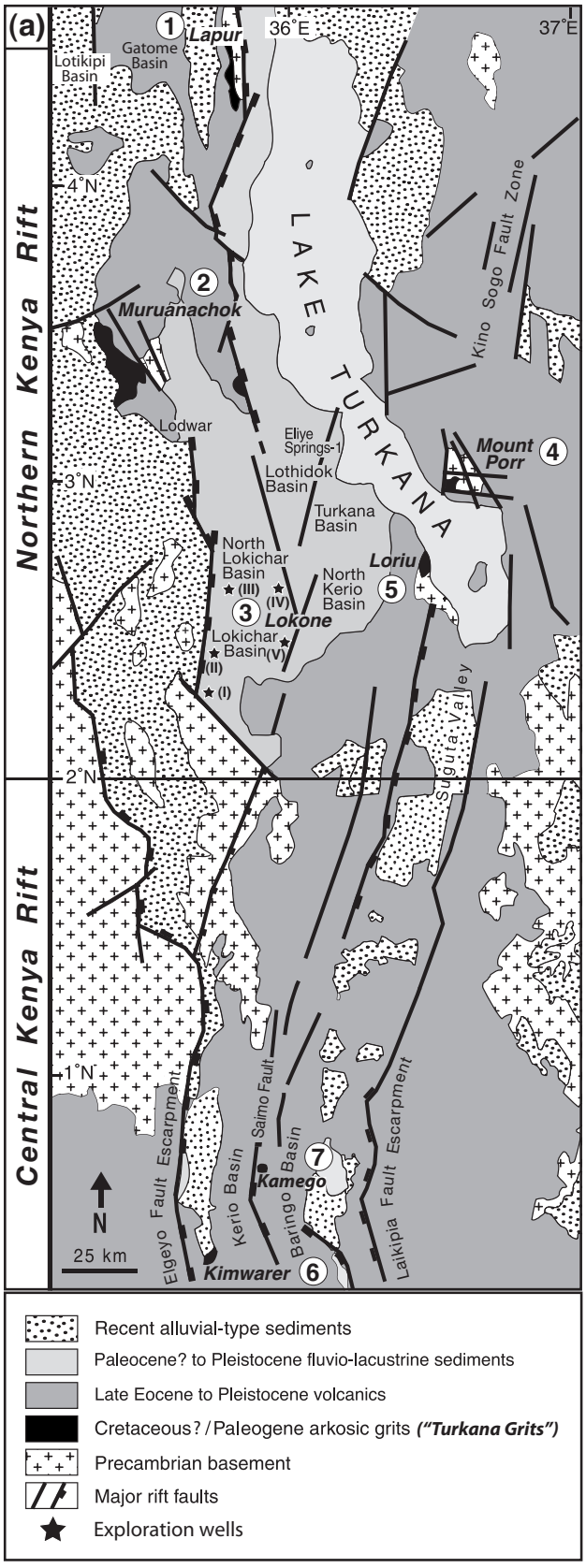

Fig. 7. *(a) Geological sketch map of the Northern Kenya Rift (NKR; Turkana depression) and the Central Kenya Rift (CKR), showing the general structural setting of the Cretaceous?-Paleogene to Neogene sedimentary basins cited in this introduction. Some of the exploration wells drilled in the Lokichar Basin are indicated by black stars: (i) Ngamia-1 (ii) Ekales-1 (iii) Twiga South-1 (iv) Etuko-1 (v) Loperot-1.*

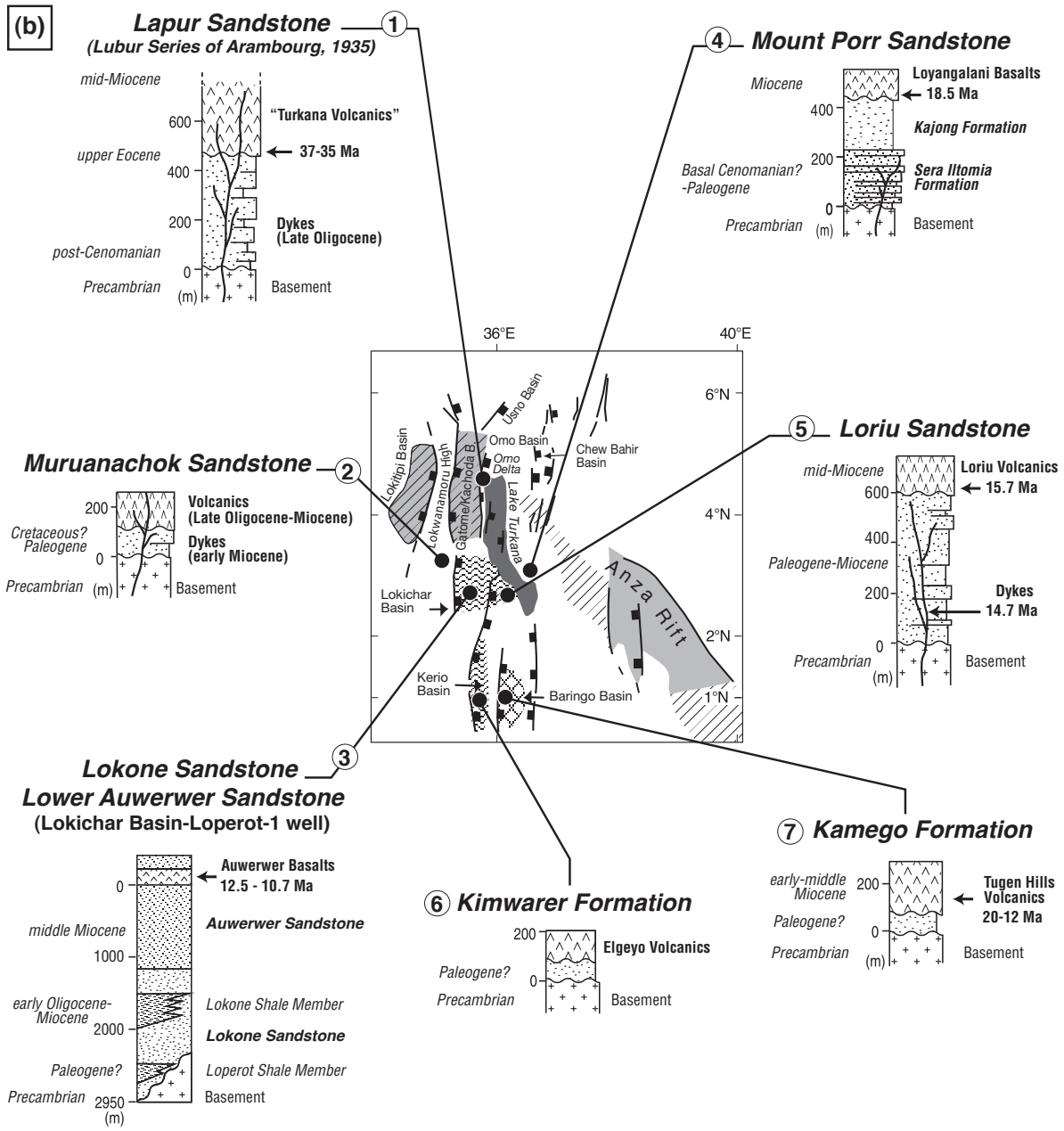

Fig. 7. *(b) The different "Turkana Grits", shown by numbers in a white circle (outcrop areas in black on the geological map), are: - In the NKR: 1: Lapur Sandstone. 2: Muruanachok Sandstone. 3: Lokone Sandstone and Lower Auwerwer Sandstone. 4: Mount Porr Sandstone. 5: Loriu Sandstone. - In the CKR: 6: Kimwarer Formation. 7: Kamego Formation.*

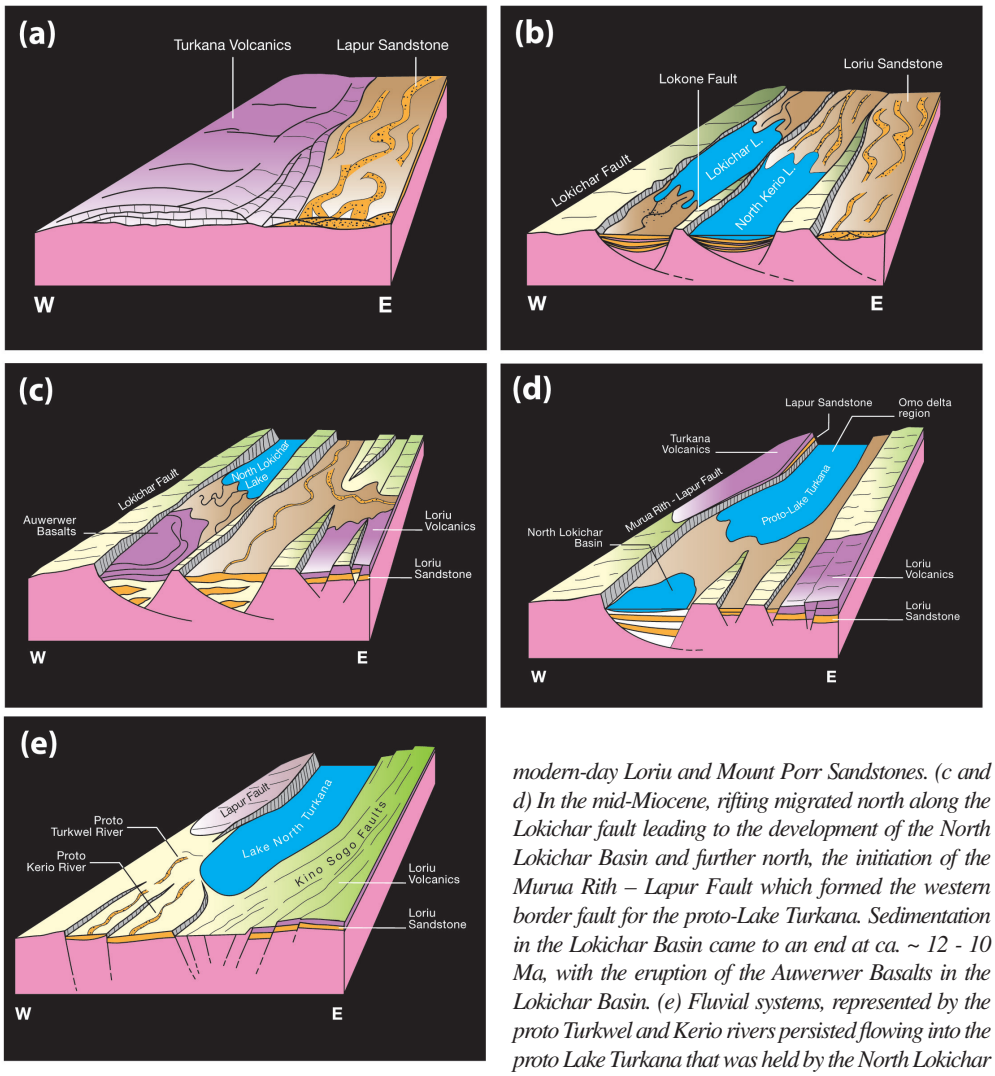

Fig. 8. *Block diagrams illustrating the palaeogeographical reconstruction of successive rift environments in the northern and central segments of the Kenya Rift from upper Cretaceous?-Paleogene to middle-upper Miocene (from Muia and Tiercelin, 2013). Northern Kenya Rift: (a) From Upper Cretaceous to Late Eocene, a wide tectonically and climatically controlled alluvial/fluvial complex, represented by modern-day Lapur Sandstone, persisted in northern Kenya within a wide peneplain that was floored by the Precambrian basement. From Late Eocene, intense volcanic activity in southern Ethiopia and northern Kenya interrupted fluvial sedimentation due to the accumulation of several hundreds of metres of basaltic lavas known as "Turkana Volcanics". (b) To the south, possibly from Eocene times, tectonic activity (rifting) resulted in the initiation of two parallel, N-S oriented half-graben basins, i.e. the Lokichar Basin and the North Kerio Basin, that were subsequently infilled by fluvio-deltaic and lacustrine series. To the immediate east of the North Kerio Basin, a large fluvial system also developed concomitantly and is represented by the modern-day Loriu and Mount Porr Sandstones. (c and d) In the mid-Miocene, rifting migrated north along the Lokichar fault leading to the development of the North Lokichar Basin and further north, the initiation of the Murua Rith – Lapur Fault which formed the western border fault for the proto-Lake Turkana. Sedimentation in the Lokichar Basin came to an end at ca. ~ 12 - 10 Ma, with the eruption of the Auwerwer Basalts in the Lokichar Basin. (e) Fluvial systems, represented by the proto Turkwel and Kerio rivers persisted flowing into the proto Lake Turkana that was held by the North Lokichar Basin. Rifting subsequently migrated to the east leading to the initiation of the development of the South Turkana Basin and the Kino Sogo Fault Zone. Central Kenya Rift: (a1) A similar complex of two parallel, N-S oriented half-grabens, i.e. the Kerio Basin to the west, and the Baringo Basin to the east, developed during the Eocene-Oligocene period, and were infilled by fluvial systems represented by the Kimwarer and Kamego Formations. (b1) Intense volcanic activity developed over the whole area from early to middle Miocene, and results in the accumulation of a 2-3 km thick pile of phonolitic lavas (i.e. the Uasin Gishu and Rumuruti Phonolites) that cover the entire rift system in this area. (c1) From middle Miocene: Reactivation of the major Elgeyo (western rift flank) and Laikipia (eastern rift flank) Border Faults, resulted in the formation of a single sedimentary basin (Kerio-Baringo) that was progressivly occupied by a fluvial environment similar to the Kimwarer-Kamego systems, which evolved with time toward a wide fluvio-lacustrine environment known as the Tambach Lake and which is represented by the Tambach Formation. (d1 and e1) Combined major*

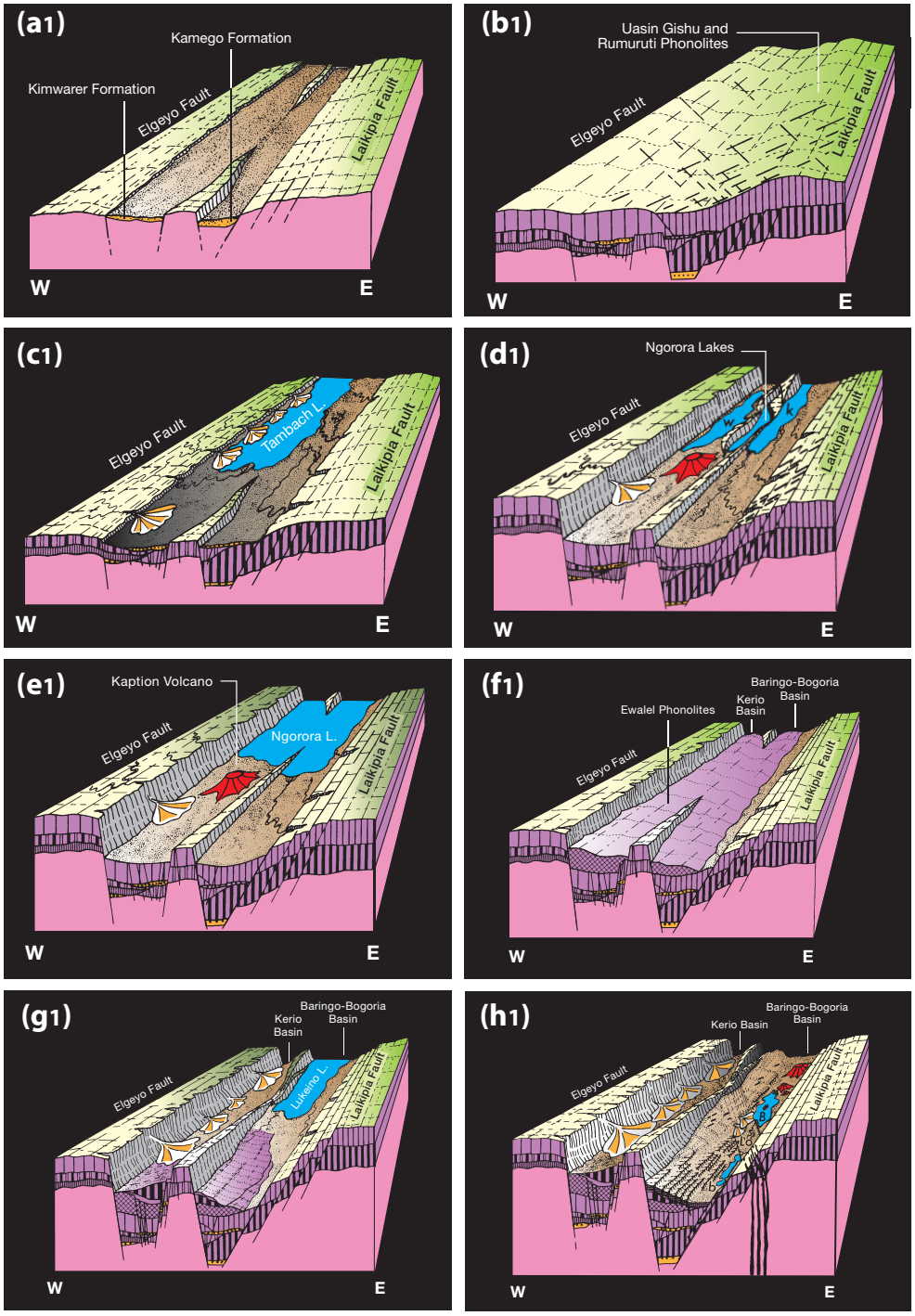

tectonic movements along the Elgeyo and Saimo Faults, minor fault movements along the eastern Laikipia Border Fault, and volcanic events located mainly along the Saimo Fault resulted in the development of multiple small, tectonically-, volcanically- and climatically-controlled sedimentary basins filled by various deposits of fluvial, lacustrine and volcanic/volcaniclastic origin. Several hundreds of metres of these deposits accumulated in the Kerio-Baringo basins and formed the Ngorora Formation, which is dated between ca. 13.06 Ma and 8.5 Ma. (f1) From ca. 9 Ma to 6.7 Ma, intense volcanic activity result in the deposition of the Ewalel Phonolites that completely filled up the Ngorora Basin. (g1 and h1) From ca. 6 Ma to present-day, a combination of faulting migration toward the east and intense volcanic activity into the Baringo Basin has resulted in the development of several sedimentary basins and associated fluvio-lacustrine deposits, i.e. the Lukeino, Chemeron and Kapthurin Formations, which are the precursors of the Pleistocene to Present-day Lake Baringo and Lake Bogoria in the Baringo Basin. To the west and during the same period, the Kerio Basin becomes an inactive rift basin.

WELLS DRILLED IN THE ALBERTINE GRABEN

SERIAL #	EXPLORATION AREA	WELL NAME	OPERATOR	WELL TYPE	YEAR DR	TOTAL DEPTH(Mmdbrt)	Status
2	EA2	Mputa-1	Hardman Petroleum Africa Pty Ltd	Exploration	2005	1,186.5	Oil ang Gas discovery
3	EA2	Waraga-1	Hardman Petroleum Africa Pty Ltd	Exploration	2006	2,010.0	Oil ang Gas discovery
4	EA2	Mputa-2	Tullow Uganda Operations Pty Ltd	Appraisal	2006	1,344.0	Oil discovery
5	EA2	Nzizi-1	Tullow Uganda Operations Pty Ltd	Exploration	2006	1,065.0	Oil ang Gas discovery
6	EA2	Nzizi-2	Tullow Uganda Operations Pty Ltd	Appraisal	2007	981.5	Oil ang Gas discovery
7	EA2	Mputa-3	Tullow Uganda Operations Pty Ltd	Appraisal	2007	973.0	Oil ang Gas discovery
8	EA2	Mputa-4	Tullow Uganda Operations Pty Ltd	Appraisal	2007	1,082.0	Oil ang Gas discovery
9	EA2	Ngassa-1	Tullow Uganda Operations Pty Ltd	Exploration	2007	1,601.5	Gas shows
10	EA2	Taitai-1	Tullow Uganda Operations Pty Ltd	Exploration	2008	1,006.0	Oil discovery
11	EA2	Ngege-1	Tullow Uganda Operations Pty Ltd	Exploration	2008	640.0	Oil ang Gas discovery
12	EA2	Karuka-1	Tullow Uganda Operations Pty Ltd	Exploration	2008	853.0	Oil ang Gas discovery
13	EA2	Kasamene-1	Tullow Uganda Operations Pty Ltd	Exploration	2008	957.0	Oil ang Gas discovery
14	EA2	Kigogole-1	Tullow Uganda Operations Pty Ltd	Exploration	2008	616.0	Oil ang Gas discovery
15	EA2	Mputa-5	Tullow Uganda Operations Pty Ltd	Appraisal	2009	1,231.0	Oil ang Gas discovery
16	EA2	Karuka-2	Tullow Uganda Operations Pty Ltd	Appraisal	2009	879.0	Oil discovery
17	EA2	Ngassa-2	Tullow Uganda Operations Pty Ltd	Appraisal	2009	3,225.0	Oil discovery
18	EA2	Nsoga-1	Tullow Uganda Operations Pty Ltd	Exploration	2009	755.0	Oil discovery
19	EA2	Awaka-1	Tullow Uganda Operations Pty Ltd	Exploration	2009	700.0	Dry
20	EA2	Kigogole-3	Tullow Uganda Operations Pty Ltd	Appraisal	2009	575.0	Oil discovery
21	EA2	Wahrindi-1	Tullow Uganda Operations Pty Ltd	Exploration	2009	1,058.0	Oil discovery
22	EA2	Ngara-1	Tullow Uganda Operations Pty Ltd	Exploration	2009	685.0	Oil ang Gas discovery
23	EA2	Kasamene-2	Tullow Uganda Operations Pty Ltd	Appraisal	2010	866.0	Oil ang Gas discovery
24	EA2	Kasamene-3/3A	Tullow Uganda Operations Pty Ltd	Appraisal	2010	1,130.0	Oil ang Gas discovery
25	EA2	Nzizi-3	Tullow Uganda Operations Pty Ltd	Appraisal	2010	974.0	Oil ang Gas discovery
26	EA2	Nsoga-5	Tullow Uganda Operations Pty Ltd	Appraisal	2010	589.0	Oil discovery
27	EA2	Kigogole-5	Tullow Uganda Operations Pty Ltd	Appraisal	2010	622.0	Oil discovery
28	EA2	Kigogole-2	Tullow Uganda Operations Pty Ltd	Appraisal	2010	738.0	Oil discovery
29	EA2	Kigogole-4	Tullow Uganda Operations Pty Ltd	Appraisal	2010	676.0	Oil discovery
30	EA2	Nsoga-5	Tullow Uganda Operations Pty Ltd	Appraisal	2010	882.0	Oil discovery
31	EA3	Turaco-1	Heritage Oil and Gas Ltd	Exploration	2002	2,487.7	Gas shows
32	EA3	Turaco-2	Heritage Oil and Gas Ltd	Exploration	2003	2,962.5	Oil and Gas shows
33	EA3	Turaco-3	Heritage Oil and Gas Ltd	Exploration	2004	2,850.0	Oil and Gas shows
34	EA3A	Kingfisher-1/1A/1B	Heritage Oil and Gas Ltd	Exploration	2006	2,125.0	Oil ang Gas discovery
35	EA3A	Kingfisher-2/2A	Heritage Oil and Gas Ltd	Appraisal	2008	3,906.0	Oil discovery
36	EA3A	Kingfisher-3/3A	Heritage Oil and Gas Ltd	Appraisal	2008	3,200.0	Oil ang Gas discovery
37	EA1	Ngiri-1	Heritage Oil and Gas Ltd	Exploration	2008	911.0	Oil ang Gas discovery
38	EA1	Jobi-1	Heritage Oil and Gas Ltd	Exploration	2008	637.0	Oil ang Gas discovery
39	EA1	Rii-1	Heritage Oil and Gas Ltd	Exploration	2008	705.1	Oil ang Gas discovery
40	EA1	Ngiri-2	Heritage Oil and Gas Ltd	Appraisal	2010	892.0	Oil ang Gas discovery
41	EA1	Mpyo-1	Heritage Oil and Gas Ltd	Exploration	2010	465.0	Oil discovery
42	EA4B	Ngaji-1	Dominion Petroleum (U) Ltd	Exploration	2010	1,769.0	Gas shows
43	EA5	Iti-1	Neptune Petroleum Ltd(now Tower Resources)	Exploration	2009	592.0	Dry
44	EA5	Avivi-1	Neptune Petroleum Ltd(now Tower Resources)	Exploration	2010	764.0	Dry

Table 1

Exploration and appraisal wells drilled in the Albertine Graben between 2002 and 2010 (PEPD, 2011).

Despite the technical success of the Loperot-1 drilling campaign that highlighted the presence of good reservoir and excellent source rock units in the Lokichar Basin, the drilling results at that time did not meet the technical threshold required to justify additional exploration in the basin. A long exploration hiatus followed in East Africa until renewed interest was elicited by discussions around the 'Peak Oil' as initially proposed by Hubbert (1956) who predicted that global petroleum consumption would surpass production at the turn of the century, and that new giant discoveries were required to come online to bridge the impending gap. Focus was again drawn to the Albertine Graben in Uganda where numerous oil seeps had been previously documented (Wayland, 1925). In the period between 2002 and 2007, seven exploration wells and four appraisal wells had been drilled in the Albertine Graben. These wells not only confirmed the existence of a working petroleum system but also the presence of multiple exploitable accumulations. Flow of hydrocarbons was confirmed in all wells (PEPD, 2014) (Table 1).

Recent geochemical analyses of the Ugandan oil seeps point to two types of depositional environment for the source rocks: a freshwater lacustrine environment, or a saline to hypersaline lake environment (PEPD, 2008; Abeinomugisha et al., 2012). The tests also reveal differential dominance of organic matter within the source rock units; i.e. the Kibuku oil seep indicates a significant contribution from higher (terrestrial) plant input while the Kibiro oil seep shows a preferential accumulation of algal derived organic matter as evidenced by the relative amounts of triterpane and sterane compounds in the former and the abundance of freshwater derived Botrycoccanes in the latter (PEPD, 2008; Kalisa, 2013).

The reservoir rocks of the Albertine Graben are mid-Miocene to Pleistocene in age and are dominated by the coarse clastics of the Kisegi and Kaiso Formations which were intercepted by the Waki-1 exploration well (Rose and Curd, 2005; Abeinomugisha and Kasande, 2012) (Fig. 9). The 427-m thick Kisegi Formation is a predominantly sandy unit made-up of stacked channel fills and has an onlapping relationship with the basement schists of the Rwenzori Mountains (Abeinomugisha and Kasande, 2012). The Kaiso Formation is 560 m thick, 200 m of which are predominantly shale units with clayey intercalations, while conglomerates with few clay units domi-

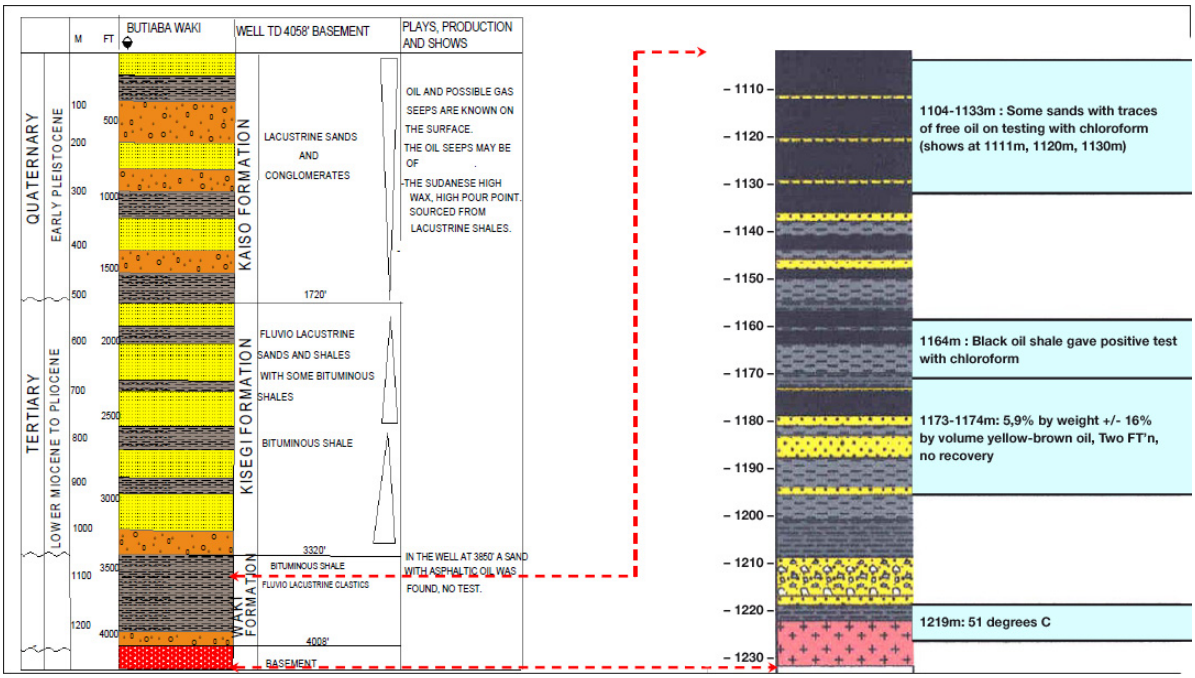

Fig. 9. *Lithostratigraphic log of the Waki-1 well drilled in the Lake Albert Basin, showing the Kisegi and Kaiso Formations (PEPD, 2008). The Waki-1 well was drilled in 1938 and was the first to reveal the stratigraphy of the Albertine Graben pre- and syn-rift sections, which comprises of conglomerates and fluvial deposited sands that are intercalated with organic-rich lacustrine shales.*

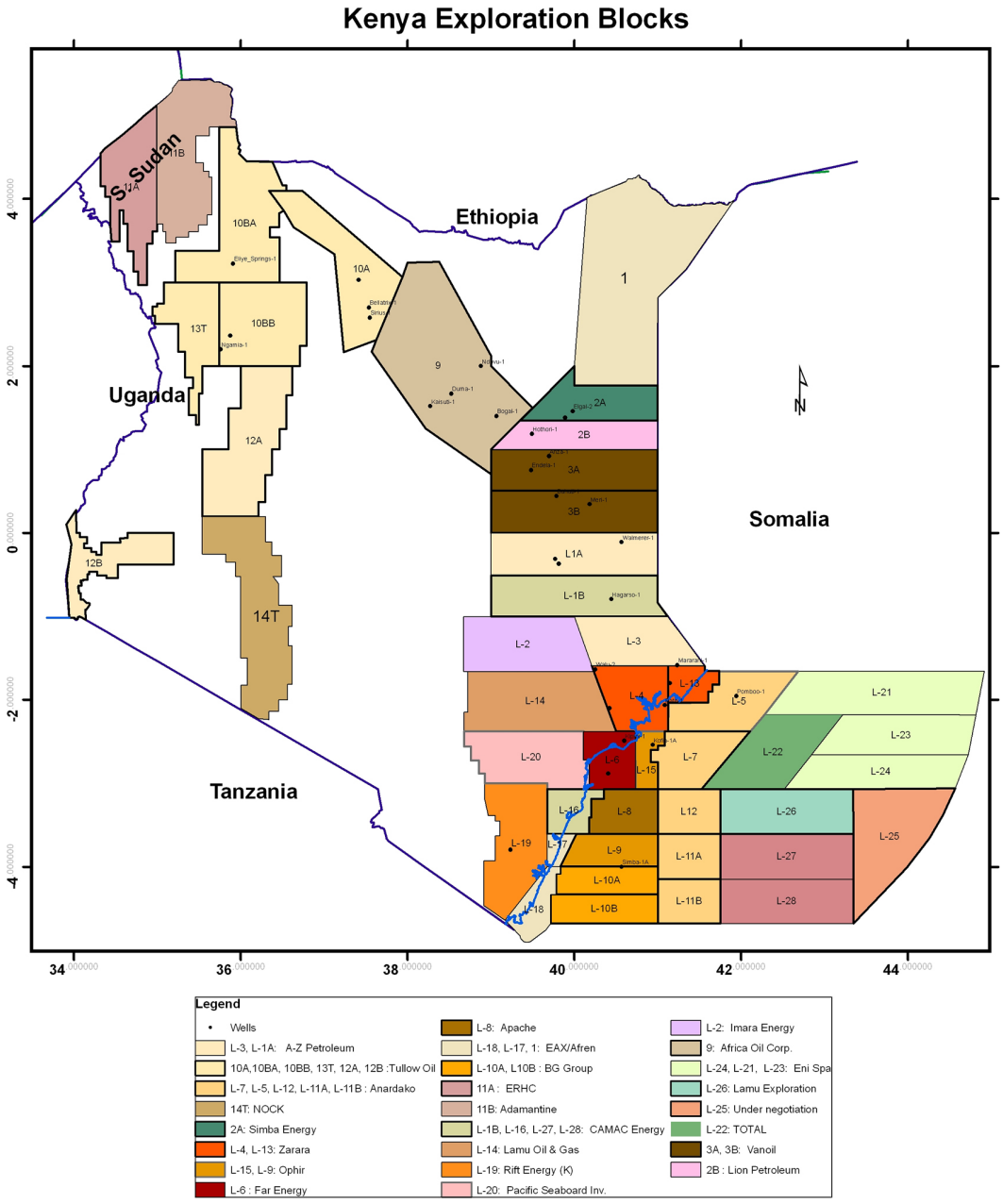

Fig. 10. *The Republic of Kenya oil and gas exploration block map showing the acreage distribution in Kenya and block operators (National Oil Corporation of Kenya, 2014).*

nate in the upper 250 m (Karp et al., 2012). The Kisegi and Kaiso Formations provide excellent reservoir quality with porosities of between 22% and 32% that were measured from shallow cores in the Kibiro and Kibuku areas. This excellent reservoir quality has been confirmed to persist at depth by the Waraga-1, Mputa-1 and Mputa-2 wells, the former having porosities ranging between 27-30% and permeabilities between 6-8 Darcies while the latter have porosities ranging between 28-32% and permeabilities ranging between 200-1000 md (PEPD, 2008).

This remarkable success in what were previously deemed to be unviable oil prospects demanded that prospects, which had earlier been discarded, be revisited and reappraised. Thus, focus was again shifted to the Lokichar Basin and surrounding deep basins in the Northern Kenya Rift. The British company Tullow Oil PLC entered Kenya in 2010, after signing agreements with Africa Oil and Centric Energy to gain a 50% operated inte-

rest in five onshore licences: 10BA, 10BB, 10A, 12A and 13T (Fig. 10). The company drilled its first well Ngamia-1 in the Lokichar Basin in 2012. This well, though it was terminated (at 1041 m depth) before its prognosed terminal depth due to excessive fluid loss, successfully recorded the presence of commercially viable petroleum accumulations in thick fluvial packages within the basin (> 100 m net pay) (Africa Oil Corporation, 2014).

Like the Loperot-1 well before it, the Ngamia-1 well perforated the Auwerwer Sandstone, then the Lokone

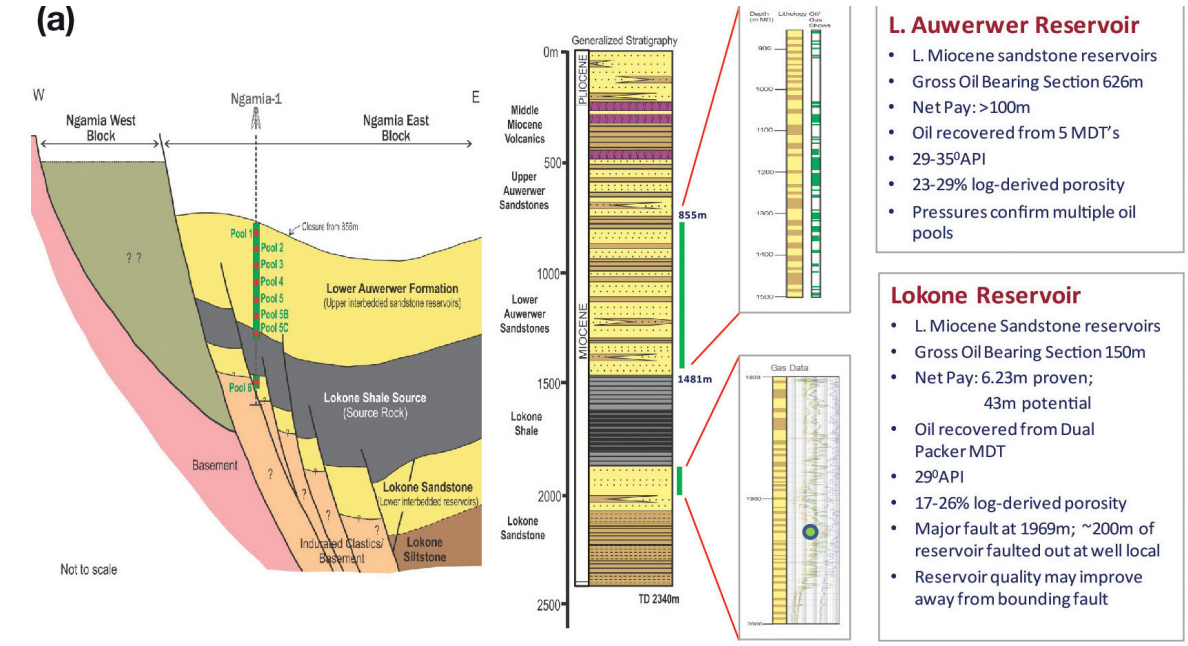

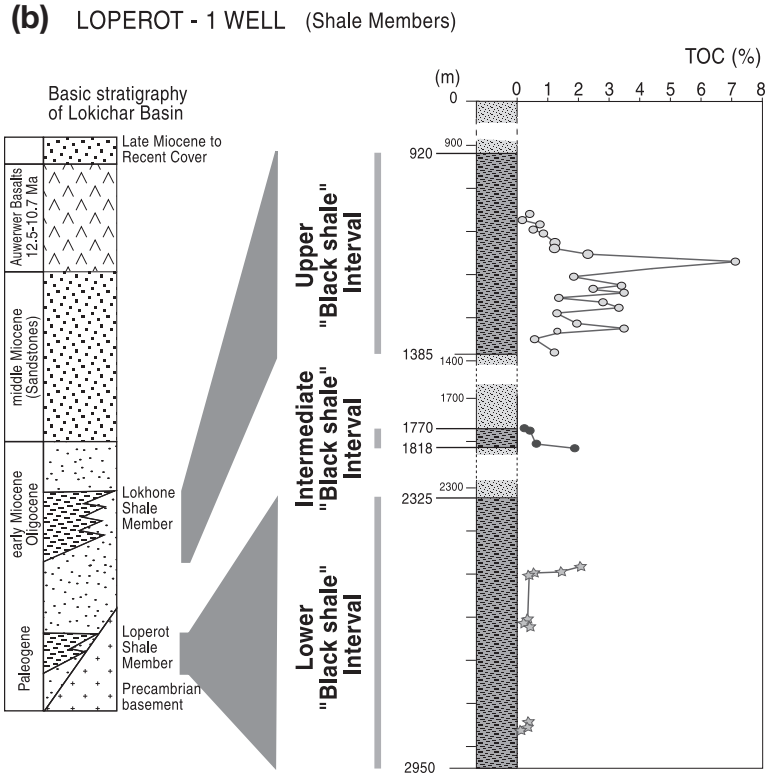

Fig. 11. *(a) Simplified cross-section diagram showing the general structural framework of the Ngamia-1 well drilled in 2012 in the Lokichar Basin, Northern Kenya Rift (from Africa Oil Corporation, 2014). (b) Lithostratigraphic log of the Loperot-1 well drilled in 1992 in the Lokichar Basin, showing the stratigraphic succession of the Paleogene to early Miocene/ Oligocene - Lokone Sandstone that encampasses the Lokone and Loperot Shale Members, followed by the mid-Miocene Auwerwer Sandstone that are capped by the Auwerwer Basalts. The Lokone Shale has considerable higher organic contents when compared to the Loperot Shale ranging between 0.5-7.6% (from Talbot et al., 2004). (c) Petrophysical logs illustrating the stratigraphic correlation between the Ngamia-1, Twiga-1, Etuko-1 and Loperot-1 exploration wells drilled in the Lokichar Basin (from Africa Oil Corporation, 2014).*

(c)

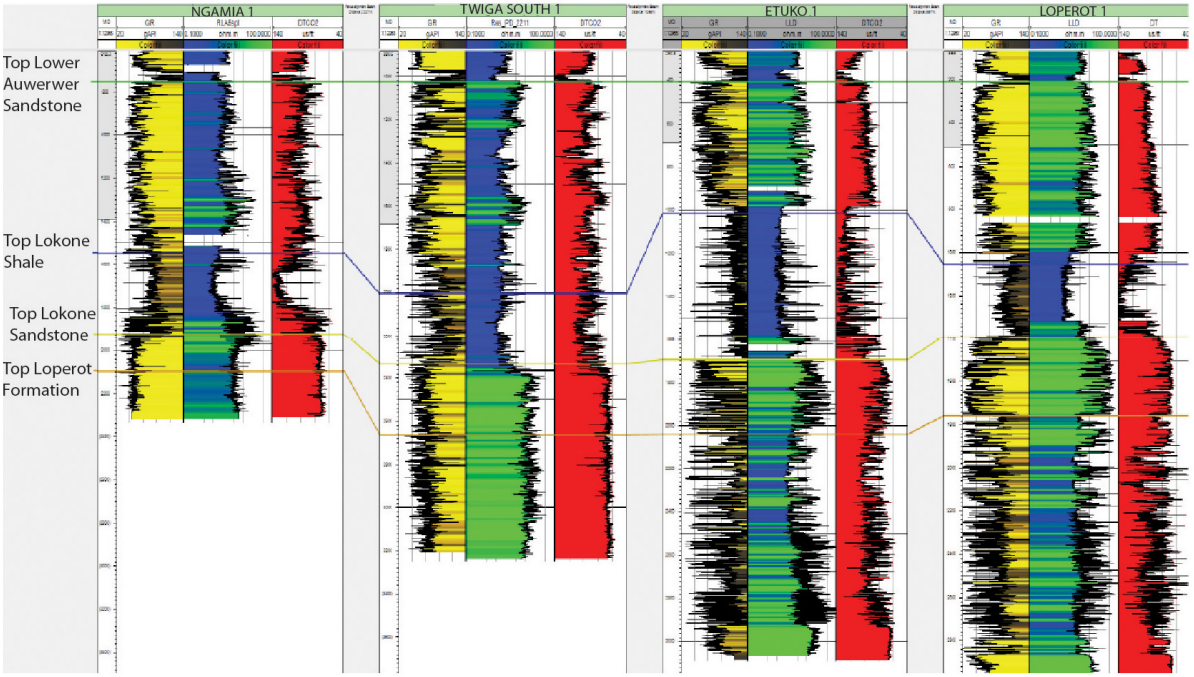

Sandstone, respectively (Fig. 11a, b). In this well, only the Lower Auwerwer Sandstone (600-m thick) was tested and it exhibits porosities between 23-29% (from core and log analysis) and permeabilities of as much as 3 Darcies (Africa Oil Corporation, 2011). Further field appraisal of the Lokichar oilfield has seen the drilling of eight new wells all of which have penetrated similar stratigraphic units (Fig. 11c).

The Lokone Sandstone and the lower part of the Auwerwer Sandstone have been previously classified as being part of the "Turkana Grits", following the original description by Murray-Hughes (1933) (Fig. 7b). This is of particular interest for petroleum exploration purposes, especially when determining potential basins and prospects for exploration. A re-look at the "Turkana Grits" is thereby imperative as those formations that have similar chrono-stratigraphic configurations as those of the Lokichar Basin could hold significant amounts of hydrocarbons.

This is particularly so for the poorly studied sedimentary formations such as the Kimwarer and Kamego Formations in the Central Kenya Rift, and the Loriu Sandstone in the Northern Kenya Rift. Until now, these three sedimentary formations have not been precisely constrained sedimentologically and chronostratigraphically. Consequently, the aim of the second part of this work, titled "The Turkana Grits: Potential Hydrocarbon Reservoirs in the Northern and Central Kenya Rifts", is to present the first results of the sedimentologic and diagenetic study of the three poorly known, basal sedimentary formations of the Northern (NKR) and Central Kenya Rifts (CKR): the Kimwarer Formation (or KF) in the Kerio Basin (CKR), the Kamego Formation (or KAF) in the Baringo Basin (CKR), and the Loriu Sandstone (or LOS) in the North Kerio Basin, at the southwest end of Lake Turkana (NKR) (Fig. 7b). A determination of the chrono-stratigraphic location of these three sedimentary formations will also be outlined here from the results of Ar-Ar dating conducted on the different volcanic units associated to them. In this second part, field observations, facies analysis, petrographic characterization and diagenetic evolution, etc., will be combined to ultimately determine the reservoir potential of the different sandstone formations discussed, and also to precisely evaluate the reservoir potential at the scale of 'Oil Provinces' for the northern and central segments of the Kenya Rift. The third and final part of this work will be the discussion and conclusion section and will then present in detail the overall potential of the reservoir quality of the "Turkana Grits" in the northern and central segments of the Kenya Rift.

The "Turkana Grits": Potential Hydrocarbon Reservoirs of the Northern and Central Kenya Rifts

Introduction

In the course of the last forty years, studies of the sedimentary basins that comprise the northern (Northern Kenya Rift - NKR), and median (Central Kenya Rift - CKR) segments of the Kenya Rift have largely been geared towards understanding the evolution of predominantly fossil mammals, their environmental significance and location within a palaeontological and palaeoanthropological chronological framework (Leakey and Leakey, 1978; Hill, 1999; Leakey et al., 2011) (Fig. 7a). As a consequence, azoic sediments identified within the NKR and CKR, i.e. the "Turkana Grits" as initially described in the pioneering works of Murray-Hughes (1933), Arambourg (1933a, b) and Fuchs (1939), have been intentionally ignored due to the absence of such fossils, resulting in a largely enigmatic history of several sedimentary basins in these parts of the Kenya Rift (Fig. 7a). Most of the "Turkana Grits" are still considered azoic with the exception of the Lapur Sandstone in which dinosaur remains have been discovered in its lowermost part (Arambourg and Wolff, 1969; Sertich et al., 2005), and the Lokone Sandstone where the oldest mammalian faunas in East Africa were recently discovered (Ducrocq et al., 2010). Nevertheless, the importance of a stratigraphic and sedimentological reconsideration of some of these sedimentary basins has been strongly enhanced by their analogous nature to the possibly older but oil-rich rift basins of Southern Sudan (Schull, 1988; Genik, 1993; Mohamed et al., 1999) and Northern Kenya (Morley et al., 1995; Talbot et al., 2004; Tiercelin et al., 2004, 2012a, b; Thuo, 2009; Neumaier et al., 2013) (Fig. 3b).

Between the equator and 1°N in the Central Kenya Rift, gravity, seismic reflection and magneto-telluric investigations have confirmed basinal depths for the Kerio (KB) and Baringo (BB) Basins, that average 6-7 km (Mugisha, 1994; Mugisha et al., 1997; Hautot et al., 2000) (Fig. 12). The eastern Baringo Basin, due to its excellent and accessible sedimentary rock exposures which have yielded important paleontological data, is well-constrained both stratigraphically and sedimentologically, as well as in terms of its deep structure and geological evolution (Tiercelin et al., 1987; Hill, 1999; Renaut et al., 1999; Hautot et al., 2000). This however is not the case in the western Kerio Basin. The general stratigraphy of the Kerio Basin was established in the 1960s and 1970s, with the identification of several sedimentary formations lying above the Precambrian basement and between series of lava flows that yielded few radiometric ages (Bishop et al., 1971; Chapman et al., 1978; Chapman and Brook, 1978). Very little is known about the subsurface geometry of the basin fill despite geophysical work stemming from the Kenya Rift International Seismic Projects (KRISP) of 1975 and 1990 (e.g. Maguire et al., 1993; Katana, 1996; Simiyu, 1996) that were focused on the deep tectonic controls and anomalous mantle dynamics that exist far below the Kerio Basin. Despite the success in creating models of the deep mantle-centric structural dynamics, these studies did not result in the enhanced understanding of the basins' shallow crustal make-up.

To fill this gap in knowledge, in 1989, the National Oil Corporation of Kenya acquired industrial reflection seismic data with an aim of constraining the volcano-sedimentary pile that comprises the Kerio Basin fill, and more importantly to determine specific sedimentary horizons that had intrinsic hydrocarbon potential either as source or reservoir rocks (Mugisha, 1994; Mugisha et al., 1997). A few years later, a detailed geophysical survey was conducted in the Baringo Basin by means of vertical electric soundings and magneto-telluric techniques. This program contributed to a new understanding of the evolution of the Kerio and Baringo Basins, particularly in terms of the early stages of basin development (Hautot et al., 2000) (Fig. 7, a1 – h1). Within the same program, a detailed field study of two major fluvio-lacustrine sequences of Miocene age identified in the Kerio Basin, i.e. the Tambach and the Ngorora Formations, originally described by Shackleton (1951), Bishop and Chapman (1970), Lippard (1972), and Bishop and Pickford (1975), respectively, was conducted to contribute to the production of a detailed palaeoenvironmental reconstruction as well as an evaluation of the possible hydrocarbon potential of these formations (Ego, 1994; Renaut et al., 1999) (Fig. 12b). However, in this study, limited attention was given to the pre-volcanic sedimentary deposits that were surprisingly not considered as priority targets for hydrocarbon exploration.

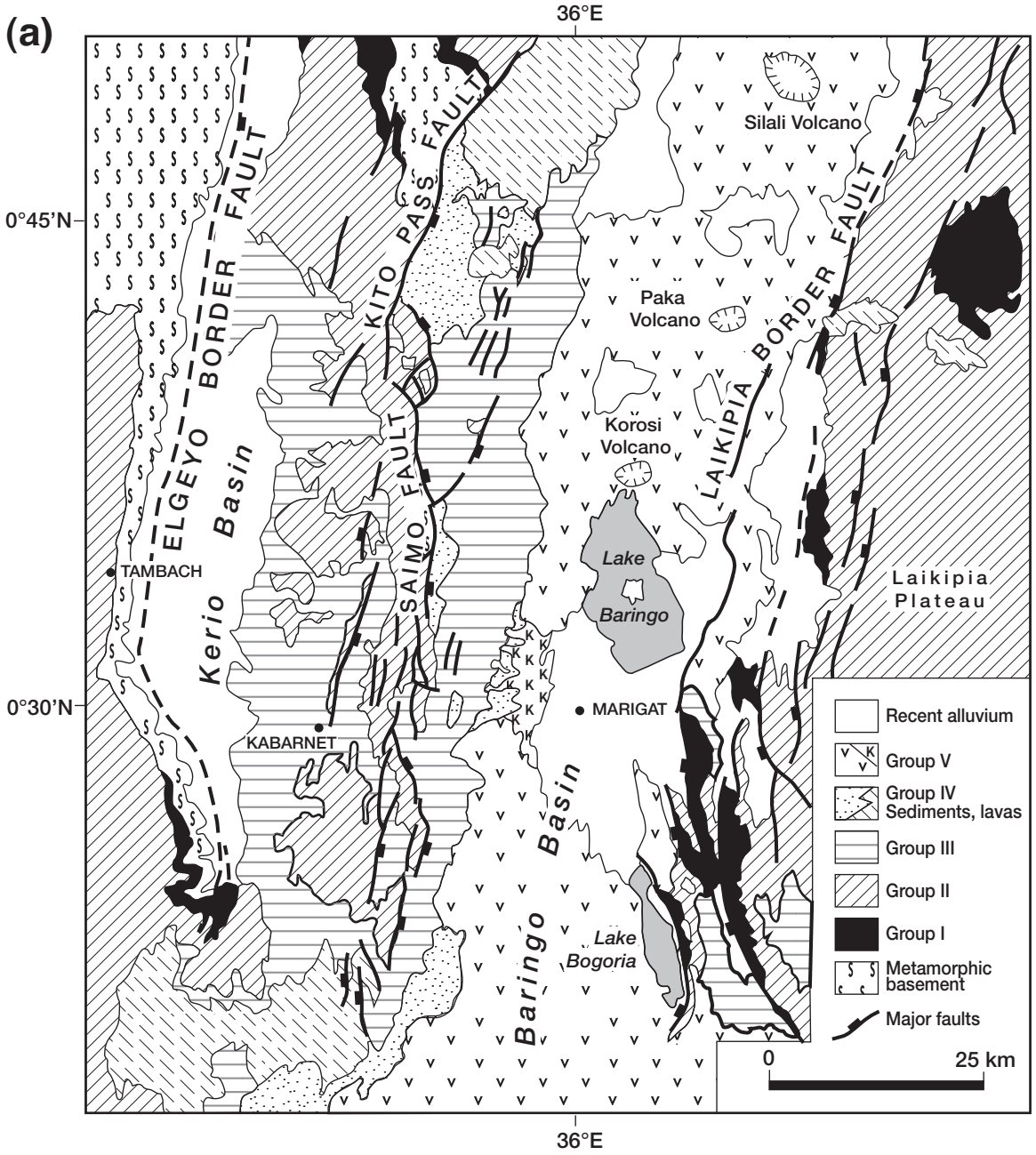

Fig. 12. *(a) Geological map of the Central Kenya Rift, showing the two Kerio (KB) and Baringo (BB) Basins, and the major border faults that delineate the central rift segment to the west (Elgeyo Border Fault) and the the east (Laikipia Border Fault), as well as the two major faults that bound the Baringo Basin to the west (Saimo and Kito Pass Faults). This map also shows the general sequence of volcanic, structural and sedimentary events in the Kerio and Baringo Basins, as defined by King and Chapman (1972) and Hackman et al., (1990): - Above the Precambrian basement: - Group I (Early Miocene) – Basalts (Elgeyo and Samburu Basalts) and associated sediments; - Group II (Middle Miocene) – Phonolites of Rift shoulders and Tugen Hills (Chof, Uasin Gishu, Sidekh and Tiim). Faulting on N- to NNE- and NW-trends; - Group III (Late Miocene) – Basalts and flood trachytes; First episode of major faulting on N- to NNE-trends; - Group IV (Pliocene) – Trachyte strato-volcanoes and associated sedimentary units; - Group V (Plio-Pleistocene) - Flood lavas and major axial volcanoes (Korosi, Paka, Silali). Faulting (second major episode) on NNE-trend. (b), (c) Representation of the rift stratigraphic series across the Kerio and Baringo Basins: SEE: Southeast Elgeyo; NEE: Northeast Elgeyo; KB: Kerio Basin; TH: Tugen Hills; BB: Baringo Basin (modified from Chapman et al. (1978) and Hautot et al. (2000). (d) Two successive evolutionary stages of the Kerio-Baringo Basins, during Paleogene to Early Miocene, and from Pleistocene to Present-day (from Hautot et al., 2000).*

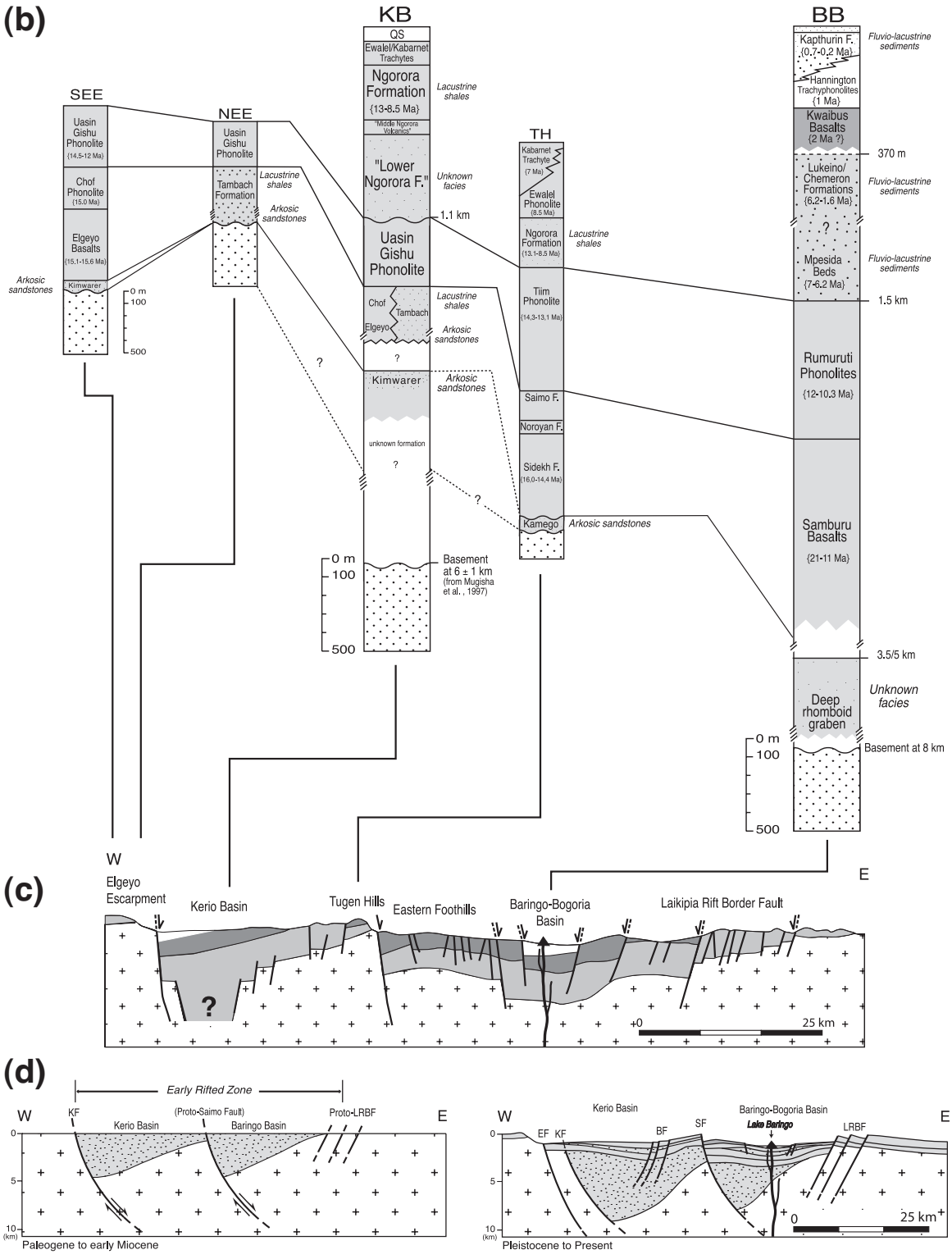
(b)
SEE
NEE
KB
TH
BB
Uasin Gishu Phonolite (14.5-12 Ma)
Chof Phonolite (15.0 Ma)
Elgeyo Basalts (15.1-15.6 Ma)
Kimwarer
Arkosic sandstones
Tambach Formation
Lacustrine shales
Arkosic sandstones
0 m
100
500
QS
Ewalel/Kabarnet Trachytes
Ngorora Formation {13-8.5 Ma}
"Middle Ngorora Volcanics"
"Lower Ngorora F."
Unknown facies
1.1 km
Uasin Gishu Phonolite
Chof
Tambach
Elgeyo
Lacustrine shales
Arkosic sandstones
Kimwarer
Arkosic sandstones
unknown formation
Basement at 6 ± 1 km (from Mugisha et al., 1997)
Kabarnel Trachyte (7 Ma)
Ewalel Phonolite (8.5 Ma)
Ngorora Formation (13.1-8.5 Ma)
Lacustrine shales
Tiim Phonolite (14.3-13.1 Ma)
Saimo F.
Noroyan F.
Sidekh F. (16.0-14.4 Ma)
Kamego
Arkosic sandstones
Kapthurin F. (0.7-0.2 Ma)
Hannington Trachyphonolites (1 Ma)
Fluvio-lacustrine sediments
Kwaibus Basalts (2 Ma ?)
370 m
Lukeino/ Chemeron Formations (6.2-1.6 Ma)
Fluvio-lacustrine sediments
Mpesida Beds (7-6.2 Ma)
Fluvio-lacustrine sediments
1.5 km
Rumuruti Phonolites (12-10.3 Ma)
Samburu Basalts (21-11 Ma)
3.5/5 km
Deep rhomboid graben
Unknown facies
Basement at 8 km
(c)
W
E
Elgeyo Escarpment
Kerio Basin
Tugen Hills
Eastern Foothills
Baringo-Bogoria Basin
Laikipia Rift Border Fault
25 km
(d)
Early Rifted Zone
W
E
KF
(Proto-Saimo Fault)
Proto-LRBF
Kerio Basin
Baringo Basin
Paleogene to early Miocene
Kerio Basin
Baringo-Bogoria Basin
Lake Baringo
EF
KF
BF
SF
LRBF
25 km
Pleistocene to Present

Introduction

In northern Kenya, many of the sedimentary basins have been extensively explored (see General Introduction) and have been interpreted as having 5-8 km thick basin fills composed of fluvial and lacustrine sediments of Paleogene to Neogene age (Wescott et al., 1993; Morley et al., 1999; Tiercelin et al., 2004; Thuo, 2009) that are locally associated with Eocene to Miocene volcanic piles (Thuo, 2009). Often discussed in conjunction with the Lokichar Basin is the poorly constrained North Kerio Basin (NKB) which is a 90 km long and 35 km wide basin that is separated from the Lokichar Basin by the Lokone Horst (Lokone Faults' uplifted footwall) and bounded to the east by the horst's eastern east-dipping scarps, which today have no topographic expression (Wescott et al., 1993; Morley et al., 1999; Tiercelin et al., 2012b) (Fig. 13). Study of the lowermost sedimentary formations within the North Kerio Basin that outcrop in the Loriu area have previously been hampered by difficult accessibility and lack of amenities due to the outcrops' remote location as well as (perceived) insecurity in the area. This has resulted in the Loriu Sandstone being one of the most poorly studied sedimentary formations in the Kenya Rift (Wescott et al., 1993; Morley et al., 1999a).

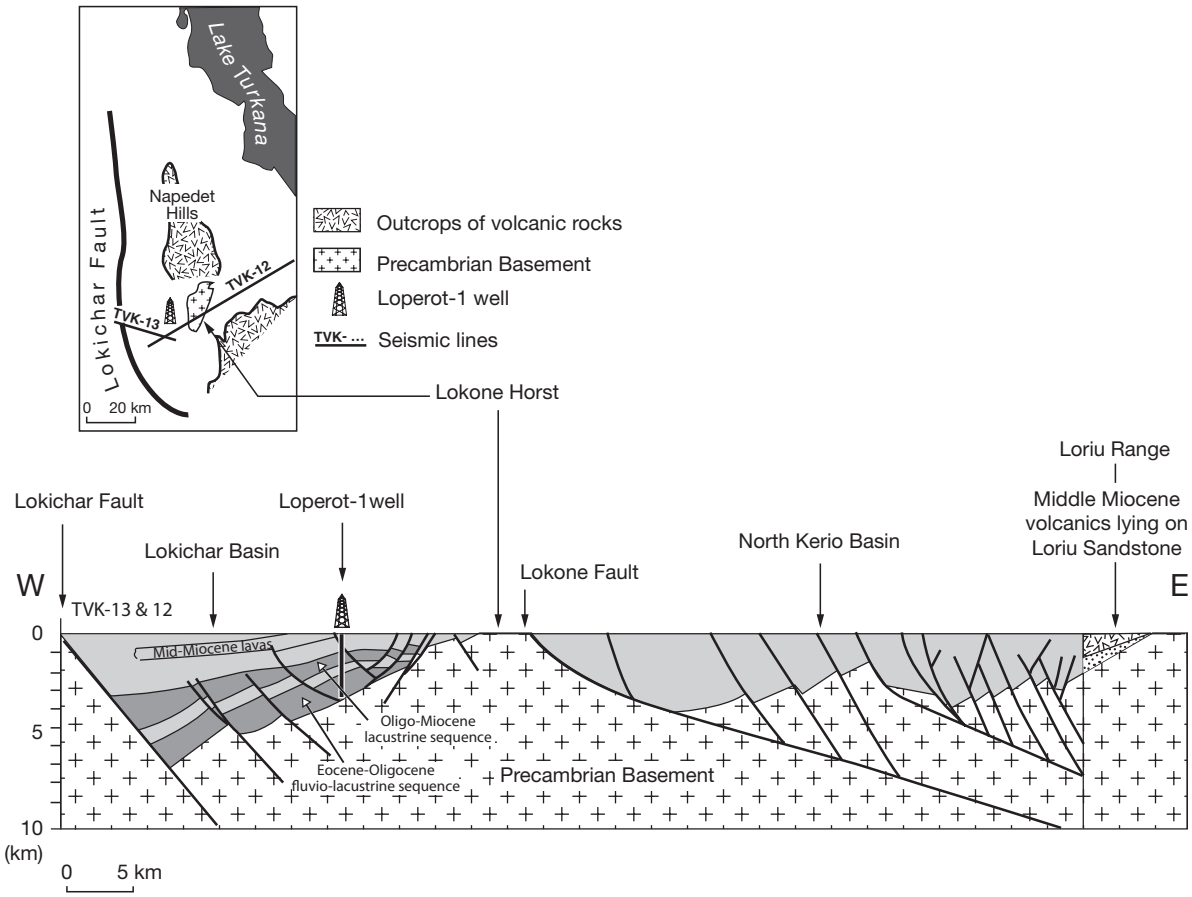

Fig. 13. *Cross-section based on the interpretation of the Amoco Kenya TVK-13 and 12 seismic lines showing the Lokichar Basin (Eocene - middle Miocene) to the west, bounded by the major Lokichar Fault, and the North Kerio Basin (Paleogene - middle Miocene) to the east, bounded to the west by the Lokone Fault. The two basins are separated by the Lokone Horst, which is made of basement and also forms the flexural margin of the Lokichar Basin (redrawn from Morley et al., 1999a).*

Introduction

The Loriu Sandstone (or LOS) (previously named Lariu Sandstone; Wescott et al., 1993) has previously been equated to the Lokone Sandstone in the adjacent Lokichar Basin (e.g. Morley et al., 1999; Thuo, 2009; Tiercelin et al., 2012), and the Mount Porr Sandstone in the Mount Porr region, southeast end of the Turkana Basin (Williamson and Savage, 1986; Wescott et al., 1993; Tiercelin et al., 2004, 2012) (Fig. 7b). The Loriu Sandstone is considered to be part of the "Turkana Grits" (sensu Murray-Hughes, 1933) owing to its occurrence above the basement and below Miocene volcanic rocks (Wescott et al., 1993). The LOS has previously been described as an up to 610-m thick, repetitive sequence of channelized, coarse-pebbly arkosic, basement-derived sandstones with few siltstone-mudstone intercalations (Wescott et al., 1993). The minimum radiometric age of the LOS has been given as 15 ± 0.7 Ma (from the age of a lava flow sampled from the base of the volcanic pile overlying the LOS), confirmed, within the uncertainties, by a dyke intruding the sedimentary formation, that has been dated at 14.7 ± 0.17 Ma (radiometric ages obtained by the Teledyne Isotopes Company, using whole rock K-Ar techniques) (Wescott et al., 1993).

The purpose of this section of the thesis is to present the results of the first detailed structural, chronostratigraphic, sedimentological and diagenetic study of the two bottom-most sedimentary formations identified in the Central Kenya Rift (Kerio and Baringo Basins), and of the last, poorly studied sedimentary formation in the Northern Kenya Rift (North Kerio Basin). Focus is drawn to the Kimwarer Formation (or KF) in the Kerio Basin that was described during the 60s-70s (Walsh, 1969; Lippard, 1972), the Kamego Formation (or KAF) that is visible along the western flank of the Baringo Basin (Chapman et al., 1978), and the Loriu Sandstone (or LOS) that crops out in the North Kerio Basin (Wescott et al., 1993). This study will permit the interpretation of the very initial deposition settings within the CKR and NKR, their relations with the early tectonic and volcanic activity in the Kenya Rift as well as a discussion on their petroleum prospectivity.

2. Field study, sampling and analytical methods

Three field campaigns were organized in February-March 2011, November-December 2012, and June 2013. These campaigns were focused on the logging and sampling of the Kimwarer Formation (February 2011), the Loriu Sandstone (November 2012), and the Kamego Formation (June 2013). The Kimwarer Formation was studied and logged in the field at the southernmost end of the Elgeyo Border Fault escarpment within the Kenya Fluorspar Company mine lease area, close to the Kimwarer village at GPS point 0°17'46.95" N; 35°37'17.95" E. Sampling was extensive and attempted to represent all major lithologies and sedimentary facies observed along the section. In order to determine the sedimentological characters and diagenetic evolution of the Kimwarer Formation, a selection of 35 rock samples were collected and studied. Macroscopic observations on hand specimens and microscopic studies of thin sections were performed at Géosciences Rennes (UMR CNRS 6118, University of Rennes 1, France) following initial studies of the same at the Core Laboratories-Integrated Reservoir Solutions Division in Redhill, United Kingdom, as part of a then ongoing study of the Kenya Reservoir Potential study (Morano et al., 2011). The thin sections were polished to the standard thickness of 30 μm and impregnated with blue-dyed epoxy resin to allow easier visualization and highlight porosity. The thin sections were studied under optical microscopy. The compositional percentages of the various components as well as the inherent sample porosity levels were visually estimated on the thin sections. Permeability within the samples analyzed was also estimated based on the connectivity of the pore spaces determined through visual examination of the samples. An Olympus BX 60 petrographic microscope which allows polarized transmitted light and reflected light microscopic observation on the thin sections was used. A digital Spot RT camera was used to take photomicrographs of samples in CL and optical microscopic studies.

A similar lithostratigraphic approach was conducted on rock samples collected within the Kamego Formation (KAF) in the Baringo Basin, Central Kenya Rift, and the Loriu Sandstone (LOS) in the North Kerio Basin, Northern Kenya Rift. One lithologic section was measured on the KAF in June 2013, from the top of the Precambrian basement to the base of the Miocene Volcanics in the Baringo Basin at GPS point 00°44'57.5" N; 035°51'02.5" E (Kipsaraman Section). Two sections were measured on the Loriu Sandstone at GPS point 02° 43' 03.54" N; 36° 25' 51.96" E for the Loriu Section, and at 02° 43' 9.36" N; 36° 25' 15.36" E for the second Kangabeiye Section. Sampling was extensive and all the different lithological units were sampled in the two formations (46 samples for the KAF, and 60 samples for the LOS) for further laboratory analysis. Hand-held macroscopic observations were additionally made at the National Oil Corporation of Kenya, Core Facility (Nairobi, Kenya) while thin sections were prepared and observations made at Géosciences Rennes following a similar procedure to that followed for the Kimwarer thin sections. Micrographs of the thin sections presented in this work were prepared at the FRE 3298 CNRS ''Géosystèmes'', University of Lille 1, France. Complementary photos of thin sections from the Kamego Formation and the Loriu Sandstone were taken at the Core Laboratories in Redhill, United Kingdom, using polarizing/epifluorescent Zeiss microscope with Axiovision software.

While previous workers have broadly discussed the sedimentological characters of the Kimwarer and Kamego Formations in the Central Kenya Rift, and the Loriu Sandstone in the Northern Kenya Rift, none has ever put forth a definite age of the formation. In order to do this, three volcanic units (and/or associated intrusive dykes) that exist in association with the Kimwarer Formation were described and sampled for radiometric dating using 39Ar-40Ar analytical procedure. Before dating, petrographic analyses were conducted on thin sections to identify the types of rock and potential mineral phases to be separated from their groundmass for dating purposes. The petrographic inspection was also aimed at diagnosing the degree of alteration, which would determine those samples subjected to geochemical analysis. The characterization process was completed by chemical analyses on the selected samples, which was performed at the Service d'Analyse des Roches et des Minéraux (SARM;

CRPG-CNRS, Vandoeuvre-lès-Nancy, France) using inductively coupled plasma-atomic emission spectroscopy (ICP-AES) for major elements and inductively coupled plasma-mass spectroscopy (ICP-MS) for trace elements. The crushing of the samples for chemistry was performed following standard procedures at Géosciences Rennes. A similar procedure was followed for the dating of two lava flows and a dyke associated to the Kamego Formation and the Loriu Sandstone, respectively.

Fifteen samples (from a total of 33 volcanic samples that were collected from the Kimwarer volcanic outcrops) were selected for 39Ar-40Ar dating from the volcanic pile associated to the Kimwarer Formation in the Kerio Basin. Two samples of volcanic rocks overlying the Kamego Formation in the Baringo Basin and one sample from a volcanic dyke form the Loriu area of the North Kerio Basin were also selected for dating. Analyses were performed on millimeter-size sanidine and/or whole rock grains carefully handpicked under a binocular microscope from crushed rocks (0.3-2 mm fraction sieves). The samples were wrapped in Aluminimum foil to form small packets (11 × 11 mm) that were stacked up to form columns within which packets of fluence monitors were inserted every 10 samples. Two distinct irradiations were performed at the McMaster reactor (Hamilton, Canada) in a medium flux location (8E) with Cd-shielding. The first irradiation, that was for the volcanic samples collected from the Kerio Basin lasted 115.8 hr (J/h ≈ 6 x 10-5 h-1). The second irradiation, for the volcanic samples from the Kamego Formation and Loriu Sandstone, lasted 52 hr (J/h ≈ 4.4 x 10-5 h-1). In both cases, the irradiation standard was sanidine TCRs (28.608 ± 0.033 Ma according to Renne et al., 2010). The sample arrangement within the irradiation allowed for the monitoring of the flux gradient with a precision of ± 0.2%.

Step-heating was performed with a CO2 laser probe at Géosciences Rennes. All experiments used single grains. Experimental procedure followed is as described in Ruffet et al. (1991, 1995). The five argon isotopes and the background baselines were measured in eleven cycles, in peak-jumping mode. Blanks were performed routinely each first or third/fourth run, and subtracted from the subsequent sample gas fractions. All isotopic measurements are corrected for K, Ca and Cl isotopic interferences, mass discrimination and atmospheric argon contamination.

Apparent age errors are plotted at the 1σ level and do not include the errors on the 40Ar*/39ArK ratio, age of the monitor and decay constants. These errors on the 40Ar*/39ArK ratio, age of the monitor and decay constants, are included in the final calculation of the (pseudo-) plateau age error margins or for apparent ages individually cited. Analyses were performed on a Map215® mass spectrometer. It is commonly considered that a plateau age is obtained when the calculated 40Ar*/39ArK ratios of at least three consecutive steps, comprising a minimum of 70% of the 39Ar released, agree within 1 or 2σ error bars with the weighted mean calculated 40Ar*/39ArK ratio of the plateau segment. Pseudo-plateau ages can be defined with less than 70% of the 39Ar released. All ages in this work are displayed at the 1σ level. Analytical data and parameters used for calculations (isotopic ratios measured on K, Ca and Cl pure salts; mass discrimination; atmospheric argon ratios; decay constants, etc.) and reference sources are available in the Appendix section.

3. Regional background of the Central and Northern Kenya Rifts

The Kenya Rift is the central major segment of the eastern branch of the East African Rift System, which together with the Main Ethiopian Rift to the north, and the North Tanzanian Divergence to the south (Fig. 3a) make up the eastern arm of the East African Rift System (EARS). The Kenyan Rift consists of a N-S-trending linear structure that extends over 900 km from the Turkana Basin at 4° 30' N to the North Tanzanian Divergence at 2° S. It can be divided in three segments; Northern, Central, and Southern. The central segment (Central Kenya Rift or CKR) lies between latitudes 2°N and the Equator (Baker, 1986), while the northern segment (NKR) extends from 2° N up to 6° N, where it connects with the NNE-trending Main Ethiopian Rift. The southern segment (or SKR) extends from the immediate south of Equator to the North Tanzanian Divergence at 2° S.

3.1. Physiography and climate of the Central and Northern Kenya Rifts

The Central Kenya Rift (CKR) is a particularly well-known segment of the East African Rift System in terms of rift development, tectonic and morphologic evolution (e.g. Chapman and Brook, 1978). Between the equator and 1° N, the CKR is a strongly asymmetric structure that comprises of a set of two major parallel N - S trending half-graben basins, separated by the Tugen Hills structural block: the Kerio Basin (KB) to the west, and the Baringo Basin (BB) to the east (Chapman et al., 1978) (Fig. 12 a-c). The Kerio Basin is ~150 km long and ~30 km wide, and can be divided into four distinct physiographical regions which include from west to east: the eastern edge of the Uasin Gishu Plateau that culminates at ~3000 m, bounded to the east by the 1500-m high Elgeyo Border Fault escarpment, then the Kerio valley that forms the basin floor, with an altitude of 1200-1500 m at its southern end, and the western slope of the Tugen Hills tilted block that bounds the Kerio Basin to the east. This block culminates at an altitude of more than 2100 m (Walsh, 1969) (Fig. 12c). Much of the drainage on the western side of the Kerio Basin, above the Uasin Gishu Plateau, flows west towards Lake Victoria except for the Sion River that flows over the Elgeyo Border Fault escarpment into the Kerio Basin. Within the Kerio Basin itself, the single-most important river is the quasi-perennial Kerio River, which is mainly fed by the Ainabkoi and Nabkoi tributaries and minor streams that drain the southern end of the Kerio Basin. The Kerio River gorges deeply into sandy alluvium that forms the floor of the Kerio Basin, and into the Kabarnet Trachytes (250-350 m thick) that outcrop over a large part of the western slope of the Tugen Hills (Walsh, 1969). The Kerio River then flows northward through a deep and narrow valley for over 300 km to form, together with the Turkwell River, a large and highly vegetated marshland delta at its interface with Lake Turkana (Cohen et al., 1986). The Turkwell River flows from Mount Elgon on the western border of Kenya with Uganda. Its principle tributaries are the Saum River, which flows from a crater in Mount Elgon, and two rivers draining the Karamoja Hills of Uganda, the Kanyangereng River and the Kunyao River (Kotut et al., 1999) (Fig. 14).

On the eastern side of the Central Kenya Rift is the Baringo Basin (BB), a ~50-km long and 20-km wide rhomb-shaped structure that can be divided into three main physiographical regions: the main Tugen Hills to the west, the adjacent rift floor, and the Laikipia Border Fault escarpment to the east (Fig. 12 a and c). The Tugen Hills extends from the Saimo and Kito Pass Faults up to the north of the Korosi Volcano. The Saimo Fault is an assemblage of en échelon faults with approximate throws of >2000 m that brings up the Precambrian basement along the length of the range (Chapman et al., 1978). Basinward, the rift floor is occupied by two small lakes: in the northern part of the basin is Lake Baringo, which is a 21-km long and 13-km wide, ~4-m deep freshwater lake which drains an area of ~6200 km2, extending from the Tugen Hills to the west, the Mau Hills to the sou-

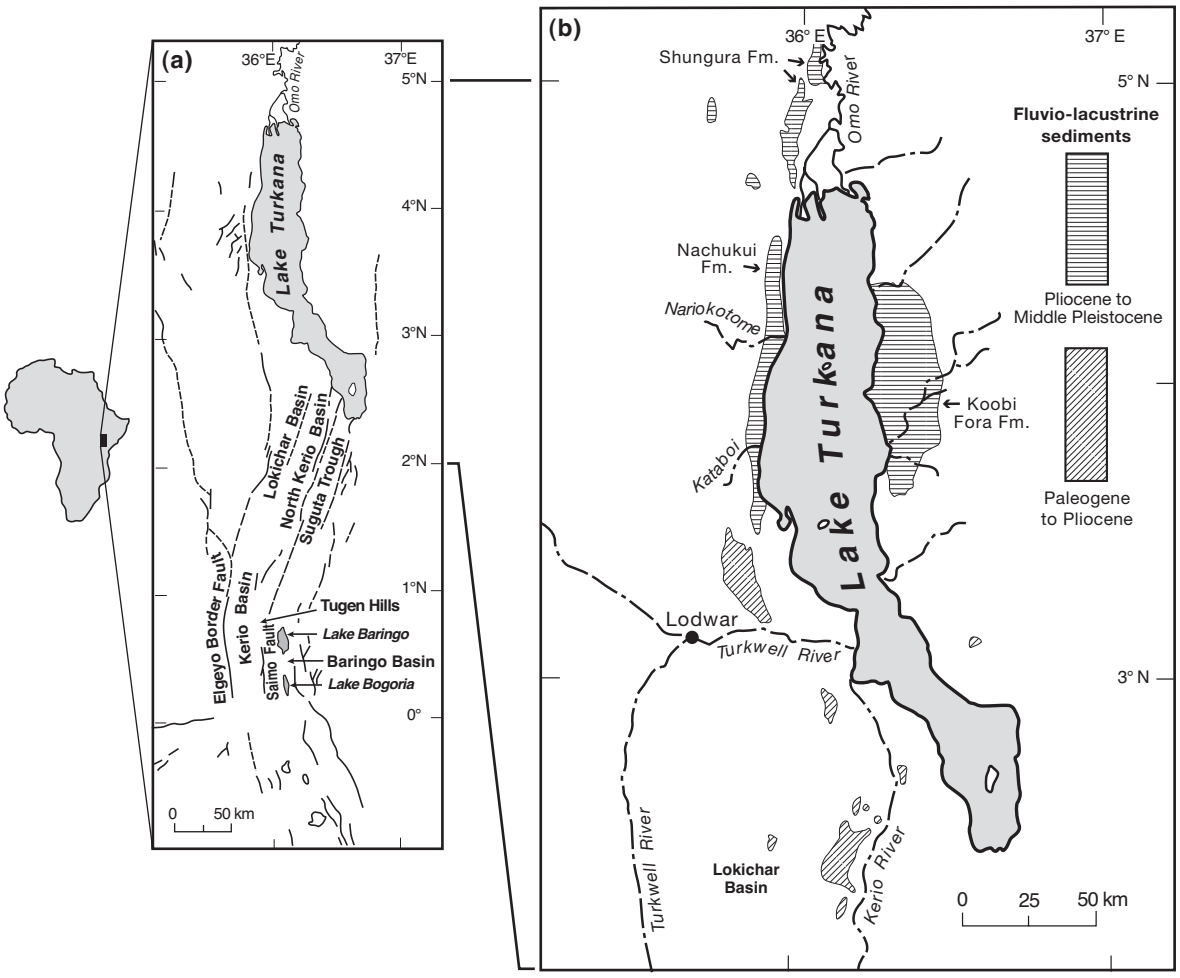

Fig. 14. *Simplified map of the northern and central segments of the Kenya Rift, showing the Lake Turkana Basin and two main tributaries flowing from the south: the Kerio River, and from the southwest: the Turkwell River. The main feeder of Lake Turkana is the Omo River that flows from the Ethiopian plateaus in the north.*

thwest, and the Laikipia Border Fault Escarpment to the east (Renaut and Tiercelin, 1994; Renaut et al., 2000; Tarits et al., 2006). This faunal-rich lake extends northward to the extreme north of the Baringo Basin, which is structurally bounded by the large Pleistocene Korosi Volcano, and southward to the flat marshland that is the Loboi Plain (Figs. 15 and 16). This marshland separates Lake Baringo from Lake Bogoria in the south, which is a 17-km long and 0.5- to 3.5-km wide saline and alkaline meromictic lake fed by almost one hundred ephemeral streams that flow from the eastern and western strongly faulted margins of the basin, and by the semi-perennial Sandai River that flows from the south and drains a 705 km^2 catchment (Fig. 15a). The lake is also fed by more than 200 tectonically- and climatically-controlled hot, warm and cold springs which merge around and under the lake (Tiercelin et al., 1987; Renaut and Tiercelin, 1994; Renaut et al., 2013) (Fig. 15c).

The imposing topography of the CKR also controls the areas' rainfall, temperature and spread of vegetation, all of which is dependent on ground elevation. To the west, areas lying on the eastern edge of the Uasin Gishu Plateau above the Elgeyo Border Fault escarpment at 2000-3000 m receive the highest amount of rainfall, i.e. >2000 mm per year, while the valley floor receives >850 mm per year (Walsh, 1969; Kerio Valley Development Authority, 2010). The temperature in the highland area of the western part of CKR is generally cool during the day averaging 17.5 °C, with mist being a common occurrence in the morning. Temperatures generally fall below

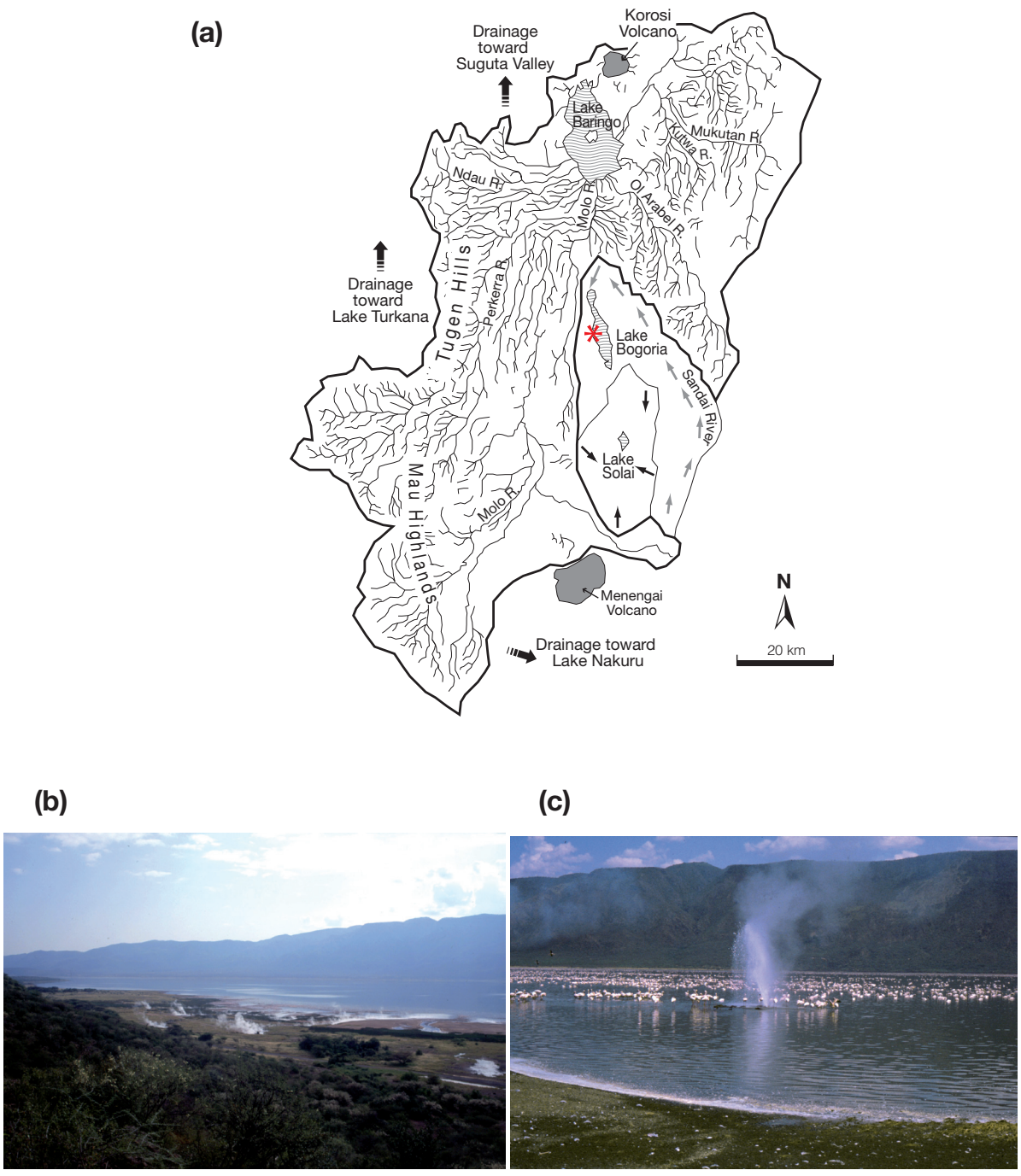

Fig. 15. *(a) Simplified map of the Baringo Basin and Lake Baringo/Lake Bogoria catchment zones and drainage patterns on the eastern side of the Central Kenya Rift (redrawn from Tarits et al., 2006). In the Lake Bogoria drainage, grey arrows indicate the fault-controlled course (from South to North, then East to West and North to South) of the semi-perenial Sandai River that fed Lake Bogoria. (b) View from the Loburu Fault Escarpment of the Loburu hydrothermal field on the western shore of Lake Bogoria, where the largest and most active hot springs in the Bogoria sub-basin are found. On the far horizon is the major Bogoria Fault Escarpment. (c) During the high rainfall periods of the 2000-2010 years, the waters of Lake Bogoria transgressed the Loburu delta, almost completely flooding the boiling jet-springs of the Loburu hydrothermal field.*

frost level during the nights. The temperature of the valley floor averages 27 °C during the day and stays relatively warm during the night (Walsh, 1969). In the central part of the CKR, the Tugen Hills rise to a maximum of 2000 m elevation. It is a sub-humid to semi-humid area that receives an average of 1500 mm of rainfall annually, with an average temperature of ~17.8 °C against a potential evapo-transpiration of 1850 mm per year (Rowntree, 1988). The eastern rift valley floor, which is occupied by the Baringo and Bogoria lakes, is on the other hand semi-arid, with precipitation rates between 600-900 mm per year versus evapo-transpiration rates between 2600-2900 mm per year. Daytime temperatures here range between 25-35 °C (Renaut and Tiercelin, 1994). Eastward, the CKR is bordered by the Laikipia Border Fault Escarpment, then by the high plateau of the Laikipia County. This area has an undulating topography with altitudes ranging from 1500 m in the Ewaso Ngiro River, to 2600 m in the Marmanet Uplands. Daily temperatures vary with altitude, with a mean annual temperature that ranges between 16 °C to 20 °C (Berger, 1989). The rainfall pattern is similar to the rest of the country with the long rains falling between April and May and the short rains falling between October and November with the exception of the central and eastern sections where three rainy seasons are experienced (Berger, 1989; Gichuki et al., 1998). The vegetation of the Laikipia area has been greatly affected by human activity but generally ranges from upland dry forest, leafy bushland and grassland (Berger, 1989). Effectively, all ground in the CKR below 1670 m supports mainly Acacia vegetation and larger trees only along watercourses (Kerio Valley Development Authority, 2010). Above 1670 m, with increasing rainfall, patches of indigenous forest still remain (Walsh, 1969). Originally, most of the CKR supported forest cover, which today can only be seen in small patches such as the Tingwa Hill Forest and the Kipkabus Forest on the Uasin Gishu Plateau.

The Northern Kenya Rift (NKR) corresponds to the northern end of the Kenya Rift and forms part of the wider region known as the Turkana depression, which is a vast lowland lying at a mean elevation of 400 m above sea level between the Kenya and Ethiopia tectonic domes (Fig. 3a). The Turkana depression is one of the most arid areas of East Africa and there are no precise climatic statistics for this area. The main geographical feature in this region is Lake Turkana, which is the largest saline-alkaline lake on the eastern branch of the East African Rift System and is essentially fed by the permanent Omo River that flows from the high Ethiopian Plateaus (Fig. 3b). Two other semi-perenial rivers, the Turkwell River, and the Kerio River (Fig. 14) flow from the south and join Lake Turkana at its southwest end, in the Loriu area in the North Kerio Basin. This region is arid and receives a mean annual rainfall >50 mm with an average daytime temperature range of ~32-40.5 °C (Dodson, 1971). Strong easterly and southeasterly winds commonly pound the uplifted fault scarps at the southern end of Lake Turkana and frequently cause dangerous and unpredictable storms on the lake. The Turkana depression generally supports sparse Acacia vegetation, with large trees only found along the main watercourses such as the Turkwell and Kerio Rivers.

3.2. Geological outline of the Kerio and Baringo Basins

The Kerio Basin is a classical west-tilted half-graben (150 km long by 30 km wide) bounded to the west by the 1500-m high, N-S-trending Elgeyo Border Fault Escarpment, and to the east by the uplifted N-S oriented Tugen Hills block. East of the Tugen Hills is the Baringo Basin whose western boundary is the Saimo and Kito Pass Faults (Walsh, 1969; Lippard, 1972; Chapman et al., 1978; Mugisha et al., 1997) (Figs. 12a, b and 16). The Elgeyo Border Fault Escarpment exposes basement gneisses of Precambrian age that are locally overlain by fluvial Miocene arkosic sandstones, which are locally capped by mid-Miocene basanites that were originally described by Lippard (1972). The exposed basement at the Elgeyo Border Fault Escarpment shows foliations that are juxtaposed to the NW-SE trending brittle shear zones, which were active during the Early Paleozoic times at the end of the Panafrican orogeny (Hetzel and Strecker, 1994). It was originally believed that the Elgeyo

Border Fault Escarpment and inherent faults in the Kerio Basin followed this steep foliation trend and change orientation when intersecting the NW-SE trending shear zones north of the basin (e.g. Smith and Mosley, 1993; Hetzel and Strecker, 1994; Mugisha et al., 1997) (Fig. 12b and c). Recent work however, centered on the dating of pseudo-tachylites from the prominent NW-SE trending Tambach strike-slip fault, shows that this 400 Ma old fault has had little influence on the topographical expression of the Elgeyo Border Fault Escarpment, a fact that is supported by the lack of influence of this fault system on the Cenozoic Uasin Gishu Phonolites and Tambach sediments (Sherlock and Heztel, 2001). Nonetheless, such an apparent lack of direct structural heritage cannot be generalized owing to the presence of fault-controlled rhomb-shaped sedimentary bodies in the deepest parts of the adjacent Baringo Basin and Loboi Plain that have been demonstrated through the magneto-telluric work of Hautot et al. (2000) (Fig. 12b and d).

The stratigraphy of the Kerio Basin infill is a complex ascending alternation of sedimentary formations intercalated amongst volcanic lava flows, all of which uncomformably rest above a basement of Precambrian age (Fig. 12b and c). The crystalline rocks of the basement underlie the entire Central Kenya Rift but are only exposed on the lower slopes of the Elgeyo Border Fault Escarpment – Kerio Basin (KB) (Walsh, 1969) as well as along the Saimo Fault – Baringo Basin (BB) (Chapman et al., 1978; Williams and Chapman, 1986). The basement is made of high-grade metamorphic rocks, predominantly coarse-grained and foliated hornblende gneisses that grade into quartzo-feldspathic gneisses. Biotite gneiss with disseminated flakes of graphite has been locally noted in the Kimwarer area, as well as garnet-rich amphibolites and migmatites (Walsh, 1969). Fluorite bodies occur in the Musgut-Kimwarer area close to the south end of the Elgeyo Border Fault escarpment, in isolated areas within the basement system where they have replaced crystalline limestone and to a minor extent minerals and rock fragments in fault breccias (Nyambok and Gaciri, 1975). These large fluorine bodies are today actively mined by the Kenya Fluorspar Company.

In the southern part of Kerio Basin, close to the Kimwarer village, is an assemblage of intercalated fluvial and alluvial fan sediments that are overlain by a thick volcanic sequence all of which sits on the Precambrian basement (Fig. 12b and c). This sedimentary sequence is known as the Kimwarer Formation. This formation was previously described as an early Tertiary age assemblage of arkosic sandstones with intercalated conglomerates and mudstones overlain by silicified cherts (Walsh, 1969; Lippard, 1972; Chapman et al., 1978; Ego, 1994). A thick (<1 km) volcanic sequence of Miocene age is described overlying the Kimwarer Formation. This volcanic sequence includes at its base the Elgeyo Formation (also known as the Elgeyo Basalts), formed by 600 m of volcanic agglomerates and lava-flows, basanitic to tephritic in composition, with locally limburgites and analcitites (Walsh, 1969; Lippard, 1972, 1973; Chapman and Brook, 1978), that have been dated using the K-Ar technique at ca. 15.6 - 15.1 Ma (Baker et al., 1971; Chapman and Brook, 1978). In concordant position above the Elgeyo Formation are the 350-m thick Chof Phonolites that crop out in the upstream valley of the Kerio River (Chapman et al., 1978). The Chof Phonolites were previously called the Lower Uasin Gishu Phonolites (e.g. Walsh, 1969). Although Chapman et al. (1978) indicate that, in the Kerio valley, the Chof Phonolites concordantly rest on the Elgeyo Basalts, the original map by Walsh (1969) show that, in fact, these widespread phonolites discordantly rest on the Kimwarer sediments and the metamorphic basement. These lavas are in terms of petrography, situated between phonolites and phonolitic nephelinites and are dated at ca. 15.0 Ma (K-Ar method; Baker et al. 1971; Chapman and Brook, 1978) (Fig. 12b and c).

Between 0°33’ and 0°50’N, further north along the Elgeyo Border Fault escarpment, colluvial, fluvial and lacustrine sedimentary rocks belonging to the 380-m thick Tambach Formation are locally exposed. The Tambach Formation sits on an irregular palaeotopography of metamorphic basement and has been indirectly dated based on the presence of a phonolitic flow that is sandwiched between its lowermost beds (Murray-Hughes, 1933; Shackleton, 1951; Lippard, 1972; Ego, 1994; Renaut et al., 1999; Tiercelin et al., 2012b) which has a similar composition to the Chof Phonolites which have been dated at ca. 15.0 Ma (Chapman and Brook, 1978;

Chapman et al., 1978) (Fig. 12b). A similar age is therefore suggested for this phonolitic flow and consequently for the lower part of the Tambach Formation (Chapman et al., 1978).

The Tambach sediments are unconformably overlain by the thick pile (480 m) of the Uasin Gishu Phonolites, which also locally overlie either the metamorphic basement or the Chof Phonolites to the south (Fig. 12b). The Uasin Gishu Phonolites are dated from ca. 14.5 to ca. 13.6 Ma (Lower Uasin Gishu) to 12.0 Ma (Upper Uasin Gishu) (K-Ar method; Baker et al., 1971; Lippard, 1973; Chapman and Brook, 1978). They cap the Elgeyo Escarpment and are overlain on the Uasin Gishu Plateau by the Tinderet Volcanics, a formation of nephelinitic phonolites and basanites that are dated at ca. 9.9-8.9 Ma at Songhor west of Tinderet and Lumbwa southeast of Tinderet (Baker et al., 1971). The upper part of the Tinderet Volcanics is dated at ca. 5.5 Ma at the summit of the Tinderet volcano (K-Ar method; Baker et al., 1971).

On the eastern flank of the Kerio Basin, formed by the Tugen Hills structural block, the oldest and lowermost volcanic formation to have been identified is the Sidekh Phonolites as described by Chapman (1971) (Fig. 12b). This formation is 1200-m thick in the north, 700-m thick in the Saimo area to the south and is dated at ca. 16.4 to 14.8-14.4 Ma (K-Ar method; Chapman and Brook, 1978). About 80 m of sedimentary beds, called the Sigatgat Complex (Chapman et al., 1978), are intercalated within the Sidekh Phonolites. Between the metamorphic basement and the Sidekh Phonolites is the undated Kamego Formation, which is described as mainly being formed by arkosic sandstones (Chapman, 1971; Chapman and Brook, 1978), and is inferred as a possible stratigraphic equivalent of the Kimwarer Formation in the Kerio Basin. Two volcanic units, the Lower Noroyan Formation (105-m thick; formed by hawaiites and mugearites), and the Upper Saimo Formation (240-m thick, formed by basanites and tephrites), dated at ca. 13.5-13.0 Ma (K-Ar method; Chapman et al., 1978), directly overlie the Sidekh Phonolites (Fig. 12b). To the east, along the Laikipia Border Fault escarpment, the oldest volcanic formation is represented by the 1000-m thick Samburu Basalts, dated in the interval 21-11 Ma (K-Ar method; Shackleton, 1946; Baker et al., 1971) (Fig. 12b).

Stratigraphically above the Saimo Formation are the Tiim Phonolites (Chapman, 1971; Chapman et al., 1978), dated at ca. 14.9-13.0 Ma for the lower unit, and ca. 12.8-9.9 Ma for the upper unit (K-Ar method; Chapman and Brook, 1978). They form the edge of the center of the Tugen Hills structural block, and are about 1050 m thick. This phonolitic formation thins to about 300 m towards the north (Fig. 12b). The Tiim Phonolites are equated to the Uasin Gishu Phonolites to which they are stratigraphically and petrographically equivalent (Baker et al., 1969; 1971; Chapman and Brook, 1978; Chapman et al., 1978; Deino et al., 1990). Chapman (1971) described two members within the Tiim Phonolites: the lower Atimet Trachyphonolite Member, and the upper Kamuiton Phonolites Member, in which there is a fossil-rich sedimentary intercalation named the Muruyur Beds or Muruyur Formation (Martyn, 1969; Chapman, 1971; Hill, 1999; Behrensmeyer et al., 2002). This formation is up to 274-m thick and is characterized by a succession of fluvial and lacustrine sediments, palaeosols and volcaniclastic horizons, whose age range is between ca. 16.0 and ca. 13.4 Ma (Ar-Ar dating on volcanic rocks lying just below and above the Muruyur Formation (Behrensmeyer et al., 2002). As discussed by Behrensmeyer et al. (2002), these Ar-Ar ages are older than the earliest K-Ar ages obtained on the Tiim Phonolites (ca. 14.9 Ma; Chapman and Brook, 1978) (Fig. 12c).

A 400-m thick accumulation of sedimentary, volcaniclastic and volcanic rocks known as the Ngorora Formation (Bishop and Chapman, 1970; Pickford, 1978; Hill, 1999; Renaut et al., 1999; Deino, 2002), crop out above the Tiim Phonolites. The Ngorora Formation is dated at ca. 13.06 Ma at its base and ca. 8.5 Ma at top (Ar/Ar method; Deino et al., 1990) (Fig. 8d1 and 12b). The sediments of the Ngorora Formation are visible along the Saimo Fault Escarpment and include fluvial, lacustrine, colluvial and volcaniclastic units that are interbedded with lava flows (Pickford, 1978). Numerous studies have been conducted on this formation owing to its rich fossil content that includes abundant mammalian fauna (including hominid fossils), e.g. Pickford (1978). Petroliferous shales known as the Poi Shales have been identified in two of the main members (Members C and E) of the Ngorora

Formation (Pickford, 1978; Ego, 1994; Morley et al., 1999; Renaut et al., 1999). A re-interpretation of seismic data from the Kerio Basin proposed a 200 to 800-m thick upper Miocene sediments pile buried within the Kerio Basin and interpreted this accumulation as belonging to the Ngorora Formation (Chapman et al., 1978; Mugisha et al., 1997; Hautot et al., 2000) (Fig. 12b). Such a thickness is compatible with sediment deposited within a time span of 4.5 Ma (Hill, 1999) in the axial part of a volcano-tectonically active rift basin (Renaut et al., 1999). Unconformably overlying the Ngorora Formation are the 180- to 600-m thick Ewalel Phonolites (Plateau-type phonolites as defined by Lippard, 1973, and Chapman et al., 1978), dated between ca. 7.6 Ma and ca. 7.2 Ma (Ar/Ar method; Deino et al., 1990), that are in turn unconformably overlain by the 250-350 m thick Kabarnet Trachytes, dated at ca. 7.2-6.8 Ma and which outcrop over a wide surface along the western flank of the Tugen Hills (Baker et al., 1971; Chapman and Brook, 1978; Chapman et al., 1978; Mugisha et al., 1997) (Fig. 12c).

3.3. Geological outline of the North Kerio Basin

The Turkana depression has been described as the most important region in Eastern Africa for studying the evolution of the East African Rift System, and its relationship with the Cretaceous-Paleogene southern Sudan and Anza Rifts (Fairhead, 1986; Reeves et al., 1987; Greene et al., 1991; Morley et al., 1999) (Fig. 3b). The present-day Lake Turkana Basin is part of a string of major N-S oriented half-grabens that developed between upper Cretaceous and Eocene-Oligocene to Pliocene-Pleistocene times, possibly as parts of the Central African Rift system (CARS), or linked to the early rifting phases of the EARS (Morley et al., 1992, 1999; Tiercelin and Lezzar, 2002; Tiercelin et al., 2004; Ducrocq et al., 2010) (Fig. 3b).

The southwest end of the present-day Lake Turkana Basin is characterized by the existence of two of the oldest sedimentary basins in the EARS, the Lokichar Basin to the west, and the North Kerio Basin to the east. The Lokichar Basin is a N-S–trending, 60-km long and 30-km wide, east-facing half graben floored by the Precambrian crystalline basement (Morley et al., 1992, 1999). Its western boundary is a prominent east-dipping listric fault, named the Lokichar Fault, which has no present-day topographic expression. As shown by reflection seismic data (Amoco Kenya Petroleum Company lines TVK-12 and TVK-13) (Morley et al., 1999), the basin fill, which is 7-km thick, consists of interbedded Paleogene to middle Miocene lacustrine and fluvio-deltaic sediments capped by a 300-m thick basaltic sequence, the Auwerwer Basalts, dated between ca. 12.5 Ma to 10.7 Ma (K-Ar method; Morley et al., 1992, 1999; Tiercelin et al., 2004) (Fig. 6). This basaltic sequence marks the end of rifting processes in the Lokichar Basin. The 3-km deep Loperot-1 exploration well (Fig. 6d) was drilled close to the Lokone Horst, a basement high that separates the Lokichar Basin from the North Kerio Basin and which is the adjacent half-graben located to the immediate east of Lokichar Basin (Fig. 13). The lithology encountered in this exploration well is described in the General Introduction, "*The Northern and Central Kenya Rifts: Emerging Exploration Provinces*", section.

Possible equivalents of the Lokone Sandstone are known to outcrop in the Loriu Range at the northeastern end of the North Kerio Basin (Fig. 13). This half-graben basin, imaged by the TVK-12 seismic line of Amoco Kenya, is north-south oriented and parallel to the Lokichar Basin. It is poorly studied by any standard, mainly because of difficult accessibility from the western side of Lake Turkana. Access is by boat either from the north coming from Eliye Springs Resort or east from Loyangalani Township. The study area in the NKB can uniformly be described as a rugged country, which is floored by a raised basement that outcrops along the Lake Turkana shoreline. The basement in the North Kerio Basin is composed of hornblende-biotite gneisses similar to those described in the area south of Lodwar (Joubert, 1957, 1966; Dodson, 1971). At Loriu, thick and locally chaotic piles of sediments overlie the basement and form multicoloured (white, purple and yellow) units that dip to the west and northwest. Wescott et al. (1993) described up to 610 m of coarse-grained arkosic sandstones with thin,

discontinuous, red, grey and yellow siltstone-mudstone units which were interpreted as deposited in broad channels forming valley fills. These sediments are locally overlain by a thick sequence of lava flows and in several places, are heavily intruded by a dense network of dykes and large igneous intrusions. A radiometric age (whole rock K-Ar technique) of 15.7 ± 0.7 Ma was provided by a sample collected at the base of the lava-flow sequence, and one dyke intruding the sediments yielded a slightly younger age of 14.7 ± 0.17 Ma (Wescott et al., 1993). The petrography and geochemistry of the magmatic rocks that outcrop in the Loriu region are unfortunately not precisely described (Wescott et al., 1993).

Facies code	Lithology	Sedimentary Structures	Bed thickness (m)	Depositional processes	Interpretations	Figures
Gmm	Massive, ungraded, matrix-supported conglomerate. Quartz and metamorphic rock fragments floating in a brown to orange-brown, fine to coarse sandstone matrix. Angular to well-rounded rock fragments, with pebbles ranging between 2-5 cm in diameter	Planar to slightly erosive lower boundaries. Flows also fill palaeotopography	0.4-1.2	Deposition of gravel by high strength debris flows (Lowe, 1979; 1982) Miall, 1996)	Sub-aerial debris flows	Fig. 19 and Fig. 20g (SAR 41/11)
Gcm	Massive, graded, poorly sorted, clast-supported conglomerate. Quartz and metamorphic rocks. Angular to sub-rounded rock fragments and pebbles ranging between 2-11 cm in diameter. Brown to buff-brown, muddy to medium-grained sandstone matrix. This facies also occurs in lenticular form	Slightly erosive basal boundary	0.15-0.5	Low strength pseudoplastic debris flow deposited from viscous, laminar or turbulent flows (Postma, 1990, Miall, 1996)	Sub-aqueous debris flow	Fig. 19 and Fig 20 d and e
Sm	Massive, silty to very coarse sandstone. Colour varying from buff brown (common throughout the formation) to deep orange-brown at the base of the formation and weakly iron stained grey-blue at the top of the formation. Most abundant facies noted in the KAF	No sedimentary structure but few beds are graded (fining up or coarsening up)	0.2-3.2	Subaerial hyperconcentrated flow (Lowe, 1982)	Rapid suspension fallout from sedimentary gravity flows and/or postdepositional modification through dewatering for those beds with faint bedding	Fig. 19 and Fig. 20c KIMW 28/11)
Sr	Medium to coarse sandstone. Buff brown colour with common iron staining which gives the beds a dirty grey appearance	Ripple cross-lamination with a wavelength and amplitude of 0.1 and 0.05m respectively (symmetrical ripples)	0.2	Deposition from viscous layer through turbulent sweeps (Nichols, 2009)	Low rate deposition from suspension during ripple migration (Miall, 1996).	Fig. 19 and Fig. 22c (SAR 47/11)
Sh	Fine to coarse sand. Buff to dark brown with local post-deposition deformation e.g. dewatering structures.	Horizontal lamination and soft sediment deformation (convolute lamination)	0.15-1.4	Plane-bed flow, critical flow regime (Miall, 1996) or traction carpets (Postma, 1990)	Planar bed flows under critical flow regime (Miall, 1996)	Fig. 19 and Fig. 21 b and c (SAR 01/11)
St	Fine to medium sand. Buff brown with local iron staining giving beds an orange tinge locally. Asymptotic bottom contacts and undulating lower boundary	Curved sets with the angle of dip < angle of repose	0.45	Migration of sinuous subaqueous dunes (Nichols, 2009)	3D dunes	Fig. 19
Fl	Claystone to silty claystone, buff brown to purple close to top of unit	Fine lamination or thinly bedded with sharp basal contact	0.20-0.30	Deposition from suspension	Overbank, abandoned channel or waning flood deposits (Miall, 1996)	Fig. 19 and Fig 21a (KIMW 32/11)
Fm	Structure-less mud commonly associated with mud cracks in the KF	Massive dessication cracks	0.1-0.5	Deposition from suspension in standing pools of water during ow stage channel abandonment	Low energy flow deposition from suspension, overbank or floodplain	Fig 19 and Fig. 21f (SAR 57c/11)
R	Structure-less, buff brown to reddish brown, fine to medium sands	Root markings	0.15	Root bed, incipient soil	Low energy flow deposition in vegetated floodplains	Fig 19 and Fig 22d (SAR 49/11)

Table 2
The Kimwarer Formation: Lithofacies attributed to fluvial (distal braided fluvial channel and distal floodplain) facies and alluvial fan facies. Facies codes are adapted from Miall (1996).

4. The Kimwarer Formation

The Kimwarer Formation (KF), previously described as "Kimwarer beds" by Walsh (1969), forms a distinct feature at the southern end of the Elgeyo Border Fault Escarpment, along the Kimwarer-Musgut road where it caps an upthrown faulted metamorphic basement block and forms a steep cliff overlooking the Kenya Fluorspar Company mining facilities. The KF is accessible from the Kimwarer-Musgut road, through a difficult, weather-beated and overgrown path that leads up the Precambrian Basement to the base of the formation. The formation can also be accessed more easily from the top walking down the volcanic succession that caps the KF in the Sarbab area. Erosion of the overlying volcanics has led to a scarp retreat of approximately 5 km (Walsh, 1969), exposing and enhancing the Kimwarer Formation's imposing character (Figs. 17 and 18). The first description of the KF was given by Lippard (1972), who defined the formation as formed by a ~50-m thick "Lower Member" and a ~12-m thick "Upper Member" (Fig. 18a). The "Lower Member" consists of indurated basement-derived, arkosic cross-bedded sandstones and conglomerates together with siltstones and shales, while the "Upper Member" consists of poorly consolidated volcanic-rich sandstones and basaltic tuffs (Lippard, 1972; Ego, 1994). Ego (1994) gives the generalised depositional environment of the lower member as fluvio-lacustrine, with the lacustrine phase covering the later stages of the basin development and resulting in the deposition of fine-grained laminated siltstones and shales as described by Lippard (1972). Overlying the Kimwarer Formation is a thick volcano-sedimentary pile consisting of agglomerates and lavas, previously described as the "Elgeyo Basalts" by Walsh (1969) but later renamed the "Elgeyo Formation" by Lippard (1972) (Fig. 18b).

4.1. Lithostratigraphy

The Sarbab Section is proposed to be the Type-Section of the Kimwarer Formation in this work. The Kimwarer Formation was logged from GPS point 0°17'46.95" N; 35°37'17.95" E, up to the top of the outcrop at GPS point 0°17'46.95" N; 35°37'17.95" E, up to the top of the outcrop at GPS point 0°17'32.27" N; 35°37'45.53" E. At Sarbab, the Kimwarer sediments sit unconformably on the Precambrian basement, which is predominantly composed of coarse-grained, strongly foliated hornblende gneisses that grade into quartzo-feldspathic gneisses along the Elgeyo Border Fault Escarpment and, in the Kimwarer area, of biotite gneiss with common disseminated flakes of graphite and garnet-rich amphibolites and migmatites (Walsh, 1969) (Figs. 20 and 21a).

The lower 70 m of sediments are designated in this work as the "Lower Kimwarer Formation" (or LKF). They mainly consist of basement-derived silicoclastics, including conglomerates (7% of the total section), coarse- to fine-grained sandstones (57.5% of the total section), and siltstones to mudstones (27% of the total section). Covered zones represent up to 8.5% of the section and may be representative of siltstone to mudstone facies (Fig. 21). A total of 9 lithofacies have been identified in the Lower Kimwarer Formation. The sedimentological descriptions and interpretations are summarized in Table 2, and illustrated on Figures 20, 21 and 22 (coarse-grained and fine-grained lithofacies). The main facies codes have been adapted from Postma (1990) and Miall (1996). Above the LKF is a ~120-m thick volcaniclastic unit that is in turn overlain by a thin (6.7 m) succession of conglomerate, sandstone, siltstone and mudstone facies, which is here designated as the "Upper Kimwarer Formation" (or UKF) (Fig. 18b and 19).

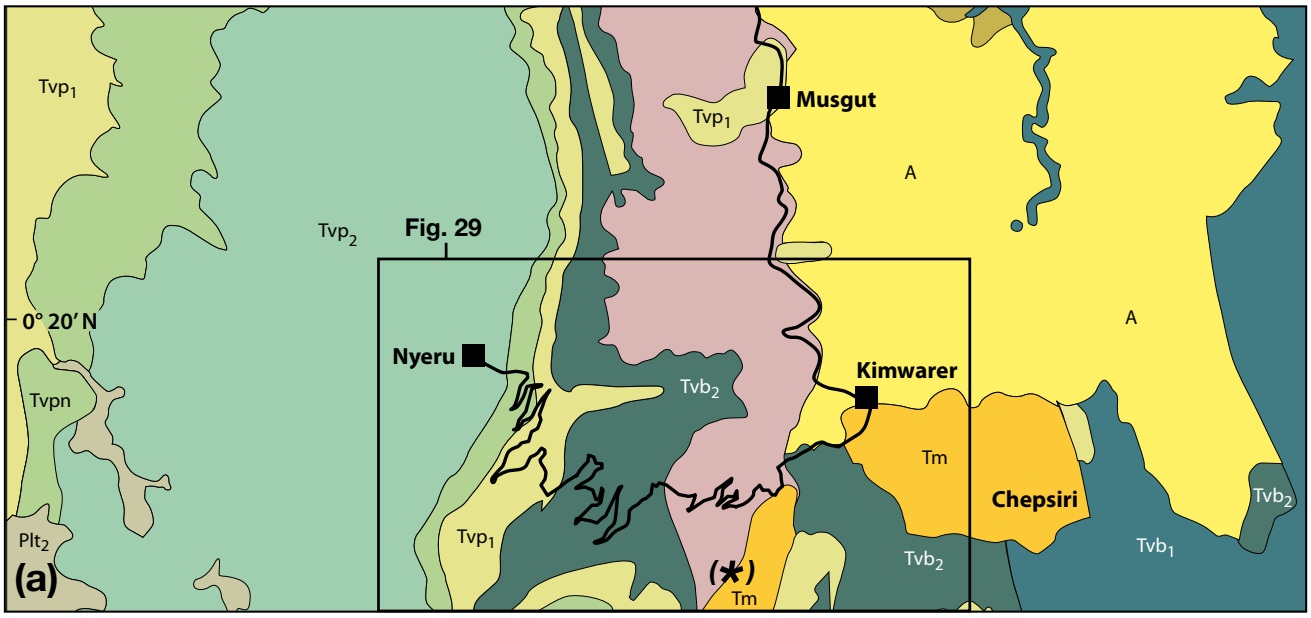
Tvp1
Tvp1
Musgut
A
Tvp2
Fig. 29
0° 20′ N
Nyeru
Kimwarer
Tvb2
A
Tvpn
Tm
Chepsiri
Tvb2
Plt2
Tvp1
Tvb2
Tvb1
(*)
Tm
(a)

Kerio Basin floor
Kimwarer Formation
Precambrian basement
(b)

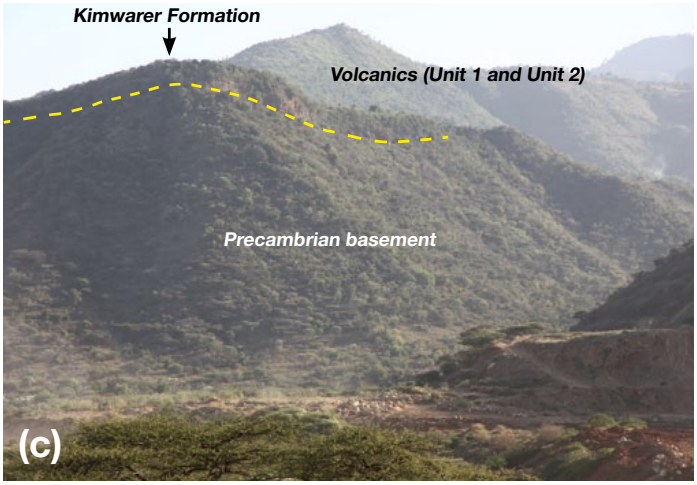
Kimwarer Formation
Volcanics (Unit 1 and Unit 2)
Precambrian basement
(c)

Photo (e)
Kimwarer Formation
(*) Sarbab Type-Section
(See (a))
(*)
Precambrian basement
(d)

(e)

(f)

Fig. 17. *The Kimwarer Formation at the Sarbab Type-Section, located 2 km southwest of the Kenya Fluorspar Company mining plan, at the southern end of the Elgeyo Border Fault Escarpment. (a) Geological map of the southwestern end of the Kerio Basin and Elgeyo Border Fault escarpment (modified from Walsh, 1969). Legend for the different geological formations: Plt2: Tuffs of Uasin Gishu Plateau; Tvpn: Tinderet Volcanics (nephelinitic phonolites); Tvp2: Tinderet Volcanics (melanocratic porphyritic phonolites); Tvp1: Uasin Gishu Phonolites (Lower Phonolites-generally non-porphyritic); Tvb2: Elgeyo porphyritic olivine basalts; Tvb1: Samburu Basalts; Tm: Kimwarer Formation; A: Kerio Valley alluvium. (b) View from the Elgeyo Border Fault Escarpment (road from Nyaru to Kimwarer) showing the Kimwarer Formation overlying the Precambrian basement, and on the foreground the Kerio basin floor. (c) View of the basement overlain by the Kimwarer Formation and volcanic units 1 and 2, from the Fluorspar mining plan. (d) Panoramic view of the Kimwarer Formation from the Kimwarer-Musgut road, which shows the emplacement of the KF atop the Precambrian basement and underlying the volcanic units (Unit 1 and Unit 2) that outcrop along the Elgeyo Border Fault Escarpment. (e), (f) Close up images of the lower part of the Kimwarer Formation. (e) The steep-sided Kimwarer section which is heavily overgrown and which is generally comprised of buff brown, approximately horizontal metre thick beds. On this part of the Elgeyo Escarpment, the Kimwarer Formation lies unconformably on the Precambrian basement. (f) Sarbab Type-Section - also shows predominantly buff brown, horizontal metre-thick sandstone beds that are partially grey stained.*

4.1.1. The "Lower Kimwarer Formation"

At the Sarbab Type-Section, above a slightly erosive contact with basement (Fig. 20a), the lowermost beds of the LKF form a 1.5 m-thick succession of fining-up, dark grey pebbly to fine-grained sandstone (lithofacies Sm) that are massive at base and faintly laminated at top. The laminated part exhibits local convolute bedding and water escape structures at its base grading up into a massive fine-grained sandstone or siltstone (lithofacies Sm and Fm) at the top (Figs. 19, 20b and 21a). These beds are then overlain by a 1 m-thick series of <10-cm thick, brown, fine-grained, laminated sandstone beds (lithofacies Sh) (Fig. 21b) that also locally exhibit convolute bedding (Fig. 21c) and grade upward to massive coarse-grained sandstones (lithofacies Sm). This is followed by a 15-m thick succession of decimetre- to metre-thick beds of silty sandstones to coarse-grained sandstones (lithofacies Sm, respectively), which are predominantly massive, locally convoluted and parallel bedded, iron-stained, buff brown to rusty orange in colour, and locally dirty pink to light grey. Desiccation cracks that have developed within light brown to rusty orange mudstone facies (Fm) are noted at 4 m, 6 m and 6.5 m from base of section (Figs. 19, 21d and e), and are locally associated with mudstone beds that contain root casts (lithofacies Fr) ~5 cm in diameter (at 5.9 m from base of section). At 9.45 m above the base of the section is a succession of five massive highly indurated rusty orange mudstone layers (lithofacies Fm), each approximately 2-cm thick (Figs. 19 and 21d), capped by a 1.5-m thick succession of alternating light grey massive, highly indurated, fine-grained sandstones and orange coarse-grained sandstones that form beds between 5 and 25 cm thick (Figs. 19 and 21f).

There is a resumption back to fine- to medium-grained sandstones between 18 to 25 m from the base of the section that is marked by centimetre- to decimetre-thick and locally lenticular beds of light orange, faintly laminated, fine- to medium-grained sandstones. Few beds exhibit parallel lamination with local convolutions (at 19 m and 23 m in the section) as well as water-escape structures (at 19 m in the section). Three 5 to 15-cm thick, massive, yellow-brown in colour, highly indurated mudstone beds (lithofacies Fm) showing desiccation cracks at their top surface are recorded 20.9 m and 23 m from the base of the section (Fig. 20). Between 25 m and 43 m (Fig. 19), the lithology of the Sarbab Type-Section changes to a succession of >0.30 m-thick beds of matrix- to clast-supported, light orange to buff brown conglomerates (with >5 cm and up to 30 cm quartz pebbles) (lithofacies Gmm and Gcm) and decimetre- to metre-thick beds of very coarse-grained massive sandstones (lithofacies Sm) (Fig. 20c-g). The matrix-supported conglomeratic beds are locally heavily channelized (Figs. 19 and 20g). This gravelly/pebbly succession is interrupted by a bluish green and orange, decimetre-thick silty mudstone (e.g. 37 m from the base of the section) (Figs. 19 and 22a). Evidence of pedogenesis is visible in the fine-grained horizons (Figs. 20, 23a and b). Although no real palaeosol profile was noted, eroded palaeosols can be observed associated to the channel systems (Figs. 20g and 21a). Angular to rounded >10 cm in diameter, rusty orange palaeosol clasts are locally observed as reworked elements in overlying sandstone beds at 34 m from the base of the section (Figs. 20 and 23b).

The part of the Sarbab Type-Section between 43 and 55 m is composed of two fining-up sequences of buff brown to light green, decimetre- to metre-thick, fine- to coarse-grained sandstones including two 0.20-m thick beds of clast- to matrix-supported conglomeratic sandstones (lithofacies Gmm and Gcm) (Fig. 19). The lower fining-up sequence shows local parallel bedding, ripple marks and root marks (Figs. 19, 22c and d) and is overlain by a 0.60-m thick, grey-green massive mudstone bed (Figs. 19, 21g and 22e). At the top of the Sarbab Type-Section, from 55 to 70 m, is a 15-m thick grey to purple-red mudstone sequence with laminated and locally highly distorted beds that is upturned to approximately 80° in the N144° direction (Figs. 19 and 22f). This sequence thins out laterally to almost 5 m as one climbs the section towards Sarbab village.

The Sarbab Type-Section terminates at an unconformable contact with a ~120-m thick volcanic/volcaniclastic unit, which comprises, from base to top, three decametre-thick volcaniclastic horizons (50-m, 30-m and 10-m thick, respectively), and two interbedded massive volcanic beds (10-m and 20-m thick, respectively) (Fig. 19). The three volcaniclastic horizons are composed of a wide range of centimetre to decimetre in size, angular to rounded clasts with a porphyritic and vesicular structure, embedded within a grey to purple sandy matrix. The two massive volcanic beds are formed by porphyritic and amygdaloidal rocks that exhibit well-developed onion-skin weathering. This volcanic/volcaniclastic unit is described in greater detail as Unit 1 in Section 4.3.1 "*Volcanic units associated with the Kimwarer Formation*".

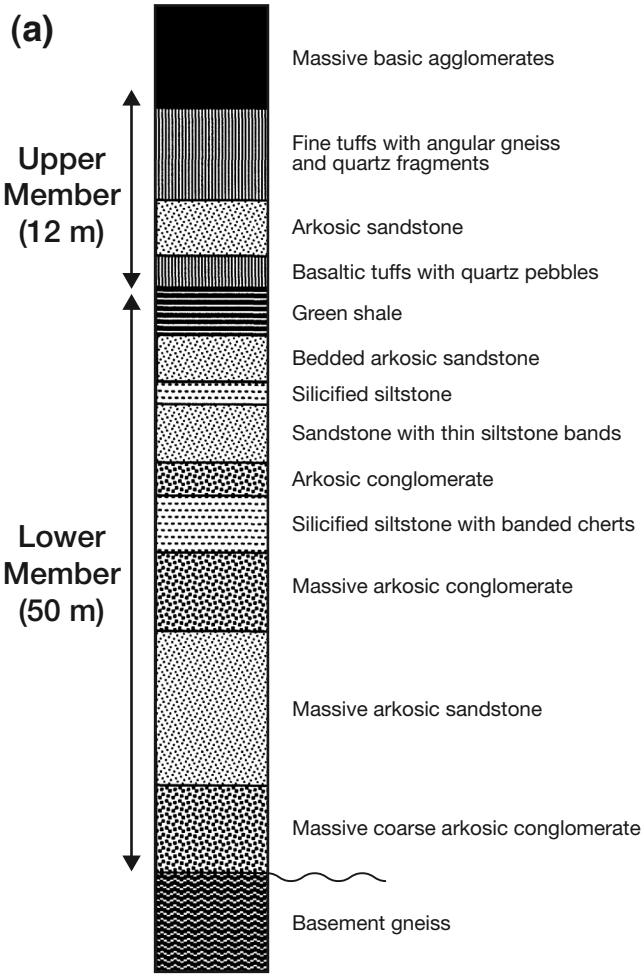

Fig. 18. *(a) Lithostratigraphic log of the Kimwarer Formation, as described by Lippard (1972), showing a 50-m thick "Lower Member" formed by basement-derived sandstones and conglomerates, together with siltstones and shales, and a 12-m thick "Upper Member" formed by volcanic-rich sandstones and basaltic tuffs.*

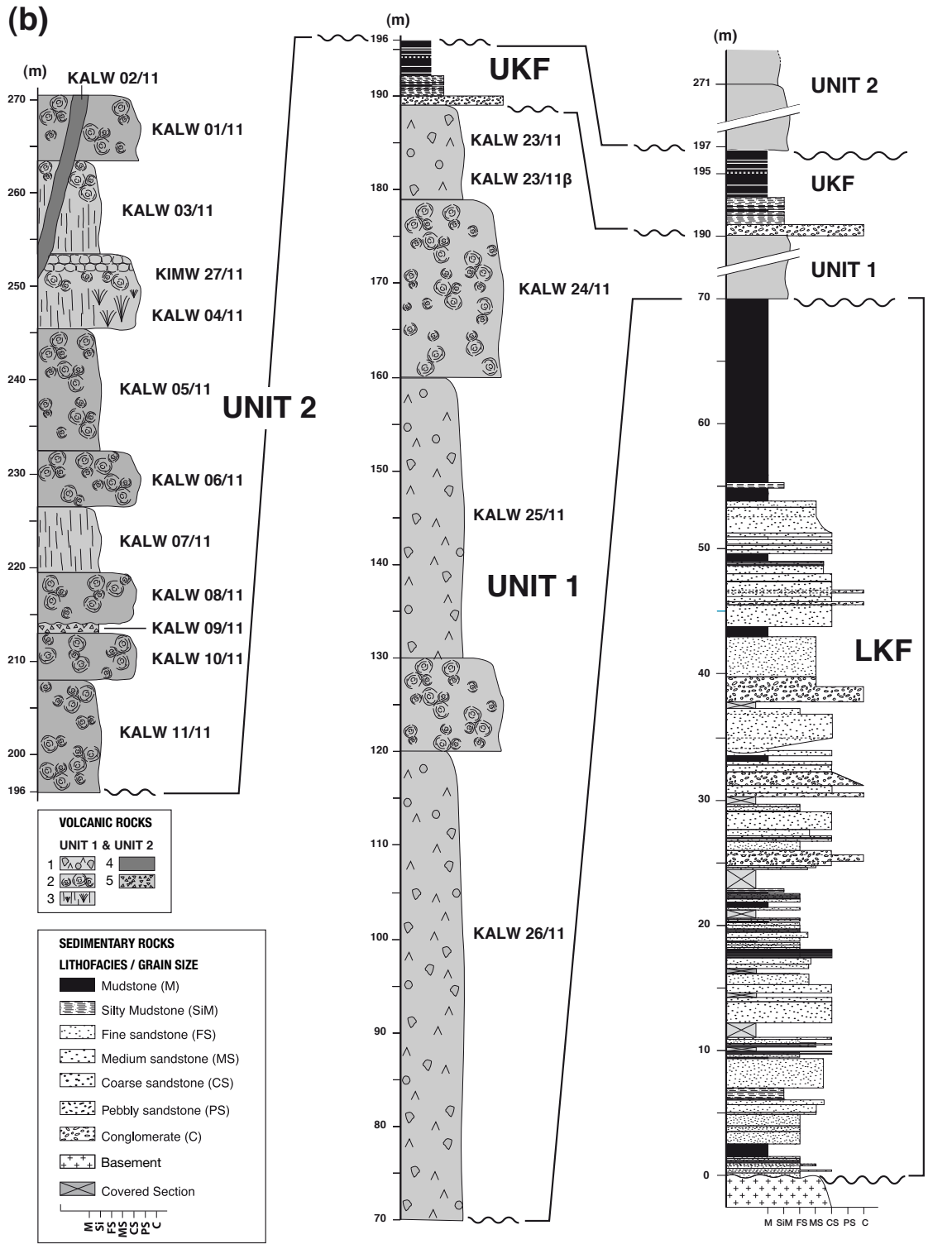

Fig. 18. *(b) General lithostratigraphic log of the Kimwarer Formation described at the Sarbab Type-Section, showing the "Lower Kimwarer Formation" (or LKF), the "Upper Kimwarer Formation" (or UKF), and the associated volcanic units (Units 1 and 2). Legend for volcanic rocks: (1) Volcaniclastic horizon/tuff/tuffite; (2) Massive horizon/ mafic lava flow with onion-skin weathering; (3) Massive horizon/mafic lava flow with columnar jonting/feather structures; (4) Mafic dyke; (5) Volcaniclastic graded horizon/tuff. Volcanic samples are indicated by: block letters (KAWL or KIMW) and differentiated by numbers (e.g. 04/11).*

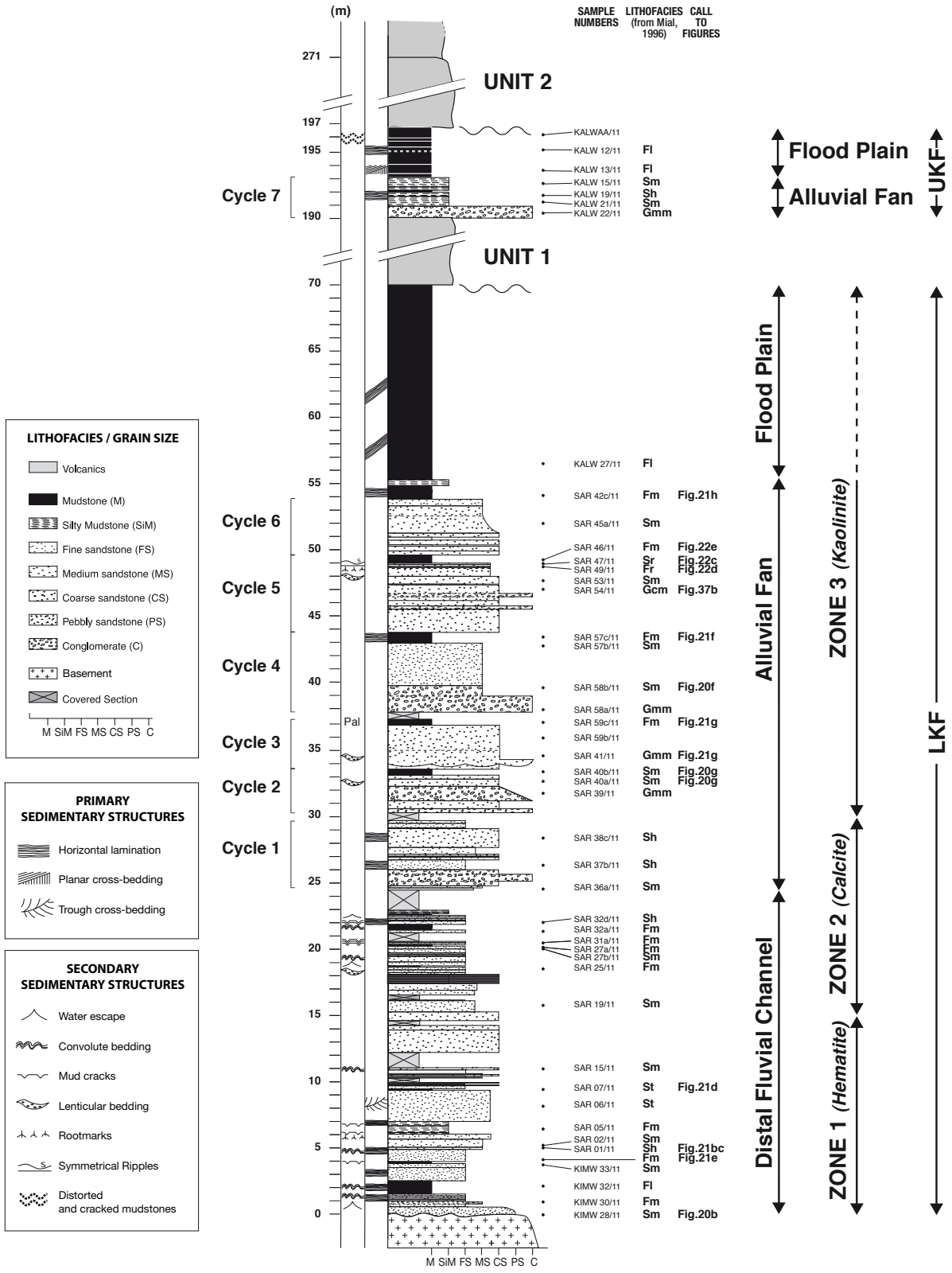

Fig. 19. *The Kimwarer Formation, Lower (LKF), and Upper (UKF): Lithostratigraphic log at the Sarbab Type-Section*

Fig. 20. . *The "Lower Kimwarer Formation": Coarse-grained lithofacies. (a) Unconformable contact (yellow dashed line) between the highly weathered metamorphic Precambrian basement and the lower beds of the "Lower Kimwarer Formation". (b) Massive pebbly sandstone (KIMW 28/11) lithofacies Sm) that sits directly on basement with abundant sub-angular to sub-rounded >5 cm diameter basement-derived clasts. Immediately above the pebbly sandstone are poorly consolidated fine-grained massive sandstones (KIMW 30/11 - lithofacies Fm) with abundant quartz granules that grade upwards into laminated mudstones (KIMW 32/11 – lithofacies Fl). This massive bed, which is locally lenticular, mergers with the underlying pebbly sandstone unit laterally and is overlain by a fine to medium-grained, laminated and locally convoluted sandstone bed (lithofacies Sh). (c) Massive, highly indurated coarse-grained sandstone with abundant basement-derived granules (SAR 59/11 - lithofacies Sm). (d) and (e) An accumulation of cemented together basement-derived rocks (quartz and metamorphic rock fragments) that range in size from granules and pebbles to boulders. This bed was noted towards the top of the Kimwarer Formation at a stratigraphic level as the interval sample SAR 45a/11 (see Fig. 19) was collected and is representative of a debris flow. (f) Microconglomeratic sandstone unit in a highly indurated massive sandstone (SAR 58b/11 - lithofacies Sm) unit. (g) Channelized coarse-grained massive sandstone (SAR – 40b/11). The incising channel is conglomeratic (SAR 41/11 - lithofacies Gmm) at base and grades up into massive, coarse-grained sandstone (lithofacies Sm), representing a high-energy fluvial deposit.*

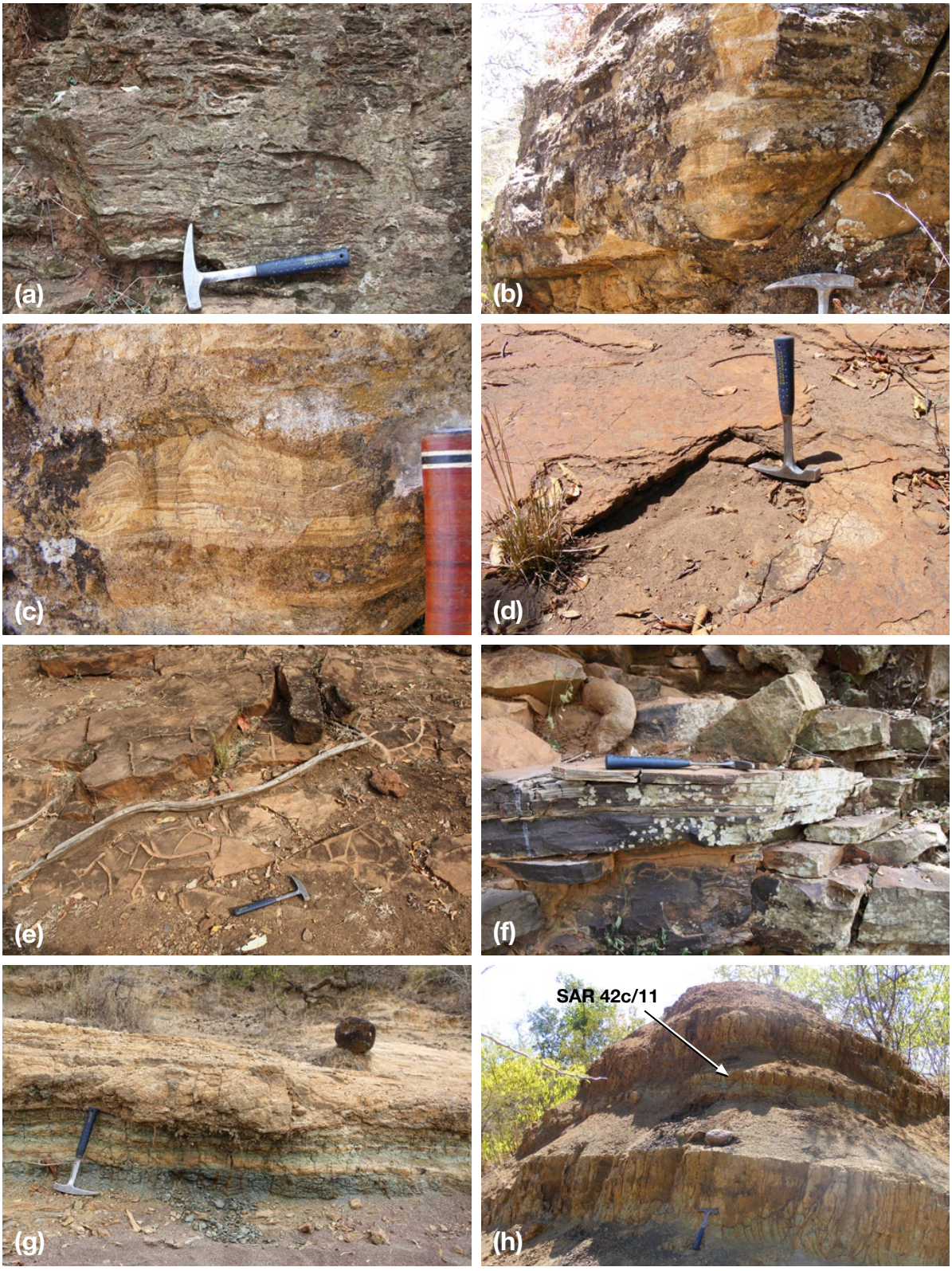

Fig. 21. *The "Lower Kimwarer Formation": Fine-grained lithofacies. (a) An alternate view of the laminated mudstones in Fig. 20b (KIMW 32/11 – lithofacies Fl). Here, this bed also shows water-escape structures and convolute bedding that is attributable to soft sediment deformation. (b and c) are other examples of soft sediment deformation in fine to medium grained laminated bed (SAR 01/11 - lithofacies Sh) of the Lower Kimwarer Formation. (d) Succession of five thin (~2 cm) highly indurated rusty orange massive mudstone beds (SAR 07/11 - lithofacies Fm) recorded 9.45 m from the base of the formation. (e) Desiccation cracks recorded 4 m from the base of the formation capping the bed represented by sample KIMW 33/11 are indicative of subaerial exposure subsequent to accumulation of mud in shallow water bodies. Both images (d and e) are illustrative of subaerially exposed mud that was previously accumulated in shallow water bodies. (f) Highly indurated massive mudstone (SAR 57c/11 - lithofacies Fm) which grades up into a finely laminated facies (lithofacies Fl). This bed is underlain by a 3 m fine grained massive sandstone bed and overlain by a 2 m coarse grained sandstone bed. (g) and (h) Massive green mudstones (SAR 59c/11 and SAR 42c/11 – lithofacies Fm) located 36 m and 54 m from the base of the section.*

Fig. 22 . *The "Lower Kimwarer Formation": Fine-grained lithofacies. (a) and (b) The development of palaeosols within the green fine-grained mudstone (SAR 59c/11 - Fig. 21g). This pedogenetic event is recognized by the presence of orange-brown palaeoclasts embedded within the fine grained green mudstone. (c) Rippled medium-grained sandstone (SAR 47/11 - lithofacies Sr) that is indicative of gently flowing fluvial systems (see Fig. 19). (d) Root marks (SAR 49/11 – lithofacies Fr, found 15cm below the rippled surface (SAR 49/11). The association ripple marks and root marks suggests a vegetated depositional setting submitted to abrupt water level changes up to complete desication, probably a floodplain/overbank depositional environment. (e) Grey-green fissile mudstone (SAR 46/11 - lithofacies Fm) that caps a fining-up sequence of sandstones at 49 m from the base of the LKF. (f) Grey to purple finely bedded and laminated mudstone (KALW 27/11 - lithofacies Fl) that cap the LKF (55-70 m). Laterally (not visible n the photo, these beds are upturned to ~80° and are unconformably overlain by the volcanic Unit 1 (Figs. 19b and 29).*

4.1.2. The "Upper Kimwarer Formation"

Above Unit 1 is the 6.7-m thick "Upper Kimwarer Formation" (UKF) (Figs. 18b and 19) which is a fining-up interval formed by a 0.9 m thick, massive, olive-grey conglomerate (KALW 22/11 - lithofacies Gmm), that is overlain by massive and locally laminated purple red fine grained sandstones (KALW 21/11 and KALW 19/11 respectively). This sequence grades up into laminated and locally cross-bedded beds of mudstones (KALW 12/11 and KALW 13/11 - lithofacies Fl) towards the top where the upper mudstone beds are intensely cracked and distorted (Figs. 19 and 22f). These sediments are unconformably overlain by a volcanic rock succession described as Unit 2 in Section 4.3.1. "*Volcanic units associated with the Kimwarer Formation*".

4.2. Structural framework of the Kimwarer Formation at the scale of the Kerio Basin

The discovery during the 90's in the Northern Kenya Rift of several deep (up to 7-km) half-graben basins (including the Lokichar Basin) (Morley et al., 1999) (Fig. 3), suggested a similar scenario for the Kerio and Baringo Basins of the Central Kenya Rift (Fig. 12d). The identification of a deeply buried sedimentary succession lying between 4 and 8 km below the Miocene volcanic rocks in the Baringo Basin using a combination of surface geology (Tiercelin, 1981; Morley et al., 1995), magnetotelluric data (Hautot et al., 2000) and a re-interpretation of seismic data obtained in 1989 from the Kerio Basin (Mugisha, 1994; Mugisha et al., 1997), suggested different mechanisms for the development of both the Kerio and Baringo Basins, from those proposed in the 70's and 80's (King, 1978; Tiercelin et al., 1981). At that time, surface geology data suggested downwarping in the CKR occurred during the early Miocene allowing for the development of an infill of not more than 2.5 km in thickness in the Kerio Basin, and less than 500 m of sedimentary infill in the Baringo Basin (Rooney and Hutton, 1977; Tiercelin, 1981). The Paleogene age suspected for these basins, and particularly for the Lokichar Basin (Morley et al., 1999), was later confirmed by the discovery of a late Oligocene mammalian fauna within sediments in the Lokone Sandstone that forms the lower part of the Lokichar Basin infill (Ducrocq et al., 2010). As a consequence, an interpreted Paleogene age was also ascribed for the deep sediments in the Kerio and Baringo Basins in the CKR.

In these two basins, the lithology of the several kilometres thick sedimentary infill is completely unknown, because of an almost complete lack of outcrops. Nevertheless, the Kimwarer Formation (KF) outcrop, which can only be observed at the Kenya Fluorspar Company leasehold area in the Kerio Basin, may represent a small fraction of the lowermost portion of the infill of this basin (Lippard, 1973; Chapman and Brook, 1978; Chapman et al., 1978; Mugisha, 1994; Mugisha et al., 1997; Renaut et al., 1999; Tiercelin et al., 2004), as does its possible stratigraphic equivalent, the Kamego Formation (KAF) in the Baringo Basin, where it mainly crops out along the Saimo Fault hanging wall (Chapman et al., 1978; Hautot et al., 2000) (Fig. 17b).

Re-interpretation of seismic data gathered from the poorly imaged basin fill of the Kerio Basin by the National Oil Corporation of Kenya in 1989 suggests much greater dimensions of the pre-volcanic sedimentary accumulation in the basin. The seismic dataset, which is of extremely poor quality, comprises of two dip lines, KV1-89 and KV 2-89, and one tie line, KV3-89. This dataset was acquired by the Haliburton Geophysical Company, as part of a project supported by the National Oil Corporation of Kenya (Fig. 24). The two east-west cross-rift lines KV1-89 and KV2-89 were shot across the Kerio Basin and both have a 3 km gap where the Kerio River intercepts the cutlines within the basin. The approximately North-South, 'along axis' tie line, KV3-89, was shot parallel to the Elgeyo Escarpment (Fig. 23).

The two E-W seismic lines were first re-intepreted by Mugisha (1994) and Mugisha et al. (1997), who identified five different lithostratigraphic units (Fig. 24), and also noted that the basin was not a simple westward-dipping tilted graben as proposed by Chapman et al. (1978) and Morley et al. (1992), but that the Elgeyo Border

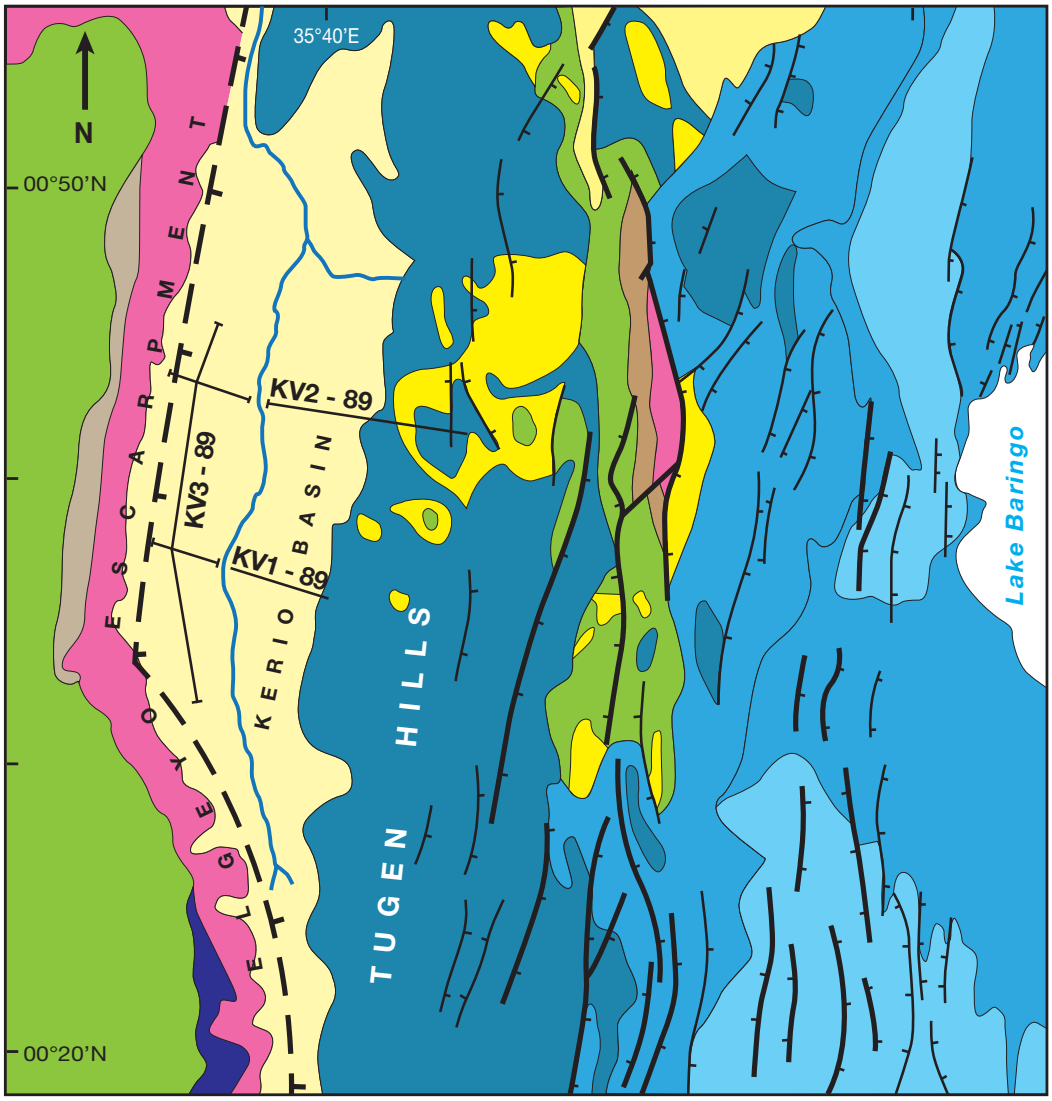

Kerio Basin Quaternary sediments
Baringo Basin Quaternary sediments
Pleistocene trachytes
Pliocene basalts
Upper Miocene flood phonolites and trachytes (Kabarnet Trachytes & Ewalel Phonolites)
Upper Miocene sediments (Ngorora Formation)
Middle Miocene Plateau Phonolites (Uasin Gishu Phonolites)
Middle (?) Miocene sediments (Tambach Formation)
Lower Miocene Basalts (Elgeyo Basalts)
Kamego Formation
Precambrian basement

Fig. 23. *Simplified geological map of the Kerio Basin and the eastern part of the Baringo Basin, showing the position of the seismic lines KV1-89 and KV 2-89 (dip lines), and KV3-89 (tie line) acquired in the Kerio Basin by NOC-Kenya (modified after Chapman et al., 1978; Mugisha et al., 1997). The fault indicated by a thick dashed line is the main Elgeyo Border Fault (EF).*

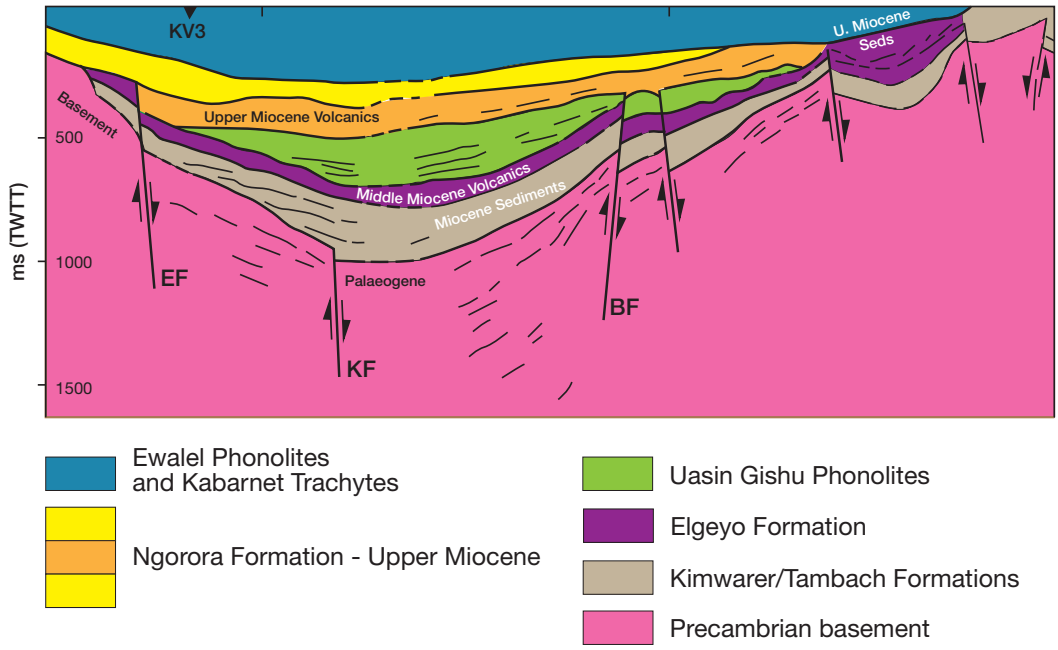

EF - Elgeyo Fault; KF – Kerio Fault; BF – Barwesa Fault

Fig. 24. *Line drawing of a previous interpretation of line KV2-89 showing the Elgeyo Border Fault (EF) and the Kerio Fault (KF) (modified from Mugisha et al., 1997).*

Fault's hanging wall, which forms the floor of the Kerio Basin, has undergone differential displacements along numerous faults resulting in an overall saucer-shape basinal configuration (Mugisha, 1994). Correlations with outcropping formations were also made based on reflectors that terminate at the surface (Fig. 24). Consequently, in order to structurally constrain the Kimwarer Formation as well as to determine its association with other components of the basin fill within the Kerio Basin, a new re-evaluation of the available and usable seismic dataset was deemed necessary and is detailed below.

4.2.1. Seismic interpretation

In this study, because of the very poor quality of lines KV1-89 and KV3-89, only the KV2-89 line has been used to study the sub-surface of the Kerio Basin. On the extreme western boundary of the basin, the Elgeyo Border Fault, though not well imaged, is inferred from reflector offset. The eastern border of the Kerio Basin is even less well defined owing to the chaotic mix of reflectors at the boundary. Nonetheless, it is possible to pick out the basin boundary by the interpolation of buried faults that are picked out following similar logic as those on the western boundary. The different horizons were picked on the basis of reflector character, i.e. reflector termination, continuity, amplitude and frequency as well as correlation of seismic surface pitchouts to field outcrops. Using these criteria, six stratigraphic packages, underlain by the basement were identified (Fig. 25).

- *Basement*: The basement rock is characterized by a system of chaotic, low amplitude and highly discontinuous reflectors. This seismic character is largely homogeneous and its upper surface delimits a slightly asymmetrical E-W syncline (Fig. 25) that is similar to the Lokichar Basin in the Northern Kenya Rift. While the top of this package is rarely obvious, its internal configuration is recognizable as forming the lowermost section in the entire dataset.

- *Package 1*: The base of this package is difficult to pick but was interpolated from reflector offsets and placed at a maximum depth of 2.2 sec TWT. On this line, Package 1 has a maximum thickness of 1.0 sec TWT. This

lowermost package is chaotic and has low amplitude and low frequency, highly discontinuous reflectors. It forms a continuous but downwarped basal layer of a syncline. The upper limit of Package 1 is noted to be structurally truncated evidenced by the termination of inclined reflectors at the boundary (Fig. 25).

- *Package 2*: This package is characterized by high amplitude, high frequency, discontinuous reflectors and attains a maximum thickness of 0.15 sec TWT (0.9-1.05 sec TWT). This package onlaps both the western boundary faults and the uplifted eastern flexural margin. On its upper surface, structural truncations in similar form as those noted in Package 1 are observed (Fig. 25).

- *Package* 3: Package 3 is a high amplitude, high frequency and relatively continuous sequence that is 0.2 sec TWT thick (at its thickest point between 1.0-0.8 sec TWT). Similar to package 2, this sequence terminates at the Elgeyo Border Fault to the west (Fig. 25).

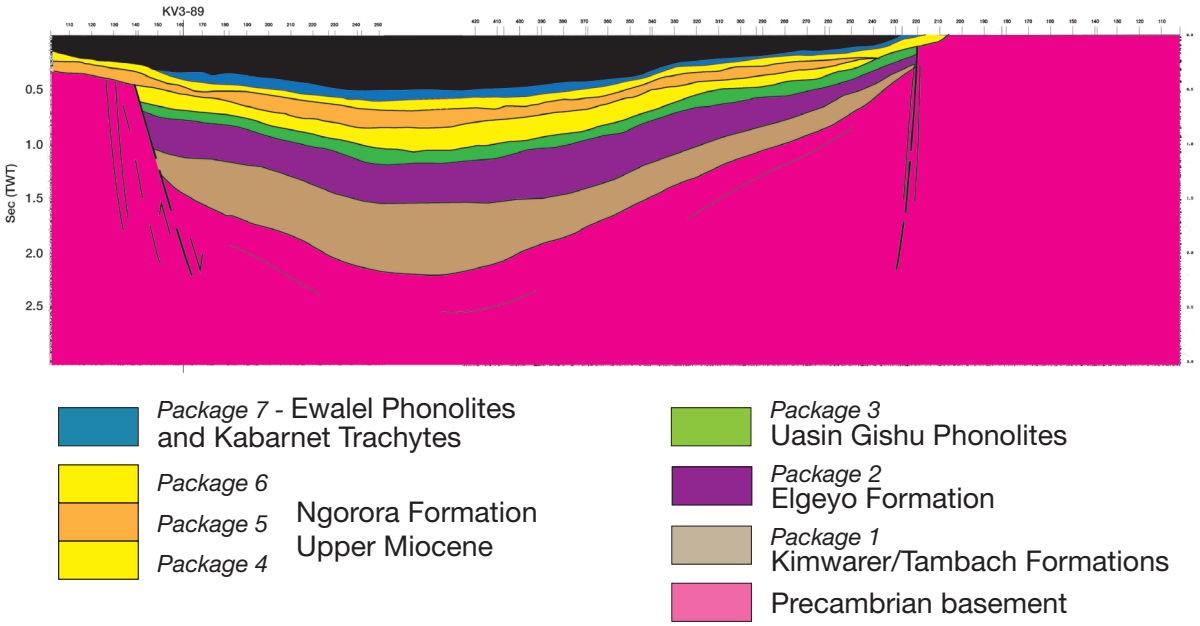

Fig. 25. *Seismic stratigraphy and structural evolution of the Kerio Basin deduced from the re-interpretation of seismic lines KV1-89 and KV2-89 (dip lines) and line KV3-89 (strike line). Seven different packages have been interpreted starting from the bottom: Basement that is defined by chaotic reflectors at the base of all the lines. Above the basement is a stratified sedimentary package that exhibits low amplitude, low frequency, highly discontinuous reflectors which abut on the main boundary fault (Elgeyo Border Fault) to the west of the lines KV1-89 and KV2-89. To the east of the line KV2-89, the package terminates at what is interpreted as a strike-slip zone that forms part of the flexural margin to the east of the Kerio Basin. This package can be attributed to the Kimwarer Formation and/or the Tambach Formation, both of which are observed to sit directly on the basement in the field. Two volcanic units are interpreted above the lowermost sedimentary package. The first unit (iii) is characterized by high amplitude, high frequency discontinuous reflectors while the second unit (iv) is characterized by high amplitude, high frequency continuous reflectors. These packages are interpreted as the Elgeyo Formation (sensu Chapman et al., 1978) and the Uasin Gishu Phonolites (Walsh, 1969; Lippard, 1973). Both these volcanic packages terminate in the west on the Elgeyo Border Fault and to the east the lower package terminates on the strike-slip fault associated with the Kabarnet flexural margin, while the Uasin Gishu Phonolites are truncated by the overlying formation towards the east on line KV2-89. Above the Uasin Gishu Phonolites are three packages that are distinguished by (v) low-amplitude, low frequency and highly discontinuous reflectors, (vi) high amplitude, laterally continuous and low frequency reflectors, and (vii) low amplitude, low frequency and highly discontinuous reflectors. Together, these three packages (v, vi and vii) are interpreted as the Ngorora Formation, which comprises of two sedimentary packages (v and vii) that are separated by a volcanic unit (vi). The Ngorora Formation outcrops in the field in the area of the seismic acquisition on both the eastern and western flanks of the Kerio Basin. The basin is then filled up by high amplitude, high frequency discontinuous reflectors that may represent the Ewalel Phonolites and the Kabarnet Trachytes, which are observed in the field as the topmost lithological units in the Kerio Basin although the seismic quality aside from the thickness of the topmost interpreted unit does not allow for the discrimination of the two.*

- *Package 4*: This package is recognized as having low amplitude, low frequency and highly discontinuous reflectors. The package is ~0.1 sec TWT thick. The package oversteps its western boundary (Fig. 25) but thins out towards the east and does not outcrop onto the surface. Rare but prominent toplap is evident on line KV2-89.

- *Package 5*: This package is recognized by its high amplitude, laterally continuous and low frequency reflectors, and is ~0.1 sec TWT thick on line KV2-89. It conformably overlies Package 4 and also oversteps the fault on the western side of the basin. This package also outcrops on the eastern section of the basin (Fig. 25).

- *Package 6*: This package is characterized by low amplitude, low frequency and highly discontinuous reflectors and generally has a thickness of ~0.12 sec TWT. Similarly, this package also oversteps the western boundary fault. On line KV2-89, rare but prominent oblique reflectors (that are interpreted as progadational clinoforms) are noted.

- *Package 7*: The topmost package that can be interpreted on this dataset is characterized by high amplitude, high frequency discontinuous reflectors. The package lies conformably on Package 6 and thins towards the western and eastern flanks of the basin where it is noted to outcrop (Fig. 25).

Interpreted	Seismic Facies	Stratigraphic correlation
Package 0	Highly distorted, discontinuous reflectors	Basement
Package 1	Low amplitude, highly discontinuous and low frequency reflectors	Kimwarer and/or Tambach Formations
Package 2	High amplitude, high frequency discontinuous reflectors	Elgeyo Formation
Package 3	High-amplitude, high-frequency, continuous reflectors	Uasin Gishu Phonolites
Package 4	Low-amplitude, low-frequency, highly discontinuous reflectors	Ngorora Formation (Sedimentary)
Package 5	High amplitude, laterally continuous, low frequency reflectors	Ngorora Formation (Volcanics)
Package 6	Low amplitude, low frequency, highly discontinuous reflectors	Ngorora Formation (Sedimentary)
Package 7	High amplitude, high frequency, discontinuous reflectors	Ewalel Phonolites and/or Kabarnet Trachytes

Table 3
Correlation of the stratigraphic interpretation of the NOCK seismic lines acquired in the Kerio Basin, to the general stratigraphy of the Kerio Basin (re-interpreted from Hautot et al., 2000).

4.2.2. Correlation of seismic packages to stratigraphic column of the Kerio Basin

The stratigraphic interpretation of the Kerio Basin seismic data, in consideration of the different seismic facies and packages described in the above Section 4.2.1. and the geological outline presented in Section 3.2. Geological outline of the Kerio and Baringo Basins (CKR), is summarized Table 3.

4.2.3. Geological evolution of the Kerio Basin

From the seismic dataset, a possible evolutionary model for the Kerio Basin can be divided into five successive phases of deformation, deposition and erosion as outlined below (Fig. 26):

- Stage 1: The earliest stages of deformation in the CKR did not necessarily involve half-graben geometries and probably the incipient Kerio and Baringo Basins were initiated as synformal structures with a random mix of fault dips (Morley, 1999) within which sediments accumulated. Sediments were probably deposited by morpho-tectonic controlled N-S trending fluvial systems similar to those described by Morley (1999), which drained into the Lokichar and North Kerio Basin in Northern Kenya Rift.

- Stage 2: Extension processes initiated fault displacement along the present-day Elgeyo Border Fault in the west and the Saimo Fault in the east. Within the palaeo-Kerio Basin, either differential fault displacement continued along smaller faults that are synthetic to the main Elgeyo Border Fault, or thermal sagging caused the hanging wall to curve and take up a synformal shape. The footwall during this phase of deformation could also have been isostatically uplifted, which allowed for the erosion of the basement and the subsequent deposition of the lowermost sedimentary pile (Kimwarer Formation) in the basin. This must have been contemporaneous with significant fault movement at the flanks and within the hanging wall of the basin as suggested by synformal basal package interpreted as the Kimwarer Formation and/or the Tambach Formation. In this basin reconstruction, the Kimwarer and Tambach Formations are considered to be laterally equivalent or at least contemporary packages owing to their stratigraphic position above the basement where they may represent the proximal (Kimwarer Formation) and distal (Tambach Formation) depositional environments of a major fluvio-lacustrine system within the Kerio Basin. The lowermost package interpreted in Section 4.2.1. Seismic Interpretation, which has been correlated to the Kimwarer Formation, shows structural truncation (toplap) pointing to relief oriented sediment bypass, that could be indicative of lake level control on sediment depositional dynamics (Fig. 26).

- Stage 3: Volcanic activity followed the deposition of these lowermost sediments, most likely concurrent with basin-wide faulting as evidenced by the synclinal shape of the volcanic packages interpreted as the Elgeyo Formation in the basin. These volcanic packages are deposited unconformably on the Kimwarer Formation in the basin, where they appear to locally truncate the underlying sediments (Fig. 25). The topography created by the emplacement of these lava flows must have been extremely flat owing to the generally uniform thickness of the overlying Uasin Gishu Phonolites. In order to develop such a horizontal horizon, the amount of lava emplaced must have been voluminous and probably filled a significant portion of the existing accommodation space. Such a scenario has been discussed in the adjacent basin Baringo Basin with regard to the deposition of the Sidekh Phonolites (Pickford, 1978). The uniform thickness of the Uasin Gishu Phonolites is also indicative of volcanic emplacement in a relatively ‘tectonically calm’ setting with limited fault movement along the major basin faults.

- Stage 4: The newly formed topography probably had a significant impact on existing drainage patterns. Large lakes including the palaeo-Ngorora Lake must have developed at this time as well as the fluvial systems draining into the lakes. These rivers were most likely morpho-tectonically controlled. The rate of growth and consequently, deposition of the Ngorora Formation in the basin outpaced fault displacement along the Elgeyo

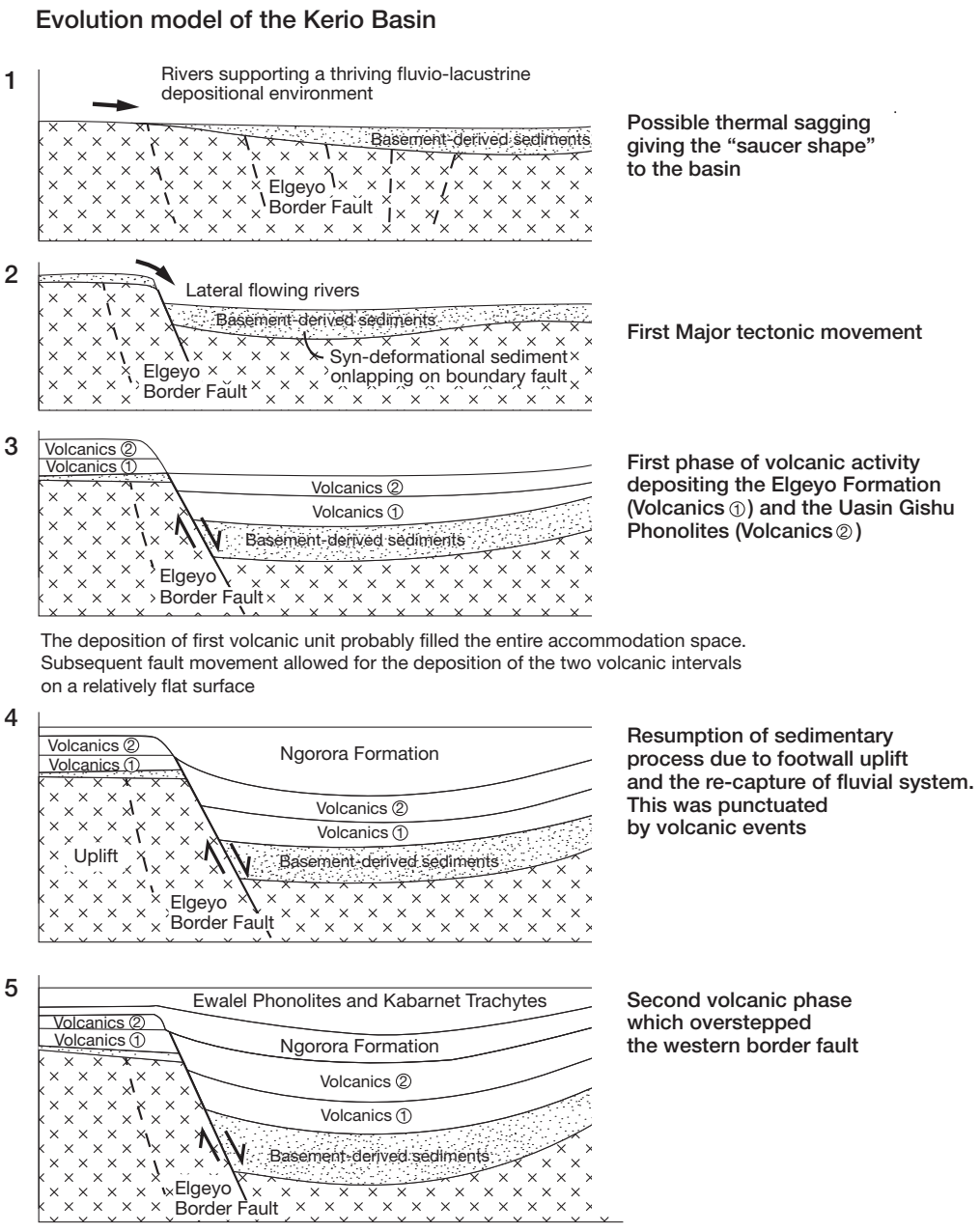

Fig. 26. *The Kerio Basin: Evolution model. Stage 1: The Kerio Basin was possibly initiated by thermal sagging that led to the development of N-S trending faults and a subsequent saucer-shaped basin in which a relatively thin layer of sediments was deposited. This was followed by a subsequent phase of faulting that involved significant vertical movement and the creation of an approximate 3 km deep accommodation space that was subsequently infilled by sediments derived from the basin flanks as well as from distal areas deposited by axial rivers flowing through the basin (Stage 1 and Stage 2). These sediments represent the Kimwarer Formation and Tambach Formation which sit directly on top of the basement. This was followed by a first series of volcanic events that resulted in the emplacement of two distinct volcanic units (the Elgeyo Formation and the Uasin Gishu Phonolites) that probably filled up the entire accommodation space which was a consequence of continued vertical displacement along the Elgeyo Border Fault and associated faults (Stage 3). Continued displacement allowed for the deposition of the fluvio-lacustrine Ngorora Formation whose deposition was punctuated by volcanic activity resulting in the intercalation of volcanic sequences within the Formation (Stage 4). A second phase of intense volcanic activity led to the deposition of the Ewalel Phonolites and the Kabarnet Trachytes (Stage 5). This intense volcanic phase, dated at ca. 7.2-6.8 Ma, produced enough volcanic material to not only fill up all the available accommodation space but also overstep the Kerio Basin flanks.*

Border Fault, leading to the overstepping of the Ngorora Formation over both the western boundary fault and the eastern flexural margin. Sediment bypass is also inferred for this formation owing to the thickening of the pile towards the centre of the basin as well as truncation of horizons within the packages on line KV2-89 (Figs. 25 and 26).

- Stage 5: The final phase of deposition within the Kerio Basin was marked by the filling up of the entire Kerio Basin accommodation space and subsequent overflowing over the Elgeyo Border Fault by the westward flowing Ewalel Phonolites and Kabarnet Trachytes at ca. 8.8-6.7 Ma (Walsh, 1969; Chapman and Brook, 1978; Pickford, 1978). By this time, it is assumed that the rifting and consequent fault displacement had completely migrated to the eastern Baringo Basin as suggested by the structural configuration of the Kabarnet Trachytes that exhibit relatively undeformed, almost horizontal flows (Figs. 25 and 26).

4.3. Chronostratigraphic setting of the Kimwarer Formation

Volcanic rocks dominate the landscape of the Kerio Basin, where the Kimwarer Formation crops out only along normal fault planes and mostly at the base of deeply eroded sections in the Elgeyo Border Fault Escarpment. Overall, the presence of volcanic rocks on both the footwall and hanging wall of the Elgeyo Border Fault is indicative that they must have covered the entire area and that, at one point, the eruptions were contemporaneous with rifting (Chapman and Brook, 1978; Chapman et al., 1978). Nevertheless, the exact ages of the volcanic rocks that crop out on the Elgeyo Border Fault Escarpment, which is documented as a post-Miocene fault scarp, remain poorly known. As a consequence, considering that no biostratigraphic fossils have been discovered within the sediments of the KF, the volcanic units associated to the KF are critical for determining time constraints on the deposition ages of the sedimentary formation. Therefore, a study of the volcanic rocks was undertaken with the aim of ascertaining absolute ages for the volcanic episodes. As most volcanic rocks cap the KF sediments, the obtained ages will obviously translate to minimum ages for the deposition of the Kimwarer Formation.

4.3.1. Volcanic units associated with the Kimwarer Formation

At the Sarbab Type-Section, the Kimwarer Formation (Lower and Upper) was observed to be associated with two volcanic units: - Unit 1 directly overlies the LKF; - Unit 2 overlies the UKF (Figs. 18b and 27). According to the geological map (Walsh, 1969), Unit 2 directly correlates to the Elgeyo Basalts (formed by porphyritic olivine basalts), also called Elgeyo Formation by Chapman et al. (1978). In addition, in order to integrate the Kimwarer Formation at a regional scale, a detailed stratigraphic logging and sampling of the Uasin Gishu Phonolites was conducted along the main Elgeyo Border Fault Escarpment, from the Kerio Fluorspar mining plant to Nyaru Town. This last volcanic series is named Unit 3 in this work (Figs. 27 and 28).

The direct field relationships between the lava flows of Unit 3 and those of Unit 2 were not directly observed in the field because of difficult outcrop conditions. However, when observed, the contacts between the different units (Units 1, 2 and 3) and the internal contacts within and between the different volcanic horizons within the three units were approximately horizontal, except locally where part of the horizons appeared to be slightly tilted. In the following section, the different units are described in their relative stratigraphic order from base to top, including field and thin section observations, new geochemical data and, when available, Ar-Ar dating results (see Appendixes 1 and 2, and Table 4).

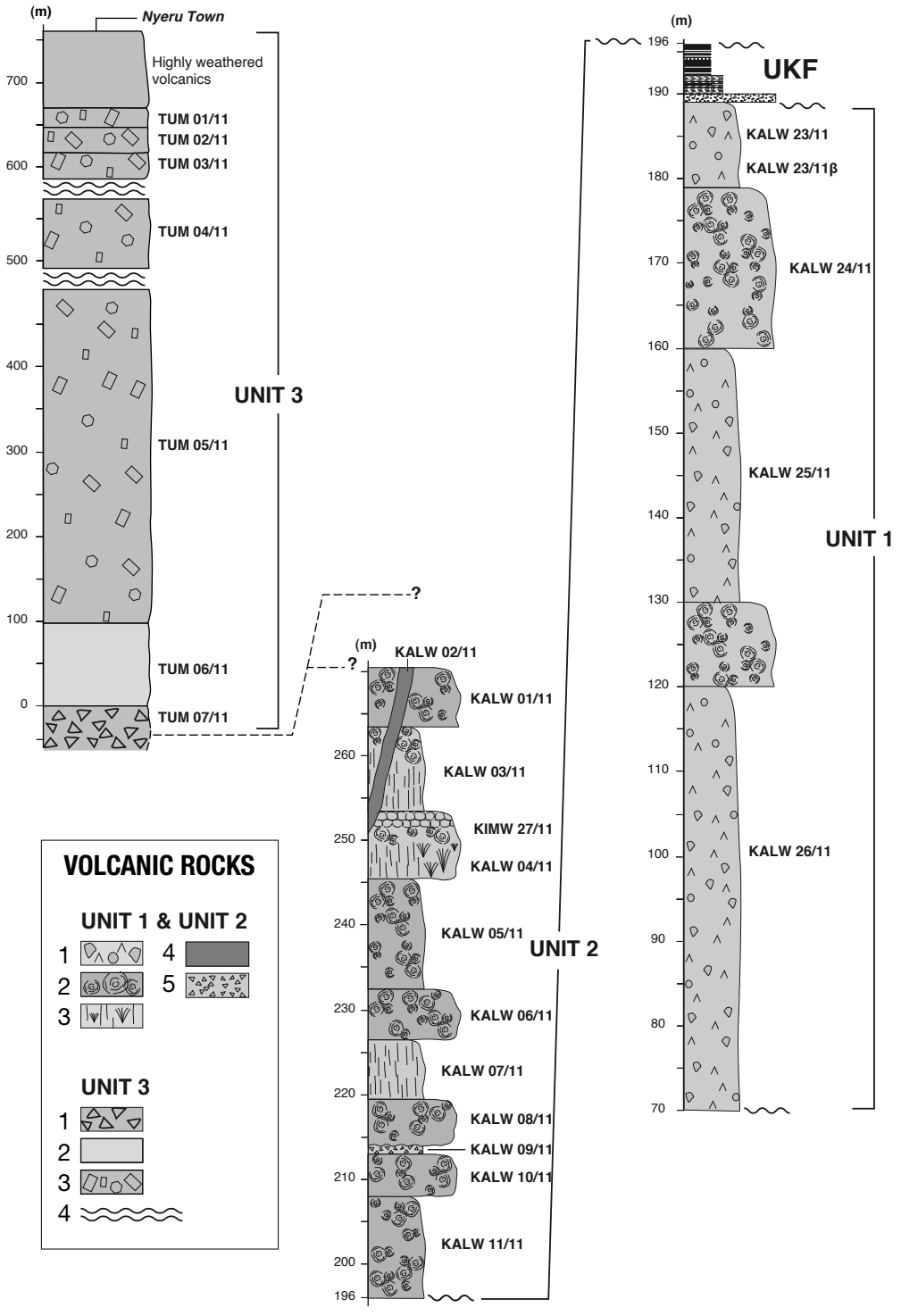

Fig. 27. *Lithological logs of the volcanic units associated to the Kimwarer Formation: Unit 1, Unit 2, and Unit 3. See Fig. 19b for stratigraphic relations with the Lower and Upper Kimwarer Formations. Legend for Units 1 and 2: (1) Volcaniclastic horizon/tuff/tuffite; (2) Massive horizon/ mafic lava flow with onion-skin weathering; (3) Massive horizon/mafic lava flow with columnar jonting/feather structures; (4) Mafic dyke; (5) Volcaniclastic graded horizon/tuff. Legend for Unit 3: (1) Consolidated mafic breccia/tuff; (2) Massive horizon/mafic lava flow; (3) Massive felsic horizon/phonolitic lava flow; (4) Gap in outcrop.*

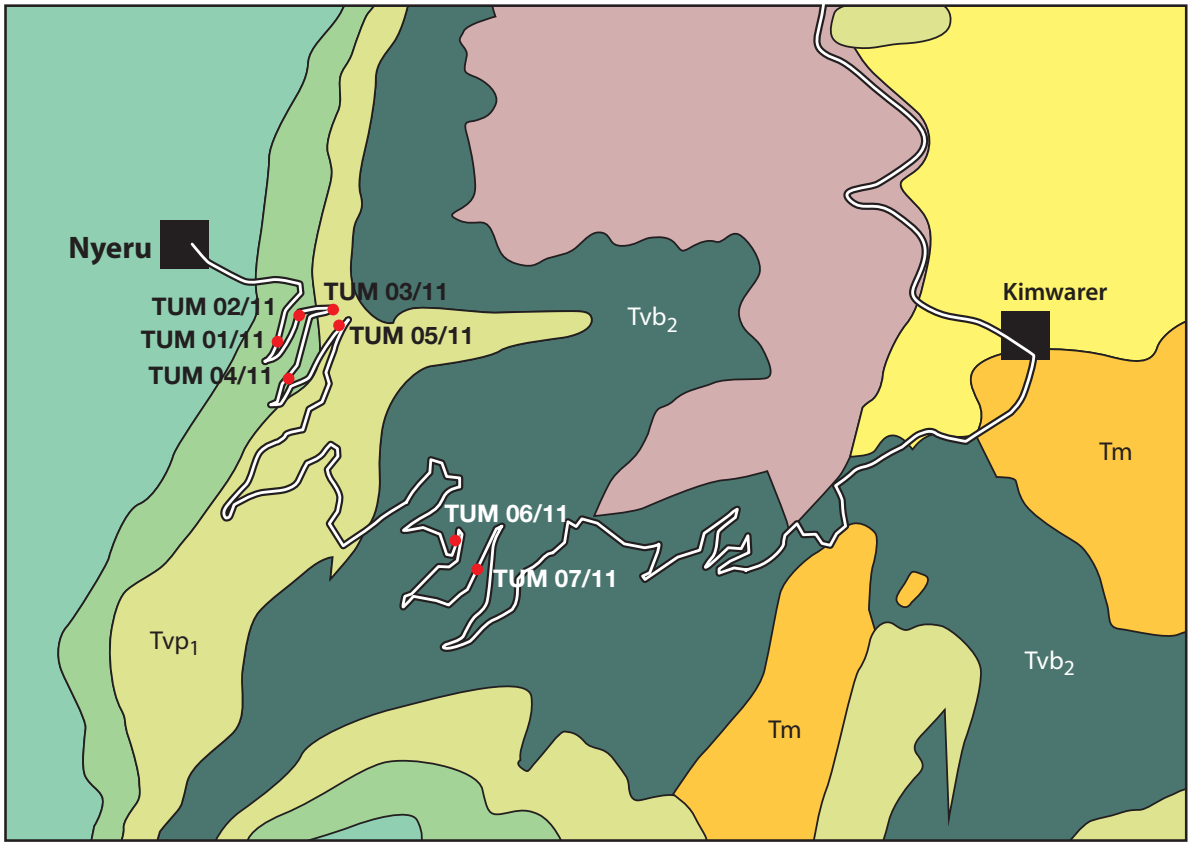

Fig. 28. *Geological map modified from Walsh (1969) and Chapman et al. (1978). Superimposed on the map are the locations of the volcanic sampling for Unit 3 along the Turesia Road from the Kerio Fluorspar mining plant to Nyaru Town. The samples have been located from their GPS coordinates and their approximal elevation provided by GPS, and also using the curves of the road, the trace of it was approximately transposed from Google Earth imagery.*

- Unit 1: This 120-m thick unit lies conformably on top of the upper, upturned purple beds of the LKF, and below the 6.7-m thick fining-up sequence of conglomerates, sandstones and highly distorted mudstones that comprise the UKF (Figs. 18b, 27 and 29a and b-b1). Unit 1 is constituted of three mafic volcaniclastic horizons (50-m, 30-m, and 10-m thick, respectively, from bottom-up) alternating with two interbedded massive mafic/ultramafic layers (10-m and 19-m thick, from bottom-up) that show onion skin peel weathering structures (Fig. 27). At the base of Unit 1, metre-sized rounded boulders of volcaniclastic material appear to be embedded within the purple mudstone forming the top of the LKF (Figs. 27 and 29a). These three volcaniclastic horizons contain ungraded clasts of different sizes and volcanic origin (from ash to blocks up to a few tens of centimetres in size) that are both sub-rounded to angular (Fig. 29b and b1). Some of the volcanic clasts are porphyritic and/or vesicular and often exhibit fluidal textures. When vesicular, the vesicles may be filled by low-temperature hydrothermal minerals (e.g. zeolites, carbonates). Thin sections of the largest and most common volcanic clasts in Unit 1 and one clast of the massive horizons were studied. The typical volcanic clasts (samples KALW 26/11, KALW 25/11, KALW 23/11ß and KALW 23/11 described in Appendix 1; see Figs. 18b and 27 for location) from the three volcaniclastic horizons of Unit 1 are porphyritic to glomeroporphyritic (Figs. 29b and 30a and b) and contain vesicles and amygdales embedded within a weathered microlitic groundmass (Fig. 30c). They are mostly basaltic in mineralogical composition and show variation in total amount of vesicles (0-30 vol.%) and phenocrysts (20-30 vol.%). The phenocrysts are predominantly plagioclase and/or zoned clinopyroxene (augite),

(a)

(b)

(b1)

KAWL/04/11
KAWL/05/11
(c)

KAWL/04/11
(d)

KALW 09/11
(e)

KAWL/10/11
(f)

(f1)

KAWL/02/11
(g)

(h)

and euhedral olivine pseudomorphs, mostly made of clay minerals, chlorite and/or serpentine and secondary opaque minerals. Plagioclase and/or pyroxene phenocrysts are elongated, up to 10 mm and 3 mm in length, respectively. Amygdales are a few millimeters in size and are filled with carbonate and fibrous zeolites. Primary opaque minerals rarely occur as phenocrysts but more commonly within the groundmass and as inclusions in the outer rim of the pyroxenes. Apatite needles also occur preferentially within the outer rims of the zoned plagioclase phenocrysts as well as in the groundmass. The groundmass is mostly composed of plagioclase microlites and weathered glass.

The decametric lava flows that are interbedded within the volcaniclastic horizons (Fig. 27) show no specific internal structures (with the exception of onion skin weathering). A representative sample (KAWL 24/11) of one of these horizons is ultramafic (Figs. 27 and 30d). It is porphyritic to glomeroporphyritic, microcrystalline and amygdaloidal (Fig. 30e and f). The main phenocrysts (locally up to 40 vol.%) are zoned clinopyroxenes (>2 mm), plagioclases (>1 mm) and olivine pseudomorphs (>2 mm), the latter being infilled by carbonate (dolomite?), brownish to greenish clay minerals and chlorite. The clinopyroxene phenocrysts usually show a colourless core and a pinkish rim suggesting Ti-rich augite. The amygdales are rimmed by iron hydroxides and filled by carbonates and zeolites. The groundmass is mostly composed of clinopyroxene and opaque mineral microcrysts, locally enclosed in minor plagioclase poikilitic microcrysts. Feldspathoids are potentially present in the groundmass but were not readily optically identifiable suggesting the rock is basaltic to tephritic in mineralogical composition.

The only one chemical analysis available for Unit 1 is from a >10 cm volcanic clast (sample KALW 26/11) (Fig. 27) collected from the basal volcaniclastic horizon and belongs to an alkaline undersaturated suite (both olivine and nepheline are present to the norm; Table 4). In the TAS diagram, the rock plots on the boundary between tephrite (less than 10% normative olivine) and trachybasalt (Fig. 31). The trace element composition (Appendix 2) shows that the rock is almost undistinguishable from the tephritic rocks from the two other volcanic units, although slightly richer in SiO_2.

An attempt of whole rock 40Ar/39Ar dating was performed on sample KALW 26/11 from Unit 1. The result was rejected despite a rather flat age spectrum (Fig. 32a) that could technically allow a plateau calculation at ca. 16 Ma. The observed age spectrum shape is rather unusual, with an increase of apparent ages for the two last steps, concomitant with a strong increase of atmospheric contamination. Usually, atmospheric contamination decreases or at least remains stable at these steps. Thus the age spectrum does not allow an irrefutable plateau age calculation. Furthermore, in the light of the 40Ar/39Ar results from the volcanic samples of Unit 2 (see

Fig. 29. *Typical outcrops from the volcanic units associated to the Kimwarer Formation (Units 1, 2 and 3). The indications on some photographs refer to the corresponding sample numbers. (a) General appearance of the basal mafic volcaniclastic horizon (tuff or tuffite) from Unit 1. At the base of Unit 1, metre-sized rounded boulders of mafic volcaniclastic material appear to be embedded within the purple mudstones that form the upper part of the LKF. (b) KALW 23/11 - a rounded and vesicular clast embedded within the purple brown matrix forming at the top of Unit 1, (b1) KALW 23/11ß- angular and porphyritic clast showing white feldspar phenocrysts also embedded in the same purple brown muddy/gravelly matrix. (c) Typical subhorizontal contact between massive horizons (tephritic lava flows) from Unit 2 represented by samples KALW 04/11 and 05/11. (d) Crude subvertical fracturing (with feather structures on the surface) corresponding to prismatic columnar jointing in a massive tephritic horizon (lava-flow) from Unit 2 (sample KALW 04/11). (e) Interbedded fine-grained volcaniclastic layer (tuff) showing upward vertical grading in Unit 2 (sample KALW 09/11). (f), (f1) Strongly weathered massive horizons (lava flows) from Unit 2 with typical onion skill peel weathering structure. (g) Subvertical tephritic dyke (sample KALW 02/11) cross-cutting the topmost massive layer from Unit 2 (sample KALW 01/11); the intrusive contacts are located where the sub-horizontal columnar joints stop to the left and right sides of the photograph. (h) General appearance of the phonolitic massive horizons from the upper part of Unit 3, approaching the top of the Elgeyo Border Fault Escarpment along the Turesia Road, near Nyaru Town.*

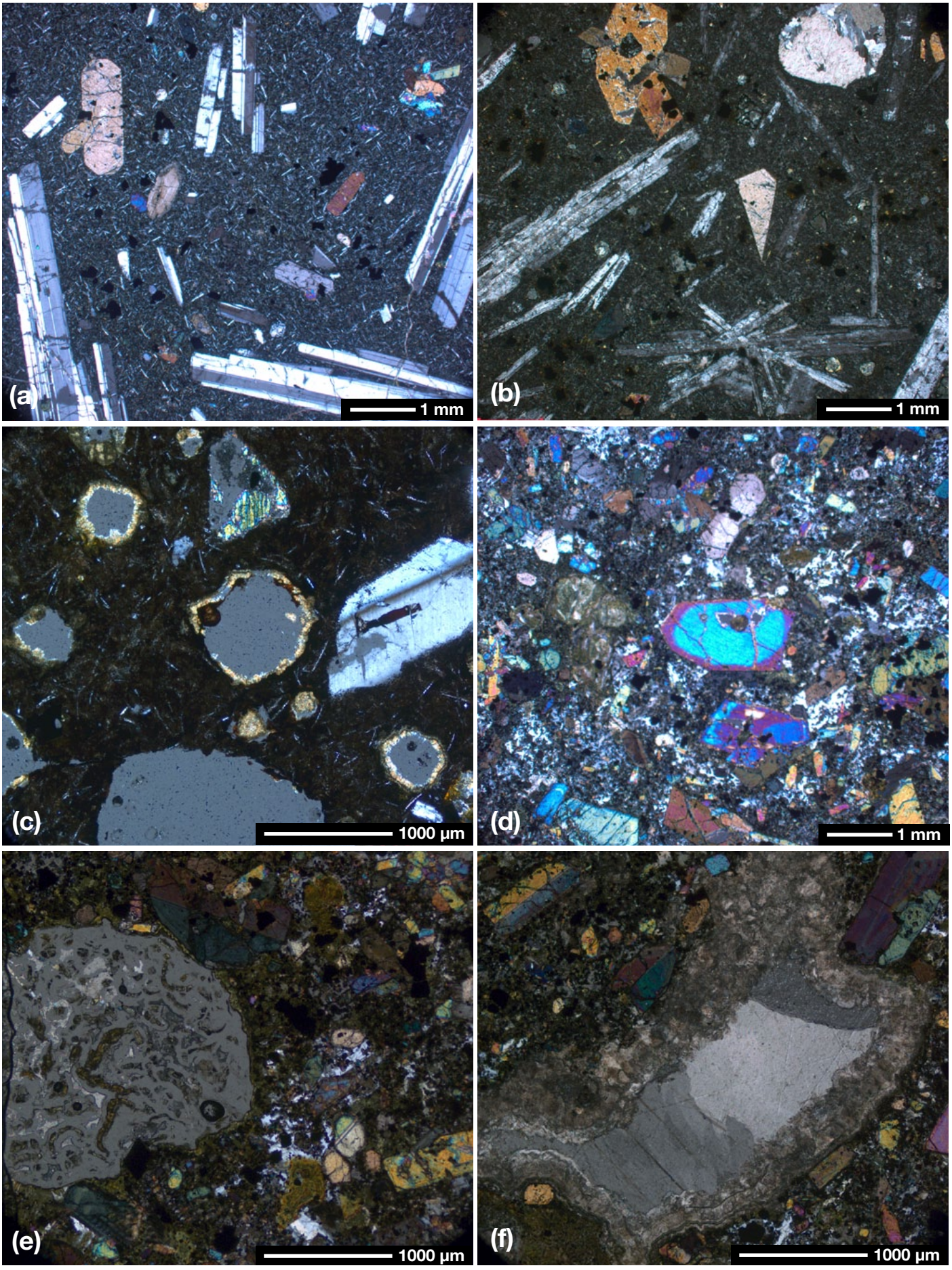
(a)
1 mm
(b)
1 mm
(c)
1000 µm
(d)
1 mm
(e)
1000 µm
(f)
1000 µm

Fig. 30. *Typical textures and mineralogy of some selected mafic volcanic rocks from Unit 1 (see Fig. 18b and 27). Thin sections under cross-polarized light. (a) Porphyritic alkaline basalt volcaniclast from the topmost volcaniclastic horizon from Unit 1 (sample KALW 23/11), showing elongated plagioclase (multiple twinned grey minerals) and clinopyroxene (colored crystals) phenocrysts in a microlitic and vesicular groundmass (vesicles: black; plagioclase microlites: white laths). (b) Porphyritic to glomeroporphyritic tephritic trachybasalt volcaniclast from the lowermost volcaniclastic horizon from Unit 1 (KALW 26/11) (also see Figs. 18b, 28 and 29a), which is a tuff or tuffite layer; see discussion in section 4.3.2.). An agglomerate of plagioclase phenocrysts is visible in the middle bottom. This sample as the same minerology as (a). (c) Amygdales partly filled with clay minerals from (a). (d) to (f) Porphyritic and amygdaloidal trachybasalt from the massive horizons from Unit 1, sample KALW 24/11 (see Figs. 18b and 28) . Note the large amount of clinopyroxene phenocrysts (colored crystals) within a microcrystalline groundmass, are made of sub-poikilitic plagioclase micro-oikocrysts (white flakes) embaying opaque minerals and clinopyroxene microcrysts. The amygdales (e) and (f) are filled by low-temperature mineral phases (carbonate, quartz, chlorite, zeolite and clay minerals).*

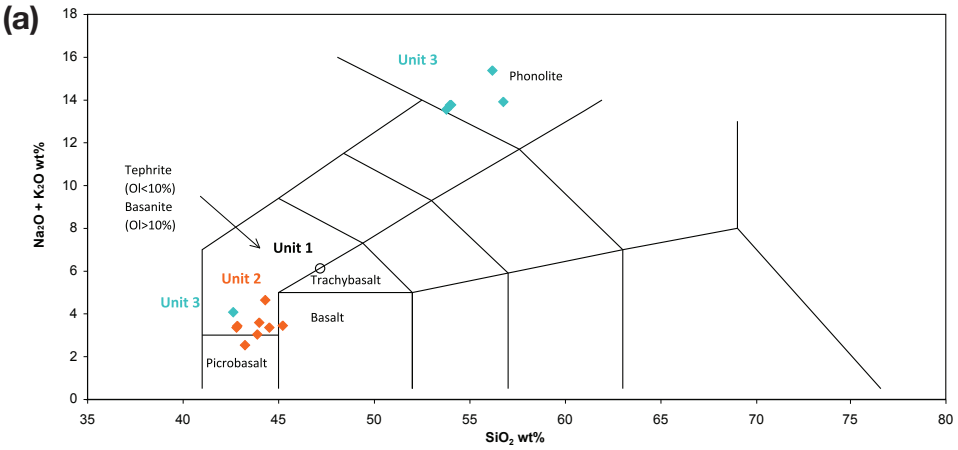

Fig. 31. *(a) Total Alkali versus Silica (TAS) diagram and sample nomenclature (after Le Maître et al., 2002). Colour-coded representation of the different volcanic units associated to the Kimwarer Formation. Unit 1 is black, Unit 2 is orange, and Unit 3 is blue. Ol refers to normative olivine content.*

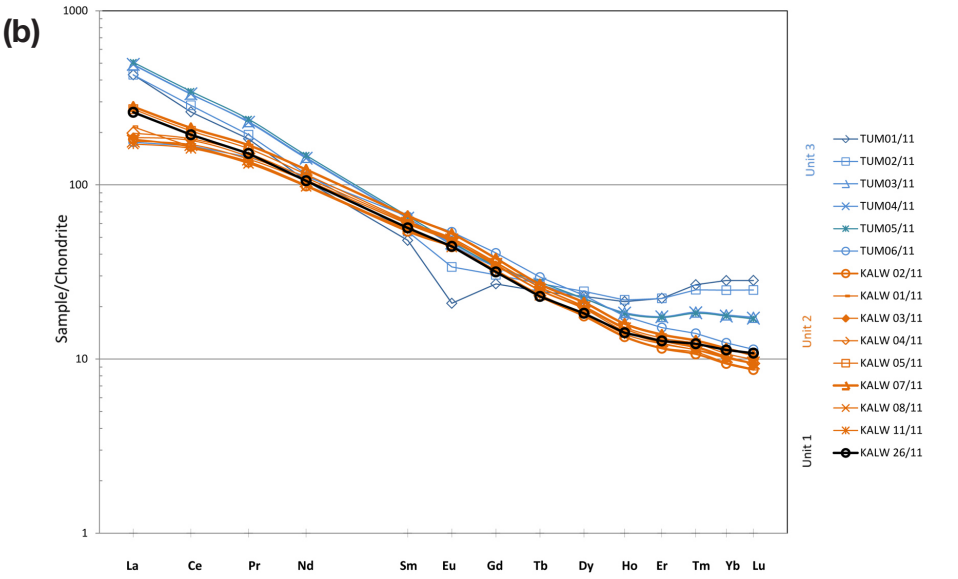

Fig. 31. *(b) Corresponding Rare Earth Elements (REE) chondrite normalized patterns. Note that the samples from Units 1 & 2, and sample TUM 06/11 from Unit 3, which all correspond to tephritic/basanitic to basaltic compositions (Table 4), exhibit very similar patterns.*

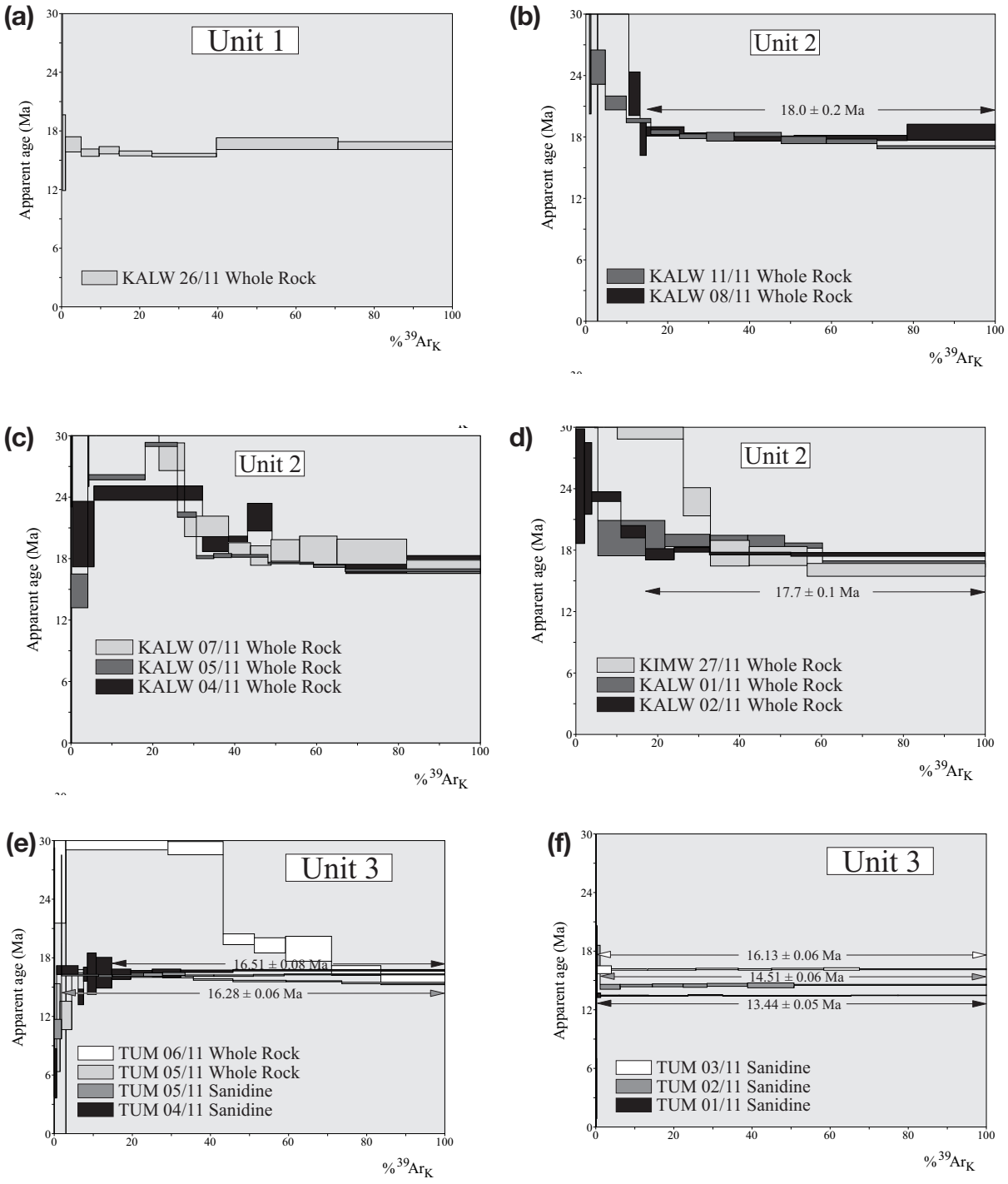

Fig. 32. *Plots showing age-spectra obtained from step-heating experiments versus cumulative 39Ar gas released for volcanic samples collected from: (a) Unit 1; (b), (c), (d) Unit 2; (e), (f) Unit 3.*

below), an age at ca. 16 Ma would be stratigraphically incoherent. Therefore this age is not interpreted as an age of solidification of the lava but more probably expresses a subsequent weathering event. Consequently, no absolute dating is available for Unit 1.

- Unit 2: Along the observed section, this unit with a total apparent thickness of 74m concordantly overlies the upper sediments of the KF (UKF), i.e. the conglomeratic to fine-grained distorted sediments (Figs. 18b and 27). Unit 2 is composed of ten mafic massive subhorizontal horizons (Figs. 27 and 29c and 29d), the thickness of which varies from 4.75 m (minimum) to 13 m (maximum), and of a 1-m thick volcaniclastic horizon at an intermediary location within the section (ca. 16 m from the base of the unit; Fig. 27). This 1-m thick volcaniclastic layer is graded from lapilli-sized dominant volcanic clasts at the base to ash-sized dominant particles to the top (Fig. 29e) and overlies two of the massive layers at the base of the unit.

The massive horizons generally have a similar homogeneous greyish black appearance and exhibit onion-skin weathering structure (Fig. 29f and 29f1), and are dotted with euhedral feldspar and pyroxene phenocrysts and/or amygdales infilled by carbonates or zeolites. Although mostly horizontal, basal surfaces of some of the horizons are locally irregular (e.g. the horizon where sample KALW 04/11 was collected; Fig. 29d). Several massive horizons also exhibit a network of sub-vertical fractures, spaced by about 1 m, resulting in a prismatic columnar jointing. On most of these joint surfaces, feather structures were observed. The horizon where sample KALW 04/11 was taken locally dips about 10° to the W-NW consistent with the inclination of the observed columnar jointing (Fig. 29c and 29d). At the top of Unit 2, a 2.4-m wide, N84°-trending dyke, dipping ~70° to the N, crosscuts the topmost massive horizons (Figs. 27 and 29g).

The thin section analysis of 12 samples show that the mafic massive horizons of Unit 2 are porphyritic to glomeroporphyritic, with abundant euhedral to sub-euhedral phenocrysts of varied sizes (usually >1 and <3 mm), including zoned clinopyroxene, plagioclases, olivine pseudomorphs (Fig. 34a) and opaque minerals. Colourless to greenish clinopyroxene phenocrysts or phenocryst cores suggest an augite to aegirine-augite (Na-rich) composition, and pinkish, often grouped clinopyroxene phenocrysts or phenocryst rims suggest a Ti-rich augite composition (Fig. 33b and 33c). The equant shapes of some weathered microphenocrysts suggest that feldspathoid was present as a primary phase. The groundmass is usually microcrystalline and more rarely microlitic and fluidal (KALW06/11 - Fig. 33d). It is composed of opaque mineral, plagioclase (often forming sub-poikilitic micro-oikocrysts) (Fig. 33e) and clinopyroxene microcrysts. Opaque minerals are also abundant as inclusions in the outer rims of the clinopyroxene phenocrysts. Apatite is a common accessory phase (Fig. 33f). When present, vesicles often form amygdales that are mostly filled by chlorite and carbonates that mostly include calcite (Fig. 33g). Sometimes the amygdales show a crude concentric organization of different rims that include carbonate, clay, opaque minerals and/or analcite?-rich zones (Fig. 33h). All the rocks from the massive horizons and the dyke crosscutting Unit 2 show about the same mineralogical content despite modal variations. For example, samples KALW 05/11 and KALW 06/11 show a larger amount of olivine pseudomorphs and sample KALW 11/11 is richer in plagioclase than all the other samples (Appendix 1). In contrast, sample KALW 02/11 (Fig. 34i), which corresponds to the dyke, shows almost no difference with the samples coming from the massive horizons it intrudes.

Eight chemical analyses are available for Unit 2 (Table 4 and Appendix 2). Representative samples were collected from seven different massive horizons in the volcanic pile and from the dyke. All the rocks are ultrabasic and show rather homogeneous compositions for both major and trace elements, consistent with their mineralogical compositions (Appendix 1). In the TAS diagram (Fig. 31), the samples are grouped within, or plot very close to the lower part of the tephrite-basanite field. Tephrites (with less than 10% normative olivine contents as in samples KALW 07/11, KALW 04/11, KIMW 27/11 and KALW 02/11; see Fig. 27 for sample location) are apparently common rocks in Unit 2, especially in its upper part. However, picrobasalts (e.g. the most alkali-lean

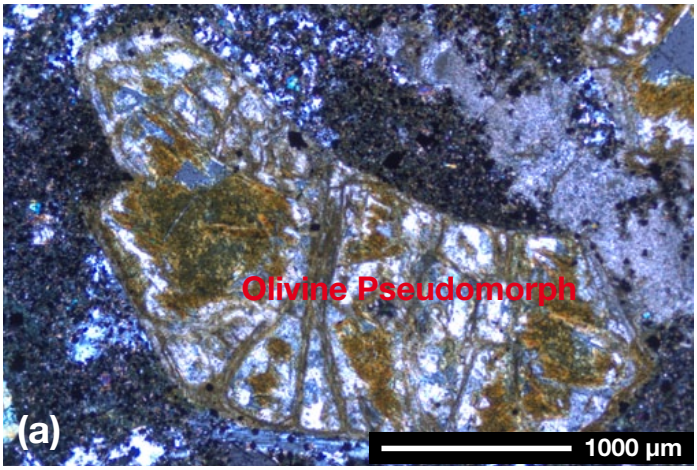
Olivine Pseudomorph
(a)
1000 µm

(b)
1000 µm

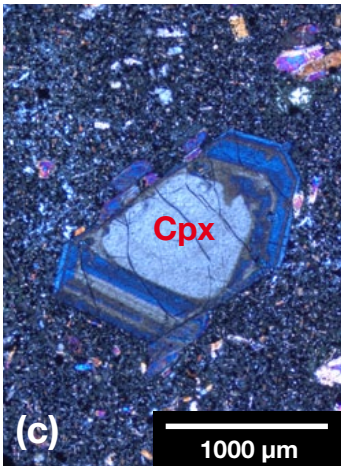
Cpx
(c)
1000 µm

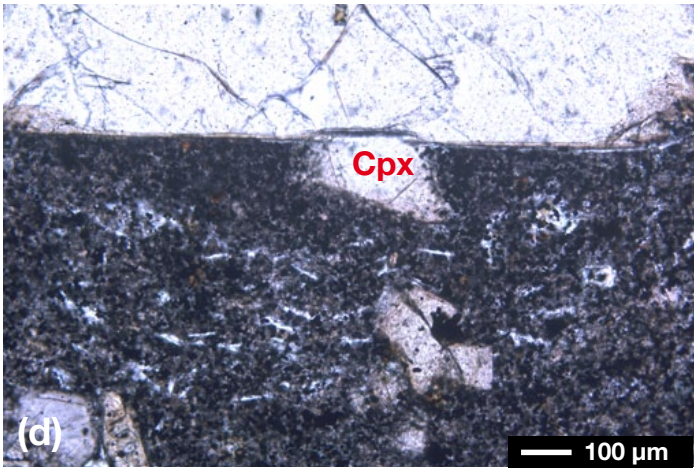
Cpx
(d)
100 µm

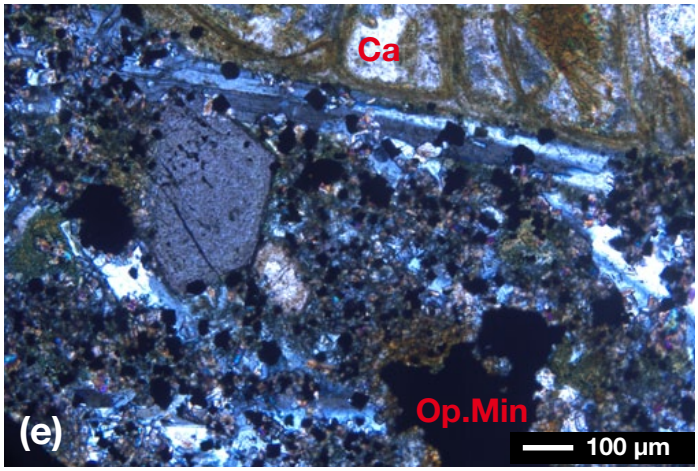
Ca
Op.Min
(e)
100 µm

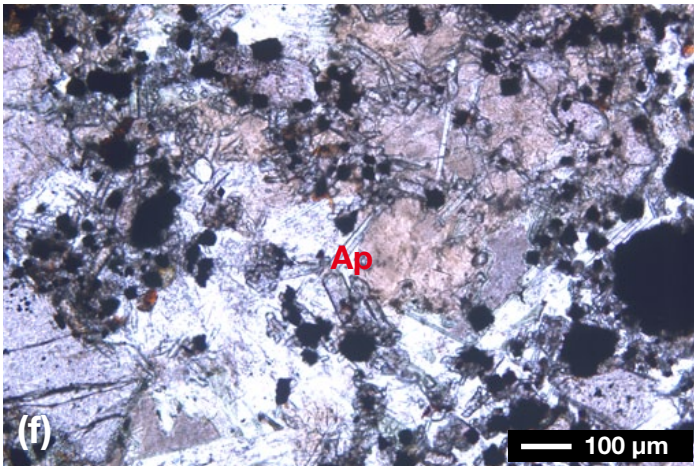
Ap
(f)
100 µm

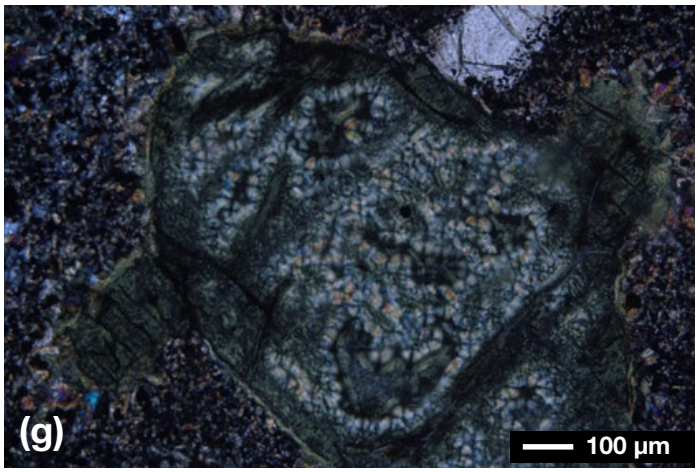
(g)
100 µm

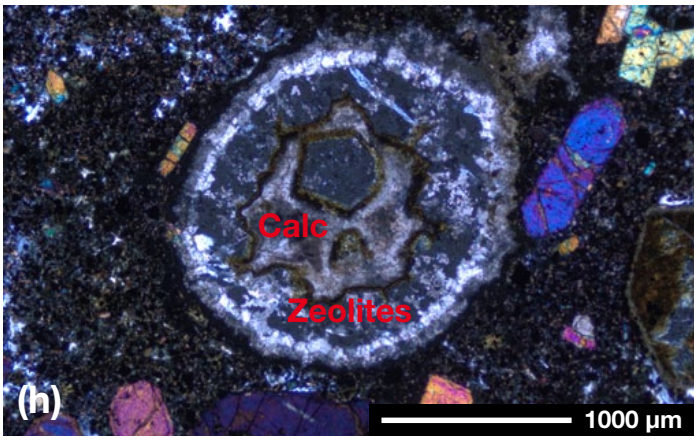
Calc
Zeolites
(h)
1000 µm

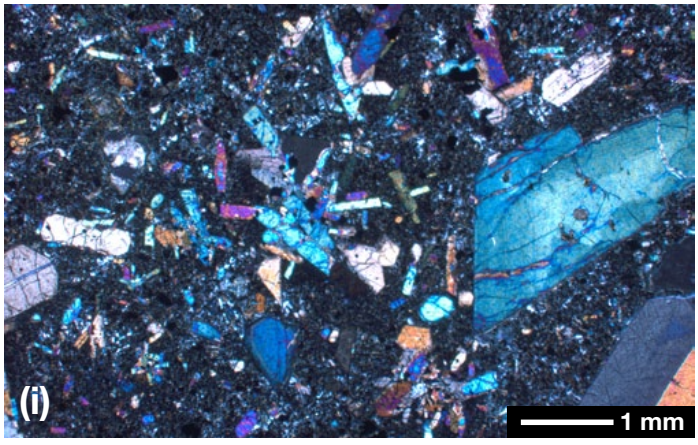
(i)
1 mm

sample KALW 08/11), basalts (e.g. the silica richest sample KALW 11/11), and basanites (e.g. sample KALW 05/11 with high normative olivine content) are also present in Unit 2. The dyke is not chemically different from the tephritic layers it intrudes. When plotted against the silica content, most chemical elements of Unit 2 samples define short differentiation trends (Fig. 34a), indicating that all the rocks belong to a single undersaturated alkaline suite possibly deriving from a unique parental magma. In addition, within this suite, the Rare Earth Element (REE) pattern of a given sample of the unit is almost indistinguishable from REE patterns of the other samples of the unit (Fig. 34b). This indicates that the magmatic differentiation processes involved to form the suite (e.g. fractional crystallization) did not significantly differentiate the REE. Therefore the REE contents of these rocks reflect those of the primary parental magma, possibly directly extracted from a mantle magmatic source.

Whole rock $^{40}Ar/^{39}Ar$ dating was attempted on the eight samples for which geochemical data are available in Unit 2 (Table 4). No reliable ages were obtained for the six samples, KALW 11/11, KALW 07/11, KALW 05/11, KALW 04/11, KIMW 27/11 and KALW 01/11 (Fig. 27). In contrast, plateau ages at 18.0 ± 0.2 Ma and 17.7 ± 0.1 Ma were obtained for samples KALW 08/11 and KALW 02/11 (the dyke), respectively (Figs. 27 and 32a and c). They are consistent at the 1σ uncertainty level and become younger following the stratigraphic order.

It is worth noting here that only 2 out of the total 9 whole-rock grains from Units 1 and 2 that were analyzed gave reliable results. The lack of K-rich mineral phases in the rocks precluded any appropriate phase separation (e.g. sanidine, biotite), from which more reliable results would be expected (e.g. see below Unit 3; Fig. 32e). Most of the whole-rock grains from Units 1 and 2 displays strongly disturbed age spectra characterized by decreasing apparent ages from low-to-high temperature steps, with the youngest apparent ages obtained at fusion steps (Fig. 32a and b).

Such age spectrum shapes could be explained through excess argon contamination but several features suggest that a more plausible explanation is that they result from the physical displacement of a part of the "mobile" 39Ar produced from the "fixed" ^{39}K during irradiation of the samples, an effect known as the 'recoil effect' (Lo and Onstott, 1989; Ruffet et al., 1991). The ^{39}Ar recoil effect is quite often observed when analyzing volcanic rocks, due to the abundance of a glassy to cryptocrystalline mesostasis. The distance of recoil of the neutron-induced ^{39}Ar (ca. 0.1µm) may be sizeable when compared to the initial location of the parent 39K and to the "size" of its possible host phase (Lo and Onstott, 1989; Ruffet et al., 1991). The resulting impact of such ^{39}Ar shifting depends on its "landing" location. Indeed, the shifted neutron induced ^{39}Ar may:

- remain in the same retentive phase or in a similar one. Overall, the ^{39}Ar implantation balance is equated and the $^{40}Ar^*/^{39}Ar_K$ ratio remains unchanged;
- be lost during irradiation because it directly reaches the atmosphere or is implanted in a weakly retentive phase (cryptocrystalline phase or glassy mesostasis) and subsequently diffuses into the atmosphere through thermally activated diffusion, either during irradiation or during baking of the material (up to 130 °C prior to the analysis).

Fig. 33. *Typical textures and mineralogy of some selected mafic volcanic rocks from Unit 2 (see Figs. 19b and 28). Thin sections under cross-polarized light, except (b), (d) and (f), that are observed under plane polarized light. (a) Subhedral olivine pseudomorph phenocryst filled by carbonates, low-grade hydrothermal minerals, and opaque minerals in the tephritic to picrobasaltic sample KALW 10/11. (b), (c) Euhedral zoned clinopyroxene phenocryst (Ti-rich augite) in the tephrite sample KALW 04/11. (d) Colourless clinopyroxene (Cpx) phenocryst (to the top) with a pinkish thin margin and pinkish grouped Cpx microphenocrysts in a microlitic to microgranular groundmass made of oriented plagioclase microlites, opaque minerals and clinopyroxene microcrysts (basanite sample KALW 06/11). (e) Detail from (a): microcrystaline groundmass made of sub-poikilitic plagioclase micro-oikocrysts (light to dark gray bluish) embaying opaque mineral and clinopyroxene microcrysts (Ca in the olivine pseudomorph to the top indicates carbonate). (f) Apatite (Ap) needles and opaque mineral forming inclusions within plagioclase and clinopyroxene (sample KALW 01/11). (g), (h) Details from amygdales filled by low temperature mineral phases (chorite, calcite – Calc –, opaque minerals, clay minerals -and/or zeolites) from the vesicular samples KALW 04/11 – tephrite – and KALW 08/11 –picrobasalt –, respectively. Note the large amount of euhedral clinopyroxene phenocrysts and the olivine pseudomorph to the bottom right in (h). (i) Porphyritic to glomeroporphyritic and microgranular texture from the tephrite dyke sample KALW 02/11 (Fig. 30g). Most of the phenocrysts and microphenocrysts are clinopyroxene and opaque minerals.*

Major element & C.I.P.W. normative compositions for Kimwarer Volcanics

Unit	Unit 1 Lava block	Unit 2 Lava flows							Dyke	Unit 3 Lava flows					
Sample Nb	KEN 39	KEN 34	KEN 31	KEN 30	KEN 28	KEN 27	KEN 44	KEN 25	KEN 26	KEN 23	KEN 22	KEN 21	KEN 20	KEN 19	KEN 18
Rock name	Tephrite / Trachybasalt	Basalt	Picrobasalt	Tephrite	Basanite	Tephrite	Tephrite	Tephrite	Tephrite	Tephrite	Phonolite	Phonolite	Phonolite	Phonolite	Phonolite
wt%															
SiO_2	44.76	43.32	41.56	42.00	42.52	41.44	41.11	42.39	42.61	41.00	51.12	50.67	50.39	53.91	54.18
Al_2O_3	14.39	11.26	10.86	12.33	12.28	11.39	11.26	10.91	10.88	11.62	21.80	21.79	21.64	19.01	18.72
Fe_2O_3*	12.01	13.36	14.71	14.02	13.20	15.22	15.15	13.67	13.53	15.57	4.17	3.93	3.98	5.20	5.73
MnO	0.26	0.17	0.21	0.21	0.22	0.22	0.21	0.21	0.20	0.22	0.20	0.20	0.19	0.27	0.23
MgO	5.20	7.72	8.61	6.20	8.48	7.56	7.45	8.72	8.41	6.66	1.07	0.93	0.94	0.77	1.16
CaO	9.13	12.91	13.36	11.48	11.61	13.29	13.08	13.87	14.02	12.38	2.19	2.26	2.72	0.94	1.45
Na_2O	2.65	2.51	1.84	3.71	2.02	2.49	2.60	1.95	2.57	3.17	7.97	7.95	7.73	9.23	7.48
K_2O	3.16	0.80	0.60	0.70	1.19	0.77	0.70	0.99	0.91	0.76	5.08	4.96	4.98	5.53	5.81
TiO_2	2.58	3.22	3.77	3.44	3.34	3.82	3.77	3.28	3.15	4.10	0.88	0.83	0.85	0.90	0.60
P_2O_5	0.76	0.55	0.63	0.74	0.68	0.65	0.65	0.63	0.60	0.72	0.29	0.29	0.29	0.20	0.12
PF	3.64	3.25	3.25	3.75	4.11	3.19	3.02	2.95	2.75	3.27	4.64	5.13	5.26	3.43	3.91
Total	98.53	99.08	99.39	98.57	99.65	100.03	99.01	99.57	99.64	99.45	99.40	98.94	98.97	99.39	99.39
CIPW Norm															
Fe_2O_3/FeO	0.2	0.2	0.2	0.2	0.2	0.2	0.2	0.2	0.2	0.2	0.3	0.3	0.3	0.3	0.3
Ap	1.9	1.4	1.6	1.9	1.7	1.6	1.6	1.6	1.5	1.8	0.7	0.7	0.7	0.5	0.3
Il	5.2	6.5	7.5	7.0	6.7	7.6	7.5	6.5	6.2	8.2	1.8	1.7	1.7	1.8	1.2
Or	19.8	5.0	3.7	4.4	7.5	4.8	4.4	6.1	5.6	4.7	31.8	31.4	31.5	34.2	36.1
Ab	16.7	14.7	11.8	16.6	15.2	9.6	10.1	8.2	7.0	11.8	25.6	25.8	24.2	25.9	31.2
Ne	3.9	4.1	2.5	9.1	1.6	6.7	7.1	4.9	8.5	8.9	24.8	25.0	24.8	23.9	19.2
An	19.2	18.0	20.6	15.9	22.1	18.4	17.9	18.9	16.1	16.0	9.2	9.7	10.4		0.4
Ac														5.6	
Ns														1.2	
Mt	6.0	5.6	6.3	6.0	5.8	6.6	6.6	5.8	5.6	7.0	2.2	2.0	2.1		3.1
Di-Hd	19.2	36.8	36.0	32.2	27.3	37.1	37.2	39.1	42.1	35.3	0.2	0.2	1.7	3.0	5.3
Ol	8.2	7.9	10.0	7.0	12.2	7.6	7.6	8.9	7.4	6.4	3.8	3.5	3.0	3.9	3.3
Total (Norm)	100.0	100.0	100.0	100.0	100.0	100.0	100.0	100.0	100.0	100.0	100.0	100.0	100.0	100.0	100.0

Fe_2O_3*: total iron; Ap: apatite; Il: ilmenite; Or:orthoclase; Ab: albite; Ne: nepheline; An: anorthite; Ac: acmite; Ns: Na silicate ; Mt: magnetite; Di-Hd: calcic clinopyroxene; Ol: olivine

Table 4

Major elements contents and C.I.P.W. normative compositions of the volcanic samples collected in the volcanic units 1, 2 and 3 associated to the Kimwarer Formation.

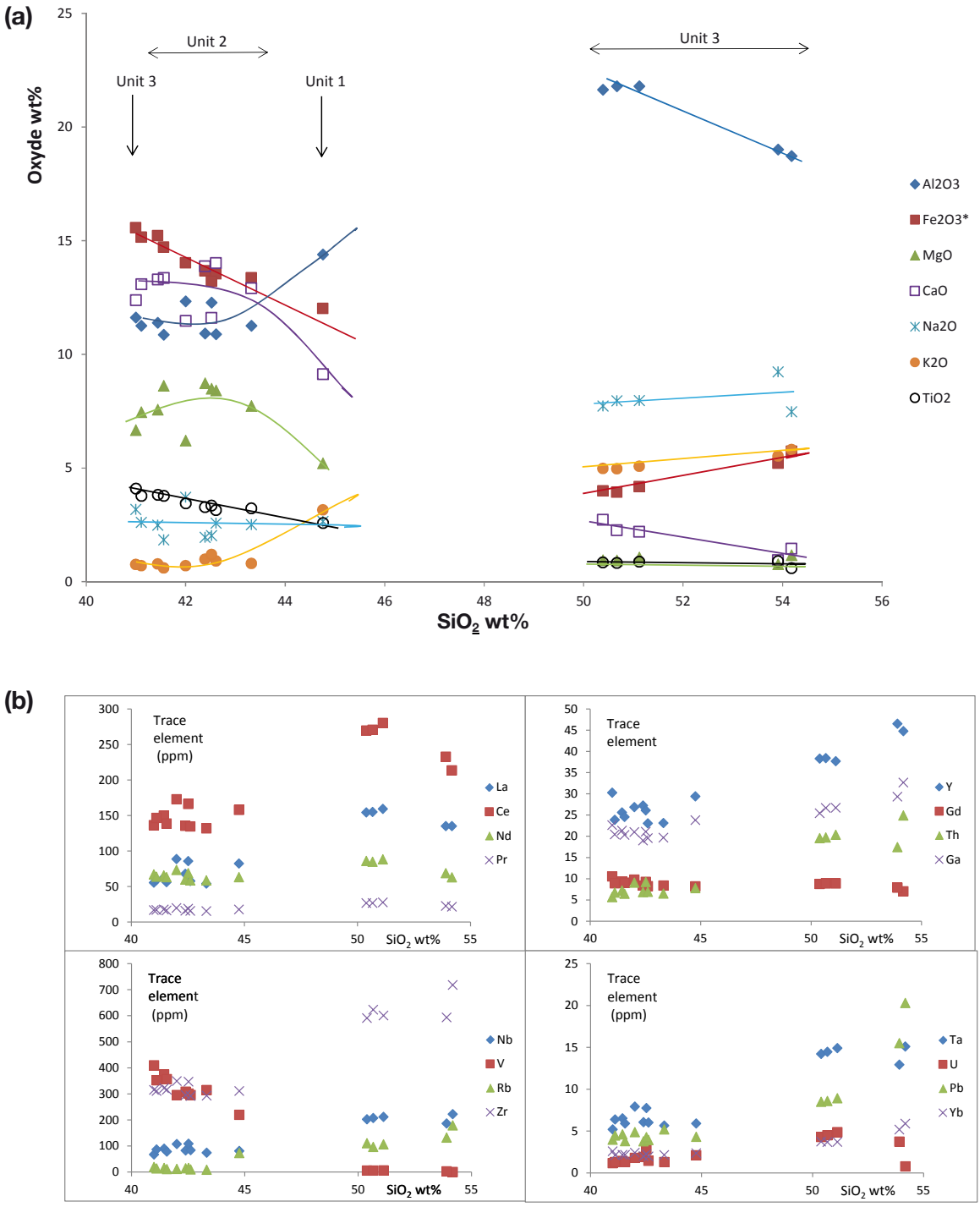

Fig 34. *(a) Major element contents versus silica content of the samples from Unit 1, Unit 2 and Unit 3 associated to the Kimwarer Formation. Note the trends shown for most elements and the gap in the range 45-50 wt% silica. Black arrows underline silica contents (vertical lines) or silica composition ranges (horizontal lines) of samples from the specified unit. (b) Selected trace element variations versus silica content of the samples from the three volcanic units. Note also the systematic trend among ultrabasic rocks (SiO2<45%) comprising samples from the 3 units.*

Such a loss of ^{39}Ar generates an artificial increase of the measured $^{40}Ar^*/^{39}Ar_K$ ratio. As weakly retentive phases degas at low temperatures, during a step-heating experiment, the first apparent age steps from the spectrum are abnormally old;
- be implanted in a highly retentive phase. The gain of ^{39}Ar generates an artificial decrease of the measured $^{40}Ar^*/^{39}Ar_K$ ratio. As retentive phases generally degas at high temperatures, during a step-heating experiment, the last apparent age steps from the spectrum become abnormally young.
An argument which favours the ^{39}Ar recoil hypothesis, is the convex trend (e.g., Appendix 4; sample KALW 11/11; Fig. 27) shown by the successive ellipses in correlation diagrams ($^{36}Ar/^{40}Ar$ versus $^{39}Ar/^{40}Ar$ with correlated errors; York, 1969; Turner, 1971; Roddick et al., 1980; Hanes et al., 1985) classically used to detect and "treat" ^{40}Ar in excess within samples. As 39Ar recoil can move points away from the correlation line on such graphs (e.g. Ruffet et al., 1991), it can be distinguished from excess argon that respects linearity of a mixing line. If the latter is corrected through isochrone analysis, the former is frequently fatal for the experiment. Additional arguments for the ^{39}Ar recoil hypothesis come from a comparison with the results from Unit 3.

As a result of ^{39}Ar recoil only two whole rock analyses (samples KALW 08/11 and KALW 02/11) display "flat" age spectra over at least the last 80% of ^{39}ArK degassing that yield coherent plateau ages at respectively 18.0 ± 0.2 Ma and 17.7 ± 0.1 Ma. From these results it can thus be assumed that the volcanic rocks from Unit 2 were emplacing and solidifying during the Burdigalian (20.44-15.97 Ma) (Cohen et al., 2013).

- Unit 3: The contact between Unit 3 and Unit 2 was not observed during logging along the Turesia Road (Figs. 27 and 28). Unit 3 is approximately 770-m thick and is composed of possibly seven massive, mostly homogeneous, several 10's of meters thick main horizons that are apparently concordantly superposed (Fig. 29h). From the field observations made along the Turesia Road (Fig. 28), the succession of samples TUM 07/11 and TUM 06/11 and that of the samples TUM 02/11 and TUM 01/11 were observed to be stratigraphicaly superposed (Fig. 27). Similarly, sample TUM 03/11 was collected in one of the horizons lying above the horizon from which sample TUM 05/11 was extracted. Locally, however, thick vegetation obscures the volcanic unit and some of the contacts between the horizons from which some of the samples were taken, were not directly observed (particularly TUM 04/11). As a result, it was impossible to verify the precise stratigraphic location of a few samples from direct field observation. This is especially true for sample TUM 04/11 relative to TUM 05/11 and TUM 03/11. Thus, based only on the relative altitudes at which the samples were collected and assuming strictly concordant, subhorizontal and unfaulted contacts in the masked zones of the area, sample TUM 04/11 was inferred to represent a horizon located in between the horizons of samples TUM 05/11 and TUM 03/11, as drawn on the schematic log of Unit 3 (Fig. 27). However, it is important to note that from the map alone (Fig. 28) sample TUM 04/11 could also have been inferred to be younger than samples TUM 05/11 and TUM 03/11. In addition, and also due to the lack of outcrop continuity along the road, some of the volcanic horizons in Unit 3 might have been missed, and not sampled, resulting in a possible overestimation of some of the individual horizon thicknesses shown Fig. 27 for Unit 3. The two successive lowermost horizons are TUM 07/11 and TUM 06/11, and are made of ultramafic and porphyritic rocks (Figs. 27 and 35). Although these two basal sub-units appeared very similar on the field, the lowermost one corresponds to a consolidated breccia and differs from the one just above which is massive and homogeneous, showing no specific internal structures. In Unit 3, these two basal horizons contrast with the five uppermost horizons composed of porphyritic felsic rocks in which the amount of phenocrysts, mostly sanidine and less abundant nepheline (up to 3 cm in size) varies significantly. Samples collected from the two basal ultramafic horizons are porphyritic to glomeroporphyritic and amygdaloidal. No significant difference can be seen in between the clasts in the breccia and the rock forming the massive horizon. The main phenocrysts in these rocks are zoned clinopyroxenes, and rare, olivine pseudomorphs, nepheline and opaque minerals. The pinkish tinge on the outer rims of the clinopyroxene phenocrysts is taken as an evidence

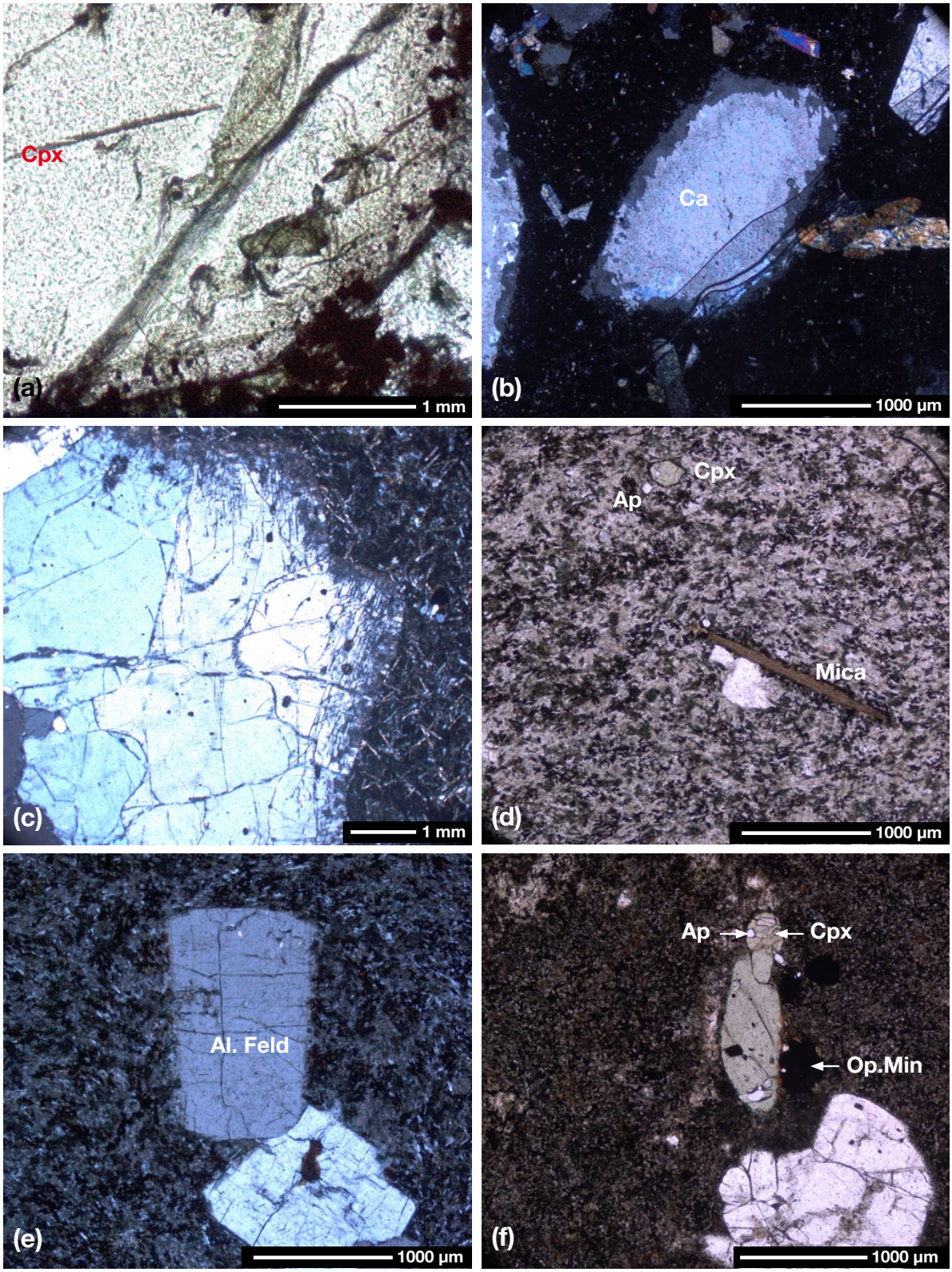

Fig 35. *Typical textures and mineralogy of selected mafic and felsic volcanic rocks from Unit 3 (see Fig. 27). Thin sections under cross-polarized light, except (b), (d) and (f) that are observed under plane polarized light. (a) Detail from a zoned clinopyroxene phenocryst, which outer pinkish rim (Ti-rich augite) contains opaque mineral inclusions, in the tephrite sample TUM 06/11. (b) Porphyritic and amygdaloidal tephritic volcaniclast (sample TUM 07/11). Amygdales are mostly filled by carbonates (Ca), rimed by quartz. Also visible are clinopyroxene phenocrysts in a cryptocrystalline groundmass. (c) Nepheline phenocrysts in a microlitic groundmass from the phonolite sample TUM 03/11. Most of the microlites are sanidine-anorthoclase laths. (d) and (e) Phenocrysts and microphenocrysts of biotite (mica), apatite (Ap.), greenish clinopyroxene (Cpx, aegyrine augite) and sanidine-anorthoclase (Al. Feld.) in the porphyritic microlitic to microgranular phonolite sample TUM 01/11. (f) Aegyrine augite (Cpx) phenocrysts with apatite (Ap.) inclusion, opaque mineral (Op. Min.) and sanidine-anorthoclase phenocrysts in the phonolite sample TUM 02/11.*

for Ti-rich augite (Fig. 35a). The amygdales in TUM 07/11 are filled by carbonates (calcite?) and rimmed by iron hydroxides while those in TUM 06/11 are filled by both calcite and zeolites (Fig. 35b). The mesostasis of the samples from the two basal horizons is composed of weathered volcanic glass, opaque minerals, and microcrysts of plagioclase and clinopyroxene.

Upward in the observed field section, the felsic horizons are represented by samples TUM 05/11, TUM 04/11 and TUM 03/11 (see Fig. 27) that are petrographically similar despite variations in the size and amount of the phenocrysts (TUM 05/11 - phenocrysts ~ 40 vol.% and up to 1 cm in size; TUM 04/11 – phenocrysts ~25 vol.% and up to 1 cm in size; TUM 03/11 - phenocrysts ~25 vol.% and up to 3 cm in size). The main phenocrysts in the three samples are euhedral, elongated sections of sanidine (sample TUM 05/11) and more equant sections of nepheline that are partly embaying the groundmass (sample TUM 03/11) (Fig. 35c). All samples are amygdaloidal with a microlitic groundmass. The amygdales are infilled by carbonates and zeolites and all samples contain apatite and opaque minerals as the main accessory phases. The groundmass of all three samples is composed of weathered plagioclase and sanidine microlites, opaque mineral microcrysts and volcanic glass. These rocks correspond to phonolites. In the successive samples, TUM 02/11 and TUM 01/11 (Fig. 27) which belong to the two topmost, still felsic, horizons within Unit 3, the rocks are petrographically similar to the ones below although the amount of phenocrysts significantly decreases: TUM 02/11 - phenocrysts up to ~10 vol.%, and TUM 01/11 - phenocrysts <10 vol.%. Both samples are porphyritic, microlitic to trachytic and locally fluidal (Fig. 35d). The main phenocrysts are euhedral sanidine, aegerine-augite, biotite (Fig. 35e) and opaque minerals (Fig. 35f). The groundmass is mostly composed of weathered sanidine microlites, and clinopyroxene and opaque mineral microcrysts. Euhedral feldspathoid microphenocrysts (noseane?- TUM 01/11 and nepheline?- TUM 02/11) are also present (Fig. 28).

Six chemical analyses were conducted for the topmost six horizons of Unit 3. No analysis was made for the basal brecciated horizon. In agreement with petrographic observations, they indicate that the topmost five horizons are all phonolitic in composition (Figs. 27 and 35; Table 4). In the TAS diagram (Fig. 31), however, the group of the underlying and strongly porphyritic phonolites (samples TUM 03/11 to TUM 05/11) slightly differenciates from the overlying group of poorly porphyritic phonolites (samples TUM 02/11 and TUM 01/11). In contrast, the ultramafic and underlying sample TUM 06/11, with normative olivine <10%, plots as a tephrite, the chemical composition of which is undistinguishable from that of the tephrites from the other units (Units 1 and 2) (Figs. 31, 35; Table 4; Appendix 2).

$^{40}Ar/^{39}Ar$ dating was performed on the six samples from Unit 3 (TUM 06/11 to TUM 01/11) for which geochemical data are available (Table 4). Unfortunately, no age was obtained for the tephritic sample TUM 06/11 (Fig. 32c) due to ^{39}Ar recoil effect, as previously discussed for most of the whole rock analyses from Unit 2. In contrast, plateau ages at 16.28 ± 0.06 Ma, 16.51 ± 0.08 Ma, 16.13 ± 0.06 Ma, 14.51 ± 0.06 Ma, and 13.44 ± 0.05 Ma were calculated for sanidine single crystals separated from the phonolitic samples (Unit 3) TUM 05/11, TUM 04/11, TUM 03/11, TUM 02/11 and TUM 01/11, respectively (Fig. 32c). For sample TUM 05/11, both a single sanidine crystal and a whole rock grain were analyzed (Fig. 32c) which yielded distinct age spectra. The sanidine isochrone calculation (Appendix 4) displays a fully concordant isochrone age at 16.3 ± 0.6 Ma and a $^{40}Ar/^{39}Ar$ initial ratio at 298.5 ± 8.3, indistinguishable of the atmospheric ration (298.56 ± 0.31), confirming the absence of an excess argon component. This isochrone calculation suggests that the sanidine age is valid, assuming that inherited argon is absent, which, if present, is undedectable through the isochrone calculation. Contrasting with the single crystal result, the whole rock experiment yields an age spectrum (Fig. 32c) showing decreasing apparent ages from the low-to-high temperature steps, and the last six steps of the experiment (>80% of $^{39}Ar_K$ degassing) yield apparent ages “younger” than the sanidine plateau age, decreasing from ca. 16.1 down to ca. 15.4 Ma at the fusion step. As for previously discussed whole rock experiments with similar age spectrum shapes these features strongly suggest ^{39}Ar recoil (see Unit 2). Indeed the “anomalous” younger apparent ages could be explained by an implantation of “additional” ^{39}Ar during irradiation from low retentive phases within

more retentive ones degassing at high temperatures.

The sanidine ages (Fig. 32c) are consistent with the inferred stratigraphic order, within the 1σ uncertainties, except for the samples TUM 04/11 and TUM 05/11, for which the ages are significantly different (at the 2σ level uncertainties) and are in the opposite chronological order than that expected from the relative altitudes at which the samples were collected. Therefore, because sample TUM 05/11, has at the 1σ level the same age as sample TUM 03/11, we infer that the lack of outcrops in the corresponding part of the sampled section possibly mask adjacent faults that separate eastern blocks exposing either the ultramafic horizons, or the TUM 05/11 and TUM 03/11 phonolitic horizons, from western uplifted blocks exposing both the older phonolitic horizon TUM 04/11 and the youngest phonolitic horizons TUM 02/11 and TUM 01/11. Based on the radiometric ages, the correct stratigraphic order of the samples and corresponding horizons in Unit 3 would be therefore, from base to top, TUM 06/11, TUM 04/11, TUM 05/11-TUM 03/11, TUM 02/11, and TUM 01/11. This succession is consistent with the previously exposed petro-geochemical results distinguishing two types of phonolite in Unit 3, and showing that sample TUM 04/11 is poorly distinguishable from TUM 05/11-TUM 03/11 but slightly differs from the phonolites TUM 02/11 and TUM 01/11. Back to the map (Fig. 28), it consistently appears that the oldest phonolite group (TUM 03-04-05/11) correlates with the Tvp1 formation (Chof Phonolites as defined by Chapman et al., 1978) that is mapped just below a younger phonolitic formation named Tvpn (Uasin Gishu Phonolites as defined by Chapman et al., 1978) from which, consistently, representative samples are TUM 02/11 and TUM 01/11. These geochronological results also indicate that the phonolitic rocks from Unit 3 are slightly younger than the mafic rocks from Unit 2 and were emplacing and solidifying throughout, the Burdigalian and Serravalian ages (20.44-11.62 Ma) (Cohen et al., 2013).

4.3.2. Dynamics of emplacement of the different volcanic units

The massive homogeneous horizons found in all the units can be assumed to represent effusive lava flows. This is based from the observations that they are individually made of homogeneous massive volcanic rocks, sometimes showing columnar jointing that relate to cooling subsequent to flow. In addition, the texture and composition of the rock forming the dyke visible in the upper part of Unit 2 (Fig. 27) being similar to that of its volcanic host-rocks indicate that the intrusion was very shallow and was transporting a magma that possibly fed other lava flows, now eroded along the section. Given the observed thicknesses of some of these massive volcanic layers, at about a few tens of meters (Fig. 27), each of these within the different units most likely corresponds to several successive eruptive events, or a single eruption that had a huge flow rate or to a lava lake, probably proximal to the emission center.

In all units, the accumulation of volcanic rock fragments within volcaniclastic horizons suggests that they could be tuffs and thus correspond to the deposition of volcanic pyroclasts following violent explosive eruptions from a proximal vent (pyroclastic flow and/or fall deposits). However, the poor sorting and the variety of rock textures displayed by the volcanic clasts in most volcaniclastic beds, as well as the ultrabasic compositions of most of the volcanic clasts, suggest that they could as well correspond to tuffites in which the reworking and redeposition of older proximal volcanic deposits occurred via erosion and sedimentary processes, as expected in any environment where volcanism and faulting are active and coeval. It is nonetheless difficult to singularly attribute one of the above depositional processes as the dominant factor controlling the deposition of the volcanic clasts. Nevertheless, the graded volcaniclastic layer within Unit 2 is interpreted as a tuff (Figs. 27, 29e), which is proposed to be related to fall deposits from a proximal source owing its upward fining-graded nature. Because of the extreme homogeneity in the nature of the clasts in TUM 07/11, the basal brecciated sub-unit in Unit 3 also corresponds to a volcanic agglomerate or tuff. The other volcaniclastic layers in Unit 1 may be either tuff or tuffite, or both. Whatever they are, as they are associated with lava flows and interbedded within the upper part of the KF, Unit 1 indicates that the regional volcanism was already contemporaneous to basin sedimentation.

4.3.3. Stratigraphy and correlations

Unit 2 can be correlated to the Elgeyo Formation as described by Chapman et al. (1978). The observations of this work, including the nature of the rocks are in good agreement with published data on the Elgeyo Formation where basalts are generally porphyritic with the dominant phenocryst being zoned clinopyroxene, altered olivine that is infilled by chlorite, plagioclase and opaque minerals. Vesicles are also infilled by patches of secondary calcite and analcite as it was observed in Unit 2 (Walsh, 1969; Chapman et al., 1978). The mineralogical description by Walsh (1969) of the Samburu Basalts (age ca. 23-16 Ma) that are found further to the east and which cover most of the Tugen Hills closely resembles the results of the petrographical analysis of Unit 1 in this work. Walsh (1969) described the Samburu Basalts petrographically porphyritic and vesicular with the main phenocrysts being large size (>3 cm) plagioclase phenocrysts and altered olivine pseudomorphs. The groundmass is composed of plagioclase, clinopyroxene and abundant magnetite. The vesicles are infilled by yellow-green zeolites as is noted in our examination of Unit 1. However, the stratigraphic position by Walsh (1969) of the Samburu Basalts directly above the Precambrian basement in the southern end of the Elgeyo Escarpment close to the Kimwarer area is contrary to the findings of this work, which places the base of KF directly on top of the basement. Other workers who have discussed the early basal sedimentary units of the Northern and Central Kenya Rifts (Chapman et al., 1978; Mugisha et al., 1997; Morley et al., 1999; Tiercelin et al., 2004) (Fig. 7 a, b) also report a similar sequence (basement-sediments-volcanics). In describing the Elgeyo Formation (580-m thick) where it overlies the KF as being constituted of massive lavas and agglomerates composed of basinites and tephrites, amongst others feldspathoidic alkaline rocks, Chapman et al. (1978) probably includes the Elgeyo Basalts within their definition of the Elgeyo Formation. This does not contradict the findings of this work and Unit 1 is therefore concluded to form the lowermost unit of the Elgeyo Formation. This is consistent with chemical data that show that the single studied sample KALW 26/11 in Unit 1 can belong to the same alkaline undersaturated magma based on differentiation trends defined by samples of Unit 2. The small differences in major element contents suggest that the sample KALW 26/11 only represents a slightly more evolved magma within the volcanic suite than those of Unit 2. It is worth to note also that, despite the magmatic differentiation, the Rare Earth Element (REE) pattern of the Unit 1 sample is undistinguishable from those of Unit 2 (Fig. 34b).

The stratigraphic location of Unit 3 relative to Unit 2, which was observed along a different section from that of Unit 3, was difficult to establish in the field owing to thick vegetation cover that obscured possible faulted zones between the two sections. Using petrography and geochemistry, however, the phonolitic upper part of Unit 3 can be inferred to lie above Unit 2. Indeed, Unit 2, and especially its upper part, is mostly tephritic in composition, as the basal part of Unit 3 is. Therefore, two possible scenarios could exist:

1) The upper portion of Unit 2 can be correlated with the base of Unit 3;

2) A gap may exist between the two sections, so that Unit 3 is overlying Unit 2. In any of these two different scenarios, the entire Unit 2 and the basal tephritic part of Unit 3 may correspond to the Elgeyo Formation, which is then capped by a formation of phonolitic rocks, as previously described in the area (e.g. Chapman et al., 1978). Earlier workers (Shackleton, 1951; Lippard, 1973; Chapman and Brook, 1978; Chapman et al., 1978) have identified two successive and "geochemically distinct" phonolitic formations above the Elgeyo Formation along the Elgeyo Escarpment; the Chof Phonolites (339-m thick), which are then overlain by the Uasin Gishu Phonolites (480-m thick). Chapman et al. (1978) refer to Lippard (1973) to highlight the geochemical differences between these two units. We also found small chemical differences between the phonolitic samples from Unit 3; however it was not possible to directly correlate these with those evidenced in Lippard (1973). Nevertheless, from the location of the samples relative to the formations known in the area (Fig. 28), and from their petro-geochemical compositions and ages, it follows that three of our older phonolite samples from Unit 3 likely represents the stratigraphically lower unit (the Chof Phonolites) as described by Chapman et al. (1978). Then it follows that the distinct younger phonolitic samples from Unit 3 could correspond to the Uasin Gishu Phonolites (more precisely to a lower member of the Uasin Gishu Phonolites; Fig. 28).

4.3.4. Chronological setting of the Kimwarer Formation

The chronological position of the KF has until now been discussed based on its stratigraphic position above the metamorphic basement in connection to the broad definition of the "Turkana Grits". Samples from different units within the Elgeyo Formation (Unit 1 - 1 sample, Unit 2 - 9 samples, and a basal sample from Unit 3) as well as the Chof and Uasin Gishu Phonolites (Unit 3 - 5 samples) were collected for ^{40}Ar-^{39}Ar dating with the ultimate goal of determining the minimum age of the Kimwarer Formation. Reliable dating was however not possible on the lowermost unit of the Elgeyo Formation (Unit 1) and most other whole rock tephritic samples from Units 2 and 3 in which K-rich minerals were absent and for which the obtained age spectra were disturbed (Fig. 32). Only two whole-rock tephritic samples from Unit 2 gave the oldest reliable ages at 18.1 ± 0.1 Ma and 17.0 ± 0.5 Ma. These ages are significantly older than had previously been determined. Indeed, the Elgeyo Formation had previously been dated at ca. 15.1-15.6 Ma using K-Ar dating techniques (Baker et al., 1971; Chapman et al., 1978). The new ^{40}Ar-^{39}Ar ages indicate that the sedimentation of the KF Formation was earlier than ca. 18 Ma.

In addition, reliable ^{40}Ar-^{39}Ar ages were also obtained from sanidine grains extracted from the phonolites above the Elgeyo tephrites. Phonolitic samples TUM 05/11 to TUM 01/11, collected from Unit 3 yielded five radiometric dates ranging from 16.51 ± 0.08 Ma to 13.44 ± 0.05 Ma (Fig. 33c). The oldest of these ages indicate the age of the Chof Phonolite (16.28 ± 0.06 Ma, 16.51 ± 0.08 Ma, and 16.13 ± 0.06 Ma from samples TUM 05/11, TUM 04/11 and TUM 03/11, respectively) and the youngest (14.51 ± 0.06 Ma, and 13.44 ± 0.05 Ma from samples TUM 02/11 and TUM 01/11, respectively) correspond to those of some the lower flows in the overlying Uasin Gishu Phonolites. Again, the ^{40}Ar-^{39}Ar ages from the Chof Phonolite are significantly older than the K-Ar ages previously known for the phonolitic formation. In contrast, those from the Uasin Gishu Phonolites are in rather good agreement with K-Ar data. Indeed, the Chof Phonolites had been previously dated at ca. 15.0 Ma (Chapman and Brook, 1978) while the Uasin Gishu Phonolites had been dated at ca. 14.5-12 Ma (Baker et al., 1971). For the Uasin Gishu Phonolite the youngest K-Ar age at ca. 12 Ma, came from upper lava flows in the formation (Baker et al., 1971; Tvb2 on Fig. 29) that were not sampled in this work. As expected, this age is significantly younger than the new ^{40}Ar-^{39}Ar data obtained from lower lava flows of the KF (Tvbn on Fig. 28). At this stage it is worth to note that the K-Ar isotopic systems, but also some of the whole-rock ^{40}Ar-^{39}Ar isotopic systems (as previously discussed), from the oldest and buried volcanic units along the Elgeyo Border Fault Escarpment, seem to have been significantly perturbed by more recent volcanic and hydrothermal activities. These perturbations in the Elgeyo tephrites and Chof Phonolites led to obtain isotopic dates (K-Ar or some of the whole rock ^{40}Ar-^{39}Ar data) that are up to about 2 Ma younger than the ages of the solidification of the flows. Another point that requires precision based on the results of the new ^{40}Ar-^{39}Ar data is the timing of the tectonic deformation in the studied area. Here, the Chof Phonolite is discordant and rests either on the metamorphic basement, the KF sediments or the Elgeyo Basalts (Fig. 27 and original geological map by Walsh, 1969). To the north, a comparable but younger unconformity characterizes the base of the Uasin Gishu Phonolites that rest either on the basement, the Elgeyo Basalts, the Chof Phonolites or the Tambach sediments (see map in Chapman et al., 1978). These unconformities may only indicate the lateral extensions reached by some of the flows over a rather stable palaeotopography, but they more probably significant tectonic activity and erosion episodes during the volcanism while the palaeotopography was changing. In such a hypothesis, as the new 40Ar-39Ar data can be used to date these two successive unconformities at ca. 17 Ma, corresponding to the apparent gap in ages in between those of the Elgeyo Basalts and the Chof Phonolites, and at ca. 15 Ma, the apparent gap in ages in between the Chof and the Uasin Gishu Phonolites, two main deformation episodes can be inferred along the Elgeyo Border Fault Escarpment. It is also likely that tectonic deformation was significantly active continuously during at least about a 4 Ma time span of active volcanism (here calculated only from the oldest and youngest reliable ^{40}Ar-^{39}Ar ages obtained in this work).

The results of the present fieldwork and dating are consistent with the seismic correlations previously ex-

posed although seismic data does not permit for the discrimination of individual volcanic formations. From both approaches, the Kimwarer Formation is identified as forming the basal unit of the Kerio Basin, unconformably overlying the Precambrian basement, and then conformably capped by the Elgeyo Formation (that includes Unit 1, Unit 2, and the base of Unit 3). The top of Unit 3 is interpreted as the superposition of the Chof and the Uasin Gishu Phonolites (Fig. 27).

Our new ^{40}Ar-^{39}Ar data set outlines an early Miocene age – Burdigalian age (18.1 ± 0.1 Ma) as the emplacement time for the mafic lavas that overlie the Kimwarer Formation. This age must be considered as the minimum age for the deposition of the Kimwarer Formation. It is indeed not possible to rule out the existence of a depositional hiatus prior to the emplacement of the volcanic rocks. Consequently, the Kimwarer Formation could be significantly older than ca. 18 Ma. In addition, while being the oldest documented age for the Elgeyo Formation, this age was not obtained from the oldest volcanic horizons found (Unit1), which would have better constrained the of the sedimentation in the KF. Indeed, as Unit 1 was found intercalated in between the Lower and Upper KF, to obtain a reliable age from this unit would have indicated both the age of the very beginning of the volcanic activity in the studied area and a maximum age for the deposition of the Upper KF.

Finally, the association between the KF and the other poorly constrained sedimentary units that exist above the basement along the Elgeyo Escarpment can also be briefly discussed, especially the possible relationship or equivalence of the KF to the Tambach Formation, which is exposed along the Elgeyo Escarpment, 34 km north of the Kimwarer Formation outcrop. Following Chapman and Brook (1978) and Chapman et al. (1978) in considering that the intercalations of volcanic lava flows and tuffs near the base of the Tambach sediments are equivalent to the Chof Phonolites, the new 40Ar-39Ar results of this work indicate that some Tambach sediments could be as old as 16.67 ± 0.08 Ma. This suggests that the Tambach sediments are a northern equivalent of the KF and younger by at least ~1.5 Ma. However the demonstration that the volcanic Tambach intercalations are strictly equivalent to the Chof Phonolites was not verified in this work.

Despite local differences discussed above between the K-Ar and new ^{40}Ar-^{39}Ar ages, the sequence of the volcanic units observed in this work are in rather good agreement with the previously documented timing of volcanic activities within the Kenyan Rift (Baker et al., 1971). The first volcanic phase in the Kenya Rift starts ca. 37-36 Ma (Tiercelin et al., 2012a) in Northern Kenya and ends at ca. 15 Ma. The first phase of volcanism in the Central Kenya Rift started around ca. 23 Ma and ended at ca. 12 Ma (Baker et al., 1971). Based on our results, all the volcanic units that we sampled fall under this bracket of initial volcanism and span three chronostratigraphic stages: 1) Burdigalian (20.44-15.97 Ma) for samples from the Elgeyo Basalts and Chof Phonolites formations (KALW 08/11, KALW 02/11, TUM 04/11, TUM 05/11 and TUM 03/11; 2) Langhian (15.97-13.82 Ma) for sample TUM 02/11 and Serravallian (13.82-11.62 Ma) for sample TUM 01/11, both from the Uasin Gishu Phonolites.

4.4. Facies analysis, depositional processes and environments of the Lower and Upper Kimwarer Formation

The lithofacies characteristics, facies associations and their interpretations in terms of depositional environments are summarized in Fig. 19 and Table 2.

4.4.1. Distal fluvial channel lithofacies associations

The basal and upper parts of the "Lower Kimwarer Formation" (LKF) in the Sarbab Type-Section (0-24.5 m) (Fig. 19) are characterized by a lithofacies association composed predominantly of fine- to coarse-grained, massive ungraded sandstones (lithofacies Sm) with intercalations of horizontally bedded sandstones (lithofacies Sh) that are locally rippled (lithofacies Sr) and associated to massive or laminated mudstone facies (lithofacies Fm and Fl). Lithofacies Sm could represent deposits developed during fluvial system bank collapse or channel overflow produced during flooding events (Miall, 1996). Lithofacies Sh could develop as suspension from slow moving (≤1m/s), shallow fluvial systems or deposited in single dynamic events such as flash floods when flow conditions remain critical for prolonged durations of time (Miall, 1996; Neves et al., 2005). Lithofacies Sr similarly could develop in shallow fluvial systems, where the rate of deposition and the speed of flow are low (≤ 1m/s; Miall, 1996). The intercalated lithofacies Fl and Fm generally represent overbank deposits. Lithofacies Fm, which in the Sarbab Type-Section is commonly associated with repetitive desiccation cracks, could represent deposits from standing pools of water during low-stage channel abandonment, that have dried and in most cases cracked under possibly seasonal hot climatic conditions, while lithofacies Fl represents overbank deposits suspended from standing pools of water or from weak traction currents (Miall, 1996). This facies association is interpreted as being representative of a distal fluvial channel environment.

4.4.2. Alluvial fan lithofacies association

Between 24.5 and 54 m in the "Lower Kimwarer Formation" (Sarbab Type-Section), six cyclic lithofacies associations are noted. A similar cycle is also identified in the "Upper Kimwarer Formation" between 190 m and 193 m (Fig. 19). These cycles characteristically fine-up, from massive clast-supported conglomerates (lithofacies Gcm) or matrix-supported conglomerates (lithofacies Gmg), through sandy intervals comprising of massive sandstones (lithofacies Sm), rippled sandstones (lithofacies Sr) with root beds (lithofacies R), horizontally bedded sandstones (lithofacies Sh), and culminate in a fine-grained assemblage (sensu Miall, 1996) comprising of finely laminated siltstones or mudstones (lithofacies Fl) at the top. In these cycles, grey to buff-brown conglomerates form the thickest units that range between 0.5-2.0 m when they fill pre-existing topography, for instance when filling pre-existing channels (e.g. Figs. 19 and 20g). For Cycle 1 (Fig. 19; 24.5-30.5 m), Cycle 3 (Fig. 19; 33.5-37.7 m), Cycle 4 (Fig. 19; 37.7-44.7 m), Cycle 5 (Fig. 19; 44.7-49.7 m), Cycle 6 (Fig. 19; 49.7-54 m), the conglomerate facies that forms the base of these cycles corresponds to lithofacies Gmm, i.e. massive, matrix-supported conglomerate with sub-angular to rounded clasts representative of low strength pseudo-plastic debris flows (Miall, 1996). In Cycle 2 (30.5-33.5 m), massive clast-supported conglomerates (lithofacies Gcm) form the lowermost beds of these cycles (Fig. 19). These clast-supported conglomerates also represent pseudo-plastic debris flows, but are more representative of deposition of inertial bedload from turbulent flows. Both gravelly units generally have slightly erosive bases, indicating the prevalence of high-energy hydrodynamic regimes such as debris flows.

The sandstone lithofacies within this facies group is dominantly massive sandstone (lithofacies Sm) ranging between 0.2 to 3.2 m in thickness that could represent deposits resulting from bank collapse or lighter fractions of debris flows deposited rapidly from turbulent flows. Lithofacies Sh and Sr are interbedded within the conglomeratic units in the Sarbab Type-Section and both represent deposition from suspension during single dynamic events such as flash floods when conditions remain in critical stage for prolonged durations of time (Miall, 1996). The fine-grained lithofacies that are associated with the alluvial fan depositional environment range between 0.50-0.70 m in thickness and are mainly massive grey-green mudstones (Fm) that are locally laminated (Fl). Lithofacies Fm, within this facies group, is believed to represent deposits from standing pools of water which can develop after dynamic events such as debris flows (that could be associated to flash floods), that lead to the restriction of water bodies and subsequent deposition of this facies. Lithofacies Fl similarly represent deposits from suspension

but dispersed by weak traction currents, a scenario which could also develop as an aftermath of a single dynamic event that restricts water bodies and but allows for limited turbulent motion of within the water mass. This facies association is thereby interpreted as being representative of alluvial fan environment and whose cyclicity can be attributed to seasonal climatic variations.

4.4.3. Floodplain lithofacies association

This lithofacies association exists between 55-70 m in the LKF, and is also represented in the 193-197 m interval in the "Upper Kimwarer Formation" (UKF) (Fig. 19). The lower interval (55-70 m) is uniformly composed of massive mudstone beds (lithofacies Fm), which are purple-red (at base) and grey (top 2 m). The purple-red beds are tilted to approximately 78° in the N144° direction while the top grey interval is crushed and distorted. This tilting and bed deformation can be attributed to the overlying volcanic unit that is interpreted to have been deposited on poorly consolidated fine-grained sediments.

Lithofacies Fm and Fl are dominant between 193 and 197 m on the UKF. These mudstone beds that change colour from grey to purple-red at the top represent sediments deposited from standing pools of water (lithofacies Fm) or from slow moving shallow water (lithofacies Fl). Both lithofacies can be deposited in a distal floodplain environment (Miall, 1996). In both these intervals, it appears that the purplish red colour of the sediments can be a secondary modification and has been attributed to the scorching of the upper sediments by hot lava (belonging to Unit 2) as it is emplaced.

4.5. Post-depositional evolution of the Kimwarer Formation

The post-depositional evolution of the KF was studied through petrographic examination of samples from the Sarbab Type-Section. This study was aimed at constraining the post-depositional modification that the KF has undergone and the causes of these modifications as well as the implications to the overall reservoir quality of the formation. As there is no deep well data for the KF, an understanding of the initial mineralogical make-up of the formation and the subsequent cementation profile is critical for predicting the reservoir characteristics of the KF at depth.

The lower part of the LKF (0-57 m from base of section) is composed of predominantly feldspathic arenites, the constituents of which are chiefly derived from the metamorphic basement. The mudstone succession (57-70 m from the base of section) did not yield any positive results under microscopic test owing to the fine-grained nature of sampled sediments (Fig. 19). The UKF was not studied under thin section but its stratigraphic position above the 120-m thick Unit 1 points to a volcanic-rich sedimentary unit (Figs. 18b, 19). The main diagenetic features observed in the LKF are cementation, predominantly by hematite and calcite, as well as compaction, which is confined to the lower half of the LKF. These cements occur in varied amounts throughout the formation in association with other authigenic phases. This zonation of diagenetic minerals has allowed for the division of the LKF into three distinct zones based on their relative abundance of the key diagenetic minerals and mode of occurrence of these minerals (Fig. 19):

- Zone 1 (0-15 m) (Abundant hematite);
- Zone 2 (15-30 m) (Abundant carbonate);
- Zone 3 (30-57 m) (Abundant kaolinite).

4.5.1. Texture

The textural characteristics of siliciclastic sediments from the KF can be summarized as follows:

- Grain size: They range from fine sand to pebbles, the latter being highlighted by the presence of quartz grains with diameters up to 5 mm;

- Grain shape: Sub-angular to sub-rounded;

- Grain contacts: Floating to concavo-convex, locally sutured (e.g. sample KIMW 28/11 - Fig. 36a) the latter being an indication of intergranular deformation probably a result of intense chemical compaction/pressure dissolution processes;

- Sorting: Sediments are poorly sorted overall.

The textural and compositional immaturity of the analyzed sediments is thus evidenced by the feldspathic-rich composition (up to 30% visual estimate) of the studied sediments, by the range of grain sizes and by the angularity of grains, which may suggest a relatively short distances from the provenance zone to the depositional environment.

4.5.2. Detrital minerals

The main detrital minerals in the KF are, in order of relative abundance: monocrystalline quartz, polycrystalline quartz, plagioclase feldspars and potassium feldspars. Other detrital grains that occur intermittently include metamorphic rock fragments, mud clasts, heavy minerals such as garnet (which is mainly concentrated at the base of the KF immediately above the basement), and sparse organic matter.

4.5.2.1. Quartz

This is the most abundant detrital mineral in the KF. Monocrystalline quartz together with the polycrystalline quartz constitute between 20-60% of the whole detrital composition, following the Compton (1962) standard visual mineral estimation chart. Quartz grain shapes vary generally from angular to locally rounded and grain sizes reach maximum diameter of 2 mm (granules), although the general range is 0.125-1 mm (see Figs. 36 and 37). The bulk of the monocrystalline quartz grains also exhibit undulose extinction suggesting the quartz grains in the LKF have undergone intense stress (sample SAR 53/11; Figs. 19 and 36b). This is consistent with sutured contacts observed within samples collected from the very base of the outcrop (sample KIMW 28/11; Figs. 19 and 36a). Intragranular grain shattering is also noted within quartz grains. The fractures resulting from the grain shattering have been subsequently infilled by authigenic iron oxides, which also occur as inclusions within the grains. Polycrystalline quartz is relatively less abundant than the monocrystalline variety and occurs as aggregate of crystals of different sizes. This quartz variety also shows evidence of both intragranular and intergranular deformation in form of grain-specific fractures and sutured grain contacts. Individual grains show undulose extinction suggestive of intracrystalline deformation of the original quartz fragments. Polycrystalline quartz of sand size, especially if more than five individual crystals are present, is considered to be an indicator of a metamorphic source.

4.5.2.2. Feldspars

Feldspars are the second most abundant detrital component of the KF where they form up to 30% of the terrigeneous detritus in the bulk of the thin sections analysed. Based on this, the KF is by definition arkosic/feldspathic (*sensu* Pettijohn et al., 1987) and is compositionally immature to sub-mature. The most abundant

feldspar group is plagioclase feldspar (e.g. sample KIMW 28/11; Fig. 36c) which are ubiquitous throughout the KF. Plagioclase is identified through its characteristic polysynthetic twinning. Alkali feldspar (orthoclase and microcline) is also noted within the KF (sample SARB 02/11; Figs. 19 and 36d). This is usually evident as growths/precipitation of microcrystalline clay minerals and replacement calcite along cleavage planes and on the surfaces of the feldspars. This latter dissolution and replacement of feldspars by calcite cement is common in the KF and is one of the diagenetic processes enhancing the porosity of the studied sediments. A discussion of authigenic phases and pore-system is presented in the Section 4.5.3. *Authigenic minerals*.

4.5.2.3. Other detrital elements

Aside from monocrystalline, polycrystalline quartz and feldspar minerals, a number of associated detrital components can be found within the sediments of the KF. These include metamorphic rock fragments, sedimentary rock fragments and heavy minerals such as zircon, garnets, micas, and organic matter. This diverse suite of detrital components could be indicative of different provenance zones for the constituents of the KF. The sedimentary lithics are predominantly composed of mud clasts, which are locally altered and replaced by siderite (sample SAR 36a/11; Figs. 19 and 36e). Organic matter was noted intermittently within the KF sandstone units, and is an indication of a proximal sedimentary source. Two intervals containing mica flakes were noted in the LKF, the first at 15 m from the base of the Sarbab Type-Section, and the second at the very top bed (Fig. 19). In both cases, the predominant mica is biotite and occurs in a relatively unaltered form. Biotite in the LKF can be explained as being sourced from the underlying micaceous, quartzo-feldspathic gneissic metamorphic basement. The matrix of the sandstones of the LKF is composed of clays, which are commonly associated with calcite, locally siderite, and hematite (e.g. sample SAR 36a/11 - Fig. 36e). In argillaceous-rich lithofacies, clays represent an ortho-matrix in which detrital components are observed to float (e.g. sample SAR 32a/11 - Figs. 19, 36f). A certain amount of pseudo-matrix is thought to be present and is linked to the alteration of ductile detrital grains (e.g. mud clasts).

4.5.3. Authigenic minerals

The LKF is characterized by two main cements, hematite and carbonates (mainly calcite), which occur throughout the entire formation, but vary in relative abundance allowing for the division of the formation into three different diagenetic zones as illustrated in Fig. 19. Hematite is concentrated at the base (0-15 m), while the mid-part of the Sarbab Type-Section (15-30 m) is dominated by calcite cement, which occurs in conjuction with dolomite and siderite. The section between 30 m and 57 m is characterized by both hematite and calcite although is distinguished from the two other diagenetic zones by a heighted amount of kaolinite authigenetic clay. Quartz cement, feldspar overgrowths and pyrite are noted but in negligible amounts.

4.5.3.1. Zone 1 (Hematite-rich)

This zone is characterized by the abundance of hematite, locally found together with pyrite (e.g. sample KIMW 32/11 - Figs. 19 and 37a). Hematite (detected under reflected light) is also present as sub-micronic crystals interspersed within the clayey matrix of some sampled beds, which thus display brownish/reddish pigmentation. Hematite in this section is not only pore filling but also occurs as grain replacive and grain rimming phases. Where the hematite is pore filling, it is noted to grow from the pore margins to the centre of the pores (e.g. sample SAR 42c/11 - Fig. 37c). Additionally, hematite seems to be an early cement predating compaction (small hematite “layers” are locally “squeezed” between two quartz grains showing sutured contacts (e.g. sample KIMW 28/11 - Fig. 36a). Intragranular cementation is also noted along cracks and grain fractures.

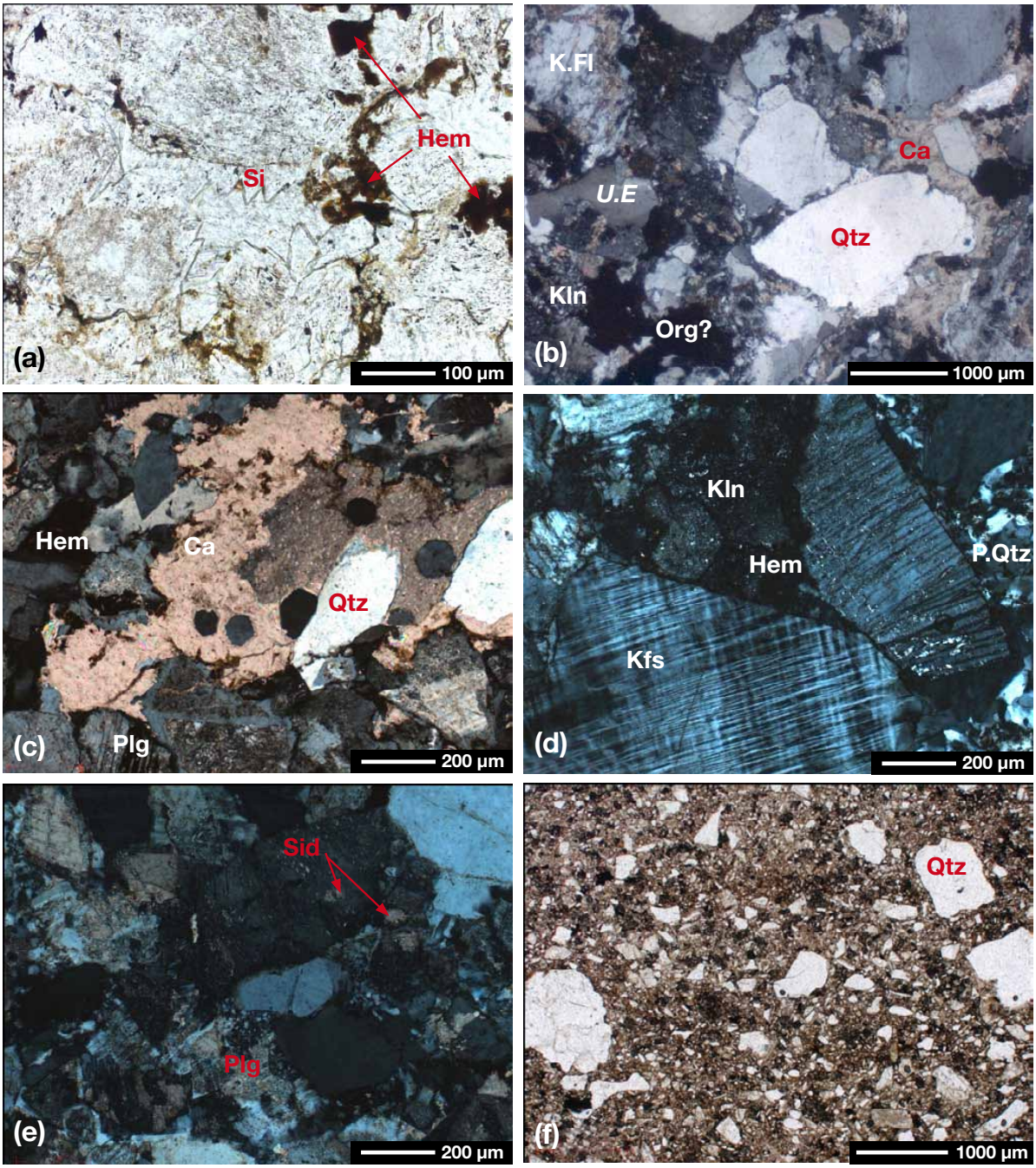

Fig. 36. *The Kimwarer Formation. Petrography of selected samples from the LKF as represented on lithostratigraphic log (Fig. 19). (a) Sutured quartz grain contacts noted in sample KIMW 28/11 which is collected from the massive sandstone bed which forms the lowermost bed of the KF. (b) Sample SAR 53/11 (XPL) showing well-preserved quartz grains (Qtz) exhibiting undulose extinction (U. E.) in massive sandstone beds. Intergranular pores occluded by calcite cement (Ca) and kaolin clays (Kln). Alkali feldspars (K.Fl) are also partially replaced by calcite cement along cleavage planes. (c) Alternate view of sample KIMW 28/11 (XPL). Feldspathic-rich arenite containing altered plagioclase feldspar (Plg) and pore filling to grain replacive calcite cement (Ca). Hematite (Hem) is also locally noted in this view. (d) Sample SAR 02/11 (XPL) showing well-preserved alkali feldspar and polycrystalline quartz (P. Qtz) grains, with intergranular pore spaces filled by kaolinite booklets (Kln) and hematite cement (Hem) in massive sandstone beds close to the base of the formation. (e) Sample 36a/11 (XPL) mainly shows altered plagioclase feldspar partially replaced by carbonate cements (e.g. Siderite; Sid.). (f) Sample SAR 32a/11 showing poorly sorted feldspathic wacke with grains floating into a clayey-rich matrix in fine grained massive sandstone beds. Open macropores are not clearly noted.*

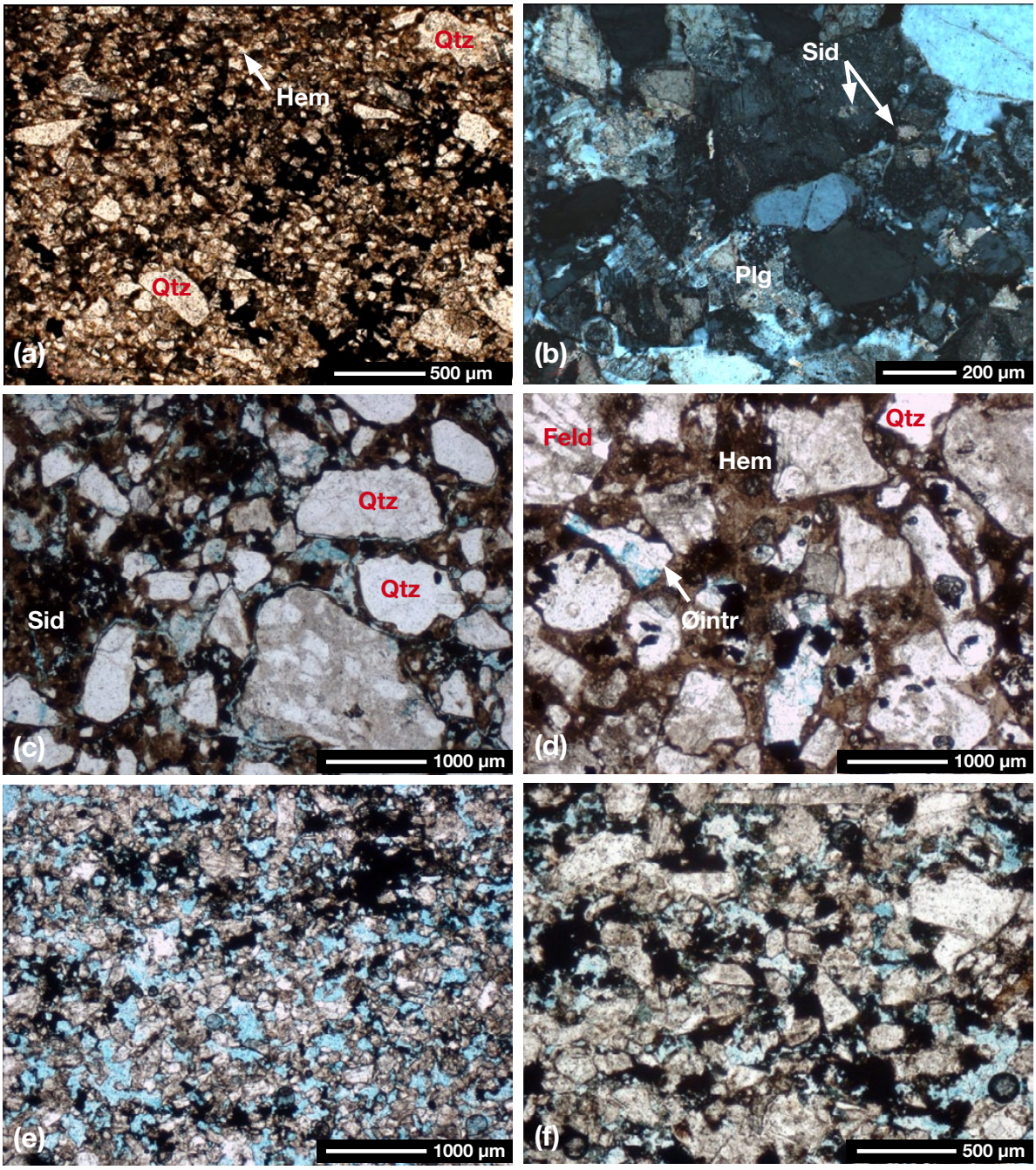

Fig. 37. *Petrography of selected samples from the LKF as represented on the lithostratigraphic log (Fig. 19) showing the different forms of porosity that can be found in the LKF. (a) Sample KIMW 32/11 showing quartz grains generally floating in the hematite-rich clayey matrix of a thinly bedded mudstone bed close to the base of the LKF (Fig. 19). (b) Sample SAR 36a/11 showing (plagioclase) feldspar replacement by carbonate (calcite) cement, predominantly along cleavage lines. Siderite is also noted rimming and filling out of pores. (c) Sample SAR 42a/11 showing moderate to good intergranular porosity which has been significantly downgraded by detrital clays which are sideritic in places as well as pore filling authigenic clays and cements (siderite and hematite). Sample SAR 36a/11 is a loosely packed feldspathic wacke with poor porosity which is mainly confined to isolated secondary pores that are linked to the dissolution of feldspar and lithic grains. The upper part of the LKF appears to have generally good porosity as evidenced by (e) and (f) which represent sample 42c/11. Abundant hematite cement is noted with local patches of carbonate cement (calcite) and kaolinite. Porosity is both intergranular and intragranular the latter being linked to the dissolution of feldspar grains.*

4.5.3.2. Zone 2 (Calcite-rich)

Calcite becomes the predominant cement from 15 to 25 m (Fig. 19), where it comprises between 10-20% of the total sample (sample KIMW 28/11 and SAR 36a/11 - Fig. 36c and 37b respecively). Calcite is noted occluding intergranular pores and secondary pores, thus significantly downgrading the porosity and permeability characteristics of the analyzed samples. A poikolotopic texture of calcite is also locally noted. In the KF, calcite is also replacive of feldspar grains (along cleavage planes) and lithics (e.g. sample SAR 36a/11 - Fig. 36e). Calcite is considered to postdate hematite authigenesis and also locally mechanical compaction, as it locally occludes remnant post compaction primary pores and secondary dissolution pores.

4.5.3.3. Zone 3 (Kaolinite-rich)

Within this zone, both hematite and calcite clays are represented. Nonetheless, there is a clear dominance of authigenic kaolin clays, which forms the basis of the segregation for this interval. This zone extends from 30 m to 57 m. Kaolin clays account for approximately 20-30% (e.g. sample SAR 42a/11 - Fig. 37c). Kaolin occurs as a pore filling and locally grain rimming secondary mineralogical component of this section.

4.6. Origin of authigenic cements associated with the Lower Kimwarer Formation

Due to the importance of the authigenic components in the LKF with regard to its reservoir potential, it is important to give an indication of the origin of such authigenic components as well as outline the impact it has had on the reservoir potential of the LKF. The main diagenetic events within the LKF are:

- Two generations of hematite precipitation;
- Carbonate precipitation;
- Feldspar dissolution;
- Formation and deposition of kaolin clays.

4.6.1. Hematite cementation

Within the LKF, hematite cement is most prominent within the lowermost 15 m of the Sarbab Type-Section. The lithofacies association in this interval has been determined to be a distal fluvial channel depositional environment, which existed in an arid to semi-arid climatic backdrop. In such a depositional environment, sediment supply is intermittent and separated by long periods of sediment starvation leading to in-situ sediment alteration. Collinson (1996) holds that in such settings, the development of red hematite pigments is a result of: i) high weathering rates of ferro-magnesium minerals due to elevated temperatures (consistent with our supposition that this lithofacies was deposited in a hot and arid to semi-arid climatic setting); ii) accelerated rates of organic decay that result in less acidic and less reducing pore waters; and iii) immobility of the resultant iron oxides that are only transported by circulating pore waters.

In addition, much of the hematite in this diagenetic zone (lowermost 15 m) is grain rimming, pore filling and only very locally grain replacive (Fig. 36a, c and 39a, d, e and f). Consequently, it is thought that the hematitic component in the LKF is entirely (or largely) secondary in nature and is formed by intrastratal alteration of ferro-magnesium silicates by oxygenated groundwaters during burial. Hematite cement could however also be sourced from the Precambrian basement on which the Kimwarer Formation sits. The basement is composed of hornblende, feldspar and amphibolites (Walsh, 1969). The weathering of the basements' amphiboles and other

iron-rich minerals as well as sediments sourced from it, could be another source of substantial amounts of iron, which would eventually manifest itself in form of hematite cement (Jones, 1965).

4.6.2. Carbonate cementation (calcite)

The zone between 15 and 30 m is carbonate-rich (calcite). The main diagenetic events in this zone were the precipitation of hematite cement, feldspar alteration and dissolution, calcite precipitation and, formation and deposition of kaolin clays. While calcite is prominent in this zone, it is considered to be both an early phase and relatively late phase cement, the latter being a product of alteration and dissolution of Ca2+ rich feldspars. Morad (1998) puts forth a number of potential sources of calcite in the subsurface including, windblown dust, groundwater enriched with Ca2+ ions transported by circulating fluids within the stratigraphic column and dissolution of Ca-plagioclase feldspar. The latter is believed to the main manner in which calcite cement has been emplaced within the KF and more specifically to the interval between 15 m and 30 m, where the bulkof the cement occurs in grain replacive mode as opposed to intergranular, pore filling mode. However, a link to the overlying volcanics can also be inferred where Ca2+ ions are precipitated as a result of chemical stability differences. This would explain why the entire Sarbab Type-Section exhibits an important component of calcite cement. The anomalous concentration at the 15-30 m interval (Fig. 19) in the section can be connected to the differential porosity and permeability within this interval allowing for greater circulation of Ca ion-rich fluids in comparison to other more tightly packed zones. This fact is supported by there being no evidence of concavo-convex grain contacts suggesting only mechanical compaction (re-organization of grains and closing on pore throats) has taken place (Fig. 36e). The association of the calcite cement to the volcanic rocks of the overlying Elgeyo Formation is plausible as the rocks of the lower portion of the Elgeyo Formation are characterized by abundant calcitic amygdales.

4.6.3. Kaolinite cementation

Kaolinite is believed to be sourced by the weathering of aluminous silicates through the leaching out of potassium, sodium, calcium, magnesium and ferrous iron and the addition of hydrogen (Pettijohn, 1975). Ion deficient water (could be meteoric waters), percolate and infiltrate the formation progressively becoming enriched in silica and aluminium by leaching them off weathering alkali feldspars. Once saturated, kaolin will begin to precipitate (Fig. 36c).

4.6.4. Chronology of main diagenetic events

The early diagenetic events of all the three zones generally followed the same sequence starting off with hematite cementation, sediment compaction (commonly mechanical and in certain intervals pressure solution), followed by calcite cementation, feldspar dissolution and finally kaolin precipitation. These processes are summarized Table 5 below for the three diagenetic zones.

4.7. Porosity

Porosity of the Lower Kimwarer Formation as determined from a petrographic analysis of the Sarbab Type-Section is very poor to poor, being mainly downgraded by the clayey-rich nature of the sediments and by hematite and carbonate (mainly calcite) cementation. Other pore filling authigenic phases (quartz cement and kaolinite clays) further reduce the pore effectiveness of the analyzed sedimentary samples. From this type-section, only one horizon (sample SAR 42a/11; Figs. 19 and 37e and f) was noted to have moderate to locally good porosity. At this horizon, primary porosity is significantly downgraded by pore filling clays and hematite cements. The macropores are mainly secondary, linked to the dissolution of feldspars and other lithics. Microporosity between

ZONE 1	**EARLY** **LATE**
Mechanical compaction	
Hematite cementation	
Compaction pressure solution	
Calcite cementation	
Hematite cementation	
Dissolution of feldspars	
Kaolin cementation	
ZONE 2	**EARLY** **LATE**
Mechanical compaction	
Hematite cementation	
Feldspar dissolution	
Calcite cementation	
2nd generation Calcite	
Kaolin cementation	
Zone 3	**EARLY** **LATE**
Hematite cementation	
Compaction	
Feldspar dissolution	
Calcite cementation	

Table 5
The paragenetic sequence within the three main diagenetic zones in the Lower Kimwarer Formation. Zone 1 represents the lowermost 15 m, Zone 2 the next 10 m, and Zone 3 the next 32 m. Relative timing and duration are indicated in the figure within the early to late axes.

Category	Name	Porosity	Typical lithologies	Risk assessment
Type 1	Tight depositional facies	Tight	Micritic limestone, marl and shale, Argillaceous siltstone sandstone and conglomerates	High Risk unless fracturing, or porosity can be predicted in deeper buried sections
Type 2	Uncertain depositional facies	Tight	Recrystallized sparry limestone, quartz cemented or metamorphosed quartz sandstones	High risk unless original fabric can be determined
Type 3	Recent pore destruction	Tight	Originally porous sandstones and conglomerates tightly cemented by recent by-products of weathering.	Very low risk for prospects shallower than pre-outcrop burial depth; variable risk for deeper prospects
Type 4	Dominantly compacted	Tight	Originally porous but now tightly compacted sandstones and conglomerates	Very high risk for prospects that are as deep as pre-outcrop burial depth unless early over-pressuring, rim cementation or dissolution can be predicted
Type 5	Early near surface cemented	Tight	Originally porous sandstones and conglomerates are tightly cemented by ancient near-surface cements	High risk unless lateral cement pinchout or cement dissolution can be predicted.
Type 6	Late burial cemented	Tight	Originally porous sandstone and conglomerates are cemented by ancient burial cements	Moderate to high risk unless lateral pinchout, dissolution or diagenetic traps can be predicted
Type 7	Recent weathering minimal	Porous	Any porous lithology whose pore-system is inherited from the subsurface (minimal recent weathering)	Very low risk for prospects shallower than pre-outcrop burial depth; variable risk for deeper prospects
Type 8	Weathered: depositional fabric porous	Porous	Originally porous depositional fabrics that became tight after compaction and cementation but leached by recent weathering	Moderate to high-risk facies; risk assessment equivalent to type 4, 5, and 6 as appropriate.
Type 9	Weathered: depositional fabric tight	Porous	Originally tight depositional fabrics that have been leached out by recent weathering processes	High risk facies similar to type 1
Type 10	Recent weathering	Porous	Any reservoir lithology whose pore system contains	Uncertain risk, but generally higher for increasing secondary porosity

Table 6
Porosity prediction of subsurface reservoir character of outcropping formations based on depositional, diagenetic and burial processes (modified after Tobin, 1997).

clay platelets is inferred to be abundant, but it is optically irresolvable under polarising microscopy. Permeability within this horizon is locally good. The reservoir quality risk assessment for Sarbab Type-Sections' equivalent subsurface sediments is high overall (Type 1, tight depositional facies sensu Tobin, 1997; Table 6), unless fracturing, dolomitization or burial dissolution processes can be predicted.

4.8. Discussion

Economically viable hydrocarbon deposits were discovered in Kenya in April 2012 in the northern part of the Kenya Rift (Lokichar Basin) in Eocene-Miocene deposits after more than two decades of petroleum exploration. Since then, ten wells (both exploratory - 8 wells and appraisal - 2 wells; Appendix 5) all of which (except the Emong-1 well) have successfully encountered hydrocarbons have been drilled in the Northern Kenya Rift. With such an abundance of hydrocarbons in this area, focus is now shifting to similar basins within the Kenya Rift of which the Kerio Basin is part of (e.g. Chapman and Brook, 1978; Tiercelin et al., 2004; Tiercelin et al., 2012b). There are no deep exploration wells that have been drilled in the Kerio Basin making it difficult to ascertain the lithostratigraphic make-up of the basin. Nonetheless, outcrop studies of the Kimwarer Formation in conjunction with a reinterpretation of vintage seismic data collected in this area and petrographic studies, allow for the prediction of the subsurface lithological configuration of the Kerio Basin as well as a determination of the reservoir potential of the clastics that form the lower part of this formation (LKF).

The sedimentological character of a basin infill is a product of the prevailing paleogeography and the paleoclimatic conditions existing at the time of deposition Palaeogeography is an important determinant of sediment source, transport mechanism, depositional style and location. Palaeoclimatology on the other hand is an important determinant of the constituents of the basin infill (Lambiase and Bosworth, 1995). The Kimwarer Formation for instance, is composed of two parts, a lower arkosic sandstone package - LKF (0-70 m) comprised of conglomerates, massive to bedded sandstones and massive to bedded fines (sensu Miall, 1996), and an upper unit - UKF (190-197 m) which comprises of a conglomeratic bed which grades up into highly distorted mudstone beds. The constituents of the two respective sections are however markedly different, with the LKF being mainly derived from a Precambrian basement provenance zone, while the UKF is sourced from a largely volcanic provenance zone. This detrital make-up has great impact on the net diagenetic effects on the KF and also determines to what extent these diagenetic modifications will affect the primary porosity and permeability of the formation, which are key determinants of the reservoir potential of a sedimentary formation. Diagenesis within the KF basically comprises of mechanical compaction (and pressure solution at the base between 0-10 m), dissolution of unstable grains (mainly feldspars), precipitation of hematite, calcite and kaolin cements. The palaeoclimatic conditions also contribute to the diagenetic products. For instance, kaolin clays similar to what is noted in the KF are commonly associated to semi-arid conditions with a well-defined wet and dry season and precipitation just exceeding the evaporation (Sellwod and Price, 1993).

4.8.1. Palaeogeographical and climatic reconstructions

Sedimentation within the entire Kenya Rift has largely been controlled by local tectonic events (including doming, rifting and volcanic activity) (Morley et al., 1992) that had impacts on local climatic conditions (Vincens et al., 2006). Chronological data obtained from this work indicate an early Miocene age for the volcanics that overlie the KF. This means that fluvial palaeogeographies represented by the KF persisted at this time (Burdigalian – ca. 18.1 Ma) or even earlier within the Central Kenya Rift.

The lower part of the LKF (0-25 m) is interpreted as distal fluvial channel environment though these sediments begin to fine-upwards from about 15 m to 25 m. This entire lithofacies association was probably depositied in a

broad synformal structure during a period of relative tectonic quiescence (Morley et al., 1992). No palaeocurrent data could be collected from the Kimwarer Formation. However, it is proposed here that sediments were probably deposited by north to northeasterly flowing fluvial systems as has previously been proposed by Chapman et al. (1978). Palaeocurrents of similar directions have also been noted in the Lokichar and North Kerio Basins in the Northern Kenya Rift (Morley et al., 1992; Tiercelin et al., 2004). The continued fining-up of the fluvial facies from the 15 m mark on the lithologic log is probably linked to the very initial phases of rifting that could have involved river capture and as a consequence the deposition of progressively finer sediments within the basin. This rifting phase could be associated with the formation of rectilinear uplands which induced an progressive increase in rainfall (Vincens et al., 2006) and which coincides well with the formation's shift in the diagenetic character of the KF at 15 m (on the lithological log) from a predominantly hematite-rich zone (0-15 m) to a dominantly calcite-rich zone between 15 m and 25 m. The hematite-rich zone (0-15m) was probably deposited in a high temperature setting that had a well-defined dry and wet season and where evaporation exceeded precipitation. The change to calcite-rich probably developed when the local climatic conditions were more humid but still evaporation exceeded precipitation.

The alluvial fan depositional environment interpreted between 25 m and 50 m could be related to an extensional phase that also involved flexural upwarping and associated rearrangement of drainage patterns through processes such as river capture, beheading and diversion leading to enhanced fluvial flow energy. During this period, the palaeo-Kerio Basin attained its saucer shape (Fig. 25) through the vertical movements that were probably distributed along numerous faults present along the Elgeyo Escarpments' footwall. This extension phase probably resulted in the modern-day morphology of the Central Kenya Rift with the Elgeyo Border Fault Escarpment developing into a medium altitude fault escarpment over and along which huge amounts of laterally derived and axial deposited sediments infilled the basin to form the alluvial fan environment. Moreover the topographical nature of the Elgeyo Escarpment allowed the development of local quasi-humid climatic conditions as is evidenced by the dominance of kaolin cements with the KF from 25 m to 57 m. For kaolin cements to form, it is generally accepted that humid conditions (where precipitation exceeds evaporation) with a distinct dry spell are required to allow for leaching of silica and aluminium from weathered K-feldspars and subsequent formation of kaolin. Such conditions probably existed during the deposition of the higher. Such weathering conditions probably existed during the deposition of the higher stratigraphic units of the Lower Kimwarer Formation (LKF) as a result of fault movements and uplift along the main Elgeyo Border Fault Escarpment, that in turn might have led to modifications of local climatic conditions in the southern part of the Kerio Basin, comparable to climate prevailing to the north, in the Lokichar Basin, during early Miocene times (Hill, 1995 ; Vincens et al., 2006)

4.8.2. Implications on the reservoir potential of the Kimwarer Formation

The key controls of the reservoir potential, i.e. porosity and permeability, are depositional and diagenetic in nature. Depositional controls are those that include mineralogy; grain type, grain size, grain packing and grain sorting, while diagenetic controls are those that include post-depositional changes, e.g. grain specific alteration, compaction and cementation. The Kimwarer Formation is composed of mainly arkosic sandstones, which normally have porosity levels of ~40% at the time of deposition (Selley, 1978). The KF, from the studied samples, has almost 0% porosity in its basal sections and up to 20% within the alluvial fan deposits where primary, secondary, intergranular, intragranular and microporosity are noted. This porosity is downgraded by compaction and cementation phases: hematite (0-15 m), calcite (15-25 m), and kaolin (25-57 m) (Fig. 19). While the overall reservoir character of the KF on outcrop appears to be negligible to low, cement dissolution and/or dolomitization within the carbonate-rich interval (15-30 m) and fracturing within the entire KF could enhance the reservoir potential of the formation. Overall, it is instructive to note that the upper portion of the Sarbab Type-Section (from 15 to 57 m), represents a more prospective reservoir zone that the lower portion of the f.ormation.

4.9. Conclusion

This part of the thesis presents the first multidisciplinary study of the Kimwarer Formation in the Central Kenya Rift, which remains poorly studied to date. It is nonetheless not exhaustive and additional, more specialized work might be required to complete this preliminary study considering the size and structural characteristics of the formations' host basin.

Nonetheless, in this work, the stratigraphic position of the Kimwarer Formation above the Precambrian basement has been confirmed contrary to previous mapping work by Walsh (1969). The LKF comprises of up to 70 m of sediments that lie on an eroded surface of the basement at the southern end of the Elgeyo Border Fault Escarpment. Within the formation, three depositional environments have been identified. These are:

- A distal fluvial channel depositional environment at the very base of the formation (0-25 m and 50-55 m);
- An alluvial fan depositional environment (25- 50 m)
- A floodplain depositional environment (55-70 m).

Within these depositional environments however, it is believed that there could be additional minor stratigraphic gaps, which could not be fully evaluated from only one lithological section and it is recommended that additional work be conducted to understand these gaps that might exist within the sedimentary unit.

The KF has not been fully chronostraigraphically constrained owing to the lack of age specific fossils and can be assumed to be as old as Oligocene based on age specific fossils that were discovered in the Lokichar Basin (Ducroq et al., 2010). In order to firmly set a minimum age for the KF however, the age of the volcanics that immediately overlie the KF has been determined from both stratigraphic fieldwork and radiometric analyses as being 18.0 ± 0.2 Ma (Early Miocene – Burdigalian). This age, which is older than any that has been previously published before, was derived from both single (sanidine) crystal and a whole rock analysis of lowermost tephrites of the Elgeyo Formation (Figs. 18b and 19). In addition, to concisely determine the chronostratigraphic order of the formations that comprise the Kerio Basin infill, geochemical analysis of the volcanic units directly above the KF was also conducted. Through this work, it was affirmed that it is the Elgeyo Formation (which is composed of Basalts and Trachy-basalts – Unit 1, and Basalts, Tephrites, Picrobasalts and Basanites – Unit 2) that lies directly above the KF contrary to previous work that placed the Uasin Gishu Phonolites and Elgeyo Basalts above and below the Kimwarer Formation, respectively. This formation is subsequently overlain by the Uasin Gishu Basalts, the Ngorora Formation and the Ewalel and Kabarnet Trachytes.

The diagenetic study of the Kimwarer Formation has shown that the cements change from dominant hematite at the base to calcite within the middle zones and back to hematite towards the top of the Formation. These cementation episodes occur during early and relatively late diagenesis in low temperature conditions (<80 °C), under significant mechanical compaction. The reservoir potential of the KF, based on visual estimates range between negligible close to the base type-section to between 3-15% at the middle part of the section. The mid-zone of the formation, which is part of the alluvial fan depositional environment, has the best-preserved porosity and therefore represents the best potential reservoir section. The porosities dramatically decrease towards the top of the section where the lithology is predominantly composed of mudstones. With regard to the petroleum prospectivity of the basin, we did not identify clearly organic-rich sedimentary intervals at the outcrop scale and did not also test the source-rock potential of the different mudstones encountered.

5. The Kamego Formation

The focus of this section is the lowermost sedimentary unit that outcrops along the major Saimo Fault on the eastern side of the Tugen Hills facing the Baringo Basin, and is known as the Kamego Formation (or KAF). This formation is generally cited in the literature as being a possible equivalent of the Kerio Basin's Kimwarer Formation presented in the previous section of this work (Chapman et al., 1978; Morley et al., 1992; Mugisha et al., 1997; Renaut et al., 1999; Hautot et al., 2000). Being a basement-derived formation sitting unconformably on the Precambrian basement, the Kamego Formation has been considered as part of the "Turkana Grits" (sensu Murray-Hughes, 1933) (Morley et al., 1999; Tiercelin et al., 2004, 2012b). Chapman et al. (1978) described the Kamego Formation as being unconformably overlain by sediments belonging to the Sidekh Phonolite Formation. The Sidekh Phonolite Formation comprises ten to twelve plateau phonolite lava flows and up to three sedimentary intercalations that bear hominoid fossils and have been named the Muyurur Beds (Behrensmeyer et al., 2002; Fig.12b). From the literature, the minimum age of the Kamego Formation is ca. 16 Ma. This age is based on the K-Ar dating of one of the lower flows of the Sidekh Phonolites that overlies the Kamego Formation (Lippard, 1973; Chapman and Brook, 1978; Chapman et al., 1978) (Fig. 13b). Up to now, no fossils have been discovered in the Kamego Formation, with the exception of pollens that have a Tertiary aspect, though an exact age was undeterminable (C. Downie, in Chapman et al., 1978).

The Kamego Formation was measured along a section that had its base at 00°45'04.3" N; 035°51'06.1" E on the track down from the Kipsaraman village at the top of the major Saimo Fault. Metre-thick massive sandstone beds form steep cliffs along the main fault scarp (Fig. 38), and can be accessed from the top of the Saimo Fault Escarpment and down the precarious, weather-beaten and winding Kipsaraman-Sibilo Lions track. Alternatively, the KAF can be accessed from the rift floor through the Nakuru-Sigor road (tarmac), past the town of Marigat and up the progressively narrowing Sibilo Lions-Rondinin road. A trek of about 2 hours up the basement is required thereafter to reach the base of the KAF. This latter route is longer and can only be used during the dry season when the three ephemeral tributaries of the Ndau River, the Rondinin River and the Seren River, which cut across the road, are dry. This section is discussed as the Kipsaraman Type-Section and described in greater detail in the lithostratigraphic log (Fig. 39). A total of 6 lithofacies have been identified in this section. The sedimentological descriptions and interpretations are summarized in Table 7, and illustrated on Figures 40 and 41. The main facies codes have been adapted from Miall (1996).

5.1. Lithostratigraphy

The Kipsaraman Type-Section starts off at GPS point 00°45'04.3" N; 35°51'06.1" E and ends at GPS point 00°45'11.4" N; 35°50'38.8" E, representing a total thickness of 72.55 m (Fig. 39). Much of this section is covered by a dense bushy forest making it difficult and in some instances impossible to access parts of the section, except in those areas that have been cleared during construction of the Sibilo Lions-Kipsaraman road. It is these cleared areas that were utilized during the field logging.

Similar to the Kimwarer Formation, which is exposed on the footwall of the Elgeyo Border Fault, the KAF is exposed on the footwall of the Saimo Fault (Fig. 38), where it sits on the Precambrian basement that comprises of para- and ortho-gneisses, amphibolites, schists, marbles and quartzites belonging to the Mozambique System (Chapman et al., 1978) (Fig. 38). Sitting unconformably on the basement is a 2.2 m thick, orange-brown with blue-grey patches, massive matrix-supported conglomerate with angular to sub-rounded >5 cm in diameter basement-derived clasts (sample KAM 18; Figs. 39 and 40a-i). This conglomerate grades laterally to a pebbly sandstone and vertically into a coarse-grained, massive sandstone bed (Fig. 40a– ii). Above the conglomeratic

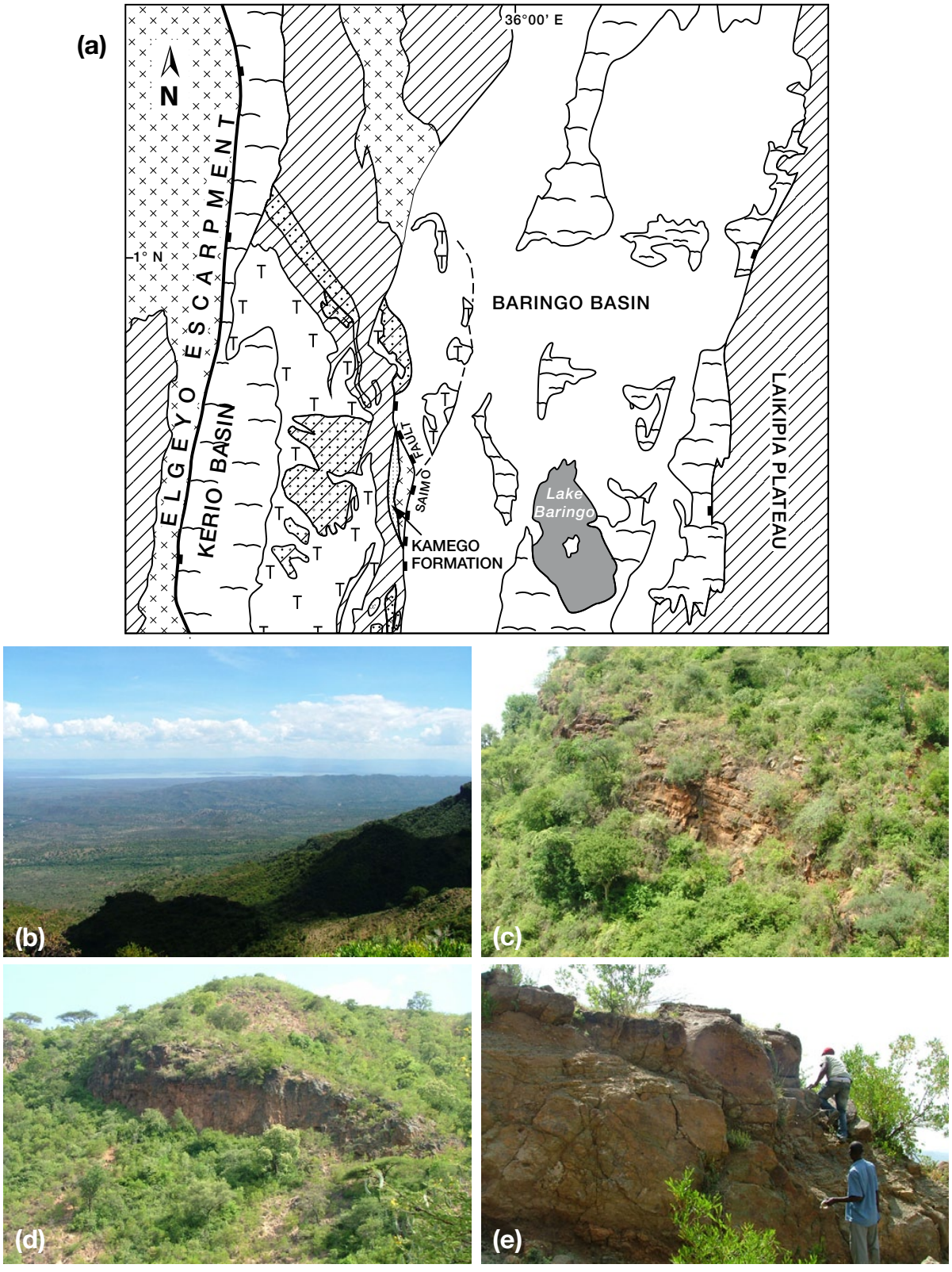

Fig. 38. *Simplified geological map of the Central Kenya Rift showing the Kerio Basin to the west and the Baringo Basin to the east. The Kamego Formation is located on the Saimo Fault which is the main western boundary fault of the Baringo Basin (redrawn after Le Turdu et al., 1995). (a) A wide angle view of the Baringo Basin from the Saimo Fault. Lake Baringo can be seen in the immediate background of the image. (b and c) Different close-up views of the Kamego Formation from the east showing the heavily overgrown, generally orange to buff brown, metric sandstone beds of the KAF. The beds of the KAF have a slight tilt (15°) dip in the general NNE direction. (d) The lowermost massive sandstone bed of the KAF which is overlain by a green mudstone bed. This sandstone bed is faulted and lies unconformably on the underlying Precambrian basement.*

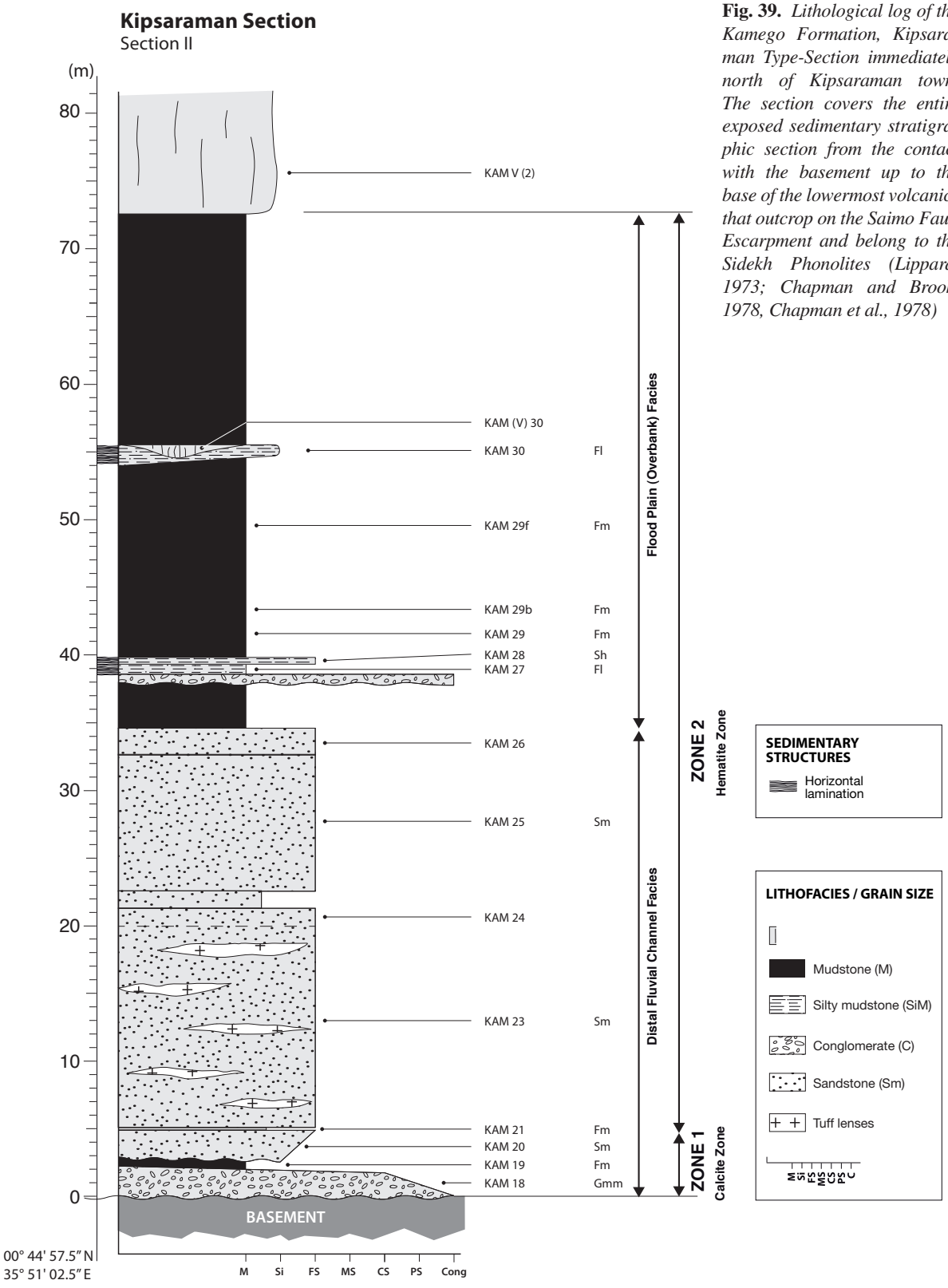

Fig. 39. *Lithological log of the Kamego Formation, Kipsaraman Type-Section immediately north of Kipsaraman town. The section covers the entire exposed sedimentary stratigraphic section from the contact with the basement up to the base of the lowermost volcanics that outcrop on the Saimo Fault Escarpment and belong to the Sidekh Phonolites (Lippard, 1973; Chapman and Brook, 1978, Chapman et al., 1978)*

Facies code	Lithology	Sedimentary Structures	Bed thickness (m)	Depositional processes	Interpretations	Figures
Gmm	Massive, ungraded, matrix-supported, decimetric to metric conglomeratic beds. Poorly sorted, angular – sub-rounded pebbles and boulders.	Erosive base especially at the basement – sediment interface	0.5-2.2	Deposition of gravel by high strength debris flows (Miall, 1996, 2006).	Sub-aerial debris flows	Fig 42 (KAM 18b – Base of section and KAM 28). Fig Fig. 43e.
Gcm	Massive, ungraded, clast-supported conglomerate. Quartz and basement derived clasts floating in a blue-green, fine to medium grained matrix. Clasts < 2cm to > 15cm, angular, elongated with few well rounded pebbles.	Erosive basal boundary.	3.5	Low strength pseudo-plastic debris flow deposited from viscous, laminar or turbulent flows (Postma, 1990, Miall, 1996).	Sub-aqueous debris flow	Fig 42 (KAM 01/13 – base of section 1).
Sm	Fine to coarse metric beds. Grey-green, buff-purple and purple with common iron staining.	No sedimentary structure but few beds are graded (fining up or coarsening up e.g. KAM 20)	0.35-15.0	Subaerial hyperconcentrated flow (Lowe, 1982, Tiercelin, 2012)	Rapid suspension fallout from sedimentary gravity flows and/or post depositional modification through dewatering for those beds with faint bedding.	Fig 42(KAM 20, 22, 23, 25) and Fig. 43a.
Sh	Rare in KAF. KAM 28 (0.2m) fine-grained silty (with possible volcanic input). Light brown to light grey with preferential iron staining along parting lineation.	Horizontal laminations	0.20	Plane-bed flow, critical flow regime (Miall, 1996) or traction carpets (Postma, 1990).	Planar bed flows under critical flow regime (Miall, 1996).	Fig 42 (KAM 28), Fig. 43f.
Fl	Grey – green laminated clays 39.15m from the base of the type-section.	Fine laminations	0.35	Deposition from suspension	Overbank, abandoned channel or waning flood deposits (Miall, 1996)	Fig 42 (KAM 27). Fig 43f (ii).
Fm	Structure-less green metric mudstone intercalated with white decimetric tuffaceous beds.	Intermittent tuffaceous beds	0.1-3.5	Deposition from suspension in standing pools of water during low stage channel abandonment with intermittent syn-sedimentary volcanic input	Low energy flow deposition from suspension, overbank or floodplain	Fig 42 (KAM 19, 21, 29 and 31) and Fig. 43g.

Table 7
Facies classification and interpretation of the depositional processes and environments of the different lithologies associated to the Kamego Formation (adapted from Miall, 1996, 2006)

bed is a 0.8 m thick orange brown, massive silty to fine-grained sandstone with intercalated 3 to 5 cm thick layers of bluish-grey massive mudstone (sample KAM 19; Figs. 39 and 40c). There is evidence of syn-sedimentary faulting in these lowermost beds, which distorts their lateral thickness and extent across the fault (Fig 40a). This massive sandstone bed is then overlain by a 2.2-m thick, brown (with local iron stains) massive, coarsening up

(silty to fine-grained) sandstone bed (sample KAM 20; Fig. 39), which fills the palaeotopography created by the fault below but also pinches out laterally in the western direction. This bed is overlain by a succession of five 2-3 cm thick layers of grey, massive silty to fine-grained sandstone (sample KAM 21; Fig. 39).

Access to the overlying beds (sample KAM 23; Figs. 39 and 40d) was difficult due to the steep terrain and vegetation overgrowth. This part of the section corresponds to a 15-m thick unit made of grey-green, fine-grained massive sandstone (lithofacies Sm) with abundant millimetre-sized vacuoles. Intercalated within this sequence of beds are thin (<0.2 m) very fine-grained, cream coloured tuffaceous beds that occur both as laterally extensive beds as well as decimetric lenses. This thick sandstone bed (sample KAM 23; Fig. 39) is laterally extensive and can be traced to an adjacent hill, which was inaccessible during the fieldwork due to the precarious terrain and the thick vegetation cover. Above this sandstone is a 1.2-m thick bed of fine-grained, cream-coloured tuffaceous bed (KAM 24; Fig. 39), which differs from those intercalated within the underlying sequence (KAM 23) only by the amount of iron staining. Iron staining is perceived to be higher in the bed numbered KAM 23.

At the 21.3 m mark from the base of the Kipsaraman Type-Section and sitting above the cream coloured tuffs is a one meter thick bed of green massive mudstone bed, overlain by two orange brown, massive fine-grained sandstone beds, 10-m (KAM 25) and 2-m (KAM 26) thick, respectively (sample KAM 25; Fig. 39 and 40e, i and ii). Both of these beds exhibit a complicated fracture pattern, and appear (from field observations) to be differentiated only by the amount of staining which is more abundant in the lower, thicker bed (KAM 25). These fine-grained sandstones are then overlain by a 3.5 m thick, slightly erosive bed of green massive mudstone, which is in turn overlain by a relatively thin (0.5 m) matrix-supported conglomerate (sample KAM 27; Fig. 40f). The clasts within this conglomerate have a varied assortment ranging from granules to angular pebbles and cobbles at the top of the bed. Locally, mud clasts probably derived from the mudstone bed below were also noted (Fig. 40f). Above the conglomeratic bed is then a 0.35 m thick, grey green, faintly laminated mudstone (KAM 27), which is in turn overlain by a 0.2 m thick light orange, faintly laminated fine-grained sandstone (KAM 28) which is also iron stained (Fig. 40g). Towards the top of this bed (KAM 28), approximately 0.15 m from its top surface, the bed becomes increasingly tuffaceous (Fig. 40g) and iron staining is preferentially concentrated along the more silty lamina.

The next 14.15 m are composed of a monotonous succession of massive, metric, green mudstones (sample KAM 29; Figs. 39 and 40g) that are interbedded with whitish tuffs. At 3.15m from the base of this monotonous succession (Fig. 42a), the beds take on a slight tilt (15° in the north-northeast direction), a trend that continues to the top of the KAM 29 succession. Moreover, within this mudstone succession, the tuffaceous beds are rarely laterally extensive and never more than 5 m in length. Many of the beds have a lenticular shape and few beds appear to be filling small palaeochannels (maximum 0.15 m thick). At 53.5 m from the base of the Kipsaraman Type-Section is a 1.5 m thick bed of dark brown, highly indurated siltstone that is massive at base but becomes laminated towards the top (sample KAM 30; Fig. 40h). Within this bed is a thin (<1 m) massive volcanic bed that appears to fill a sort of palaeochannel. This volcanic bed (KAM (V) 30) is described in detail in the following Section 5.2. *Chronostratigraphic setting of the Kamego Formation*.

Above bed KAM 30 is a second monotonous succession about 20-m thick of fissile, green massive mudstone with numerous tuffaceous intercalations that are ~5-10 cm thick. At the top of these mudstones is a succession of volcanic lava flows, known to belong to the Sidekh Phonolites (Chapman and Brook, 1978), the first flow of which was sampled at 72.55 m from the base of the Kipsaraman Type-Section (sample KAM (V) 2) for dating purposes as described in the following section 5.2. *Chronostratigraphic setting of the Kamego Formation*.

10/18
(a)

(b)

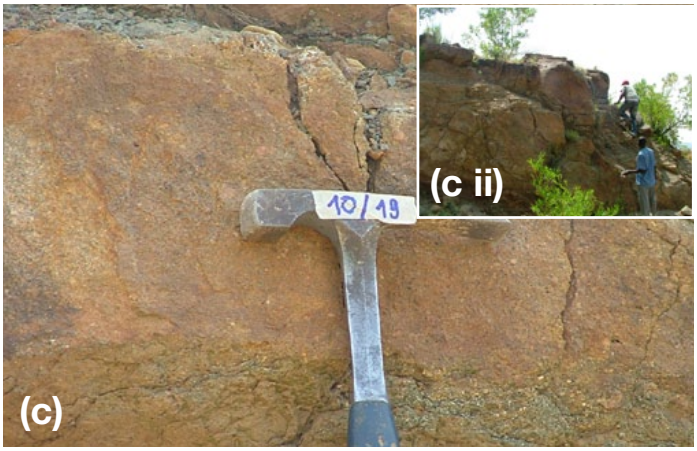
10/19
(c ii)
(c)

(d)

(e)

10/28
(f)

(g)

(h)

5.2. Chronostratigraphic setting of the Kamego Formation

Two samples of volcanic rocks were collected near the top of the Kipsaraman Type-Section, to constrain the chronostratigraphic position of the Kamego Formation using 39Ar/40Ar dating methods. Sample K1 (corresponding to the field number KAM (V) 30) was collected from a thin (<1 m) massive lava flow situated 55 m above the contact of the sedimentary pile with the basement in the Kipsaraman Type-Section (Fig. 39). It is a laterally restricted lava flow interbedded within the sediments, and apparently fills a small channel structure affecting the green mudstones. Sample K2 (corresponding to the field number KAM (V) 2) was collected at 72.55 m above the basement, from the base of a volcanic flow that belongs to a thick phonolitic succession that overlies the green mudstones at the top of the Kamego Formation and extends westward and northward (Fig. 39). According to the geological map covering the sampling area by Chapman et al. (1978), this volcanic succession that directly overlies the Kamego Formation corresponds to the Sidekh Phonolites (see also Hautot et al., 2000) that emplaced from ca. 16 Ma. In the Kamego area, this volcanic succession is about 700 m thick, and includes 5-6 flows and up to 80 m of interbedded sediments (Behrensmeyer et al., 2002).

In thin section, sample K1 appears to be poorly porphyritic (<10% vol of phenocrysts that are <0.3 mm in size) with a microlitic and fluidal groundmass (Fig. 41a and b). The main phenocrysts are clinopyroxene (augite) and sanidine-anorthoclase. The microlites are predominantly sanidine-anorthoclase with rare plagioclase. Opaque mineral microcrysts are often grouped in the groundmass. Feldspathoid is not readily identifiable. The sample also contains veinlets of quartz and carbonate. Sample K2 is similarly poorly porphyritic (<10% vol. of phenocrysts that are up to 1 mm in size), with a microlitic groundmass that is locally fluidal (Fig. 41c-e). The main phenocrysts are subhedral sanidine-anorthoclase with inclusion rich outer rims (mostly developed at both extremities of elongated sections), brownish (augite) to greenish (aegyrine augite) clinopyroxene and, often weathe-

Fig. 40. *The Kamego Formation. (a) Bed KAM 18 (see Fig. 39) - Orange brown, matrix-supported conglomerate (lithofacies Gmm) with abundant grey green patches immediately above the Precambrian Basement. The grey green patches are attributed to fluorite precipitation by cacite-rich brines subsequent to fluorite leaching of the metamorphic basement and evaporite dissolution of the resultant brine as discussed by Tritlla et al., (2004). This is in agreement with our deduction of the base of the KAF being rich in calcite cement and field observations of asphalt-bearing fluorite veins in the Kasowe locality approximately 200m from the Kipsaraman outcrop. This bed grades laterally (west) into a clast-supported conglomerate (lithofacies Gcm) and pinches out further west (100m). Both the conglomeratic lithofacies (Gmm and Gcm) are composed of angular to sub-rounded pebbles <6 cm in length. (b) Above this bed is a decimetric sequence of alternating green massive mudstone (lithofacies Fm) intercalated with orange brown silty to fine grained sandstone which also pinch out laterally approximately 100m to the west. (c) i) Bed KAM 20 (see Fig. 39) which is composed of massive sandstone (lithofacies Sm). (ii) Syn-deformational sedimentation is evident below this massive sandstone bed which was deposited after faulting separated the sequence of massive mudstone and fine sandstone on the left and right hand side of the figure respectively. This is evidence of syn-sedimentary tectnonic activity during the early stages of basin formation and deposition of the lower most sedimentary beds of the Kamego Formation. (d) Bed KEN 25 (See Fig. 39) Fine-grained, iron stained, massive sandstone with a complicated fracture pattern that is attributed to weathering processes that are associated with sediment exposure. (e) Matrix-supported conglomerate (locally clast-supported) with a buff brown matrix immediately below bed KAM 27 (see Fig. 39). The clasts within this bed are poorly sorted, ungraded and include angular to sub-angular pebbles and boulders. This conglomeratic bed is located within the Flood Plain lithofacies and is attributed to mass debris flows that are linked to violent volcanic activity and associated seismic shock waves within the Baringo Basin. The presence of tuffaceous material in the beds above and below this conglomeratic bed supports this supposition. (f) Bed KAM 28 (see Fig. 39) - Laminated and bedded, cream coloured, silty to very fine grained sandstone with abundant vacuoles. Below these sandstones are laminated green mudstones. (g) Bed KAM 29 (see Fig. 39) – Decametric massive green mudstone intercalated with decametric cream coloured tuffaceous beds. These tuffaceous beds indicate the continuation of volcanic activity in the Baringo Basin. (h) Bed KAM 30 (see Fig. 39) which is a 1.5m thick dark brown, highly indurated massive siltstone bed (laminated towards the top) that contains an intercalated massive volcanic bed (KAM (V) 30). The volcanic bed exhibits vertical fracturing and appears to be filling a paleochannel. This volcanic bed is probably one of the early proximally sourced lava flows that was only sufficient to fill the deepest part of the existing topography*

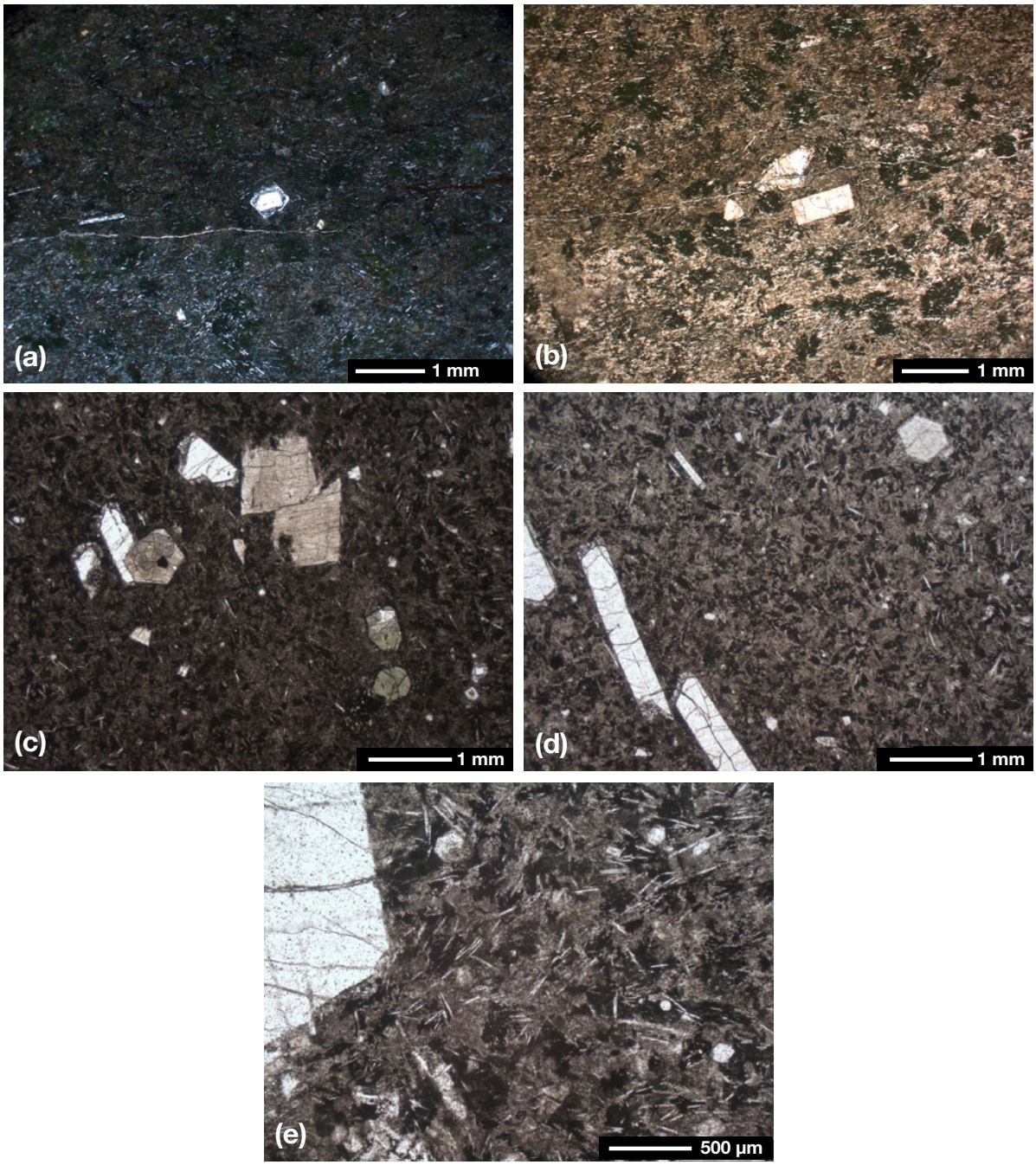

Fig. 41. *Typical textures and mineralogy of the phonolite samples associated to the Kamego Formation. Thin sections under plane polarized light, except (a), cross-polarized light. See scales on the microphotographs. (a), (b) Microlitic and fluidal texture from sample K1 (KAM (V) 30). Note also rare sanidine-anorthoclase and clinopyroxene small phenocrysts and quartz-carbonate veinlets. (c)-(e) Porphyritic texture and microlitic groundmass from sample K2 (KAM (V) 2). Main phenocrysts and microcrysts are sanidine-anorthoclase alkali feldspars (white rectangular sections with "spongy" - groundmass inclusion-rich – extremities and microlites), augite-aegyrine clinopyroxenes (greenish to brownish rectangular sections) and nepheline (white to weathered brownish sub-hexagonal sections). Abundant opaque mineral microcrysts also form flakes in a brownish groundmass of nanocrysts and glass*

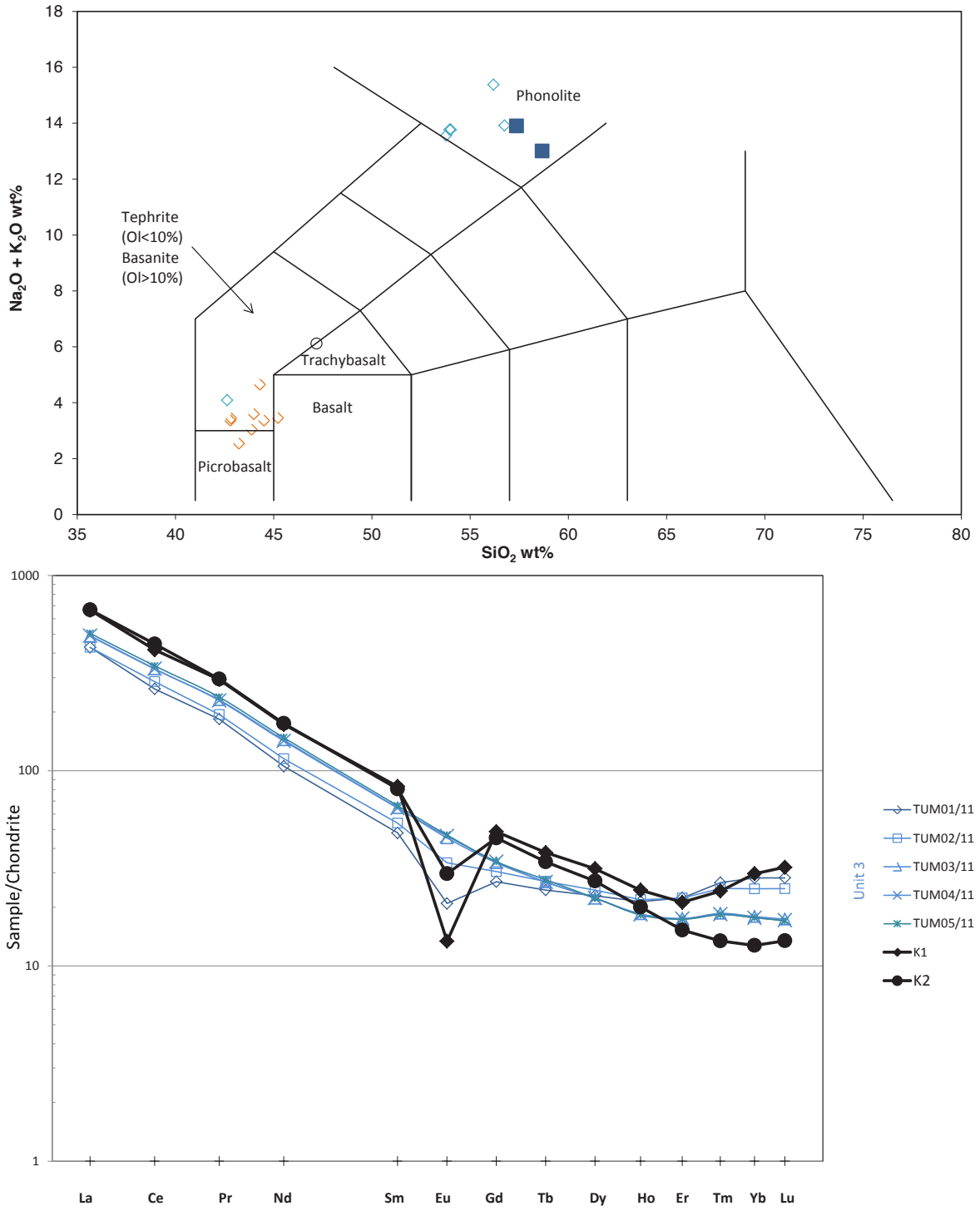

Fig. 42. *(a) Total alkali versus silica (TAS) diagram, and (b) Chondrite normalized Rare Earth Element (REE) patterns of the Kamego phonolitic samples K1 and K2 (black filled symbols). Comparison with the samples from the Kimwarer section (open symbols, this work): intermediate rocks (Unit 3) from the Chof and Uasin Gishu Phonolites on (a) and (b); ultrabasic to basic rocks (black, -Unit 1-, brown, -Unit 2- and blue, -Unit 3) from the Elgeyo Basalt formation are also shown on (a). Ol refers to normative olivine content. Note that, except for Eu and the heaviest REE, the Sidekh Phonolites (that immediately overlie the Kamego Formation) are enriched in REE relative to the Chof and Uasin Gishu Phonolites*

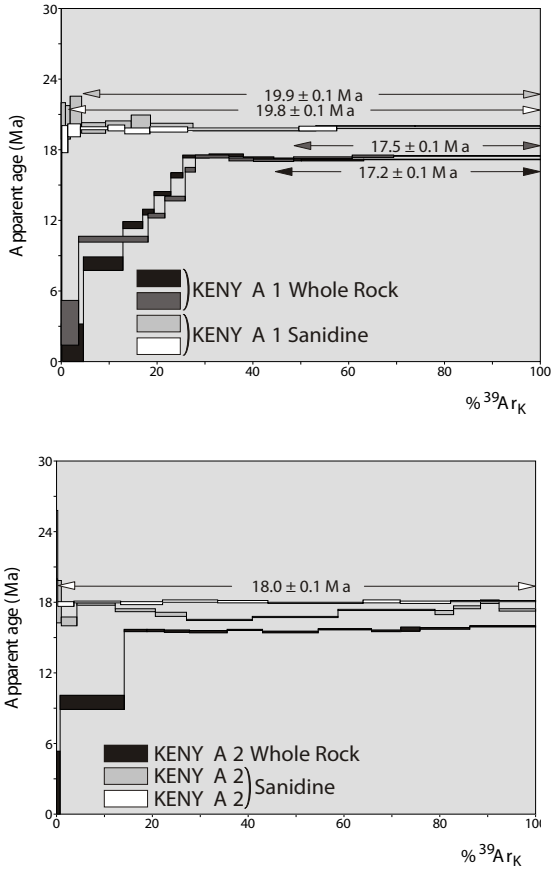

Fig. 43. *Plots showing age-spectra versus cumulative 39Ar gas released obtained from step-heating experiments (39Ar/40Ar dating methods) from the phonolite samples K1 (KAM (V) 30), and K2 (KAM (V) 2) respectively collected within the upper green mudstones (as a channel infill), and immediately above the last Kamego sedimentary beds.*

Table 8
Major and trace elements of volcanic rocks associated with the Kamego Formation

Section		Kamego	
Sample name		KAM (V) 30 K1	KAM V2 K2
Rock name		Phonolite	Phonolite
wt%			
SiO_2		55,40	54,67
Al_2O_3		18,36	18,85
Fe_2O_3*		6,38	6,06
MnO		0,36	0,35
MgO		0,24	0,40
CaO		1,13	1,15
Na_2O		5,94	7,57
K_2O		6,34	5,68
TiO_2		0,29	0,52
P_2O_5		< d.l.	0,05
PF		4,55	3,83
Total		98,97	99,12
ppm	d.l. (ppm)		
As	1,20	< d.l.	2,11
Ba	1,50	98,05	24,14
Be	1,00	10,58	7,93
Bi	0,10	< d.l.	< d.l.
Cd	0,15	1,10	0,79
Ce	0,1	338,50	362,60
Co	0,40	1,03	1,14
Cr	5,00	< d.l.	< d.l.
Cs	0,15	2,19	1,14
Cu	5,00	5,99	< d.l.
Dy	0,007	10,23	8,85
Er	0,003	4,51	3,25
Eu	0,004	0,97	2,14
Ga	0,20	38,43	34,31
Gd	0,02	12,62	11,73
Ge	0,10	2,44	1,90
Hf	0,04	21,16	18,80
Ho	0,001	1,78	1,46
In	0,10	0,10	0,10
La	0,05	209,30	210,20
Lu	0,001	1,03	0,44
Mo	0,35	0,60	5,91
Nb	0,06	321,30	291,20
Nd	0,03	103,10	104,30
Ni	4,50	5,76	< d.l.
Pb	1,40	19,97	18,15
Pr	0,01	34,00	34,22
Rb	0,35	215,50	147,20
Sb	0,20	< d.l.	1,09
Sc	1,00	0,44	0,32
Sm	0,01	15,95	15,50
Sn	0,40	7,37	5,84
Sr	1,20	119,40	75,48
Ta	0,02	22,68	21,96
Tb	0,006	1,87	1,67
Th	0,02	15,30	11,33
Tm	0,005	0,73	0,40
U	0,04	0,43	0,61
V	0,60	< d.l.	< d.l.
W	0,30	2,19	1,57
Y	0,40	47,04	38,31
Yb	0,003	6,18	2,65
Zn	11,00	221,60	206,70
Zr	1,30	923,40	701,80

Fe_2O_3*: total iron; d.l.: detection limit

red, nepheline. Nepheline, clinopyroxene and opaque mineral microcrysts, and sanidine-anorthoclase microlites form most of the groundmass, as expected for a phonolite. The chemical compositions of the two samples are comparable despite minor differences in a few element contents (e.g. Na_2O, TiO_2, P_2O_5, Ba, Sr, Ni or Yb; see Appendix 2). Consistent with their mineralogical content, both samples plot as phonolite in the TAS diagram (Fig. 42). Overall, these phonolites exhibit the general petro-chemical characteristics of the plateau phonolites as defined by Lippard (1973) (see also Chapman et al., 1978), but, for example, they are richer in Zr than the Sidekh Phonolites exemplified on Figure 6 from Lippard (1973).

$^{39}Ar/^{40}Ar$ dating was performed from both sanidine grains and whole-rock groundmass fragments extracted from the K1 and K2 phonolites (Fig. 43). Two sanidine grains were selected per sample, as well as two whole-rock fragments and a single one for samples K1 and K2, respectively. Step heating experiments on the whole-rock fragments systematically gave dates up to about 2.5 Ma younger than those on the sanidine crystals. In addition, the shapes of the spectra from the whole-rock fragments appear strongly perturbed, especially for the first increments (up to 25%) of Ar release. In contrast, and excepting the saddle shape obtained for one of the sanidine grains from sample K2, the shapes of the sanidine spectra are flat, resulting in plateau ages at 19.8 ± 0.1 and 19.9 ± 0.1 Ma for sample K1, and 18.0 ± 0.1 Ma for sample K2.

From the results on the sanidine grains, an excess argon (s.l.) hypothesis hardly explains why they give older ages than the wholes-rocks. Indeed, isochrone calculations do not evidence any excess argon linked to the atmospheric component (excess argon s.s.), and the presence of inherited argon, linked to the radiogenic component, is very unlikely in the sanidines. Indeed, in such a hypothesis, as the two sanidines from sample KAM (V) 30 gave very concordant ages (Fig. 43), identical ratios between radiogenic and inherited 40Ar would be required within the two analyzed grains. More likely is that the whole-rocks grains, corresponding to groundmass fragments from the samples, underwent hydrothermal alteration or weathering after cooling, resulting in perturbations (“rejuvenation”) of the isotopic system, which, in this case, did not affect the alkali feldspar phenocrysts of the samples. The perturbed shapes of some of the age spectra, including the saddle shape of the sanidine grain from KAM (V) 2 (Fig. 43), which was a groundmass inclusion-bearing crystal fragments typical from an extremity of a feldspar phenocrysts (Fig. 41d), provide good support to such a hypothesis.

Therefore, based on this assumption that the groundmass is not as fresh as required for 39Ar/40Ar dating, only the results on the sanidine grains are retained as representative of the initial cooling of the lavas. A mean cooling age can be calculated from the sanidine results at 19.85 ± 0.06 Ma for sample KAM (V) 30. As expected from the superposition observed on the field, it is older than the cooling age of the overlying sample KAM (V) 2 at 18.0 ± 0.1 Ma.

Compared to the known K-Ar ages for the Sidekh Phonolites from ca. 16 Ma (Chapman and Brook, 1978), the oldest new age from this work is significantly older by about 4 Ma. In the area, the Sidekh Phonolites represent the very first episodes of emplacement for the Plateau-type Phonolites (e.g. Lippard, 1973), which therefore, from now, must be considered to start at ca. 20 Ma. One can note, in addition, that whole-rock data from this work are in rather good agreement with the oldest published K-Ar ages for the Sidekh Phonolites. This supports the alteration and weathering hypothesis mentioned above, in which not only $^{39}Ar/^{40}Ar$ on groundmass but also K/Ar isotopic systems appear particularly sensitive to post- primary cooling events in providing rejuvenated ages (see also previous discussion on the comparisons of the new $^{39}Ar/^{40}Ar$ ages and published K-Ar ages for the Elgeyo Basalts Elgeyo Formation, Chof and Uasin Gishu Phonolites above the Kimwarer sediments). Finally, because the phonolite KAM (V) 30 was found interbedded within the sediments, the age at 19.85 ± 0.06 Ma can be assumed as corresponding to the age of the Kamego sedimentation in the corresponding upper part of the pile. However, along the studied section, the unconformity expected between the Kamego beds and the very first sediments from the Sidekh Phonolite Formation (Chapman et al., 1978) was not observed. As a result, the upper

sedimentary layers studied in this work have been assigned to the Kamego formation. Nonetheless, they could also correspond to basal Muyurur Beds, which were found interbedded within the Sidekh phonolites (Behrensmeyer et al., 2002), and above the unconformity mentioned by Chapman et al. (1978). As sample KAM (V) 30 comes from the upper part of the pile, these two possibilities indicate that either most of the Kamego beds or the whole of the Kamego beds had been deposited before the emplacement of the corresponding phonolitic flow. Therefore, we conclude that most or the whole of the Kamego beds deposited before ca. 20 Ma.

5.3. Facies analysis, depositional processes and environments of the Kamego Formation

The depositional processes and environments of the KAF were determined through the study of the lithology, sedimentary structures and textures of samples collected from the Kipsaraman Type-section. These were further augmented with petrographical analysis both at a macroscopic and microscopic scale (Figs. 40 and 41) Facies modelling of the KAFs' different lithologies lead to the interpretation of two distinct lithofacies associations: - the first association extends from the base of the section to the 34.3 m mark of the Kipsaraman lithological log; - the second association extends from the same point to the base of the first laterally extensive volcanic unit referred to in this work as KAM (V) 2 (Fig. 39).

5.3.1. Distal fluvial channel lithofacies association

The lower lithofacies association of the Kipsaraman Section (0-34.3 m) is composed of matrix- (lithofacies Gmm; Fig. 40a) and locally clast-supported conglomerates (lithofacies Gcm) made-up of basement-derived clasts and massive fine-grained sandstones (lithofacies Sm; Fig. 40b ii), which takes up the bulk of the section and few mudstone intercalations (lithofacies Fm; Fig. 40c). The relatively thin gravelly phase, (2.2-m thick conglomerate) which occurs at the very base of the formation, is attributed to low strength pseudo-plastic debris flows (Miall, 1996). Lithofacies Sm forms the bulk of this lithofacies association and is thought to have formed from rapid suspension fallout from gravity flows (Miall, 1996; 2006), though the granulometry is characteristic of a distal depositional environment. The KAF facies association for the lower 34.3 m can therefore be attributed to deposition in the distal fluvial depositional zones by subaerial, hyperconcentrated flows, related to dispersed floodwaters (overbank) during periods of flooding, discharged onto distal alluvial fans (Hayfaa et al., 2003; Miall, 2006).

5.3.2. Floodplain lithofacies association

The upper 35.7 m of the KAF Type-Section is dominated by massive green mudstones (lithofacies Fm) with intercalated cream-buff coloured tuffs (Figs. 39 and 40d and g) (Table 7). Intercalated within this mudstone interval is one massive, matrix supported conglomeratic bed, 39.2 m from the base of the section (lithofacies Gmm) (Figs. 39 and 40f), two faintly laminated, buff coloured, silty to fine-grained sandstones (lithofacies Sh) (Figs. 39 and 40g). The lithofacies association is therefore composed of lithofacies Gmm, Sh and Fm, the bulk of which is dominated by lithofacies Fm and is overall interpreted as representing overbank flood deposits (Miall, 2006). The presence of a gravelly unit which would normally be associated with high energy pseudo-plastic debris flows uncommon in floodplain settings is considered to have been triggered by volcano-associated seismic activity in the area that led to the deposition of large unconsolidated clasts in the floodplain setting. The tuffs that are intercalated within the green muds and immediately above the conglomeratic bed support such a supposition as they indicate the occurrence of violent volcanic activity in the vicinity of the basin that could trigger off such seismic activity.

5.4. Post-depositional evolution of the Kamego Formation

Similar to the Kimwarer Formation, the post-depositional evolution of the Kamego Formation has been studied through petrographic examination of samples from different intervals within the formation (Figs. 44 and 45). The aim of this part of the study is constraining the post-depositional modification that the KAF has undergone and the causes of these modifications as well as the implications of these modifications to the overall reservoir quality of the formation. As there is no well data for the KAF, an understanding of the initial mineralogical make-up of the KAF and the subsequent cementation profile is critical for predicting the reservoir characteristics of the KAF at depth.

The main diagenetic features observed are cementation, predominantly by hematite and calcite cements as well as kaolin clays. Compaction also contributes to the diagenetic evolution of the KAF, especially with regard to the porosity of the different lithofacies. These cements and clays occur throughout the formation in relative amounts and in association with other authigenic phases, allowing for the distinction in cement zonation within the KAF as is outlined in Section 5.4.3. *Authigenic minerals*.

5.4.1. Texture

A similar format to what has been previously used for the textural description of the Kimwarer Formation has been employed here. The textural characteristics of sediments from the KAF can be summarized as follows:
- Grain sizes: They range from silt to pebbles, the latter being highlighted by the presence of feldspar grains with diameters >1 mm under thin section);
- Grain shape: Majorly sub-angular to sub-rounded;
- Grain contacts: Floating to concavo-convex, the latter being an indication of inter-granular deformation resulting from compaction/pressure dissolution phenomena and being concentrated at the base of the outcrop;
- Sorting: Sediments are poorly sorted overall..

The KAF can be described as compositionally immature owing to the wide range of clasts (quartz, feldspar, metamorphic lithics and other accessory minerals; see section 5.4.2 below) that comprise the sediments that make up the formation. Texturally, the formation can be also considered to be immature owing to the poor sorting, angular to sub-rounded nature of grains in the different studied lithofacies and wide range of grain sizes of the grains.

5.4.2. Detrital minerals

The main detrital minerals in the KAF are, in order of relative abundance: monocrystalline quartz, lithics (including sedimentary and metamorphic), clays, feldspars and polycrystalline quartz

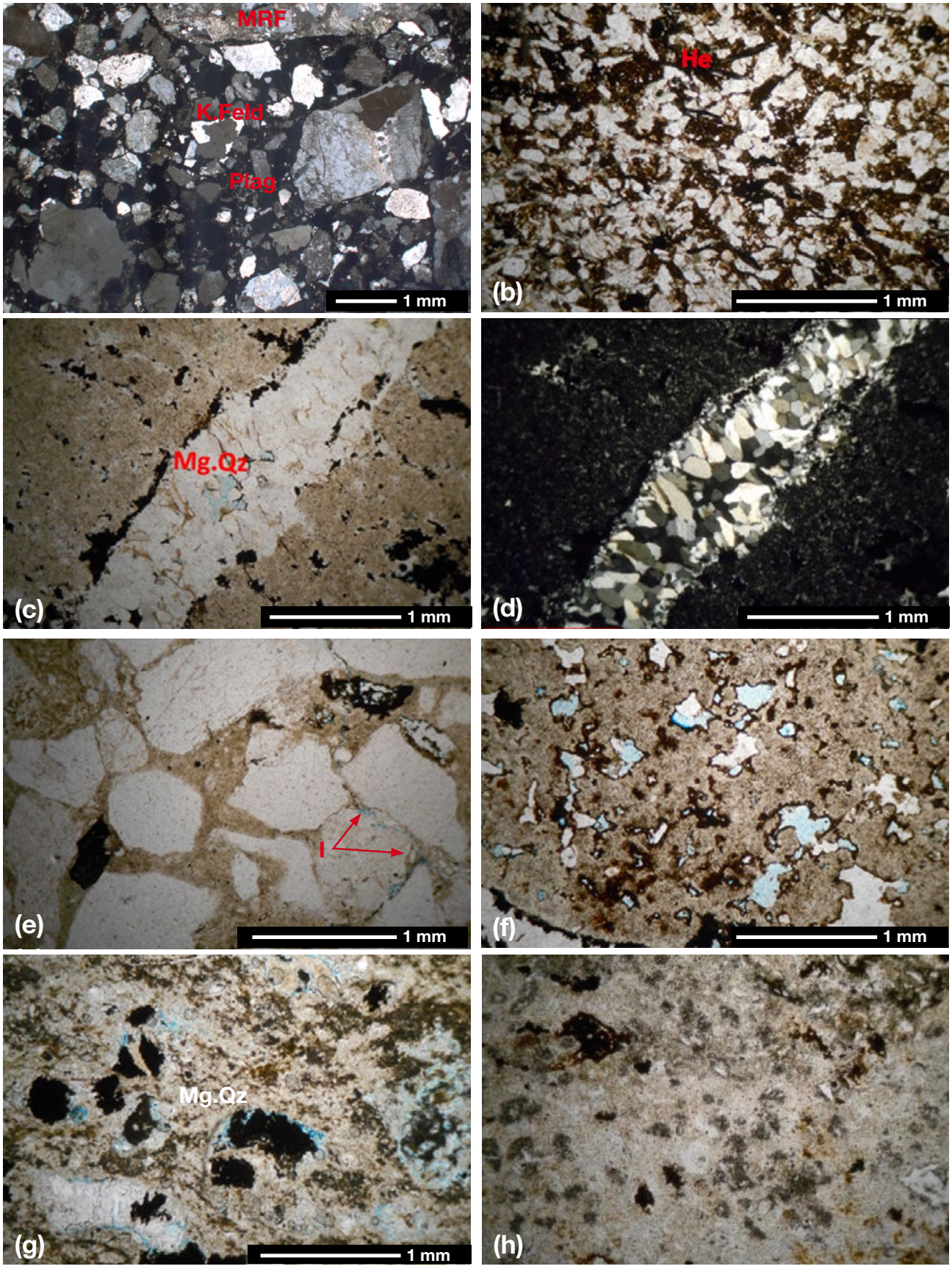

Fig. 44. *Different aspects of the granulometric make-up of sedimentary rocks of the Kamego Formation (a) i) Sample KAM 18 (see Fig. 39) - Paraconglomerate with predominantly metamorphic rock fragment and quartz granules/pebbles floating in a detrital muddy matrix b) Sample KAM 24 (see Fig. 39) showing sutured contacts between two quartz grains that suggest intense compaction leading to pressure solution. (c and d) Sample KAM 23 (see Fig. 39) Buff yellow tuffaceous mudstone with common fractures occluded by microcrystalline quartz and megaquartz (Mg.Qz). Hematite cement is also relatively common. (e) Sample KAM 18 (see Fig. 39) Rare polycrystalline quartz with altered K-Feldspars. (f) Altered plagioclase and alkali feldspars. Calcitic cement occurs in grain replacive mode. Metamorphic rock fragments are also noted within this sample (KAM 18 – see fig. 39) collected at the base of the outcrop. (g) Sample KAM 28 (see Fig. 39) A wacke with detrital mica, altered feldspar, opaque minerals and rare quartz. Hematite cements are also noted in grain replacive and pore filling mode. (h) Sample KAM 29 (see Fig. 39) showing tuffaceous mudstone with common authigenic silica, hematite and siderite*

5.4.2.1. Monocrystalline quartz

This is the most abundant detrital mineral in the KAF and together with the polycrystalline quartz constitutes between 15-40% of the whole detrital composition, following the Compton (1962) standard visual mineral estimation chart. Quartz grain shapes vary generally from angular to sub-rounded and grain sizes reach maximum diameters of >1 mm (under thin section) although the fine grains (0.125-0.25 mm) dominate (Fig. 44a-e). The monocrystalline quartz within the KAF shows moderate to strong undulation suggestive of stress. Pressure solution indicated by the sutured contacts between quartz grains is also noted (Fig. 44b). Intragranular deformation (grain shattering) is also noted within the quartz grains as evidenced by fractures within the quartz grains (Fig. 44f). Authigenic monocrystalline quartz was also noted within the mudstone facies in form of tightly packed crystals within the veins in this lithofacies (Fig. 44 c and d).

ZONE 1	**EARLY** **LATE**
Hematite cementation	
Compaction	
Calcite cementation	
Hematite cementation	
ZONE 2	**EARLY** **LATE**
Hematite cementation	
Quartz precipitation	
Hematite cementation	
Carbonate (calcite) cementation	

Table 9.
The paragenetic sequence within the two diagenetic zones in the Kamego Formation. Zone 1 represents the lowermost 5 m, Zone 2 the next 70 m (5-75 m). Relative timing and duration are indicated in the figure within the early to late axes.

5.4.2.2. Polycrystalline quartz

Polycrystalline quartz is generally represented by grains with more than five individual quartz crystals and is generally considered to be an indicator of a metamorphic source. Within the KAF, polycrystalline quartz is rare but when noted, the grain sizes though varied and can be as large as 2 mm under thin section (Fig. 44c). Intragranular deformation is exhibited by undulose extinction while the grain shapes are generally angular to sub-angular. The intercrystal boundaries vary from straight polygonal shapes to sutured contacts. Iron oxide inclusions are common suggestive of filling of pre-existing grain fractures. Grain shattering is also common and has resulted in the formation of numerous irregularly oriented thin fractures that are commonly filled by iron oxides.

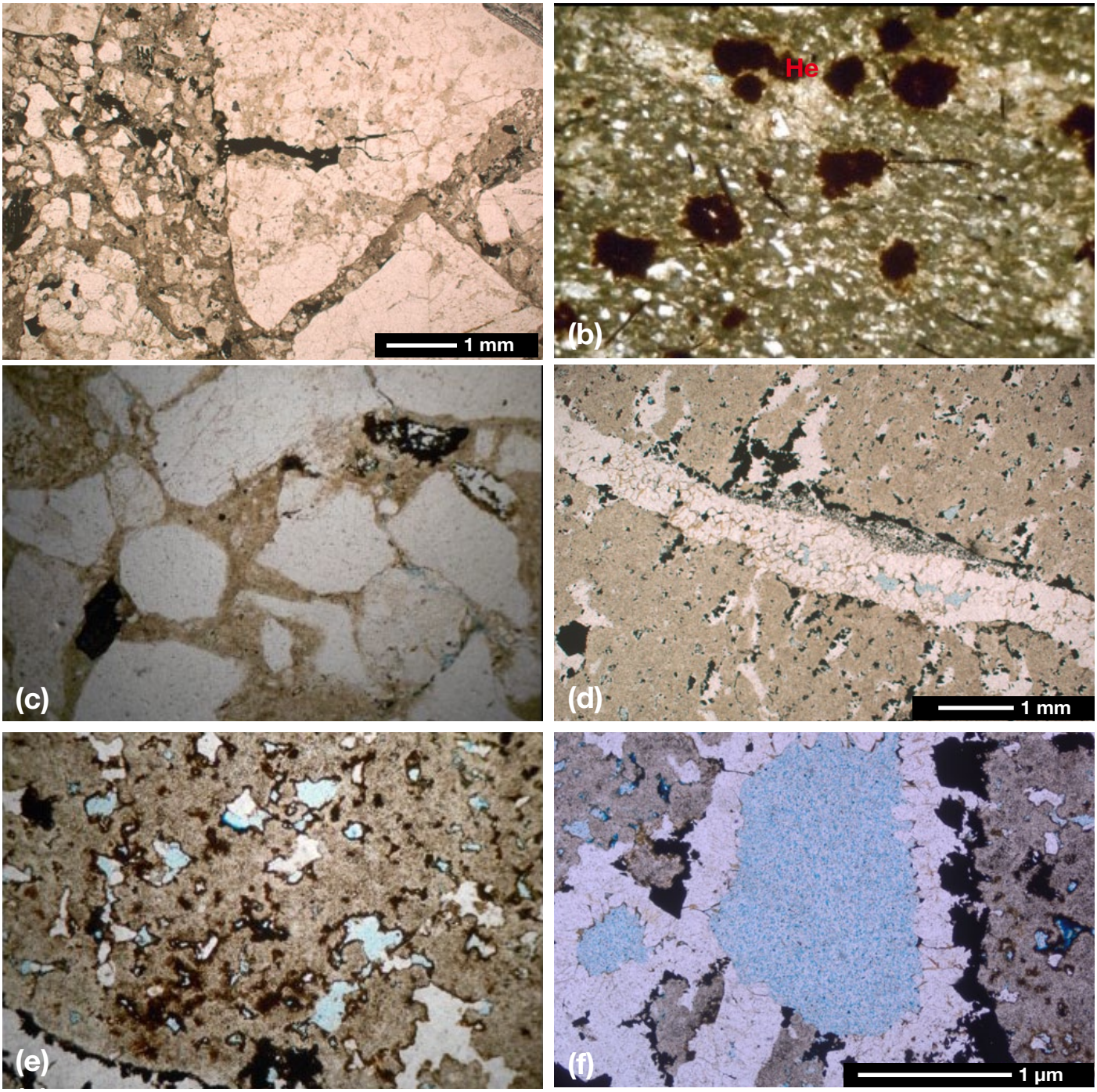

Fig. 45. *Different cement and porosity types in the Kamego Formation. (a) Sample KAM 18 (see Fig. 39) Feldspathic wacke comprising of metamorphic rock fragments and quartz grains floating in a detrital mud matrix. Common grain replacive to fracture filling calcite cement is noted reducing already poor porosity. This bed therefore has very poor reservoir quality. (b) Sample KAM 21 (see Fig. 39) Silty mudstone with cryptocrystalline matrix and common siderite (Si) and hematite (He) concretions. This bed also has poor to negligible reservoir potential. (c) An alternate view of sample KAM 18 which shows isolated secondary pores along the margins of some of the fractured quartz granules and pebbles that comprise the feldspathic wacke. (d) Sample KAM 23 which is a tuffaceous mudstone with good secondary solution porosity (Sp, mainly vugs). Pore filling megaquartz and hematite are common. (e and f) Sample KAM 24 (see Fig. 39) tuffaceous mudstone with good secondary solution porosity mainly in form of vugs. Pore filling megaquartz and hematite are common as pore rimming and pore filling form*

5.4.2.3. Feldspars

In the KAF, feldspars form up to 30% of the terrigenous detritus in some of the units analysed. The grain sizes range between silt to very coarse-grained sandstone, with the most abundant feldspar group being plagioclase feldspars. Alkali feldspars are also common (Fig. 44d) but subordinate in quantity to the plagioclase feldspars. Plagioclase usually shows polysynthetic twinning, while alkali feldspars (microcline dominant) are recognizable from their crosshatched twinning in cross polars. Alteration has significantly affected the feldspathic component of the KAF, leading to the growth/precipitation of microcrystalline clay minerals and replacement mainly by calcite along cleavage planes and on the surfaces of the feldspars (Fig. 44d).

5.4.2.4. Other detrital components

Aside from the quartz and feldspars, a number of associated detrital components including detrital clays, metamorphic lithics, and micas are found in the sedimentary assemblage of KAF. This diverse suite of detrital components, owing to their susceptibility is indicative of different provenance zones for the constituents of the KAF. Metamorphic rock fragments (MRFs) are the most common lithics in the KAF (Fig. 44f) and are composed of feldspars (both plagioclase and alkali feldspars), quartz and opaque minerals. These MRFs are angular and generally >3 mm in size. Mica flakes were also noted in the KAF (Fig. 44g), at the base and mid-section of the Kipsaraman Type-Section. The dominant mica is muscovite, which occurs in a relatively unaltered form. Organic matter is also preserved in the lowermost conglomeratic units. The matrix of the sandstones of the KAF is composed of clays, which are commonly associated with hematite (Fig. 44 e and f).

5.4.3. Authigenic minerals

Unlike the Kimwarer Formation, the KAF is not very well cemented with total cement content ranges between 5% and 10%. Much of the original pore space is filled by detrital clays. Nonetheless, two cements, hematite and carbonates (mainly calcite and siderite), are noted within the KAF (hematite being the dominant). Siderite occurs throughout the formation and cannot be used as discriminant cement. Nonetheless, the relative abundance of calcite and hematite within the formation has allowed for the segregation of the formation into two different diagenetic zones: a calcite-dominated base (0-5 m), while the rest of the formation (5-75 m) is dominated by hematite.

5.4.3.1. Zone 1 (Calcite-rich)

Calcite is the dominant cement at the base of the KAF between 0-5 m where it comprises between 1-5% (visual estimate) of the total sample (sample KAM 18; Fig. 44f). Calcite is noted mainly as replacement of the feldspars and the feldspathic component of the MRFs.

5.4.3.2. Zone 2 (Hematite-rich)

This zone (5-75 m) is characterized by the dominance of hematite cement, which is also present as submicronic crystals interspersed within the clayey matrix of some petro-types, which as a result display a dark brownish pigmentation sample (KAM 23; Fig. 44h). Hematite in this section occurs in pore filling and grain rimming phases. Where the hematite is pore filling, it is noted to grow from the pore margins inwards towards the centre of the pores (Fig. 44c and d).

5.4.3.3. Chronology of main diagenetic events

The early diagenetic events of the two zones follow a similar sequence starting off with hematite cementation, sediment compaction (commonly mechanical and in certain intervals pressure solution) and followed by calcite cementation and feldspar dissolution. These processes are summarized Table 9 for the two diagenetic zones.

5.4.4. Porosity

The porosity of the KAF sandstones ranges from negligible to good, the former being a consequence of tight packing (KAM 24; Fig. 44b), clays occluding pore spaces (KAM 18 - Fig. 45a), and porosity downgraded by the cements highlighted above (KAM 21 – Fig. 45b), whose major contribution is the occlusion of intergranular pore-spaces. In the same sample, hematite is noted occluding secondary porosity in form of fractures in quartz grains. Limited primary porosity is noted in some samples within the type-section (KAM 18 - Figs. 39 and 45c), which is found in section that we have classified as the distal fluvial channel depositional environment. Good secondary porosity is also noted in KAM 23 and KAM 24 (Figs. 39 and 45d and e), which is within the distal fluvial channel depositional environment. This secondary porosity is in form of vugs (KAM 24) within the tuffaceous silty to fine-grained sandstones and in fractures that are occluded by microcrystalline quartz and megaquartz (KAM 23). The secondary pore spaces are lined by hematite cement (KAM 23 and 24) suggestive that the cementation is linked to a porous system that is inherited from the subsurface (Tobin, 1997). Microporosity between clay platelets is inferred to be considerable but it is optically irresolvable under polarising microscopy. Consequently, following the Tobin (1997) reservoir assessment criteria highlighted in Table 6, the reservoir quality risk assessment for equivalent subsurface sediments is uncertain (Type 10, which refers to any reservoir whose pore system contains undeterminable secondary porosity, sensu Tobin, 1997).

5.5. Discussion

From the samples analysed, the KAF can be classified as a feldspathic wacke for the interval between 0-34.5 m and a tuffaceous mudstone for the interval 34.5-75 m on the Kipsaraman Type-Section lithological log (Dott, 1964). The detrital component of the Kamego Formation appears to be distally sourced owing to the predominantly fine-grained nature of the bulk of the formation. The few gravelly intervals (sensu Miall, 1996) are considered to be the result of episodic, high energy, pseudo-plastic flows, depositing in a relatively calm distal fluvial channel depositional environment. Such debris flows could have been caused by seismic shocks caused by rifting processes, a supposition that is consistent with the syn-sedimentary fault noted at the base of the Kipsaraman outcrop. Similar logic can be applied to the conglomeratic bed below bed KAM 27 (Fig. 39) in the overlying tuffaceous mudstones, which are interpreted as deposited on an extensive floodplain. The change in depositional environment is considered to have been due to volcanic activity that could have led to river capture and/or the beheading of rivers within the Baringo Basin.

The overall porosity of the KAF is principally downgraded by compaction with cementation acting as a secondary pore reduction mechanism. Long to sutured grain contacts, that are evidence of compaction, are common towards the base of the KAF below 5 m. Hematite is considered to be an early cement as it is noted in the pre-compaction phase, tightly squeezed between quartz grains. In this lowermost interval however, calcite is dominant and occurs as a secondary cement occluding most of the pore space. The porosity noted here (between 0 and 5 m in the section) is negligible to poor. Moderate to good secondary porosity (ca 20% visual estimation) is nonetheless detected higher up the stratigraphy (KAM 23 and KAM 24; Fig. 39), still within the distal fluvial channel. Between 5 m to 34.3 m, vuggy porosity is dominant with individual vugs generally occurring as hematite rimmed pores within a largely muddy matrix. Nonetheless, while the porosity might be high (20% - visual estimate), the high mud content could hamper pore throat connectivity meaning that the high porosity might not necessarily translate into high permeability. Nonetheless, as microporosity cannot be ruled out at this stage, the KAF can be concluded to have poor to moderate reservoir potential specifically within the portion that is defined as distal fluvial channel depositional environment.

5.6. Conclusion

This section presents the first multidisplinary study of the Kamego Formation. While a complete log from the base of the outcrop where the KAF sits on the basement, to the lowermost volcanic unit has been presented here, it is recommended that this work be complemented by work aimed at constraining the source rock potential of the Kamego Formation in order to have a holistic picture of the petroleum potential of this formation.
Nonetheless, this work is significant for also determining the minimum age of the KAF and placing the formation in a proper chronostratigraphic position. A minimum age for the KAF has been fixed at 19.8 ± 0.1 Ma (early Miocene-Burdigalian) based on the Ar-Ar dating of the lowermost volcanic unit found intercalated within the uppermost sediments of the KAF. This is consistent with the previous studies that have placed the first volcanic phase in the Central Kenya Rift as spanning the period between ~23-14 Ma (Baker et al., 1971). It is however this volcanic activity ca. 18 Ma that stopped early sedimentation within the Baringo Basin. A similar scenario is believed to have existed in the adjacent Kerio Basin at approximately the same time period, suggesting that widespread rifting accompanied by large scale volcanism took place in the Central Kenya Rift approximately ca. 18 Ma and that it is this volcanic phase that led to the cessation of sedimentation of both the Kimwarer and Kamego Formation in the Kerio and Baringo Basins, respectively.

Two depositional environments have also been identified within the KAF. These are:
- A fluvial system whose distal depositional environment is preserved at the base of the formation (0-34.5 m);
- A floodplain (overbank) depositional environment that extends from 34.5-75 m on the Kipsaraman Type-Section. The floodplain facies is characterized by numerous tuffaceous intercalations, which may point to the commencement of volcanic activity in the Baringo Basin during the deposition of the KAF. Chapman et al. (1978) mention fine-grained tuffs, shales and mudstones that are considered as part of the Sidekh Phonolites. However, these sedimentary beds are all intercalated within the formation, which allows therefore for the conclusion that all the studied section corresponds to the Kamego Formation.

The diagenetic study of the KAF has shown that the cement material changes from dominant calcite at the base (0-5 m) to hematite (5-75 m) for the rest of the formation. These cementation episodes occur during early diagenesis in low temperature conditions (<80 °C), under significant mechanical compaction. The reservoir potential of the KAF therefore, based on visual estimates range between negligible close to the base of the outcrop to approximately 20% on other measured sections on the formation. The best porosities are in fact secondary vuggy porosities noted in the fine-grained, tuffaceous, massive sandstone sections, between 5 m to 21 m that we have interpreted as being deposited in a distal fluvial channel depositional environment.

6. The Loriu Sandstone

Some of the sedimentary basins of the Northern Kenya Rift have been extensively explored (see General Introduction), and have been interpreted as having 5-8 km thick basin fills composed of fluvial and lacustrine sediments of Upper Cretaceous? to Miocene age (Williamson and Savage, 1986; Wescott et al., 1993; Morley et al., 1999; Tiercelin et al., 2004; Thuo, 2009; Tiercelin et al., 2012a, b) that are locally associated with Eocene to Miocene volcanic piles (Thuo, 2009) (Figs. 3 and 7a and b). In contrast, however, is the North Kerio Basin (NKB), which has received limited attention owing to its difficult accessibility, and particularly to the Loriu Range (also named Lariu Range) on the southeastern shore of Lake Turkana, which can be assumed to have contributed to the poor study of the regional geology and outcropping volcanic and sedimentary formations including the almost unknown Loriu Sandstone (or LOS). Access from the west (from Lodwar Town, about 150 km from the Loriu Range), over the monotonous harsh and jaded volcanic terrain is impossible by car, while access from the east is only possible after a bumpy boat ride from either Loyangalani Town on the eastern shores of Lake Turkana or from the Eliye Springs Town on the northwestern shores of Lake Turkana. Consequently, the Loriu Sandstone is one of the more poorly studied sedimentary formations in the Kenya Rift. The most extensive fieldwork to study the LOS was conducted in the 90's by Amoco Kenya geologists who had the good fortune of using a helicopter, which allowed them easy and safe access to the different outcrops of the Loriu Sandstone. Unfortunately, these investigations by oil geologists resulted in a small number of publications (Wescott et al., 1993; Morley et al., 1999b).

For this study, the formation was accessed in the month of November 2012 during a joint expedition with palaeontologists from the French CNRS and the Universities of Poitiers and Montpellier (France), via the offshore route from Eliye Springs Lodge in the central-eastern shores of Lake Turkana. The boat trip from Eliye Springs Lodge took approximately four hours and the entire fieldwork was conducted in only seven days. Access to the different outcrops of the Loriu Sandstone was only possible by foot, which was time-consuming, or sometimes by boat for the outcrops located along the shoreline.

6.1. Lithostratigraphy

The Loriu Sandstone and its surrounding geology in the Loriu Range were mapped for the first time by Amoco geologists (Wescott et al., 1993). Five main geological units were identified:1) A highly deformed and metamorphosed Precambrian basement, unconformably overlain by: 2) Arkosic grits referred to here as the Loriu Sandstone, overlain in turn by: 3) Post-grit lavas ; and 4) intruded by a dense system of dykes and igneous intrusions, covered by: 5) Post-volcanic (Plio-Pleistocene? and Holocene) fluvio-lacustrine deposits.

Fig. 46. *Geological background of the Loriu Sandstone. (a) Geological map of Loriu Range on the western shores on Lake Turkana showing the juxtaposition of the Loriu Sandstone above the Precambrian basement and the overlying volcanics and Plio-Pleistocene to Holocene fluvio-lacustrine sediments (mainly shell beds) (redrawn from Wescott et al., 1993, and Google Earth imagery). (b) The Loriu Sandstone overlying the Precambrian basement (dark coloured horizon at the centre of the image). Above the unconformable contact of the Loriu Sandstone (which dips to the northwest) and the Precambrian basement is a distorted, chaotic mix of slumped beds of the Loriu Sandstone. (c) A wide angle view of Lake Turkana from the top of the Plio-Pleistocene beds above the Loriu Sandstone. At the centre of the image is the Mount Porr region on the eastern shore of the Lake Turkana, whose underlying sediments are considered to be the lateral equivalents of the Loriu Sandstone (Wescott et al., 1993; Tiercelin et al., 2004, 2012b). (d) One of the numerous volcanic dykes that intrudes the Loriu Sandstone. This particular dyke is approximately 5 m wide at its widest and could be followed at least 400 m. Such a dyke has previously been dated at 14.7 ± 0.17 Ma using the K/Ar technique (Wescott et al., 1993). (e) Miocene volcanics in the background with lava flows with similar dip and trend to the Loriu Sandstone in the foreground (13° in N262°). A sample collected from the base of this flow sequence yielded a K/Ar date of 15.7 ± 0.7 Ma (Wescott et al., 1993).*

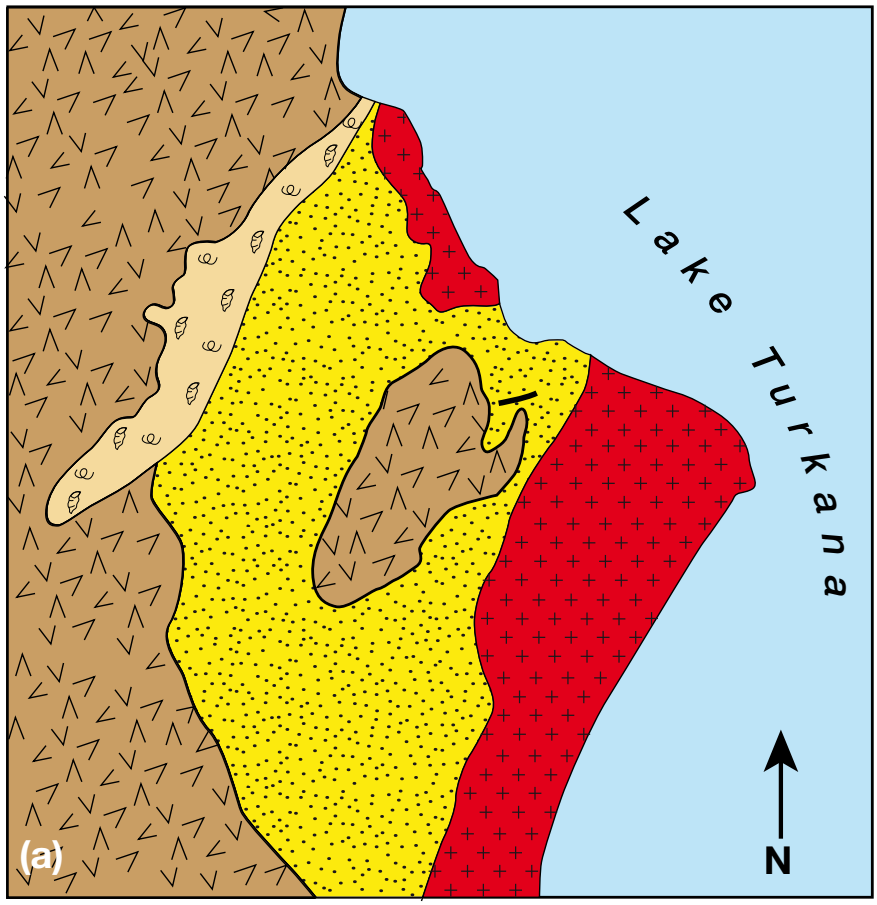

Tertiary Lavas

Plio-Pleistocene (?) lacustrine sediments

Loriu Sandstone

Precambrian Crystalline Basement

Sampled dyke (Loriu 1)

0 1 2 3 km

The Loriu grits were described as coarse-grained, arkosic, pebbly sandstones forming a repetitive sequence of channelized, lenticular sandstone bodies showing cross-bedding, horizontal laminations and graded-bedding, associated with thin, discontinuous red and green siltstone to mudstone units. Thickness estimates by Amoco geologists, based on the dip of bedding and from measured sections, indicated about 610 metres of grits from the top of basement to the base of volcanics. The grits appear to be derived from a local basement source and are interpreted as deposited by a system of braided streams. Measured palaeocurrents generally indicate transport to the north-northwest suggesting a source area south of the Turkana region (Wescott et al., 1993).

By mid-Miocene, volcanism that was previously centred in the north of the Turkana area shifted progressively to the central and southeastern parts of the general Turkana area, which includes the Loriu Range. Previously deposited sandstones were heavily faulted and intruded by dykes (Fig. 46d), and were later completely covered by lava flows. These lava flows that overlie the Loriu Sandstone are intercalated with relatively thin volcano-sediments, assumedly deposited between successive volcanic eruptions (Morley et al., 1992; Wescott et al., 1993). Only two lithostratigraphic sections were measured on the Loriu Sandstone, as the fieldwork only lasted for seven days, and that the access to the different outcrops was only possible by foot and as a consequence time-consuming. The first section, named the Loriu Section (Fig. 47), which is representative of the lowest part of the LOS, was measured from GPS point 02° 43' 03.54'' N; 36° 25' 51.30" E up to GPS point 02° 43' 4.92" N; 36° 25' 46.67" E through mid-point (1) 02° 43' 06.54'' N; 36° 25' 50.28" E and mid-point (2) 02° 43' 05.34'' N; 36° 25' 48.24" E (Fig. 47). This section is 79 m in total thickness. However, up to the 24 m mark, thick rock debris (e.g. Fig. 46b) cover parts of the section and not all of the lower third of the lithological column could be studied in detail. The second lithostratigraphic section, named the Kangabeiye Section (Fig. 48), was measured from GPS point 02° 43' 9.36'' N; 36° 25' 15.36" E up to GPS point 02° 43' 17.88" N; 36° 25' 15.36" E. Access to the lower part of this section was possible by boat, then by foot.

6.1.1. The Loriu Section

The contact with the basement was not visible at the base of this section but it was clearly identified approximately 100 m north of the base of the section in an area that was only accessible by boat (Fig. 46b). The first 24 m of the Loriu Section consist in a succession of metric (from 0.50- to 2-m thick) beds of massive, coarse-grained sandstones that are locally pebbly (lithofacies Sm) (Bed 01/12/04; Figs. 47a and 48a) with few matrix-supported conglomerates (lithofacies Gmm) (Bed 01/12/12; Figs. 47a and 48b), which are often present in the form of metric-sized lenses. Both sandstone and conglomerate lithofacies are poorly sorted and characterized by abundant angular to sub-rounded metamorphic rock lithics, quartz (often forming lenses with >5 cm quartz pebbles), cobbles >20 cm, and mud clasts >10 cm. Colours are generally from grey to purple grey and the sandstones are locally micaceous. Cracked quartz pebbles were locally observed, similar to the ones observed in the Mount Porr Sandstone, that outcrops along the eastern shoreline of Lake Turkana, facing the Loriu area (Tiercelin et al., 2004) (Fig. 46c). At least 50% of the section between 0 and 24 m was impossible to describe as it was densely covered by thick rock debris. Those covered section (Fig. 47a) could possibly be interpreted as representative of less indurated fine-grained sediments, thus being more easily affected by erosion processes.

Between 24 and 56 m from the base of the section, the outcrop conditions are better as the section is not covered by rock debris. Between 24 and 36 m are three 3- to 4-m thick beds of coarse to pebbly sandstone that are characterized by a generally greyish pink colour, with common planar cross-bedded structures (lithofacies Sp, Bed 01/12/17; Figs. 47a and 48c) and local channel features. This series of beds also contains lenses of conglomerate that have sub-angular to sub-rounded, >8 cm in diameter quartz and metamorphic lithic pebbles. Bed 01/12/16, located 29 m from the base of the formation (Figs. 47a and 48d) however breaks the sandstone monotony and is a massive, grey-green, 0.10 m thick mudstone (lithofacies Fm). This bed is overlain by a coarse-grained sandstone unit with planar cross beds and also contains evidence of localized (root casts) bioturbations.

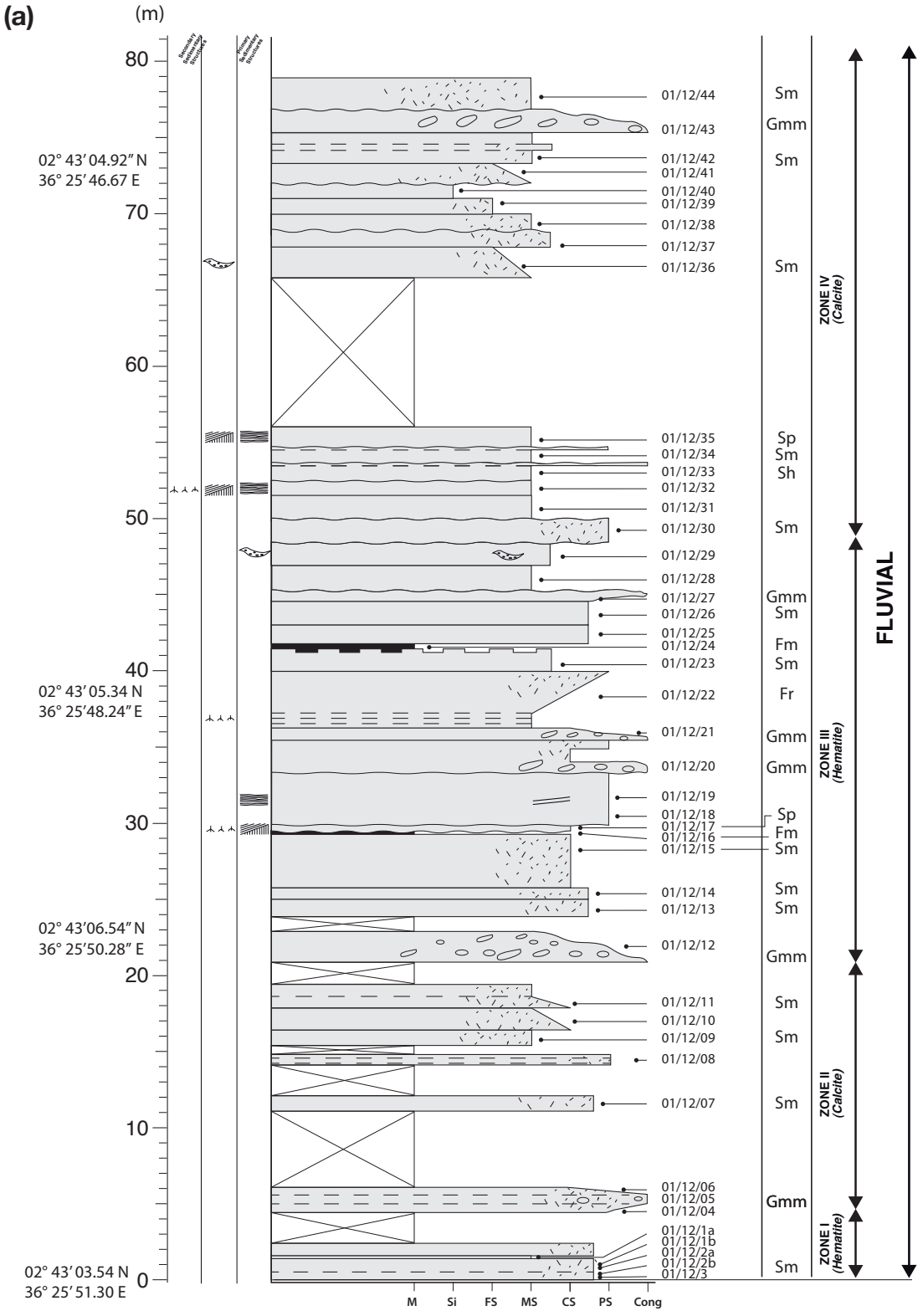

Fig. 47. *Lithological logs of the Loriu Sandstone. (a) The Loriu Section (78.05 m total thickness) measured at 02° 43' 03.54" N; 36° 25' 51.30" (base of the log).*

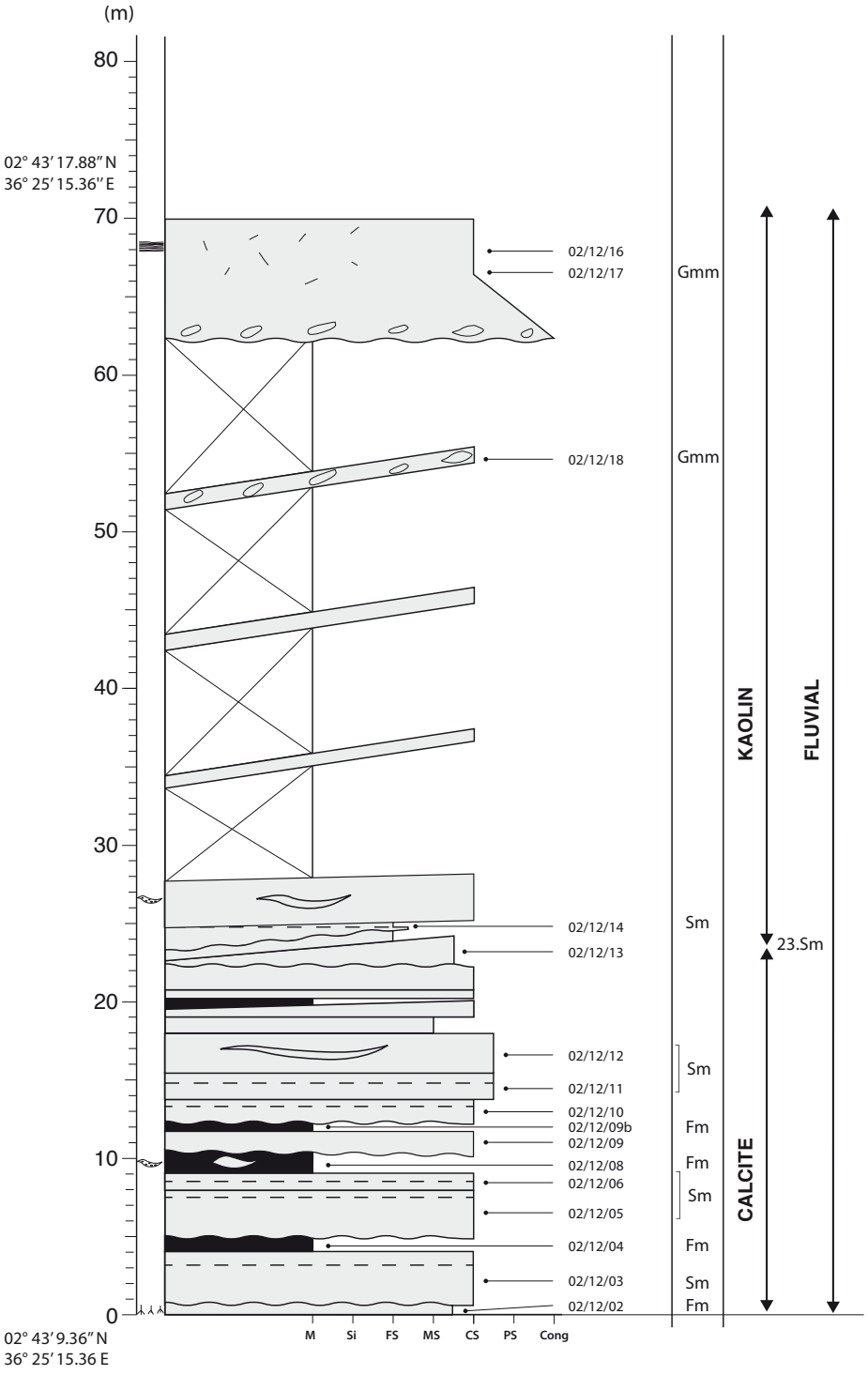

Fig. 47. *Lithological logs of the Loriu Sandstone. (b) The Kangabeiye Section (69.90 m total thickness) measured at 02° 43' 9.36"N; 36° 25' 15.36"E (base of the section. The crossed out portions of the lithological log are those parts of the section that were inaccessible due to their being covered by rubble. The Loriu Section represents the lower fringes of the Loriu Sandstone while the Kangabeiye Section, shows the stratigraphy of possibly the mid-section of the LOS or an interval above the Loriu Section. It was not possible to correlate these two sections owing to the lack to laterally extensive marker beds and the high amount of detritus that covers much of the Kangabeiye Section.*

Fig. 48. *The Loriu Section: (a) Bed 01/12/07 (Fig. 47a): Massive pinkish grey massive, metric thick sandstone (lithofacies Sm) with intercalated pebbly lenses that represent fallout from hyperconcentrated or sediment gravity flows in the fluvial system floodplain setting. (b) Bed 01/12/12 (Fig. 47a): Massive ungraded matrix supported conglomerate (lithofacies Gmm). This 2.5 m thick, light grey, conglomeratic bed that has an erosive base, contains quartz and mudclast cobbles that are greater than 10 cm in diameter, indicative of high energy flow regimes. (c) Bed 01/12/17 (Fig. 47a): Medium to coarse grained, pinkish grey, decametric bed with truncuated planar cross beds. This bed is indicative of lower energy flow regimes. Laterally, this bed grades into a root-bed (sensu Miall, 1996) and overlies (d) Bed 01/12/16 (Fig 47a), which is the only mudstone bed that was noted in the Loriu Section. The juxtaposition of these two lithofacies implies a general decrease in the flow energy of the fluvial system depositing the Loriu Section. It is this reduction in flow energy that allowed for the development of vegetation along the river channels or at the periphery as is evidenced by the rootbed (lithofacies R) that are noted close to the planar crossbeds of bed 01/12/17 (e) Recemented sandstone concretions at the top within the Loriu Section. These concretions could be due to the onset of pedogenesis after deposition (lithofacies P). (f) Bed 01/12/35 (Fig. 47a): Dark brown, horizontally bedded, medium grained, metric thick sandstone bed (lithofacies Sh). This bed is indicative of low energy flow regimes (≤ 1 m/s; from Miall, 1996).*

Fig. 49. *The Kangabeiye Section, which represents a stratigraphically higher position than the Loriu Section within the general stratigraphic column of the Loriu Sandstone. (a) Bed 02/12/13 (Fig. 47b): Massive sandstone (lithofacies Sm) that represents fallout from hyperconcentrated flows. (b) Bed 02/12/02 (Fig. 47b): Metric thick, purple, highly indurated mudstone with abundant root moulds (lithofacies R) at the observable base of the Kangebeiye Section. These root beds located between 0 m and 12 m above the base of the section (Fig. 47b) could correspond to the proximal overbank or floodplain setting of a fluvial system. (c and d) (i) Beds 02/12/07 and 02/12/08 (Fig. 47c) are fine-grained, purple, massive mudstone beds with (ii) abundant bioturbations (possibly Naktodemasis bowni) (Smith et al., 2008a). This is suggestive of overbank or abandoned channel deposits that accumulate in from stagnant pools of water during low stage channel abandonment and create a conducive environment for post-depositional modification through biological processes, e.g. burrowing (Miall, 1996). (e) Bed 02/12/17 (Fig. 47b): Horizontally bedded sandstone (lithofacies Sh). (f) Bed 02/12/018 (Fig. 47b): Massive ungraded matrix-supported and locally clast-supported conglomerate (lithofacies Gmm). This 7-m thick, brown, conglomeratic bed contains quartz, metamorphic rock fragments and mudclast cobbles that are generally between 5 and 10 cm in diameter, and the two conglomerate types are both indicative of high energy flow regimes.*

Due to erosion, the remaining part of the section from 36 m from the base of the section, was traced laterally and picked up at GPS point 02° 43' 5.34'' N; 36° 25' 48.24" E. At this point, is a 4-m thick bed of buff coloured, massive and coarsening up (from medium-grained to pebbly) sandstone with numerous root casts (>5 cm in diameter and >10 cm in length) at its base. Between 40 and 50 m is a succession of seven metre-thick, massive, medium-grained to pebbly sandstone beds that are characterized by erosive bases and contain local lenses of fine to coarse granules. At 41 m is a layer characterized by purple-brown, fine-grained concretions that are assumed to be tubular rhizoliths (Bed 01/12/23 - Figs. 47a and 48e). A set of five metre-thick beds of medium-grained massive, strongly indurated, purple grey in colour sandstones that contain sub-angular to rounded quartz pebbles, is visible between 50 and 56 m. All these beds have erosive bases with parallel and cross bedding (lithofacies Sh - Bed 01/12/35 – Figs. 47a and 48f) being common sedimentary structures within the lower and upper beds. The interval between 56 and 66 m represents a covered section, which could be interpreted as a fine-grained facies. From 66 m to the top of the section at 79 m, are nine beds that are grey to purple-grey, massive, medium-grained sandstone beds with scattered pebbly sandstone lenses (pebbles within these lenses are >5 cm). The lowermost five beds fine up from medium-grained sandstone to siltstone. Scattered carbonaceous concretions are also noted in the bed 01/12/40. In the four topmost beds, locally matrix-supported conglomerate facies are noted at the base of bed 01/12/43 (75 m). This conglomerate contains scattered sub-angular to sub-rounded metamorphic lithic pebbles with diameter >7 cm.

6.1.2. The Kangabeiye Section

The second lithostratigraphic section (Fig. 47b) is a 70-m thick relatively homogeneous section that is only fully accessible at base. Past the 28 m mark, the section is essentially covered by debris up to the 62 m mark and only three metre-thick sandstone beds are exposed within this covered section that is capped by an 8-m thick conglomeratic to coarse-grained sandstone unit at the very top of the outcrop.

The lowermost 13.5 m are composed of a series of 1-m to 3-m thick beds of purple, massive, medium- to coarse-grained and highly indurated sandstone (lithofacies Sm) (e.g. Bed 02/12/13 Figs. 47b and 49a). The lowermost bed in the section (sample 02/12/02) shows abundant root moulds (lithofacies R) (e.g. Bed 02/12/02 - Figs. 47b and 49b). Within this section are three metre-thick massive mudstone beds (lithofacies Fm) (e.g Bed 02/12/04 – Figs. 47b and 49c) with a grey to purple colour located at 4 m, 10.9 m and 12 m from the base of the outcrop, respectively. Unique about the Kangabeiye Section is the high amount of bioturbations present in most of the grey to purple coloured mudstone beds. These burrows are recorded on beds 02/12/07, 02/12/08 and 02/12/09 (Bed 02/12/08; Figs. 47b and 49d), which also are interpreted as pedogenetic intervals. In plan view, the burrows are arcuate and variably oriented and composed of a series of distinct >1-2 cm in diameter and 5-7 cm long, ellipsoidal packets which contain thin tightly spaced menisci whose colour locally alternates and which are sub-parallel to the bounding packet similar to those described by Smith et al. (2008a) in the Willwood Formation of the Bighorn Basin in Wyoming, USA. Smith et al. (2008b) collectively described such burrows as Adhesive Meniscate Burrows (AMB) and specifically interpreted burrows similar to those noted in the Kangabeiye Section as Naktodemasis bowni (Smith et al., 2008a) and attributed the same to the locomotion and dwelling traces of burrowing insects (Fig. 49e). The presence of N. bowni indicates periods of subaerial exposure that are associated with pedogenic modification under moderately to well-drained soil conditions, or during periods of better drainage in imperfectly drained soils. This fits well with our interpretation of the beds that contain N. bowni as pedogenetic intervals developed in overbank fines (sensu Miall, 1996). The top most bed of the section at 62 m is a 8-m thick unit formed at base by a yellow brown massive matrix-supported conglomerate (lithofacies Gmm) (Bed 02/12/17; Figs. 47b and 49f).

6.2. Chronostratigraphic setting of the Loriu Sandstone

The Loriu Sandstone is overlain by a thick sequence of lava flows that are also heavily intruded by a complex system of dykes and small circular pipe-like igneous bodies, some of which may represent volcanic vents. On aerial imagery, the dykes apparently follow different trends but resulting in two dominant strike directions at about N135° (e.g. sampled dyke – Loriu 1 – Fig. 50b) and in an approximate NE – SW strike direction (Fig. 50c). Both the intrusions and the lava flows have previously been dated using whole rock K-Ar techniques providing minimum ages for the LOS deposits (Wescott et al., 1993). A radiometric age at 15.7 ± 0.7 Ma was obtained for a sample collected at the base of the lava-flow sequence, and one dyke intruding the sediments has also been previously dated and yielded a slightly younger age of 14.7 ± 0.17 Ma (Wescott et al., 1993). The sandstones are undated, but it follows from the middle Miocene ages obtained from the overlying volcanism that they could correspond in the North Kerio Basin to the lower tectonic unit representing a Paleogene-early Miocene extensive phase observed on seismic lines TVK-110 and TVK-132 (Morley et al., 1999c).

Only one volcanic sample (Loriu 1) was collected during the November 2012 field trip, from a 1.2-m thick, N110°-trending vertical dyke at GPS point 02° 42' 50.34'' N; 36° 25' 46.80" E (Fig. 50d). This dyke, intrusive within sediments belonging to the Loriu Section (i.e. lower part of the Loriu Sandstone), corresponds to a fine-grained mafic and porphyritic rock. In thin section, the mineralogy of the rock appears basaltic (Fig. 51). Indeed, no feldspathoid is observed. Porphyritic (phenocrysts are up to 2 mm in size) to glomeroporphyritic with a microlitic to nanocrystalline groundmass, the rock also contains subangular enclaves up to 0.5 cm in size of microgabbro -or dolerite- with a typical doleritic texture (Fig. 51a and b). No broken crystal was however observed along the margins of the enclaves. In contrast, locally, the microcrysts of the dolerite were observed to dismantle in the groundmass, providing euhedral, isolated crystals, undistinguishable from phenocrysts (either by their size, or nature), but which, from a strict point of view, correspond to xenocrysts. The absence of visible reaction rims around these crystals indicates that thermodynamical equilibrium was established between the dolerite and the magma in the dyke. These observations suggest that these enclaves only represent fragments of earlier intrusions that were: (i) crystal-rich but, possibly, not completely solidified since they dismantled as euhedral unbroken crystals; (ii) made by a magma of the same composition as that in the dyke; and (iii) torn from deeper in a unique magmatic plumbing system under construction. Whatever the time laps that separated the solidification of the microgabbro from that of the dyke, both likely developed from the same general magmatic event. The main phenocrysts, and thus, doleritic xenocrysts in the dyke are euhedral-subhedral zoned clinopyroxene, the rims of which are pinkish and suggest Ti-rich augite, plagioclase, euhedral olivine and opaque minerals. The groundmass is mostly composed of plagioclase microlites, opaque mineral, clinoyroxenes (Ti-rich augite) and olivine micro- to nano-crysts. Apatite occurs as a common accessory phase. From a chemical point of view the rock correspond to a tephrite (Fig. 52a and b; Table 10; Appendix 2) that is poorly distinct from those of the Elgeyo Basalts (Table 4) that lie above the Kimwarer sediments.

Two 39Ar-40Ar dating analyses were attempted on whole rock groundmass portions from the dyke sample. Unfortunately no plateau age was obtained. Indeed, less than 3 consecutive steps, comprising a minimum of 70% of the 39Ar released, agree within 1 or 2 σ error bars with the weighted mean calculated 40Ar*/39ArK ratio of the plateau segment. The obtained spectra display very similar shapes characteristic of a 39ArK recoil effect (Lo and Onstott, 1989; Ruffet et al., 1991; see also 39Ar-40Ar results from Unit 2 above the Kimwarer Formation in this work). Nevertheless, for increments in between 10 and 65% of Ar release, seven steps in the spectra stabilize at about 18.5 Ma, defining a pseudo-plateau age (Fig. 53). This is not a plateau age as it is estimated over less than 70% of the 39Ar released, but ca. 18.5 Ma provides a reasonable estimate for the emplacement, crystallization, and cooling of this N135°-trending dyke. As the dyke contains dismantled doleritic enclaves, in apparent thermodynamic equilibrium with the groundmass, this age also represents a minimum age for the whole magmatic episode in the basin.

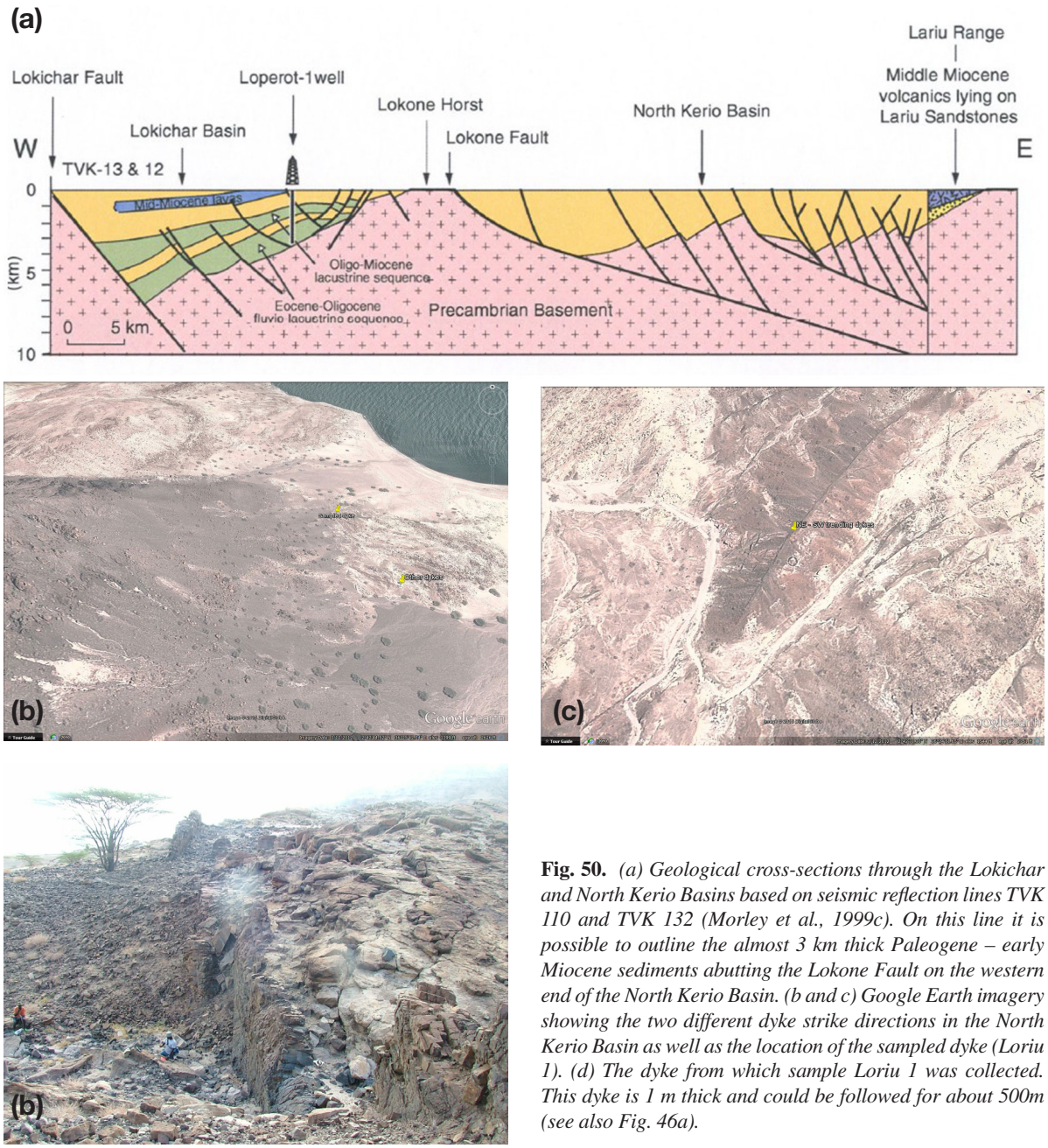

Fig. 50. *(a) Geological cross-sections through the Lokichar and North Kerio Basins based on seismic reflection lines TVK 110 and TVK 132 (Morley et al., 1999c). On this line it is possible to outline the almost 3 km thick Paleogene – early Miocene sediments abutting the Lokone Fault on the western end of the North Kerio Basin. (b and c) Google Earth imagery showing the two different dyke strike directions in the North Kerio Basin as well as the location of the sampled dyke (Loriu 1). (d) The dyke from which sample Loriu 1 was collected. This dyke is 1 m thick and could be followed for about 500m (see also Fig. 46a).*

As the dyke was found intrusive into the sediments identified in the Loriu Section, considered as forming the lower part of the Loriu Sandstone, the value of ca. 18.5 Ma also represents the minimum age for the LOS. This minimum age for the sedimentation is older by about 3.5 Ma than what was previously estimated using K-Ar methods by Wescott et al. (1993) from a sample that was collected at the base of the flow sequence overlying the LOS. Unless K-Ar isotopic systems in the overlying lava flows were disturbed by younger events, the age at ca. 18.5 Ma on this dyke could suggest that early volcanic units were largely eroded in the Loriu area before they were overlain and obscured by the younger flows dated at ca. 15.7 Ma.

In such a hypothesis, the dykes in the sediments form remnants of older volcanic episodes and only limited evidence of the earliest volcanic intrusions have been left. Following this hypothesis, as Wescott et al. (1993) also

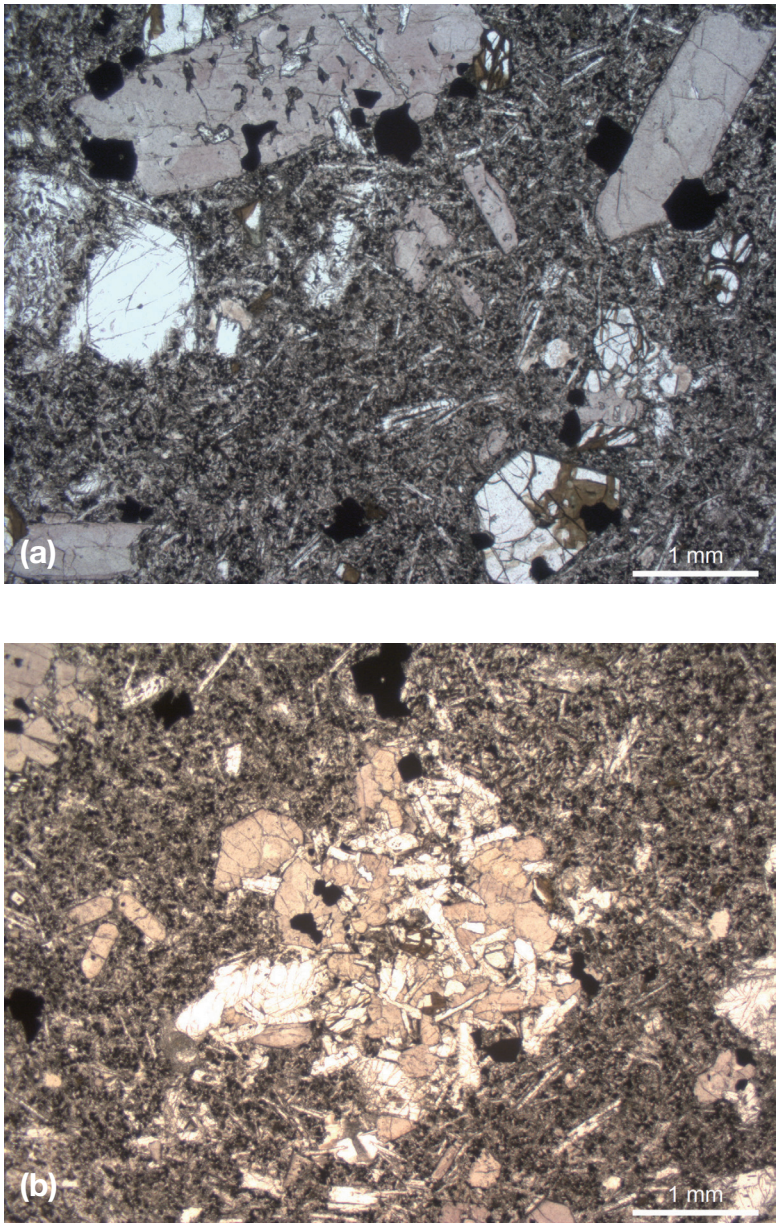

Fig. 51. *Typical textures and minerology of the mafic Loriu 1 dyke intruding the lower parts of the Loriu Sandstone collected during the November 2012 field trip. Thin sections under plane polarized light. See scales on the microphotographs. (a) Porphyritic, microgranular to microlitic tephrite showing clinopyroxene (Ti-rich augite, brownish to pinkish crystals to the top), plagioclase (colorless crystal to the left side), olivine (colorless crystals weathered into brownish clay minerals to the right and bottom right), and sparse opaque mineral phenocrysts. Microcrysts and microlites of plagioclase, clinopyroxene and opaque mineral are also visible. (b) Microgabbroic enclave with a typical doleritic texture showing intergranular to subophitic clinopyroxene partly embaying plagioclase, olivine and opaque mineral. Note that the crystals in the enclave (b) are undistinguishable from the phenocrysts (a) in the dyke.*

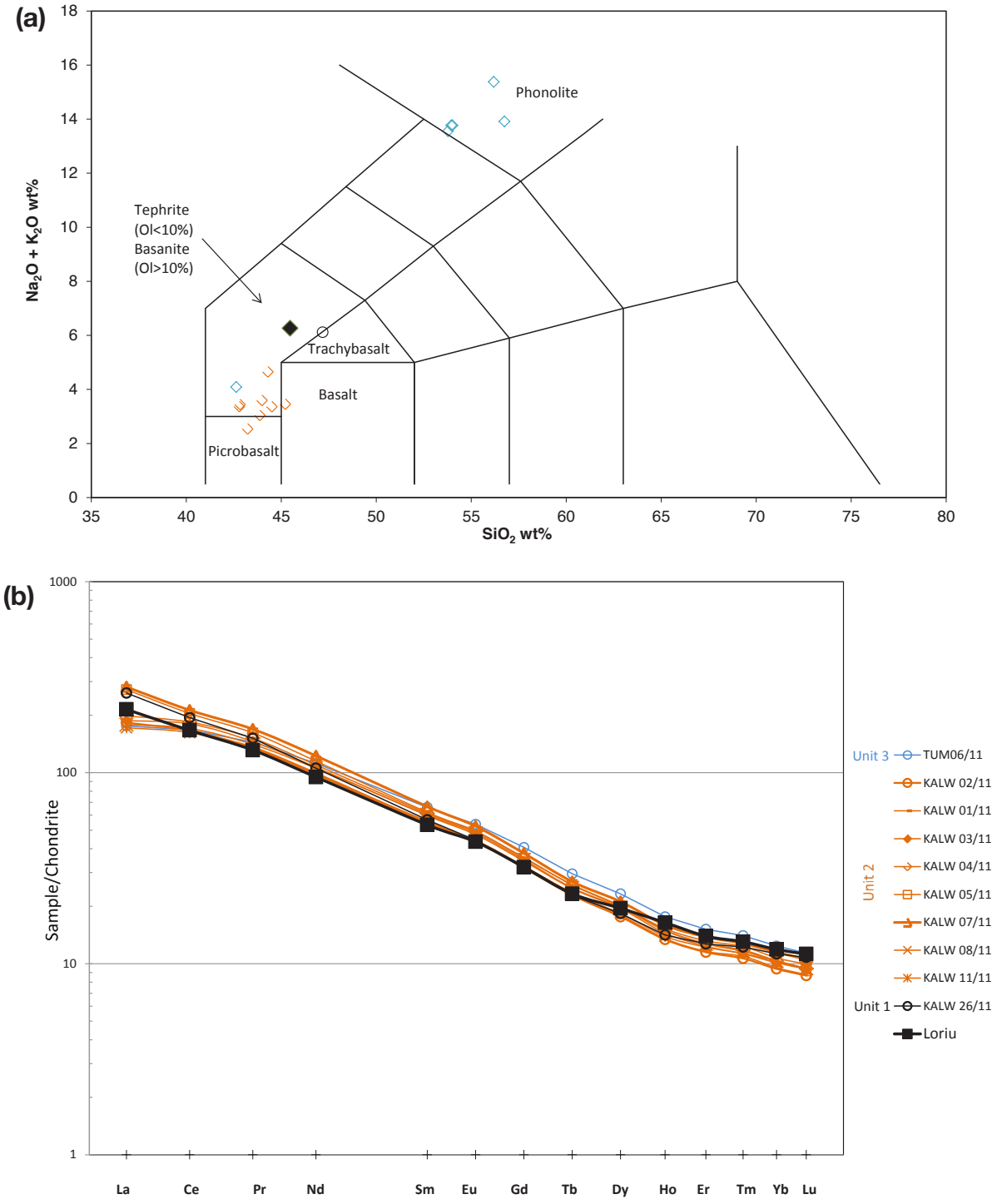

Fig. 52. *(a) Total alkali versus silica (TAS) diagram, and (b) Chondrite normalized Rare Earth Element (REE) pattern of the Loriu dyke, tephrite sample K7 (black filled square). Comparison with the samples from the Kimwarer Formation (open symbols, this work): ultrabasic to basic rocks (black, -Unit 1-, brown, -Unit 2-, and blue, -Unit 3-) from the Elgeyo Basalts (Elgeyo Formation) on (a) and (b); intermediate rocks (Unit 3) from the Chof and Uasin Gishu Phonolites are also shown on (a). Ol refers to normative olivine content. Note the compositional similarities of sample K7 with the tephritic rocks from the Kimwarer section, especially with Unit 1*

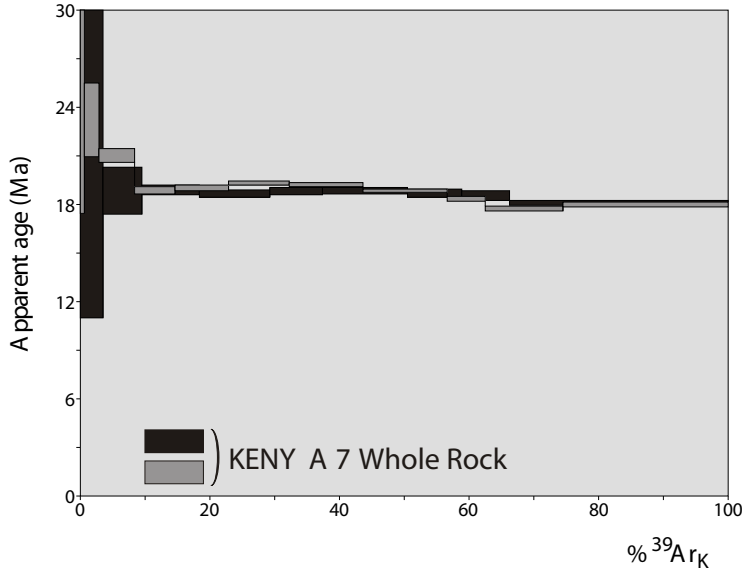

Fig. 53. *Age-spectra versus cumulative ^{39}Ar gas released obtained during step-heating experiments on whole-rock fragments of the Loriu dyke sample.*

describe intrusions in the younger lava flows, one of which was dated at ca. 14.7 Ma, at least two successive episodes of dyke intrusions must be assumed in the area. It is therefore possible that the different trends of the dyke in the area (Fig. 50) reflect distinct intrusive episodes related to distinct extensional tectonic phases within the Loriu Range. Alternatively, considering that the K-Ar isotopic systems could have been strongly perturbed by younger events, leading to significant under estimations of the K-Ar cooling ages of the rocks, the dykes in the sediments could also represent feeders of the lava flows just above the sediments. Following this alternative hypothesis, and in the absence of new dating of the lava flows, both the dykes and the flows could have about the same emplacement ages. A single main episode of intrusions feeding volcanism thus remains a possibility despite different dyke trends. Unfortunately, in their 1993 publication, Wescott and colleagues did not provide information on the composition of the lavas above the Loriu sediments to compare with the composition of the intrusions. The questions of the number and of the duration of magmatic events affecting the Loriu Range, and that of their relationships with the main deformation phases, remain unsolved.

Table 10
Major and trace elements of volcanic rocks associated with the Loriu Sandstone.

Section		**Loriu**
Sample name		LORIU DYKE K7
Rock name		Téphrite
wt%		
SiO_2		43,90
Al_2O_3		14,72
Fe_2O_3*		13,17
MnO		0,21
MgO		5,08
CaO		9,59
Na_2O		4,45
K_2O		1,60
TiO_2		3,12
P_2O_5		0,74
PF		2,81
Total		99,36
ppm	d.l. (ppm)	
As	1,20	1,62
Ba	1,50	592,10
Be	1,00	2,28
Bi	0,10	< d.l.
Cd	0,15	0,32
Ce	0,1	135,40
Co	0,40	42,23
Cr	5,00	79,33
Cs	0,15	0,36
Cu	5,00	144,50
Dy	0,007	6,34
Er	0,003	2,97
Eu	0,004	3,14
Ga	0,20	22,93
Gd	0,02	8,29
Ge	0,10	1,40
Hf	0,04	6,08
Ho	0,001	1,20
In	0,10	0,12
La	0,05	67,49
Lu	0,001	0,36
Mo	0,35	2,56
Nb	0,06	90,00
Nd	0,03	56,63
Ni	4,50	63,19
Pb	1,40	4,79
Pr	0,01	15,22
Rb	0,35	38,78
Sb	0,20	17,70
Sc	1,00	< d.l.
Sm	0,01	10,22
Sn	0,40	2,63
Sr	1,20	779,70
Ta	0,02	6,59
Tb	0,006	1,14
Th	0,02	7,80
Tm	0,005	0,39
U	0,04	2,03
V	0,60	261,40
W	0,30	0,66
Y	0,40	30,68
Yb	0,003	2,47
Zn	11,00	134,70
Zr	1,30	273,60

Fe_2O_3*: total iron; d.l.: detection limit

In the Lokone area of the Lokichar Basin, which is located immediately to the west of the Loriu Range (Figs. 7a and 13), the sediments belonging to the Lokone Sandstone (Fig. 50) are also densely intruded by 2- to 10-m wide, N50° to N170°-trending igneous dykes. Other dyke systems are present in several other areas east and south of Lokichar (Lojamei) and north of Lodwar (Dodson, 1971; Joubert, 1966; Wescott et al., 1993). For example, two of these dykes sampled in the Lokichar/Lojamei area are characterized as alkaline basaltic rocks, and yielded K/Ar ages between ca. 17 and 13 Ma (Tiercelin et al., 2004). All available data thus suggest rather young ages and a long lasting event for this rather intensive mafic magmatism. In addition, it follows from the new Ar pseudo-plateau age obtained during this work that the Loriu sediments should be now considered as being older than about18.5 Ma, which thus makes the sedimentation older than previously thought.

6.3. Facies analysis, depositional processes and environments of the Loriu Sandstone, Loriu Section

Similar to previous studied sections in this work, depositional environments of the sandstone beds of the Loriu Section were determined through the study of the lithology, sedimentary structures and facies associations. Thin sections as well as hand specimens of samples collected from the two sections were analyzed to determine the mineralogical composition as well as the authigenic and diagenetic constitution of the Loriu Sandstone in the Loriu Section. From an analysis of the structural make-up, grain size and colour variation within the Loriu Section, a total of 6 different lithofacies were identified whose characteristics are summarized in Table 11. The facies code employed here has been adapted from Miall (1996, 2006).

Facies code	Lithology	Sedimentary structures	Bed Thickness (m)	Depositional processes	Interpretation	Figures
Gmm	Massive ungraded matrix-supported conglomerate mainly constituted of quartz and metamorphic rock fragments and rounded to sub-angular mud clasts floating in a medium- to coarse-grained sandstone matrix	Planar to strongly erosive lower boundaries	Maximum >2.0	Non-tractional deposition by high strength viscous plastic debris flow (Miall, 1996)	Sub-aerial plastic debris flow	Figs. 47a and 48b;saùples 01/12/05, 01/12/12, 01/12/27 and 01/12/43
Sm	Massive, ungraded, poorly sorted, medium- to very coarse-grained sandstone, commonly associated with floating quartz pebbles. Purple-grey to buff brown in colour. Most abundant facies in the Loriu Section	Commonly contains conglomeratic lenses	0.1-3.5	Sub-aerial hyperconcentrated flows or sediment gravity flows (Miall, 1978; 1996)	Rapid suspension fallout from sedimentary gravity flows and/or post-depositional modification through dewatering for those beds with faint bedding	Fig. 47a and 48a; samples 01/12/02b, 01/12/07, 01/12/13
Sh	Fine- to coarse-grained sandstone. Colour from buff grey to purplish grey	Horizontal stratifications up to 2 cm thick, that grade to massive at the top	1.2	Planar bed in shallow waters (0.25-0.5 m) by low to medium velocity waters (0.4 – 1 m/s) (Miall, 1978, 1996)	Plane bed flow, under critical flow regime	Fig. 47a and 48f; sample 01/12/35
Sp	Medium to coarse, cross-bedded, indurated light grey to grey pink	Grouped, truncated planar cross-beds with an erosive base and local convolute bedding	1.2	Medium part of lower-flow regime (Miall, 1978)	Migrating 2D-dunes	Fig. 47a and 48c; sample 01/12/17
Fm	Silty mudstone, friable grey green mudstone	Massive, with sharp contact at base, with muds filling palaeotopography	0.1-0.2	Deposition from suspension	Overbank or abandoned channel deposits that accumulate in from stagnant pools of water during low stage channel abandonment (Miall, 1996)	Fig. 47a and 48d; 01/12/16
R	Medium to coarse, cross-bedded, indurated light grey to grey pink	Massive, rootbed closely associated with planar crossbeds (Sp)	0.4	Medium part of lower-flow regime	Proximal overbank or abandoned braided fluvial channel	Fig. 47a and 48c; sample 01/12/17

Table 11

Facies classification of the lower part of the Loriu Sandstone: Loriu Section (adapted from Miall, 1996, 2006).

Despite the differences in granulometry and presence or absence of sedimentary structures in different levels of the LOS, lithofacies recorded from the Loriu Section are all consistent with deposition in a braided fluvial system. Lithofacies Sm (massive sandstone) and Sp (horizontal bedded sandstone) are the dominant lithofacies recorded in the Loriu Section with other lithofacies appearing intermittently and normally grading into either massive sandstone (Sm). This is typical of laterally aggrading river deposits where planar cross bedded sands are deposited as 2D migrating bars within an incised river channel while the massive sandstones could represent bank collapse or channel overflow deposits (Miall, 1996). The only gravel-type lithofacies that was noted in the Loriu Section is lithofacies Gmm (massive matrix-supported conglomerate), which commonly grades up to massive sandstones. This is also consistent with the fluvial depositional environment interpretation as gravel bars commonly form in rivers as a result of high-energy flows that deposit poorly sorted clasts that are supported by an equally poorly sorted mix of sand, silt and mud. The finer grained facies type in the Loriu Section are represented by massive mudstones which occur as relatively thin centrimetric beds that could be attributed to deposition in standing pools of water during low stage channel abandonment.

6.3.1. Texture

The sediments that comprise the Loriu Section were deposited in mainly fluvial depositional environments. These environments were determined through the petrographic examination of samples from different intervals within the formation. From visual estimation, the Loriu Section is composed of basement-derived terrigenous clasts that comprise polycrystalline quartz (20-30%), monocrystalline quartz (15-20%), feldspars (5-15%), metamorphic rock fragments (5-10%) and detrital carbonate grains at the top of the formation. The textural characteristics of the Loriu Section are summarized as follows:

- Grain sizes: They range from mud to pebbles, the latter being highlighted by the presence of metamorphic rock fragments with diameters >6 mm;
- Grain shape: Angular to sub-rounded;
- Grain contacts: Floating to concavo-convex;
- Sorting: Sediments are poorly sorted overall.

The textural and compositional immaturity of the sandstone beds of the Loriu Section, suggests a short travel distance from the sediments provenance zone.

6.3.2. Detrital minerals

6.3.2.1. Polycrystalline quartz

Polycrystalline quartz (Beds 01/12/35 and 01/12/04 - Figs. 47a and 54a and b) is generally considered to be an indicator of a metamorphic source and is the most abundant detrital mineral in the Loriu Section with grains ranging between 0.01-2 mm (granules) and with the number of micro-crystals per polycrystalline grain being greater than 5 micro-crystals. Intra-crystalline contacts are almost always sutured while many of the polycrystalline quartz grains are commonly stretched and/or fractured suggestive of development under great pressure. When fractured, grain-cutting fractures are common although in few cases fracturing along intra-crystalline suture lines was noted.

6.3.2.2. Monocrystalline quartz

Monocrystalline quartz (Beds 01/12/35 and 01/12/04 - Figs. 47a and 54a and b) is subordinate only to polycrystalline quartz and the two constitute approximately between 35-50% (visual estimate) of the detrital mineral content of the Loriu Section. The monocrystalline grains range from angular to rounded and have a maximum size of ~2 mm (granules). The dominant grain size is however coarse lower to coarse upper (0.5 mm ≥X≤ 1.0 mm

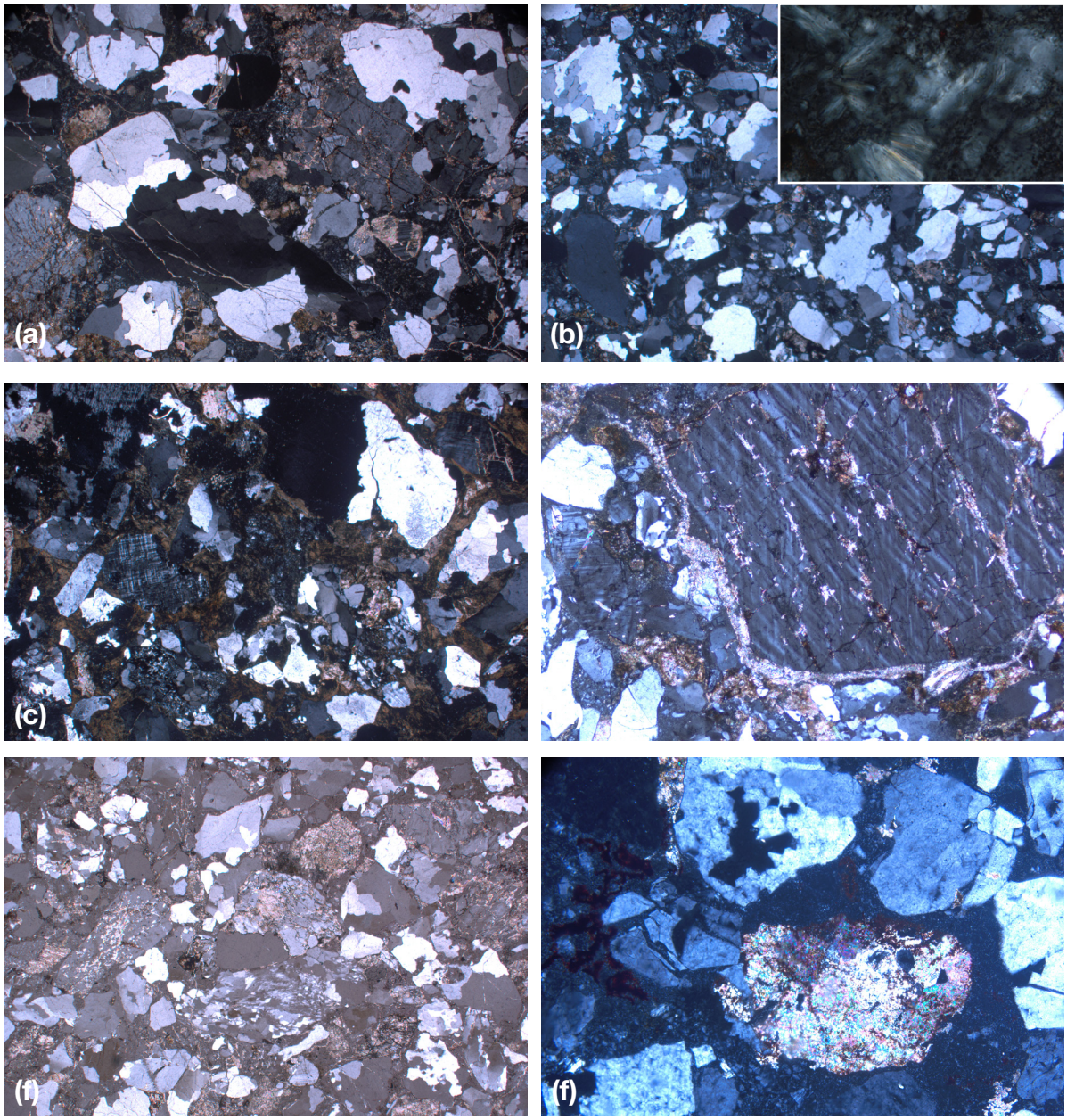

Fig. 54. *Petrographic micrographs of selected studied sandstone beds from the Loriu Section. (a) Bed 01/12/35 (Fig. 47a): Planar cross-bedded sandstone with abundant kaolinite clays. The main cement is calcite, which occurs in grain replacive (predominantly of the feldspathic component) and pore filling phases. Polycrystalline quartz is dominant in the Loriu Section and together with monocrystalline quartz. (b) (i) Bed 01/12/04 (Fig. 47a) constitute about 35 to 50% of the detrital minerals within the Loriu Section. (ii) In the same sample from bed 01/012/04, kaolinite clays are noted. (c) Bed 01/12/20 (Fig. 47a): Matrix-supported conglomerate with abundant fractured quartz and alkali feldspar floating in a hematite-rich matrix. Calcite cement is noted locally within this bed. (d) Bed 01/12/26 (Fig. 47a) is a coarse-grained sandstone floating in a largely hematite-rich matrix although calcite and kaolinite are also noted within the sample. Calcite occurs both in grain rimming and grain replacive mode, the latter being concentrated along the plagioclase grain cleavage lines. (e) Bed 01/12/44 (Fig. 47a): Matrix-supported conglomerate with abundant polycrystalline and monocrystalline quartz. The polycrystalline quartz shows evidence of stretching which is indicative of a metamorphic source. Authigenic kaolinite clays are also present. In this sample, as well as in (f), Sample 01/12/36, detrital carbonate grains are observed within which unidentified black opaque inclusions are noted. In the latter, the carbonate grain is noted to be floating in a kaolinite-rich matrix together with monocrystalline quartz grains.*

where Xmm = grain size). The quartz grains of the Loriu Section exhibit undulose extinction though few grains with uniform extinction were noted. Few of the quartz grains have been shattered as evidenced by numerous fractures within the quartz grains. Both the undulose extinction as well as the shattering are evidence of strain which could be prior or after deposition (Bed 01/12/36 - Figs. 47a and 53f).

6.3.2.3. Feldspars

Both alkali and plagioclase feldspars are noted in the samples collected from the LOS. Alkali feldspars are relatively more abundant in the Loriu Section as they are more resistant to chemical weathering in comparison to their calcic equivalents (Adams et al., 1984), and are represented mainly by microcline which is recognized through its characteristic cross-hatch twinning (Bed 01/12/20 - Figs. 47a and 54c) while plagioclase feldspars are recognized by the characteristics polysynthetic twinning (Bed 01/12/26 - Figs. 47a and 54d). The coarse grain feldspar component of the Loriu Section is significantly rimmed, altered and replaced by calcite (Fig. 54a and 54d). Feldspar grains are dominantly medium-grained but can also be found as very coarse grains (~1 mm).

6.3.2.4. Lithics, accessory minerals and matrix

Metamorphic rock fragments – MRF (Bed 01/12/44 - Figs. 47a and 54e) and other minerals such as micas (biotite) occur throughout the Loriu Section. The MRF are commonly medium grained but can also be noted in granule size. The MRF are commonly composed of quartz and feldspars. The lithics and accessories do not appear to be restricted in any bed or level of the Loriu Section except for detrital carbonate rock fragments (Bed 01/12/36 - Figs. 47a and 54f), which occur only within the two top sandstone beds of the Loriu Section. These carbonate grains are lime-mudstones and are well-rounded coarse-grained (0.5 mm in thin section) clasts, that commonly occur with minute opaque minerals inclusions

6.4. Post-depositional evolution of the Loriu Sandstone, Loriu Section

6.4.1. Matrix/authigenic components

The total matrix (cement and clays) content of the Loriu Section is approximately 15-20% visual estimate. The main authigenic components observed are clay formation (kaolin), cementation (predominantly by iron oxides and calcite) as well as compaction. Surbodinate cements such as siderite are also present in the Loriu Section. Iron oxide and calcite cements occur throughout the formation in relative amounts but always in association with kaolin. This preferential cement dominance allows for the division of the Loriu Section into four distinct cement zones, two of which are rich in hematitic cement (0 - 4 m and 20.75 - 49.25 m) and the two others are dominated by calcite cements (4 - 20.75 m and 49.25 - 78.05 m). Kaolin cements are present throughout the formation but are always subordinate to hematite and calcite.

6.4.1.1. Zone 1 (Hematite-rich)

Two iron oxide-rich intervals were noted in the Loriu Section, between 0 - 4 m and 20.75 - 49.20 m from the base of the section. These zones are characterized by the abundance of iron oxides, probably hematite, in comparison to calcite and kaolinite cement. The oxides occur as submicronic crystals within the clayey matrix of some analyzed samples, which display a dark brownish to reddish pigmentation (e.g. sample 01/12/20 - Figs. 47a and 54c). Hematite in the Loriu Section is generally pore filling but also occurs rarely in grain rimming and grain replacive phases. Where the hematite is pore filling, it is noted to grow from the pore margins to the centre of the pores. Hematite is a relatively early cement, predating compaction (small hematite “layers” are locally “squeezed” between two quartz grains showing sutured contacts. Intragranular cementation is also noted along cracks and grain fractures.

6.4.1.2. Zone 2 (Carbonate-rich)

Two zones rich in carbonate (predominantly calcite) cement are noted on the Loriu Section, between 4 - 20.75 m and 49.25 - 78.05 m from the base of the section. Carbonate cements are noted occluding intergranular pores and replacing feldspar grains. In the measured section, the poly-generational carbonate cements are also noted to be grain rimming (sample 01/12/44 - Figs. 47a and 54e).

6.4.1.3. Zone 3 (Kaolinite-rich)

In terms of distribution throughout the formation, this is the most widely distributed authigenic component in the Loriu Section as it occurs throughout the outcrop where it accounts for approximately 10-20% of the total intergranular pore-space in some of the samples (sample 01/12/35 - Figs. 47a and 54b and b-ii). Platy kaolin occurs commonly with detrital clays and leached feldspars suggestive of the alteration of detrital clays and dissolution of feldspars to be replaced by kaolin. Kaolin also occurs commonly as pore-filling cement forming within pores in association with other cements such as iron oxides and carbonates.

ZONE 1	EARLY	LATE
Hematite cementation		
Compaction		
Calcite cementation		
Hematite cementation		
Kaolin cementation		
ZONE 2	**EARLY**	**LATE**
Hematite cementation		
Compaction		
Calcite cementation		
Kaolin cementation		
Feldspar dissolution		
Calcite cementation		
Zone 3	**EARLY**	**LATE**
Hematite cementation		
Compaction		
Kaolin cementation		
Feldspar dissolution		
Calcite cementation		
Zone 4	**EARLY**	**LATE**
Kaolin cementation		
Compaction		
Calcite cementation		
Feldspar dissolution		
Calcite cementation		

Table 11
The paragenetic sequence with the four main diagenetic zones in the Loriu Section. Zone 1 represents the bottom 4 m, Zone 2 represents the section between 4 to 20.75 m, Zone 3 represents the section between 20.75 m to 49.25 m, and Zone 4 represents the section between 49.25 m and 78.05 m. Relative timing and duration of the various events is indicated by the position within the early and late domain. Bold lines within the time domain represent high levels of certainity (e.g. there is a high level of confidence that hematite was the first cement to form in Zone 1) while thin lines indicate high levels of uncertainty (e.g. kaolin appears to be the first cement to have formed in zone four but this cannot be confirmed owing to the lack of continuous kaolinite rims around all grains and local calcite rimming cements).

6.4.2. Chronology of diagenetic events

The early post-depositional development of the three lowermost diagenetic intervals – 0 - 4 m; 4 - 20.75 m and 20.75 - 49.20 m - of the Loriu Section are similar starting off with hematite cementation followed by sediment compaction. In the lowermost zone (0 - 4 m), this compaction is followed by calcite cementation, which is later followed by hematite cementation and finally kaolin precipitation. In the second zone (Zone 2; 4 - 20.75 m), compaction is followed by cementation by calcite and kaolin, which precedes feldspar dissolution. It is in the newly created feldspathic intragranular pores that second generation calcite is precipitated. The third diagenetic zone (Zone 3; 20.75 - 49.20 m) is very similar to Zone 2 with the exception that the first phase of calcite cementation is absent. In the fourth diagenetic zone, kaolin is first to be precipitated in the pore spaces. This is followed by sediment compaction that is followed by two phases of calcite precipitation that are separated by a period of feldspar dissolution. The first generation of calcite cement is therefore principally located in the intergranular pore spaces, while the second generation of calcite cement is observed mostly in the intragranular feldspar pore spaces.

6.4.3. Porosity

The porosity of the Loriu Section ranges from negligible to good (0-2%), a consequence of porosity reduction from the original pore space at deposition, by detrital clays (sample 01/12/04 - Figs. 47a and 55a), as well as associated post-depositional modification predominantly in form of hematite and carbonate cement precipitation and sediment compaction as evidenced by the long contact between the quartz grains. Moreover within the Loriu Section, porosity is depth dependent and decreases with corresponding increase in depth a consequence of sediment compaction (long to sutured contacts become more apparent with depth). Sparse intragranular (secondary porosity) is noted mainly with the feldspathic component of the Loriu Section. Within quartz grain, secondary porosity is recognized within the fractures many of which are occluded by carbonate cements that is partially dissolved (sample 01/12/12 - Figs. 47a and 55b). Microporosity is observed in some of the feldspathic grains and is a result of alteration and dissolution (Fig. 55b). In clay-rich lithotypes, microporosity between clay platelets is also inferred, but it is optically irresolvable under polarizing microscopy. Porosity generally increases with a reduction in burial depth. However, it has been observed that there is a corresponding increase in the amount of clay and cements with reduction in depth, which results in an overall reduced formation porosity (sample 01/12/38 - Figs. 47a and 55c and d). Intergranular porosity when observed is poor and is largely confined to the upper fringes of the section (sample 01/12/42 – Figs. 47a and 55e) Permeability, similar to the KAF and KF is considered to be poor to very poor as pores, when observed appear to be sparse and isolated. Owing to the generally poor porosity and inferred poor permeability, the reservoir quality risk assessment for equivalent subsurface sediments is thereby thought to be high (Type 1, tight depositional facies, sensu Tobin, 1997; Table 6), unless fracturing or burial dissolution processes in equivalent subsurface sediments can be predicted.

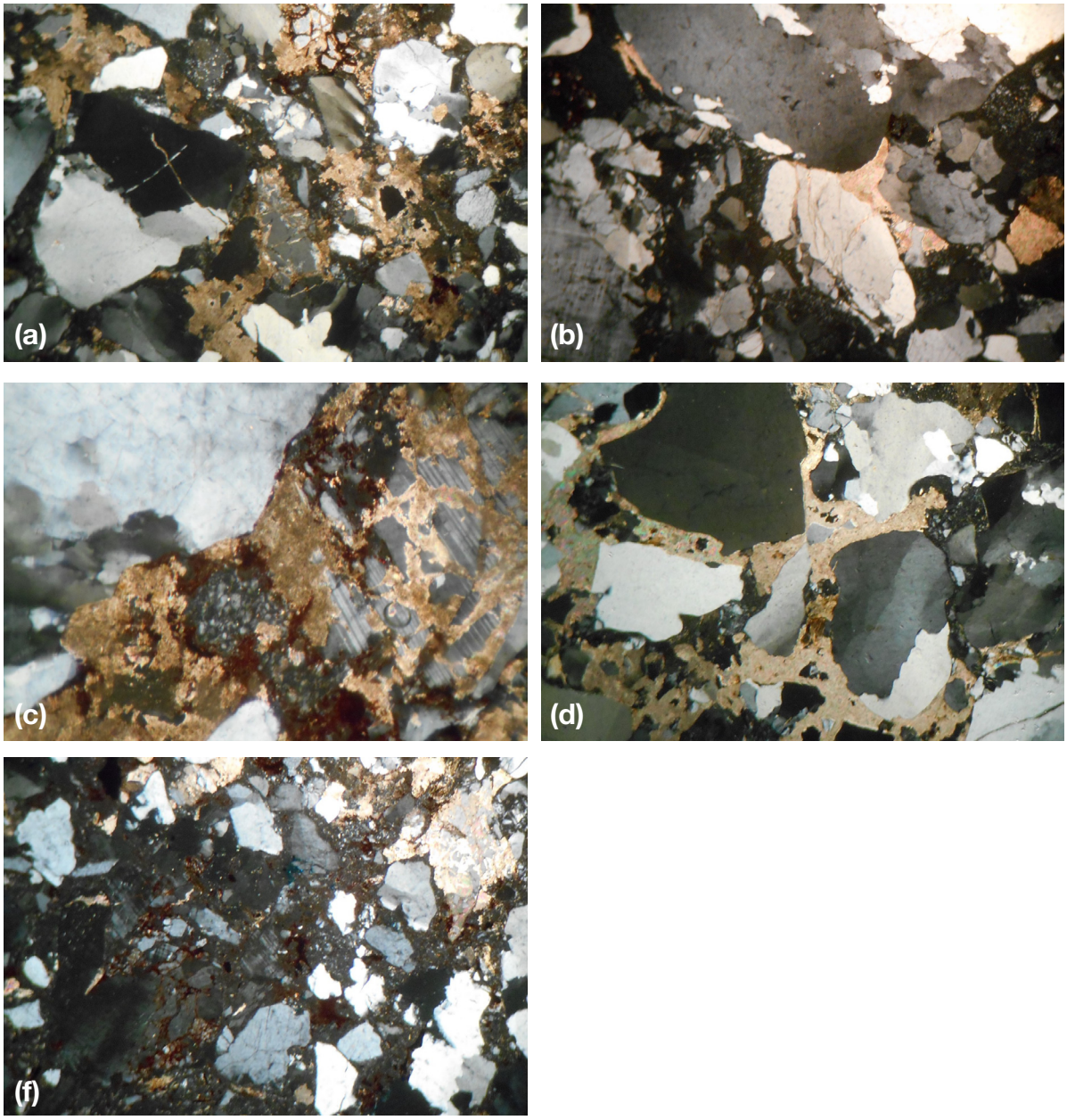

Fig. 55 *Micrographs showing the nature of porosity system in the Loriu Section. (a) Sample representing bed 01/12/02b collected from the base of the Loriu section (Fig. 47a) is hematite cemented, poorly sorted granular arenite (feldspathic), with sparse fracture-occluding calcite and no visible porosity. (b) Sample from bed 01/12/12 shows an argillaceous, poorly sorted sublithic-subfeldspathic arenite with isolated secondary dissolution pores (Sp), likely due to the dissolution of feldspars. The overall reservoir potential is poor. (c and d) Sample representing bed 01/12/37 shows a pebbly arenite to paraconglomerate with common clays (also authigenic kaolinite booklets) and grain replacive to pore filling calcite (Ca). Porosity/reservoir potential is poor overall. (e) Sample from bed 01/12/42 shows a wacke to microconglomerate with abundant clays and grain replacive to pore filling brownish siderite (Si) cement. The porosity is very poor.*

Facies code	Lithology	Sedimentary structures	Bed Thickness (m)	Depositional processes	Interpretation	Figures
Gmm	Massive, graded, matrix-supported conglomerate, mainly constituted of quartz and metamorphic rock fragments and rounded to sub-angular mud clasts floating in coarse sandy matrix	Strongly erosive lower boundary	Maximum ~ 4.0	Non-tractional deposition by high strength viscous plastic debris flow (Miall, 1996)	Sub-aerial plastic debris flow	Figs. 47b and 49f; Bed 02/12/18
Sm	Massive, ungraded, poorly sorted, medium- to very coarse-grained sandstone. Purple to buff brown in colour	Commonly contains conglomeratic lenses	0.8 - 4.0	Sub-aerial hyperconcentrated flows or sediment gravity flows (Miall, 1978; 1996)	Rapid suspension fallout from sedimentary gravity flows	Figs. 47b and 49a; Beds 02/12/09, 02/12/13
Sh	Coarse to pebbly, bedded, buff grey to purplish grey sandstone	Horizontal bedding	2	Medium part of lower-flow regime (Miall, 1978)	Suspension fallout from slow moving fluvial systems during initial sand bed movement	Figs. 47b and 49e; Bed 02/12/17
Fm	Mudstone, light grey to purple	Massive, indurated, heavily bioturbated (*N. bowni*) (Smith et al., 2008a)	1	Deposition from suspension	Overbank or abandoned channel deposits that accumulate in from stagnant pools of water during low stage channel abandonment. (Miall, 1996). Post-depositional modification through biological processes, e.g. intense burrowing and root growth	Figs. 47b and 49c; Beds 02/12/07 and 02/12/08
R	Medium- to coarse-grained sandstone, purple grey to buff brown	Root beds with ~5 cm diameter roots	0.6	Medium part of lower-flow regime	Proximal overbank or abandoned braided fluvial channel	Figs. 47b and 49b; Beds 02/12/02 and 02/12/09b

Table 12

Facies classification of the Kangabeiye Section (adapted from Miall, 1996, 2006).

6.5. Facies analysis, depositional processes and environments of the Kangabeiye Section

The depositional environments of the Kangabeiye Section were determined through the study of the lithology, sedimentary structures and facies associations. Thin sections as well as hand specimens of samples collected from the section were analysed to determine the mineralogical composition as well as the authigenic and diagenetic constitution of the section. From an analysis of the structural make-up, grain size and colour variation within the Kangabeiye Section, a total of 5 different lithofacies were identified whose characteristics are summarized in Table 12. Similar to previous sections, the facies code employed is adapted from Miall (1996, 2006).

The lithofacies recorded in the Kangabeiye Section, similar to those described above for the Loriu Section, are consistent with deposition in a largely fluvial depositional environment. Lithofacies Sm (massive sandstone) and Fm (fine-grained massive mudstone) are the main lithofacies recorded in the Kangabeiye Section where they could form through bank collapse and from the deposition in standing pools of water respectively. As part of the fine grained massive sandstone, biotubation has greatly affected these fine-grained beds as discussed in Section 6.1.2. These Adhesive Meniscate Burrows (AMB) - Naktodemasis bowni (Smith et al., 2008a) are considered to represent low stage channel abandonment and subsequent exposure that is associated with pedogenic modification under moderately to well-drained soil conditions. The matrix-supported, fining-up conglomerate (lithofacies Gmm) noted at the top of the Kangabeiye Section is also consistent with the interpretation of a fluvial depositional environment interpretation where such matrix-supported conglomerates form as a result of high-energy flows that deposit poorly sorted clasts that are supported by an equally poorly sorted mix of sand, silt and mud.

6.5.1. Texture

From visual estimation, the Kangabeiye Section is composed of basement-derived terrigenous clasts that comprise monocrystalline quartz (30-40%), polycrystalline quartz (10-15%), feldspars (5-10%), metamorphic rock fragments and detrital carbonate grains. The textural characteristics of the Kangabeiye Section are summarized as follows:

- Grain sizes: They range from silt to very coarse sand;
- Grain shape: Angular to sub-rounded;
- Grain contacts: Floating to point and locally long;
- Sorting: Sediments are poorly sorted overall.

Similar to the Kimwarer Formation, the textural and compositional immaturity of the Kangabeiye Section suggests a short travel distance from the sediment provenance zone.

6.5.2. Detrital minerals

6.5.2.1. Monocrystalline quartz

Monocrystalline quartz range from angular to sub-rounded and have a maximum size of ~2 mm (granules). The dominant grain size is however coarse lower to coarse upper (0.5 mm ≥X≤ 1.0 mm where Xmm = grain size). The quartz grains of the Kangabeiye Section, similar to those of the Loriu Section exhibit undulose extinction though few grains with uniform extinction were noted. Few of the quartz grains have been shattered (Bed 02/12/06 – Figs. 47b and 56a) as evidenced by numerous fractures within the quartz grains. Both the undulose extinction as well as the shattering are evidence of strain prior or after deposition.

6.5.2.2. Polycrystalline quartz

Unlike the Loriu Section, polycrystalline quartz, which is generally considered to be an indicator of a metamorphic source, is subordinate in terms of abundance to monocrystalline quartz. The two however constitute approximately between 40-55% (visual estimate) of the detrital mineral content of the Kangabeiye Section. The polycrystalline quartz grains are also smaller ranging between 0.01-1 mm and with the number of micro-crystals per polycrystalline grain however remaining greater than 5 micro-crystals. Intra-crystalline contacts are almost always sutured. When fractured, cement infilled fractures follow intra-crystalline suture lines as noted in thin section analysis of sample (Bed 02/12/06 – Figs. 47b and 56a).

6.5.2.3. Feldspars

The feldspathic component of the Kangabeiye Section is highly weathered. However, both alkali and plagioclase feldspars were noted in the samples collected. Alkali feldspars are relatively more abundant in the LOS as they are more resistant to chemical weathering in comparison to their calcic equivalents (Adams et al., 1984), and are represented mainly by microcline which is recognized through its characteristic cross-hatch twinning (Bed 02/12/03 - Figs. 47b and 56b) while plagioclase feldspars, (though heavily weathered) are recognized by their characteristic polysynthetic twinning (Bed 02/12/05 - Fig. 47b and 56c). Feldspar grains are mainly medium-grained.

6.5.2.4. Lithics, accessory minerals and matrix

MRFs' are rare within the Kangabeiye Section as are other accessory minerals such as biotite that was only noted in one sample (Bed 02/12/13 – Figs. 47b and 56d). Similar to the Loriu Section is the presence of detrital carbonate grains that are noted in some of the samples collected from the Kangabeiye Section (Bed 02/12/14 – Figs. 47b and 56e). Also similar to the detrital carbonate clasts noted in the Loriu Section, the carbonate grains in the Kangabeiye Section are well rounded, fractured lime-mudstones, which are 0.5 mm in thin section.

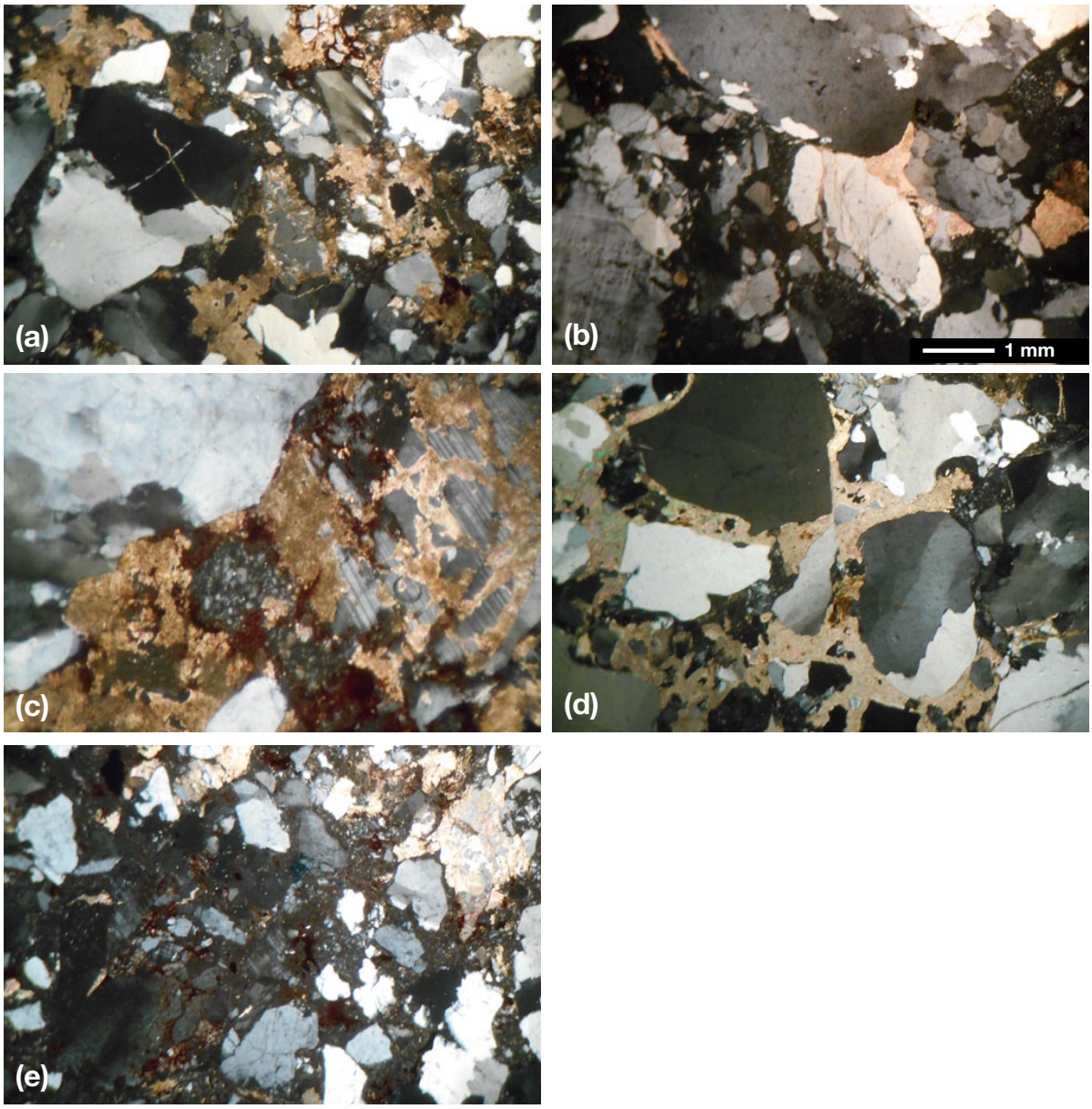

Fig. 56. *Thin sections photomicrographs of selected studied sandstones from the Kangabeiye Section. (a) Sample representing bed 02/12/06 (Fig. 47b) showing both polycrystalline and monocrystalline quartz. The monocrystalline grains show strong undulose extinction suggestive of a metamorphic origin. Also noted is the abundant calcite cementation both in pore filling and grain rimming phase. Calcite cement also fills out fractures in the quartz grains. (b) Sample representing bed 02/12/03 showing calcite cement in grain rimming and pore filling phase. Also noted in this sample is kaolinite clay which also exists in pore filling phase. Locally, calcite cement is noted in grain replacive phase in the alkali-feldspar grain in the bottom left of the figure. Calcite here is concentrated along the cleavage lines of the feldspar grain. (c) Calcite cement replacement of a plagioclase feldspar grain. Calcite is also noted in grain rimming mode with respect to the larger quartz grain on the top right of the image. (d) Sample representing bed 02/12/13 showing monocrystalline quartz crystals floating in a calcite rich matrix spotted with local kaolinite clays. (e) Sample representing bed 02/12/14 showing abundant quartz and feldspars floating in a clay-rich (kaolinite) matrix.*

6.6. Post-depositional evolution of the Kangabeiye Section

6.6.1. Matrix/authigenic components

The total matrix (mainly detrital mud and authigenic cement) content of the Kangabeiye Section is approximately 20-25% (visual estimate) the bulk of which is composed of clays of uncertain composition. The main authigenic components observed are kaolinite booklets and vermicules and other cements (predominantly calcite and to some extent iron oxides). Subordinate cements such as siderite are also present in the Kangabeiye Section but owing to their relatively minor quantity, they are not discussed further. The relative abundance of calcite cement and kaolin clay dominance has allowed us to distinguish two main zones of the development of authigenic minerals within the Kangabeiye Section.

6.6.1.1. Zone 1 (Calcite-rich)

Between 0 to 23.5 m from the base of the Kangabeiye Section, calcite cement is dominant. Calcite is noted as grain rimming, pore filling and grain replacive phases the latter being confined to replacement of feldspar grains. In some cases the replacement of the feldspar grains is so advanced that it is difficult to determine the feldspathic composition (e.g. Bed 02/12/05 – Figs. 47b and 56c). Calcite is generally to be an early cement predating all other cements and clays in this section as it rims grains the bulk of the detrital components in this interval of the section. However, calcite may also locally post-date mechanical compaction as it is also noted to occlude thin fractures cutting quartz grains (Bed 02/12/06 – Figs. 47b and 56a).

6.6.1.2. Zone 2 (Kaolinite rich)

This zone is characterized by the abundance of kaolinite clays, in comparison to calcite and hematite cements. Platy kaolinite occurs commonly with detrital clays and leached feldspars suggestive of the alteration of detrital clays and feldspars into kaolinite. In the Kangabeiye Section, kaolinite is also a common pore-filling noted filling primary and secondary pores and it also occurs together with calcite and to some extent iron oxide cements (Bed 02/12/14 – Figs. 47b and 56e).

6.6.2. Chronology of main diagenetic events

The early post-depositional event of the lowermost diagenetic interval (0-23.5 m) of the Kangabeiye Section starts off with the precipitation of calcite cement, which forms the dominant grain rimming/pore filling cementation phase in this interval. There is evidence of moderate compaction in this diagenetic zone as some samples are moderately packed, with most of the contacts being long. A few sutured contacts were noted overall. This compaction phase was followed by feldspar dissolution and finally kaolinite precipitation. Similar to the Loriu Section, a second phase of calcite cement is precipitated in the newly created intragranular and moldic pores linked to the partial or complete dissolution of feldspar grains. In the third diagenetic zone (23.5-70 m) kaolinite seems to be relatively more abundant and also associated with hematite and calcite. Summarizing paragenetic sequences of diagenetic events are reported hereinafter (Table 14).

6.6.3. Porosity

The porosity within the Kangabeiye Section ranges from negligible to moderate (0 to 5%), a consequence of porosity reduction from the original pore space at deposition, by detrital clays (Bed 02/12/02 - Figs. 47b and 57a), as well as associated post-depositional modification predominantly in form of kaolinite, calcite and hematite cement precipitation. Sediment compaction was also noted in the Kangabeiye Section giving rise to long

ZONE 1	EARLY	LATE
Calcite cementation		
Compaction		
Hematite cementation		
Kaolinite precipitation		
Feldspar dissolution		
Zone 2	**EARLY**	**LATE**
Kaolinite precipitation		
Calcite cementation		
Hematite cementation		
Feldspar dissolution		

Table 14. *The paragenetic sequence of the two main diagenetic zones in the Kangabeiye Section. Zone 1 represents the bottom 23.5 m and Zone 2 represents the section between 23.5 m to 70 m. Relative timing and duration of the various events is indicated by the position within the early and late domain. Bold lines within the time domain represent high levels of certainty (e.g. there is a high level of confidence that calcite was the first cement to form in Zone 1) while thin lines indicate high levels of uncertainty (e.g. feldspar dissolution appears to be the last diagenetic process in Zone 2 but this cannot be confirmed as kaolinite partially rims some grains in the diagenetic interval.*

grain contacts. This however does not appear to be a major control on porosity within this section of the Loriu Sandstone as the bulk of the porous (primary porosity) beds are concentrated in the lower half of the Kangabeiye Section (samples 02/12/03, 02/12/08 and 02/12/09; Fig. 47b). Intragranular/moldic porosity (secondary porosity) is also noted in the dissolved feldspars of the Kangabeiye Section (Bed 02/12/03; Figs. 47b and 57b). Secondary porosity in form of fractures is also noted in the clay-rich lithotypes (Bed 02/12/08 – Figs. 47b and 57c) while microporosity between clay platelets is also inferred, but it is optically irresolvable under polarising microscopy. Permeability, is considered to be poor to very poor as pores, when observed are sparse and isolated. Owing to the generally poor porosity and inferred poor permeability, the reservoir quality risk assessment for equivalent subsurface sediments is thereby thought to be high (Type 1, tight depositional facies, sensu Tobin, 1997; Table 6), unless fracturing or burial dissolution processes in equivalent subsurface sediments can be predicted.

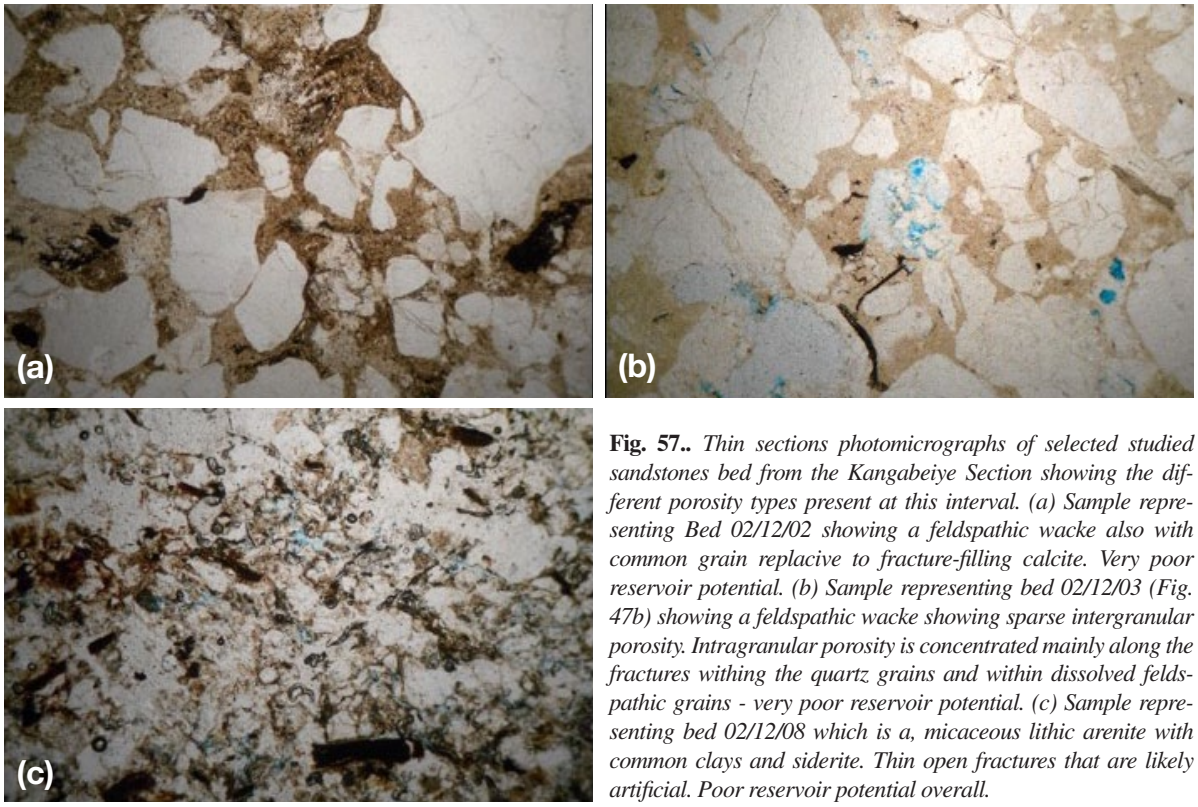

Fig. 57.. *Thin sections photomicrographs of selected studied sandstones bed from the Kangabeiye Section showing the different porosity types present at this interval. (a) Sample representing Bed 02/12/02 showing a feldspathic wacke also with common grain replacive to fracture-filling calcite. Very poor reservoir potential. (b) Sample representing bed 02/12/03 (Fig. 47b) showing a feldspathic wacke showing sparse intergranular porosity. Intragranular porosity is concentrated mainly along the fractures withing the quartz grains and within dissolved feldspathic grains - very poor reservoir potential. (c) Sample representing bed 02/12/08 which is a, micaceous lithic arenite with common clays and siderite. Thin open fractures that are likely artificial. Poor reservoir potential overall.*

6.7. Discussion

The main components of the Loriu Section are quartz (50%), feldspar (15%) MRF (10%) and detrital mud (>15%) (visual observation) which are sourced from a proximal, highly deformed metamorphic basement provenance zone as well as from a distal source indicated by the texturally mixed character of the detrital component of the sandstone units collected from the Loriu Section. These include large angular to sub-rounded grains and a smaller fraction of fine, well rounded quartz grains. These two systems can be attributed to fluvial systems laterally draining the flanks of uplifted rift shoulders flowing into axial, morpho-tectonic rivers. Towards the top of the Loriu Section, detrital carbonate grains are noted (sample 01/12/36; Fig. 54f). These could be a result of clastic input of allochotonous carbonate particles derived from the drainage basin or could be indicative of inorganic precipitation of generally associated with photosynthetic activities of plants following the development of shallow water accumulations or small lakes within the drainage area (Talbot et al., 1978). Whichever the case, it can be assumed that at one point, during the emplacement of the sandstone beds that comprise the Loriu Section, lacustrine systems within the basin drainage area existed and prevailing climatic and basin conditions allowed for the sustenance of such systems. From the data available, it is not possible to distinguish exactly the prevailing climatic conditions however, it is possible to assume a more humid climatic condition which would be in line with previous studies that indicate the regional climatic condition prevailing in East Africa during the Burdigalian (18.5 Ma), similar to the modern Central African rainforest where rainfall exceeds 1000 mm/year and which also has a well-defined dry season (Vincens et al., 2006). Such climatic conditions would then have allowed for the development of small to large paleolakes within the North Kerio Basin.

Within the sandstone beds of the Loriu Section, the few intercalated mudstone facies (Beds 01/12/16 and 01/12/24 – Fig. 47a) are indicative of deposition by low energy fluvial systems probably in the overbank depositional environments or abandoned channels. The relative thinness of the muddy units and the subsequent re-

sumption of coarse grained deposition within the larger context of the LOS has connotations of climatic controlled modification of depositional patterns such as short-lived reduction in the amount of rainfall that in turn affects the transmissive capacity of fluvial systems.

Arkosic sandstones generally have porosity levels as high as 40% (Selley, 1978). Within the Loriu Section, the overall porosity is significantly downgraded by the presence of detrital clays, authigenic cements, as well as by compaction. The high amount of mud in poorly sorted sediments is believed to be a consequence of mixed load transportation common in high-energy fluvial systems that are proximal to the source and which did not allow for the depositional segregation of sediments into different granulometric classes. Continued sediment loading increased the overburden on the underlying sediments that led to grain shattering and pressure solution which has further decreased (and in most cases, totally obliterated) the porosity of the lowermost sediments.

Cements such as hematite and carbonates are very important within the Loriu Section and are believed to have started forming immediately after deposition of the beds that constitute the Loriu Section. Hematite is the first cement to develop within the Loriu Section and is believed to be a result of precipitation at or near the ground surface immediately after deposition by Fe-enriched fluids that are due to the dissolution of iron-rich minerals. Calcite cement is also considered to be a result of shallow circulating fluids that contain dissolved carbon that could be derived from the decay of plant remains within soil horizons and from atmospheric CO2. Calcretes commonly develop in fluvial channel sandstones and are dominant in the coarse grained proximal facies. Sources of calcium for calcretes in the Loriu Section includes windblown dust or groundwater which brings carbonate ions from carbonate terrains to siliclastic sequences, rainwater and dissolution of Ca-plagioclase (Morad, 1998) which are abundant in the Loriu Section. The numerous dykes that cut across the LOS could also be a potential source of calcium cement (e.g. Thuo, 2009). Their alteration by late magmatic fluids or most probably by diagenetic fluid circulations activated by the thermal effect of this magmatic phase could mobilize calcium by intensive alteration of magmatic minerals (Daoudi et al., 2002).

Ideally therefore, the lowermost interval of the LOS, which is represented by the Loriu Section, should have moderate (and possibly good) reservoir potential if the porosity noted in this work is extrapolated to the subsurface equivalent that are inferred from previously acquired seismic data collected from the North Kerio Basin. These porosities are depth dependent rising from 2% at the base of both the Loriu Section up to 10% (visual estimate) at the very top of the formation (Fig. 47a). In extension thereby, it can be assumed that the porosities recorded in the lower portion of the Loriu Sandstone that is represented by the Loriu Sections can only increase upwards along the infill of the North Kerio Basin, implying good porosity levels are expected higher up the stratigraphy. Moreover, the diagenetic composition of the Loriu Section appears to be linked to hydrological processes that leach of minerals from surficial rocks and precipitate them as the waters percolate and infiltrate subsurface formations. Consequently, this could translate to a retention of porosity by the deeper equivalents of the LOS outcrop, which might be less affected by the diagenetic modifications noted on outcrop.

From field observations, the Kangabeiye Section is considered as stratigraphically higher than the Loriu Section. The main components of the Kangabeiye Section include monocrystalline quartz (30-40%), polycrystalline quartz (10-15%), feldspars (5-10%), metamorphic rock fragments and detrital carbonate grains. Similar to the Loriu Section, these are sourced from both a proximal metamorphic basement provenance zone as well as from a distal source indicated by the texturally mixed character of the detrital component of the sandstone units collected from the Kangabeiye Section. This is similar to our earlier interpretation of the lower Loriu Section that is also characterized by sediments derived from a proximal and distal source and can be attributed to fluvial systems laterally draining the flanks of uplifted rift shoulders flowing into axial, morphotectonic rivers. The Kangabeiye Section however has more abandoned channels or floodplain intervals that are heavily bioturbated and which show evidence of pedogenesis. This suggests a general reduction in fluvial strength of drainage systems within the North Kerio Basin with time as the granulometric composition of the stratigraphically lower Loriu

Section is characteristic of high-energy fluvial systems while that of the Kangabeiye Section is characteristic of deposition from weaker traction currents and deposition from suspension for the mudstone facies. Rootmarks are also common in the Kangabeiye Section indicative of a well-established vegetation system. This ties well with our previous assumption of a relatively wet climatic condition (where rainfall exceeds 1000 mm/year) and which has a well-defined dry season.

Despite the high porosities normally recorded in arkosic sandstones (Selley, 1978), the porosity within the Kangabeiye Section of the LOS is significantly downgraded by the presence of both detrital clays as well as authigenic cements. In fact the bulk of the Kangabeiye Section should be considered as feldspathic wacke (>15% matrix and < 90% quartz – Dott's classification of terrigeneous sandstone) as opposed to an arkosic arenite. Although compaction was locally noted, it does not play a significant role in porosity reduction as it does in the Loriu Section, as the Kangabeiye Section is stratigraphically higher than the Loriu Section. The high amount of detrital mud within the Kangabeiye Section can be assumed to be a result of mixed sediment source, one being proximal, depositing laterally derived sediments from across the main bounding fault, while the other was depositing distally derived sediments morpho-tectonically oriented fluvial systems similar to the modern Kerio River in the Central Kenya Rift. Samples collected from the Kangabeiye Section also show the authigenic content of the section is majorly calcite cement and kaolinite clays. In the lower section (0-4 m), the dominant cement is calcite, which could be a result of shallow circulating fluids that contain dissolved carbon derived from plant decay within soil horizons and from atmospheric CO2. Calcretes commonly develop in fluvial channel sandstones and are dominant in the coarse grained proximal facies. Sources of calcium for calcretes in the Kangabeiye Section include windblown dust or groundwater which brings carbonate ions from carbonate terrains to siliclastic sequences and rainwater and dissolution of Ca-plagioclase (Morad, 1998). Similar to the stratigraphically lower Loriu Section, the volcanic dykes that cut across the LOS could also be the origin of calcium cement. Their alteration by late magmatic fluids or most probably by diagenetic fluid circulations activated by the thermal effect of this magmatic phase could mobilize calcium ions by the alteration of volcanic minerals (Daoudi et al., 2002; Thuo, 2009).

The high amount of authigenic cements and clays as well as detrital mud are the main cause of low porosity levels within the Kangabeiye Section of the LOS. These have relegated the Kangabeiye Section to an average range of between 2-5%. However, similar to the Loriu Section that is discussed above, a subsurface equivalent of the Kangabeiye Section could have better reservoir porosity (possibly moderate to good porosity) as the diagenetic composition of the Kangabeiye Section is linked to hydrological processes that leach of minerals from surficial rocks and precipitate them as the waters percolate and infiltrate subsurface formations. Consequently, this could translate to a retention of porosity by the deeper equivalents of the LOS outcrop, which might be less affected by the diagenetic modifications noted on outcrop

.

6.8. Conclusion

While the entire stratigraphy of the ~610-m thick Loriu Sandstone has not been fully recorded in this study, this work presents the first detailed sedimentological study of the lowermost portions of the Loriu Sandstone. Additional work is required to fully understand the basin infill considering the size and structural characteristics of the North Kerio Basin. Chronostratigraphically however, this work has determined a new minimum age for the Loriu Sandstone, which we have fixed at ca. 18.5 Ma. This is the earliest depositional age that has been determined for the North Kerio Basin, being slightly older than those presented by Wescott et al. (1993) (ca. 14.7 Ma) for dykes in the North Kerio Basin. The age is also older than recently published ages for dykes in the adjacent Lokichar Basin that ranged between ca. 17-13 Ma (Tiercelin et al., 2004). However, the age of the dyke as determined in this work is consistent with previous work that suggest that a major volcanic event that affected both the northern and central Kenya Rift System took place between 23 and 14 Ma; Samburu Basalts dated 23–16

Ma; Shackleton, 1946; Turkana Volcanics dated 23–14 Ma; Thuo, 2009 Baker et al., 1972; Joubert, 1966; Walsh and Dodson, 1969. With regard to the North Kerio Basin infill, this suggests that the basin lowermost sedimentary basin infill that comprises of the LOS formation was emplaced prior to the dykes intrusion (Burdigalian times) which can therby be put forth as the minimum age of the LOS.

The two studied sections, the Loriu Section, and the Kangabeiye Section, are composed predominantly of braided fluvial channel deposits with few intercalated overbank fines (more present in the Kangabeiye Section) that can be attributed to either local climatic changes or basin structural modifications that affected drainage depositional patterns leading to progressively lower energy drainage systems higher up the LOS stratigraphic column. The diagenetic study of the Loriu Section has shown that the cement material changes from dominant hematite at the base (0m - 4 m) and (20.75m - 49.20 m) to calcite at (4m - 20.75 m) and (49.20m - 78.05 m). For the Kangabeiye Section, calcite cement is dominant between 0m and 23.5 m in the section, while kaolinite clays are dominant between 23.5 m and 70 m. In both sections, these cementation episodes occur during early diagenesis in low temperature conditions (<80 °C). In the Loriu Section, significant mechanical compaction was additionally observed and the combined effects of cementation and compaction have led to a reduction in porosity to approximately 10% (visual estimate). The sediments of the Kangabeiye Section are characterized by a higher detrital mud content. The resulting porosity levels recorded in this level are thereby considerably lower (negligible to 5%), the bulk of which is attributed to the dissolution of feldspar grains.

Overall however, it is believed that as the cementation is a major pore-reducing factor in the LOS, the subsurface equivalents of the outcrop could have moderate to good porosity as the cements noted on outcrop are all linked to surficial hydrological processes, which might not have affected deeper-seated sediments within the basin. A detailed study of those sections that have not been covered in this work and possibly equivalent sections to those studied but are deeply buried is strongly recommended and envisaged as a follow-up to this study in future. Wescott et al. (1993) proposed that Lokichar-type shales possibly extended further eastwards into the North Kerio Basin, over the barrier that was posed by the Lokone Horst. These sediments were not recorded in the course of these studies and should also form the basis of future works with specific interest in their potential as hydrocarbon source units.

.

7. Discussion: The Reservoir Potential of the "Turkana Grits" of Central and Northern Kenya Rifts

The discovery of commercially viable, classical rift basin hydrocarbon accumulations in both the Albertine Graben on the western branch of the EARS in Uganda, and the Lokichar Basin in the eastern branch of EARS in Kenya, has culminated in unprecedented hydrocarbon exploration in the East Africa Rift System. To date (December, 2014), seven successful wells have been drilled in the Lokichar Basin since the first discovery was made in 2012 through the Ngamia-1 exploration well (Appendix 5). These discoveries, all of which have been made by the British exploration company Tullow Oil PLC and its main partner Africa Oil Corporation, have catapulted the Lokichar Basin to the realm of a 'Giant Oil Field' as defined by Mann (2003), having an estimated resource base of over 600 MMbbl of oil (Africa Oil Corporation, 2014).

Exploratory tests of the potential hydrocarbon play types within a rift basin have revealed the dominance of 'border fault plays' and have also pointed to the existence of 'rift flank plays' as evidenced most recently through the drilling of the Etuko-1 and Ewoi-1 exploration wells (Table. 15). The 'border fault plays' within the Lokichar Basin are all characterized by having three way dip closures along the main rift bounding fault, i.e. the Lokichar Fault, and similar stratigraphic configurations, albeit slight variations in stratigraphic thickness of different formations within the different wells. In the Ngamia-1/1A well, which was the first major discovery well in the

Name	*Announcement date*	*Total depth (m)*	*Net Pay (m)*	*Block*	*Basin*	*Play type*	*Test Results*
Ngamia-1	July 4, 2012	2,340	Auwerwer - 200 Lower Lokhone - 43	10BB	North Lokichar	Tertiary	3,200 bopd (5,400 bopd with optimised equipment)
Twiga South-1	November 26, 2012	3,250	Auwerwer - 30 Lower Lokhone - 796 (gross)	13T	North Lokichar	Tertiary	2,812 bopd (5,200 bopd with optimised equipment)
Etuko-1 and Etuko-2 Sidetrack	May 13, 2013	3,100 Etuko-2	Auwerwer - 200 potential Lower Lokhone - 50+	10BB	Eastern Flank of Lokichar Basin	Tertiary	550 bopd
Ekales-1	July 24, 2013	2,554	Auwerwer - 41	13T	Lokichar	Tertiary	1,000 bopd
Agete-1	Sep 26, 2013	1,930	Auwerwer - 100	13T	Lokichar	Tertiary	Pending
Amosing-1	Nov 22, 2013	2,351	Auwerwer btwn 160 to 200 m	10BB	Lokichar	Tertiary	Pending
Ewoi-1	Nov 22, 2013	1,911	Auwerwer - btwn 20 to 80 m	13T	Eastern Flank of Lokichar Basin	Tertiary	Pending

Table 15.

Deep wells drilled and proposed in the Lokichar Basin as at 25th April 2005 (Africa Oil Corporation, 2014).

Lokichar Basin and whose characterization can be considered as being representative of the 'border fault plays' in the Lokichar Basin, hydrocarbon discoveries have been made between 858 m and 1330 m, in an interval referred to as the 'Lower Auwerwer Sandstone'. In the Loperot-1 well, oil shows were noted in the section between 949 m and 2547 m in an interval referred to as the 'Lokone Sandstone', which is stratigraphically lower than the 'Lower Auwerwer Sandstone'. The existing model for the sedimentary component of the Lokichar Basin is that it consists of two sedimentary formations, a lower fully basement-derived sandstone formation called the 'Lokone Sandstone' and an upper sandstone formation called the 'Auwerwer Sandstone', which comprises two distinct lithologies: the 'Lower Auwerwer Sandstone', which is predominantly basement-derived and sits directly above the 'Lokone Sandstone', and the 'Upper Auwerwer Sandstone', which is lithologically characterized by a strong volcanic character (Tiercelin et al., 2004).

In the Ngamia-1 well, the prospects' seal is the mid-Miocene shale unit that is referred to as the mid-Auwerwer Shale (which is explained in greater detail in the subsequent Section 7.1. The 'Lokone Sandstone', Lokichar Basin: the best hydrocarbon reservoir in the Kenya Rift?) (Tullow Oil, 2012). This shale unit is assumed to form a basin-wide seal although additional appraisal wells are required to confirm the lateral extent of this unit. Currently, appraisal drilling (Table 15) and flow testing aimed at confirming the total reserves in place as well as those quantities that can be recovered from these reserves is ongoing. Consequently, a review of previously generated geological models for the Lokichar Basin as well as studies of other sedimentary basins within the Kenya Rift (such as those represented by this work) that accommodate the group of sediments referred to as the 'Turkana Grits' are imperative for a full appreciation of the petroleum potential of the Kenyan Rift.

7.1. The Lokone Sandstone, Lokichar Basin: the best hydrocarbon reservoir in the Kenya Rift?

The Cretaceous/Eocene? to middle Miocene infill of the Lokichar Basin is divided into two main packages: 1) the Lokone Sandstone, and 2) the Auwerwer Sandstone (Morley et al., 1999; Tiercelin et al., 2004; Ducrocq et al., 2010).

1) The 'Lokone Sandstone' (670-m thick in the Ngamia-1/1A well; >1100-m thick in the Loperot-1 well, and over >1500 m in the Twiga-1 well); (Morley et al., 1999; Tiercelin et al., 2004; Tullow Oil, 2012; Africa Oil Corporation, 2014) is represented by basement-derived pebbly sandstones and conglomerates that have porosities ranging between 10-20%, deposited in a majorly fluvial/deltaic depositional environment that is punctuated by transgressive lacustrine phases;

2) The 'Auwerwer Sandstone' (>620-m thick in the Loperot-1 well, and 1065-m thick in the Ngamia 1/1A well) above it, is formed by alternating beds of coarse to pebbly sandstones with intermittent fine-grained sandstones that collectively represent braided fluvial to marginal lacustrine units both of which exhibit porosities between 1-15% (Tiercelin et al., 2004).

The Lokone and Auwerwer Sandstones are both basement-derived although a shift to a more volcanic constitution (>50% of the detrital minerals) is noted in the upper levels of the 'Auwerwer Sandstone' (Morley et al., 1999b; Tiercelin et al., 2004, 2012b), probably as a result of a change in sediment provenance zone from a purely metamorphic basement source area to a more volcanic-rich provenance zone. In the Ngamia-1/1A well, this transition within the 'Auwerwer Sandstone' from predominantly basement-derived to largely volcanic is well illustrated. In this well, the 'Auwerwer Sandstone' has been interpreted to extend from 265 m to 1330 m RT. Within this section, below 856 m RT, the lithology is composed primarily of basement-derived, fine- to coarse-grained fluvial deposited sandstones with thin mudstone interbeds, which grade to argillaceous siltstones with rare limestone stringers (Tullow Oil, 2012). Hydrocarbons shows were noted through out this section where

the basement derived sandstone beds have moderate to good porosity (10-25%). Within this interval, oil shows are characterized by a fair pale, yellow to uniform bright yellow direct fluorescence, which increases with depth down to 1330 m RT (Tullow Oil, 2012). This interval (856-1330 m), which fits the description previously given by Murray-Hughes (1933) of the 'Turkana Grits', has previously been referred to as the 'Lower Auwerwer Sandstone'. In this work, we however propose to incorporate this lithologic unit to the 'Lokone Sandstone', owing to the lithological similarity of the two.

Additional drill stem tests in other exploration wells that have been drilled in the Lokichar Basin show this upper part of the 'Lokone Sandstone' (according to our new definition) has the highest quality of reservoir sandstone, with between 23-29% porosity, and between 100 md-3 darcy permeability within the Twiga South-1 well (Fig. 11c; Table 15). This high porosity and permeability has allowed the well to produce 2,812 bopd from three drill stem tests. The 'Lokone Sandstone' is then overlain by 100-m (from 754 to 856 m in the Twiga South-1 well) of a mid-Miocene shale unit, which is referred to as the Auwerwer Shales and which form the regional oil seal in the Lokichar Basin. Within the 'Auwerwer Sandstone' (from 265 m to 754 m in the Twiga South-1 well), the sedimentary package within this section comprises of volcanic-derived sandstones with minor claystones and dark grey, microcrystalline and brittle volcanics stringers. Within this section, porosity was poor and no hydrocarbon shows were recorded (Tullow Oil, 2012). This unit (Auwerwer Sandstone) corresponds to the Lomerimong Sandstones that outcrop in the Lakhapelinyang area which is to the north-north-east of the Loperot area (Tiercelin et al., 2004) which are generally composed of a clayey matrix (0-25%), carbonate cements (29-45%), detrital quartz (24-47%) and feldspar (6-11%) as well as significant amounts of pyroxene, biotite and muscovite, the latter three of which are <5%. The volcanic content in some samples was >50% (Tiercelin et al., 2004).

From a chronostratigraphic point of view, the infill of the Lokichar Basin, as discussed by previous authors (e.g. Morley et al., 1992, 1999b; Talbot et al., 2004; Tiercelin et al., 2004; Thuo, 2009) was determined mainly by the prevailing regional structural configuration that controlled the drainage from the sediment source area to the basin. Sediment deposition within a rift basin is mainly from axial sources and erosion of the hanging wall flexural surface (Cohen, 1990; Tiercelin et al., 1992; Cohen et al., 1994; Tiercelin et al., 2004), with limited amounts of lateral input flowing down relay ramps along the boundary fault (Athmer et al., 2011).

During the deposition of the 'Lokone Sandstone', the sediment source was mainly from outcropping basement rocks from the south possibly through fluvial systems flowing from the southern part of the Kerio Basin (similar to the present-day Kerio River that flows from the southern end of the Kerio Basin into Lake Turkana) as well as the immediate north of the Lokichar Basin (Morley et al., 1999; Tiercelin et al., 2004). The 'Lokone Sandstone' depositional environment are attributed to fluvial braided systems connected to axial deltaic environments at the northern and southern ends of the Lokichar Basin. There is no evidence of volcanic input in the 'Lokone Sandstone', as the areas of volcanic activity were restricted during the upper Eocene to early Miocene ('Turkana Volcanics') to the northwestern part of the Kenya Rift (Zanettin et al., 1983; Tiercelin et al., 2012a).

This lowermost depositional environment of the Lokichar Basin (2950-2776 m RT in the Loperot-1 well) (Shell, 1993) is composed of highly compacted fluvial sediments (Morley et al., 1992, 1999b). These sediments, which comprise of silty sands with intercalations of reddish brown clays, probably correspond to the axial-derived inputs with local influx of laterally derived sediments. During the time of deposition of these lowermost sediments, the developing Lokichar Basin's sediment source was distal in nature and was probably deposited by morpho-tectonic controlled fluvial systems. Fault movement along the main boundary fault – the Lokichar Fault, with concomitant uplift of the flexural margin led to the development of new accommodation space that allowed for the development of the first lacustrine conditions in the Lokichar area that were fed predominantly by this axial fluvial system. We refer to this lake as the palaeo-Lake Lokichar and whose existence is illustrated by the presence of a thick (165 m; 2600 m-2435 m RT) black shale interval that has rare intercalations of silt and fine sands, called the Loperot Shale (Shell, 1993; Morley et al., 1992; Morley et al., 1999b; Talbot et al., 2004; Tiercelin et al., 2004, Tullow Oil, 2012).

Continued uplift of the flexural margin and the development of this margin into a major topographic feature in the Lokichar area with accompanied fault movement along the Lokichar Fault, led to resumption of fluvial depositional conditions with higher energy rivers flowing into the palaeo-Lake Lokichar as is noted in the interval between 2254-1385 m RT in the Loperot-1 well. A combined sediment deposition model is thought to have prevailed during the time of this deposition to include not only axial depositing fluvial systems but also laterally depositing rivers flowing from the uplifted flexural margin as well as proximally derived sands that were carried down relay ramps along the main boundary fault. The sediments in this section of the well are red-brown to greyish white sandstones and silts with occasional grey clays. Red beds are common in this interval, which suggests that there was occasional exposure of these sediments that allowed for the development of lateritic soils (Collinson, 1996). For Lake Lokichar, this could mean that there was occasional lowstand periods during the existence of the lake or that sediment supply was greater than the rate of fault movement which then led to the filling up of the available accommodation space and consequent sediment exposure. This is reflected on outcrops of the Lokone Sandstone at the Lokone Horst (Jean-Jacques Tiercelin, March 25, 2015) (Fig. 58). Considering the documented prevailing climatic conditions of the Lokichar area during Miocene times where rainfall exceeded 1000 mm/yr (Vincens et al., 2006), the latter proposition is unlikely.

Intensified fault movement and further uplift of the flexural margin led to the creation of additional accommodation space in which a new lake formed. We refer to this lake as Lake Lokichar whose existence is recorded between 1385 m and 1057 m RT of the Loperot-1 well and 1481 m to 1845 m RT in the Ngamia-1 well in form of the Lokone Shale (Morley et al., 1992; Shell, 1993; Morley et al., 1999; Talbot et al., 2004; Tiercelin et al., 2004, Tullow Oil, 2012). This shale unit is dominated by dark grey to dark brown and locally green claystones with minor 1- to 5-m thick sandstone beds (Shell, 1993; Tullow Oil, 2012). While palynological recovery within this interval was erratic, the recovered palynofloras from the Loperot-1 well are indicative of freshwater lacustrine conditions while homogeneity of the black shales indicates deposition in a well-established deep anoxic lake with influx of shoreface, deltaic and fluvial sandstones.

From 28 Ma, intense volcanic activity, represented by the Kalakol Basalts (Boschetto et al., 1992), either within the Lokichar Basin or within the then existing catchment area of the fluvial system that drained into the Lokichar Basin, took place. This volcanic activity probably led to the development of new topographical barriers that could have increased the source to basin distance of fluvial systems in the Lokichar Basin vicinity giving rise to the regional mid-Auwerwer Shale unit atop the then existing sedimentary infill of the Lokichar Basin and subsequently a mixed volcanic and basement-derived sediment load. These fine-grained sediments are today considered to form a regional seal in the Lokichar Basin that is then overlain by the fluvial deposited 'Auwerwer Sandstone' as described above.

Today, the remarkable hydrocarbon success within the Lokichar Basin is a direct manifestation of the Lokichar Basin's basin evolution and associated basin infill. As the basin evolution along the Kenyan Rift is very similar, the variability of basin prospectivity within the rift could therefore be determined more by basin infill than by basin evolution. The prolific nature of the "Turkana Grits" in the Lokichar Basin thereby necessitates an evaluation of the other grit formations that have previously been defined as 'Turkana Grits' within the Kenya Rift basins. In this discussion chapter, we will first focus on the three last 'Turkana Grits' formations (Kimwarer Formation, Kamego Formation, and Loriu Sandstone) that have previously not been fully characterized. They will be discussed in terms of lithofacies depositional environments, chronology, diagenetic evolution and reservoir characterization, and will be then compared to the 'Lokone Sandstone', which is considered as the case example of a prolific reservoir in the Kenya Rift.

Then, this comparison will be extended to the other examples of 'Turkana Grits', i.e. the Lapur Sandstone, the Muruanachok Sandstone, and the Mount Porr Sandstone. In order to fully present the reservoir characteristics of the 'Turkana Grits', below is a synthesized table of previously published data as well as original data concerning all the 'Turkana Grits' (Table 16), and in addition, photographic plates of lithofacies and thin section illustrations (Figs. 58 and 59.).

7.2. The Kimwarer Formation, Kerio Basin

7.2.1. Lithology and depositional environments

Similar to the Lokone Sandstone of the Lokichar Basin, the Kimwarer Formation, which is composed of basement-derived sandstones at the base comprises of a basal fluvial lithofacies association (0-25 m) grading up to an alluvial fans lithofacies association (25-56 m) and finally fining up to an overbank lithofacies association between 56 m and 70 m. From the basal and alluvial fan lithofacies section, it was not possible to collect palaeocurrent data. However, deposition by north to northeasterly flowing fluvial systems (Chapman et al., 1978) seems probable and would confirm to the palaeocurrent directions noted in the Lokone Sandstone (Morley et al., 1992). Consequently, the basal fluvial lithofacies is inferred to have been deposited at the inception of the Kerio Basin, by northern directed axial and laterally draining fluvial systems that were operating concomitantly as is illustrated by the mixed granulometry of the fluvial interval that is the sedimentation of both fines and sands (sensu Miall, 1996). There could have been periods of arid climate or prolonged dry spells as it is indicated by the presence of a number of mudcracked horizons (Khalifa et al., 2008).

Tectonic activity that involved uplifting of the rift shoulders of the Kerio Basin and possibly fault reactivation throughout the entire north and central Kenya Rift triggered a change to a higher energy drainage regime that led to the deposition of the alluvial fan system in the Kerio Basin. This fault reactivation probably coincides with the abrupt change that led to a similarly rejuvenated drainage system in the Lokichar Basin that induced the deposition of the proximally derived sands atop the Loperot Shale in the Lokichar Basin (Morley et al., 1999b). The abrupt change from alluvial fan to overbank/floodplain depositional environments corresponds to the initiation of volcanic activity prior to the Burdigalian times (18.1 ± 0.1 Ma) in the vicinity of the Kerio Basin drainage catchment area that could have led to the beheading of rivers and change in the depositional regime from alluvial fan to distal fluvial systems. This volcanic phase corresponds to volcanic activity that racked the part of the Kenya Rift and coincides with the eruption of the mid-Miocene volcanics as discussed above.

7.2.2. Chronology

Based on our new 40Ar-39Ar results, the volcanic units that we sampled just above the KF span three chronostratigraphic stages from ca.18 Ma: (i) Burdigalian (20.44-15.97 Ma) for samples from the Elgeyo Basalts and Chof Phonolites formations (KALW 08/11, KALW 02/11, TUM 04/11, TUM 05/11 and TUM 03/11); (ii) Langhian (15.97-13.82 Ma) for sample TUM 02/11 and (iii) Serravallian (13.82-11.62 Ma) for sample TUM 01/11, both from the Uasin Gishu Phonolites. These ages fall under the bracket of the initial volcanism in the northern and central Kenya Rift regions (Shackleton, 1946; Joubert, 1966; Walsh and Dodson, 1969; Patterson et al., 1970; Baker et al., 1972). However, as the lava cap the KF, they indicate that the sediments are at least ca. 18 Ma old, which is older than expected from available K-Ar data on the Elgeyo Basalts. Therefore the detritic sedimentation, related to a first phase of regional extensional deformation or reactivation along the Elgeyo Border Fault Escarpment, probably started significantly before 18 Ma, and possibly before the Burdigalian. It therefore becomes a possibility that the KF started to deposit at approximately the same time as the reservoir sands of the Lokichar Basin, from approximately 23 Ma (Morley et al., 1999b, Tiercelin et al., 2004). In addition, although apparently concordant at the reference section (Fig. 27), the Chof Phonolite is discordant and rests either on the metamorphic basement, the KF sediments or the Elgeyo Basalts at the regional scale (Fig. 28) and original geological map by Walsh, 1969). Thus a second deformation phase, or a major pulse during a continuum, at about 17 Ma (in between the emplacement of the Elgeyo last flows and the Chof earliest ones), is recorded by the lavas. Possibly the Tambach sediments to the north are to be linked to the erosion of newly created relief made by the basement in the area. Then, also discordant on the basement, the Elgeyo Basalts, the Chof Phonolites or the Tambach sediments (see map in Chapman et al., 1978), came the Uasin Gishu plateau Phonolites, that apparently

achieve the local volcanic activity. This unconformity, which is dated at ca. 14 Ma, in between the oldest Chof flows and the youngest Uasin Gishu ones, marks an additional deformation phase or major reactivation pulse that affected the Elgeyo Border Fault Escarpment.

7.2.3. Reservoir characterization

Petrographically, the KF potential reservoir sediments are predominantly composed of feldspathic arenites, the constituents of which are chiefly derived from the metamorphic basement. Grain sizes range from fine sand to pebbles, grain shapes are sub-angular to subrounded, grain contacts range from floating to concavo-convex, locally sutured. Sediments are poorly sorted overall. The textural and compositional immaturity of the analysed sediments may suggest a relatively short travel distance from source areas of sediments to the basin. The main detrital minerals in the KF are, in order of relative abundance: monocrystalline quartz, polycrystalline quartz, plagioclase feldspars and potassium feldspars. Other detrital grains include metamorphic rock fragments, volcanic lithics, mud clasts, heavy minerals and organic matter. The matrix of the sandstones of the KF is composed of clays, which are commonly associated with siderite and hematite.

Porosity of the arenites from the KF is very poor to poor, being mainly downgraded by the clayey-rich nature of the sediments and by carbonate cementation (mainly calcite). Other pore filling authigenic phases (quartz cement, hematite and so on) further reduce the pore effectiveness of the analysed lithologies. Only a few samples offer good reservoir potential due to a larger amount of connected macropores. These are primary and secondary, the latter linked to the dissolution of unstable feldspar and lithic grains, and likely also of carbonate cement. In clay-rich lithologies, microporosity between clay platelets is inferred to be abundant.

Permeability is very poor to poor, only locally good; reservoir quality risk assessment for equivalent subsurface sediments is high overall (Type 1, tight depositional facies, sensu Tobin, 1997; fig. 9), unless fracturing, dolomitization or burial dissolution processes can be predicted. Nonetheless, fracturing and dissolution of feldspars, lithics and carbonate cement, can enhance the reservoir potential of subsurface sediments. There are hints of such processes where the reservoir potential of the analyzed petro-type is considered to be very good. Visual estimation of porosity in this level is between 20-30%.

7.2.4. Lateral and vertical extension of reservoirs

While the Kimwarer Formation exists as a relatively thin outcrop in comparison to others in the Northern Kenya Rift, such as the Lapur Sandstone (485 m) or the Loriu Sandstone (610 m) (Wescott et al., 1993; Thuo, 2009; Tiercelin et al., 2004, 2012a), the KF is nonetheless understood to attain an appreciable thickness and lateral extent within the Kerio Basin as suggested from the seismic interpretation conducted as part of this work. In the Kerio Basin, the KF appears to be completely covered by thick volcanic piles. Considering the reservoir potential of the KF in outcrop (very poor to locally very good) though this could be different in the basin due to differential diagenetic evolution, in conjunction with evidence of anticlinal structures with four-way dip closure, in the southern portion of the Kerio Basin (Kenya Tertiary Rift Study, 1986), the area that straddles the boundary between Block 12A and Block 14T should be considered to be a potential target for oil exploration. Complementary seismic surveys and new exploration wells will help to test such potential.

7.3. The Kamego Formation, Baringo Basin

7.3.1. Lithology and depositional environments

The Kamego Formation is represented by a relatively thin (~80 m) sediment pile outcroping along the Saimo Fault Escarpment, which is the western bounding fault of the Baringo Basin. Previous geophysical (magneto-telluric) studies within the Baringo Basin show the existence of a 7-8 km deep basin that is infilled by thick sediments at base, which are in turn overlain by a thick sequence of volcanic units (Hautot et al., 2000). These thick (>100 m) (Hautot et al., 2000) lowermost sedimentary beds are interpreted as the Kamego Formation. Our outcrop study objectives were therefore two pronged, first the study was aimed at firmly determining the chronostratigraphic position of the formation and secondly to describe the broad reservoir characteristics of the inferred sedimentary pile at depth.

Two depositional environments have been determined for the KAF through facies association of the largely massive ungraded, fine-grained sandstones that are floored by relatively thin conglomeratic units and intercalated and capped by thick massive fines (sensu Miall, 1996). The lowermost ~35 m is intepreted as a distal fluvial channel facies depositional environment. Palaeocurrent data could not be collected within this facies association, however, due to the proximity of the Baringo Basin to the Kerio Basin whose lowermost sediments (0-34.3 m) were deposited by north- to northwest-oriented fluvial systems, it is inferred that the rivers in the Baringo Basin were also similarly oriented. The depositional environment grades up into a floodplain depositional environment (34.3-70 m) probably as a result of tectonic movements similar to those outlined above for the Kerio Basin which include the uplifting of the rift shoulders and fault reactivation could have led to the rearrangement of the trajectories of fluvial systems that resulted in the dominance of lower energy rivers within the basin. This tectonic activity was accompanied by volcanic eruptions that are recorded within the stratigraphic column in form of relatively thin, massive tuffaceous horizons within predominantly green mudstones that are indicative of an overbank facies. Sporadic climatic changes could have occurred within this time that lead to the deposition of the rare gravelly sands (sensu Miall, 1996) within this depositional environment.

7.3.2. Chronology

The chronological position of the KAF has until now been discussed based upon its position above the metamorphic basement in relation to the broad definition of the ‘Turkana Grits’ and more importantly the radiometric dates of the overlying Sidekh Phonolites (ca. 16.4-14.8 Ma; Chapman et al., 1978). Based on our new 40Ar-39Ar results, the volcanic units sampled within and above the Kamego Formation (19.8 Ma for sample KAM V 30, and 18.0 Ma for sample KAM V2), volcanic activity in the Kamego Formation probably started much earlier in the Burdigalian stage (20.44 – 15.97 Ma). This fits well with previously published data for volcanic activity in the Kenya Rift (Shackleton, 1946; Joubert, 1966; Walsh and Dodson, 1969; Patterson et al., 1970; Baker et al., 1972). Similar to the Kimwarer Formation, these lava cap or atleast are only noted in the topmost sediments of the Kamego Formation (Fig. 39) giving the formation a minimum age of ca. 19Ma and suggesting that the first phase of regional extensional deformation in the vicinity of the Baringo Basin probably started much earlier than 19Ma and possibly earlier than the Burdigalian. This is in agreement with our findings in the adjacent Kerio Basin as discussed above (see section 7.2.2).

7.3.3. Reservoir characterization

Petrographically, the KAF sediments can be classified as feldspathic wacke to mudstone, the constituents of which show a mixed origin, both from basement as well as volcanic origin. The KAF as studied on the Kipsaraman Type-Section is largely volcanic with only the lowermost 5 m of the total Kipsaraman section (75.5 m)

being basement-derived. The rest of the outcrop is composed of volcaniclastic-rich sandstones and mudstones. When focused on the sandstones collected from the Kipsaraman Type-Section, the KAF is considered to be texturally immature owing to the poor sorting, angular to sub-rounded nature of grains in the different studied samples, as well as the wide range of grain sizes which range from fine sand to pebbles and whose contacts range from floating to concavo-convex. These dual classifications suggest a relatively short travel distance from the provenance zone to the basin. The main detrital minerals in the KAF are, in order of relative abundance: monocrystalline quartz, polycrystalline quartz, plagioclase feldspars and potassium feldspars. Other detrital grains include metamorphic rock fragments, volcanic lithics, mud clasts and organic matter. The matrix of the sandstones of the KAF is composed of detrital muds. The main diagenetic features observed are cementation, predominantly by hematite and calcite as well as compaction, the latter of which is confined to the lower half of the formation. While the cements occur throughout the formation, relatively lesser amounts of quartz cement, feldspar overgrowths and authigenic kaolinite are also noted.

The overall porosity of the KAF is very poor to poor, being mainly downgraded by the clayey-rich nature of the sediments and by cementation (mainly by hematite and calcite). A few samples located mainly in the tuffaceous muddy section exhibit good reservoir potential (10-25%, visual estimate) in form of secondary vuggy porosity attributed to dissolution of unstable feldspar and lithic grains, and likely also of carbonate cement. Similar to the Kimwarer Formation, microporosity between clay platelets is inferred to be abundant. However, permeability is very poor to poor, and was not noted as good in any of the samples collected for analysis. The reservoir quality risk assessment for equivalent subsurface sediments is therefore high overall (Type 10, which refers to any reservoir whose pore system contains undeterminable secondary porosity, sensu Tobin, 1997; Table 6). Nonetheless, fracturing and dissolution of feldspars, lithics and carbonate cement, can enhance the reservoir potential of subsurface sediments.

7.4. The Loriu Sandstone, North Kerio Basin

7.4.1. Lithology and depositional environments

The Loriu Sandstone has been previously described in relation to the Lokone Sandstone in the adjacent oil rich Lokichar Basin. The lowermost infill of the North Kerio Basin is an assortment of fluvial deposits called the Loriu Sandstone. On outcrop, this formation is estimated to be ~610-m thick (Wescott et al., 1993) although a much thicker sedimentary pile is expected within the basin based on the seismic data that was acquired by Amoco Kenya in the 1990's, which illustrate the existence of over 5-6 km of basin infill of Paleogene-Miocene age within the North Kerio Basin (Morley et al., 1999b) and which are comparable to the fluvial/fluvio-deltaic sediments of the Mt. Porr Sandstone on the eastern side of Lake Turkana (Fig. 50).

7.4.2. Chronology

The chronological position of the LOS has until now been constrained by its position above the metamorphic basement in relation to the broad definition of the "Turkana Grits", and more importantly the radiometric dates of one of the lava flows (ca. 15.7 Ma) and dyke (ca. 14.7 Ma) respectively in the Loriu area (Wescott et al., 1993). In this work, a new age (18.5 Ma) has been determined from the whole rock Ar-Ar isotopic of a dyke (sample Loriu 1) that cross cuts the Loriu Sandstone. This age is consistent with the ages that we have determined for the Kimwarer Formation and the Kamego Formation in the Central Kenya Rift. The similarity of this ages under the broad sense of volcanism in the Kenya Rift which has previously been bracketed between ca. 23 – 14 (Shackleton, 1946; Joubert, 1966; Walsh and Dodson, 1969; Patterson et al., 1970; Baker et al., 1972) makes it possible to assume a similar depositional age for the Loriu Sandstone, the Lokone Sandstone, both in the North Kenya Rift as well as the Kimwarer Formation and the Kamego Formation in the Central Kenya Rift.

7.4.3. Reservoir characterization

Petrographically, the LOS sediments can be classified as feldspathic wackes. Similar to the KAF, the LOS can also be described as compositionally and texturally immature owing to the wide range of clasts (quartz, feldspar and metamorphic lithics) as well as the poor sorting, angular to sub-rounded nature of grains and the wide range of grain sizes with multiple contact types within the LOS. This dual classification suggests a relatively short travel distance from the provenance zone to the basin. The main detrital minerals in the studied section of the LOS are, in order of relative abundance: polycrystalline quartz, monocrystalline quartz, plagioclase feldspars and alkali feldspars. Other detrital grains include metamorphic rock fragments, mud clasts, mica and organic matter. The matrix of these studied sandstones from the LOS is composed of detrital muds (>15%) and authigenic cements which are mainly hematite and calcite with lesser amounts of quartz cement, feldspar overgrowths and authigenic kaolinite. Post-depositional deformation in form of compaction is also noted.
The overall porosity of LOS from the data acquired from the two outcrops is negligible to poor, being mainly downgraded by the clayey-rich nature of the sediments, compaction and by cementation (mainly by hematite and calcite). Primary porosity is depth dependent and decreases with corresponding increase in depth a consequence of sediment compaction (long to sutured contacts become more apparent with depth). Sparse intragranular (secondary porosity) is noted mainly with the feldspathic component of the LOS as a result of dissolution. Within quartz grain, secondary porosity is recognised within the fractures many of which are occluded by carbonate cements that is partially dissolved. Microporosity between clay platelets is inferred to be abundant. Permeability is very poor to poor, and the reservoir quality risk assessment for equivalent subsurface sediments is therefore high overall (Type 1, tight depositional facies, sensu Tobin, 1997; Table 6.

7.5. The "Turkana Grits": Potential reservoirs in the Kenya Rift?

Within the Kenya Rift, there exist basins that have similar lithological infills to the Lokichar Basins' Lokone Sandstone. The knowledge of these basins and their infill is essential in the determining of new trends in hydrocarbon exploration within the Kenya Rift. To achieve this target, a comparison between the entire set of the seven formations that comprise the 'Turkana Grits' under the following criteria:

- Age of the basin;
- Depositional environment of the main reservoir formations;
- Structure and seal properties within the basin;
- Prospectivity rank of the different "Turkana Grits".

These different points are summarized in Table 16 and are presented below.

The suite of sedimentary formation that have been refered to as the Turkana Grits exhibit moderate to good reservoir potential. Generally, for all the Turkana Grits, their quality as reservoir rocks is however highly dependent on the dominant rock type within their provenance area, the transport distance and the energy of the transporting medium (Morley 1999b). In all the basins, the lowermost sedimentary pile is composed of basement derived sandstones which include alluvial and fluvial/ fluvio-deltaic assemblages. In these arkosic rocks, the main detrital constituents are quartz (both monocrystalline and polycrystalline), feldspars (both alkali and plagioclase feldspar) and metamorphic and sedimentary rock fragments. These are often found in a mix of detrital mud. These sandstones are best typified by the Lokone, Loriu, and Lapur Sandstones and the Kimwarer Formation (LKF). These sandstone formations are however characterized by a marked reduction in porosity. Ideally, arkosic sandstones generally have high porosity levels (~40%; Selley, 1978). None of the seven Turkana Grits presented in Table. 16 shows such porosity levels largely due to compaction and more importantly due to

porosity downgrade by authigenic components. This authigenic phase includes carbonate (calcite and siderite) and hematite cements as well as kaolinite clays which are noted in varying amounts in all the Turkana Grits presented here. These clays and cements are largely attributed to climatic changes that occurred in the East African region from the mid Cretaceous times as well as post depositional hydrothermal fluid circulation occasioned by the intrusion of volcanic dykes as discussed by Thuo (2009).

Of the seven Turkana Grits presented in Table. 16, only four show appreciable porosity levels. These are the Lokone Sandstone (19% – 27%), the Lapur Sandstone (3% – 25%) and the Kimwarer Formation (5% - 30%) and the Kamego Formation (5% – 15%) (Table 16) whose porosity levels compare well to other observed porosity levels in similar depositional environments in the southern Sudanese Muglad Basin where porosity value ranging between 8% - 38% have been recorded (Schull, 1988). Similar values (25% - 35%) have also been recorded in the Albertine Graben's Nzizi fluvio-deltaic reservoir sandstones, which have little or no detrital mud component with authigenic clays (kaolinite, illite, chlorite and smectite) being the only pore occluding component of the sandstones (Ochan and Amusgut, 2012). In extension, based on Tobin's (1997) subsurface reservoir quality prediction model which attempts to predict the quality of sandstone units in the sub-surface based on the lithologies observed at the surface (Table. 6), the seven sandstone formations that comprise the Turkana Grits (Table. 16) can be generally grouped as early near surface cemented sandstones whose risk assessment is high unless lateral cement pinch-out or cement dissolution can be predicted. Dissolution, especially of the feldspathic component of the Loriu, Kimwarer and Kamego Formations is high (Fig. 59) and high amounts of secondary- as well as micro-porosity (though not optically visible) are expected. Consequently, based on such an assessment, it can thereby be supposed that the Turkana Grits are potential reservoir units within the Kenya Rift.

With specific regard to the trapping mechanisms associated to rift basins, it has been noted that when seals are thin and widely separated vertically, traps normally involve the same seal as a top seal and a juxtapositioning seal across a low displacement faults in order to allow for the continuity of the sealing formation. Such traps have been noted in the Unity Field - Sudan rift basins (Schull, 1988; Morley, 1999d) as well as in the oil-rich Lokichar Basin. Contrary to previous suppositions, reserves associated to such trapping settings which are normally relatively small holding a few hundred million barrels (Morley, 1999), can be quite large as is the case with the Lokichar Basin where over 600 million barrels of recoverable oil have been discovered. In the Lokichar Basin, the 100m, mid-Auwerwer Shale is considered to be a regional seal (see section 7.1). This seal despite being extensively cut by low displacement faults forms an apt trapping mechanism owing to its lateral continuity and the relative juxtapositioning of the reservoir unit (Lokone Sandstone) below it and the source (Lokone Shale) further below this.

Such a scenario can be extended to the Central Kenya Rift where the Ngorora Formation (Fig. 12b and 25) fills up the entire CKR, extending from the Elgeyo Border Fault on the western side of the Kerio Valley to the eastern extreme of the rift valley, along the upraised Laikipia Plateau. Within the Kerio Basin, through the long offset faults that do not cut through the regional seal could juxtapose stratigraphically distant source and reservoir units or act as hydrocarbon pathway between source-rock and reservoir units. In the case of the Kerio Basin, this could be the Tambach Formation (source-rock) and the Kimwarer Formation (Fig 12b) that are connected by faults such as those identified by Mugisha (1999) e.g the Barwesa Fault and the Kerio Fault (Fig. 24). In the Baringo Basin, though there are no seismic sections to determine the configurations of underlying faults, it is possible to theorize a similar setting for the structural traps within the basin, juxtaposing the Kamego Formation to the extensive Ngorora Formation above it (Fig 12b).

8. Conclusion

8. Conclusions

The studied basins in Central Kenya Rift (Kerio and Baringo Basins) and the North Kerio Basin in the North Kenya Rift have moderate to good reservoir potential which is a result of lithological make-up which a consequence of the sediment provenance zone (Morley, 1999b; Tiercelin et al., 2012), the distance of this provenance area to the depositional site and post-depositional sandstone modifications. The early stage of development for the studied basins is characterized by alluvial fan or fluvial environments, which later grade up (except in the case of the Loriu Sandstone) to more low energy depositional environments. The lowermost sandstones which in all cases sit directly on the metamorphic rock from which they are derived are tightly packed arkosic sandstones and fit the definition given by Murray-Hughes (1933) of the expansive "Turkana Grits". Despite arkosic sandstones generally having very high porosity levels (~40%; Selley, 1978), the three formations studied in this work exhibited reduced porosities levels owing to post-depositional evolution of the sandstone key of which is cementation. In all three formations, the major cements are hematite, calcite and kaolinite. This is similar to previous studies which also identify these among other cements and clays in the Lapur Sandstone, the Muruanachok Sandstone and the Mount Porr Sandstone (Table. 16) These cements are believed to be associated with both climatic changes that prevailed in the East African region during Paleogene to recent times as well as hydrothermal fluid circulation associated to volcanism in both the Central and Northern Kenya Rifts.

The Kimwarer and Kamego Formations, both in the Central Kenya Rift, recorded porosity levels of between 10-20% (visual estimate) while 5-10% was recorded from the Loriu Sandstone. This fits well with porosity levels collected from similar sandstone formations in the region such as the Lokone Sandstone (as per our definition) from which porosity levels between 15-30% have been recorded from the Ngamia well 1-1A and previously from the Loperot-1 well (Tiercelin et al., 2012b).

In terms of hydrocarbon prospectivity ranking, aside from the Lokone Sandstone where hydrocarbon accumulations have already been found, the next highest ranking formation is the Loriu Sandstone. This is due to its thick sedimentary infill and the very likely assumption that the highly petroliferous Lokone-type shales overshot the Lokone Horst and were also deposited in the North Kerio Basin. In addition, owing to the proximity and similarity of depositional environment to the Lokone sandstone, it can be assumed that the regional seal, the Auwerwer Shale could be could occur within the basin infill, thereby offering similar sealing qualities as it does in the Lokichar Basin.

We rank the Kimwarer Formation second after the Lokone Sandstone which has already been proven. This is because the formation has an appreciable sedimentary thickness (approximately 2km) with poor to excellent porosities (5% - 30%) and poor to good reservoir quality. In addition, the Kimwarer Formation has the highest possibility of having a good regional seal – the Ngorora Formation and a high possibility of source-rock (Tambach Formation – TOC= 5% (NOCK, 2010) to reservoir juxtapositioning through long offset faults such as the Barwesa Fault identified by Mugisha (1999). The Kamego Formation (Rank 3) and the Lapur Sandstone (Rank 4) and the Loriu Sandstone (Rank 5) also show good prospectivity theoretically. For the Kamego Formation, no seismic data is available to study the configuration of the fault lines in the sub-surface of the Baringo Basin. However, from surface data (Fig. 38), and inference from the adjacent Kerio Basin, it is possible to infer the juxtaposing of reservoir rocks (Kamego Formation – 5% - 15% porosity) with prolific source-rock units (Ngorora Formation – TOC=20%) through long offset faults in the subsurface. The Loriu Sandstone is also considered to be a prime exploration target despite no potential source-rock units being noted in the studied stratigraphy presented in this work. Being proximal to the Lokichar Basin, it has been inferred that the paleo-lake Lokichar traversed a wide area in the Turkana region and that Lokone-type shale units were deposited not only in the Lokichar Basin but also in the adjacent North Kerio Basin similar to the Ngorora Formation in the CKR. If this is the case, then juxtaposed to good reservoir rock (assuming dissolution occurs in the studied lithologies in this work), then it is possible to propose a similar petroleum system to that which exist in the Lokichar Basin.

Fig. 58.
Kimwarer Formation: *Petrographic micrographs of selected samples from the Kimwarer Formation. (a) Sample (49/11) – Medium grained, poorly sorted, feldspathic arenite. Detrital component comprises of quartz and feldspar, with common detrital clays and scattered quartz cement and local hematite. Porosity is good (20% - visual estimate) and permeability is moderate. (b) Sample (KIM 5) Very fine grained, moderately well sorted, feldspathic arenite, comprising of monocrystalline quartz, feldspars (dominantly plagioclase) and detrital mud. Authigenic component comprises of hematite, siderite and calcite. Primary porosity is good and limited secondary porosity is noted. (c) Sample (02/11) - Medium grained poorly sorted feldspathic arenite. Detrital component comprises of monocrystalline and polycrystalline quartz, alkali and plagioclase feldspar. Mudclasts and lithic fragments are sparsely present. Authigenic component comprises of abundant hematite, feldspar and quartz overgrowths. Porosity is negligible owing to compaction and quartz and feldspar overgrowths. (d) Sample (KIMW 28/11) medium grained, very poorly sorted argillaceous sandstone. Detrital component comprises of monocrystalline and rare polycrystalline quartz, plagioclase feldspar. The authigenic component comprises of calcite cement and sparse hematite cement. Porosity is negligible due to downgrade by detrital clays, hematite and calcite pore occlusion.*
Kamego Formation: (a) Sample (KAM 25) Cherty? tuffaceous mudstone with good secondary solution porosity (Sp, mainly vugs). Pore filling megaquartz & hematite are common. (b) Sample (KAM 23) Light greyish tuffaceous mudstone mostly with replacement silica & hematite. Very poor reservoir potential. (c) Sample (KAM 28) Feldspathic wacke with clays (Cl) intermixed with siderite & hematite. The main detrital component is composed of monocrystalline quartz and feldspar. The main authigenic mineral and pore occluding mineral is pore filling hematite. Very poor reservoir potential. (d) Sample (KAM 18) Feldspathic wacke to paraconglomerate with metamorphic rock fragment granules/pebbles and isolated secondary pores. Main pore occluding agent is detrital mud and pore filling and grain replacive calcite cement. Porosity is poor and predominantly secondary and associated with feldspar dissolution.

Loriu Sandstone: *(a) Sample (01/12/42) Wacke to microconglomerate comprised of polycrystalline quartz and sparse monocrystalline quartz, both alkali and plagioclase feldspar and abundant clays. Main authigenic mineral is grain replacive to pore filling brownish carbonate cement. Porosity is very poor and is secondary - mainly associated with the dissolution of feldspars and fracturing of detrital quartz grains. (b) Sample (01/12/12) Argillaceous poorly sorted sublithic-subfeldspathic arenite. The main detrital components are polycrystalline and sparse monocrystalline quartz, with plagioclase feldspar. Porosity is mainly confined to isolated secondary dissolution pores attributable to the dissolution of feldspars. Porosity is poor overall. (c) Sample (01/12/11) - Wacke (quartz-rich overall) with cryptocrystalline matrix. Main detrital component is quartz, metamorphic rock fragments, sparse feldspars and detrital clays. The authigenic components are mainly pore filling calcite (and siderite). Porosity is negligible. (d) Sample (02/12/08) Fine grained, micaceous lithic arenite. Detrital component is polycrystalline quartz, metamorphic rock fragments and detrital clays. The authigenic component comprises mainly of kaolinite clays and siderite. Porosity is poor and is concentrated to thin open fractures.*
Lapur Sandstone: (a) Coarse grained poorly sorted subfeldspathic arenite that is cemented by calcite/dolomite. Artificial pores are common. Porosity is moderate to good. (b) Polymictic paraconglomerate with common pore filling calcite/dolomite. Microporosity is locally noted. (c) Medium grained, moderately well sorted subfeldspathic-sublithic arenite with pore-filling clays and calcite. Porosity/permeability is poor. (d) Coarse grained, moderately sorted subfeldspathic arenite with common pore filling kaolinite. Porosity os good (mainly secondary pores and micropores) (Core Laboratories, 2011).

Lokone Sandstone: *(a) Fine grained, moderately well sorted feldspthic arenite with common pore filling kaolinite. Porosity is moderate to locally good. (b) Moderately well sorted calcite/dolomite cemented feldspathic arenite. Porosity is negligible. (c) Fine grained, well sorted lithic-rich feldspathic arenite with common calcite and clays. Porosity and permeability is poor. (d) Medium grained poorly sorted clayey lithic-rich feldspathic arenite with poor porosity overall. (Core Laboratories, 2011).*

Mount Porr Sandstone: *(a and b) Moderately sorted, medium grained feldspathic arenite with common pore filling kaolinite. Porosity is good to very good: secondary pore and micropores, the latter being concentrated within dissolved grains and between coarse kaolinite booklets. (c) Coarse grained poorly sorted feldspathic arenite with poor porosity. Porosity is occluded by pore filling and locally grain replacive calcite cement. (d - i) Poorly sorted feldspathic arenite with abundant pore filling calcite, poor to locally moderate porosity. (Core Laboratories, 2011).*

Muruanachok Sandstone: *(a) Wacke with common alkali feldspar with mudclasts and abundant clays. The porosity is poor. (b) Fine grained sublithic arenitewith abundant pore filling to grain replacive kaolinite booklets. Porosity is concentrated within the micropores between clay platelets. (c) Coarse grained, poorly sorted feldspathic wacke with poor porosity which is downgraded by clays. (d) Coarse grained, moderately sorted quartzite with common detrital and authigenic clays. Porosity is moderate overall. (Core Laboratories, 2011).*

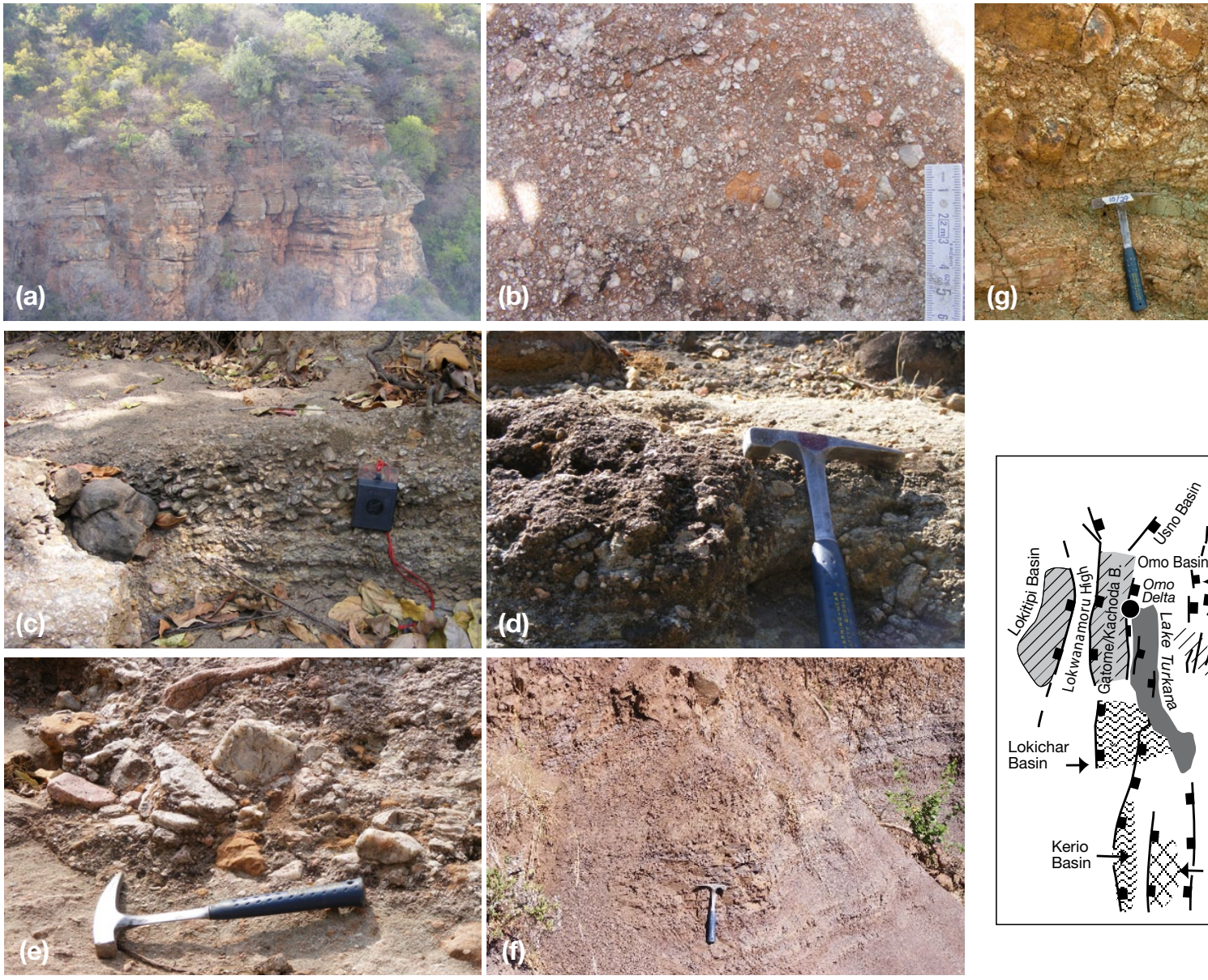

Fig. 58. The Kimwarer Formation. *(a) the Kimwarer Formation outcrop showing horizontally bedded metric thick, beige coloured sandstones. The Lower Kimwarer Formation comprises largely of (b) massive, decimetric to metric, fine to coarse grained basement-derived sandstones (lithofacies Sm) that are intercalated with horizontally, cross bedded, and locally rippled sandstones, that occur together with fine grained laminated and massive mudstones. This facies association is attributable to a distal fluvial channel depositional environment. The mid-section (24m – 54m) is characterized by a series of fining up clast and matrix -supported conglomerates (lithofacies Gcm and Gmm) (c, d and e) which represent alluvial fan depositional environment. (f) The LKF as well as the UKF are both topped by massive mudstone with those capping LKF being upturned to almost vertical, assumedly due to traction force exerted upon them while still in a semi-solidified state by the overlying volcanic sequence (Unit 1).*

The Kamego Formation *comprises largely of (g) metric thick, green, massive mudstones (lithofacies Fm) that are intercalated numerous cream-coloured tuffaceous intervals and few massive, fine grained sandstones (lithofacies Sm). These form the upper half (35m – 70m) of the outcrop that represents a floodplain depositional environment. (h) The lithofacies association of the lower half is characteristic of a distal fluvial channel depositional environment and is characterized at base by a metric thick matrix supported conglomerate composed of basement derived fragments, overlain by (i) a thick sequence of massive brown sandstones (Sm) with common tuffaceous lenses and few green mudstone intercalations.*

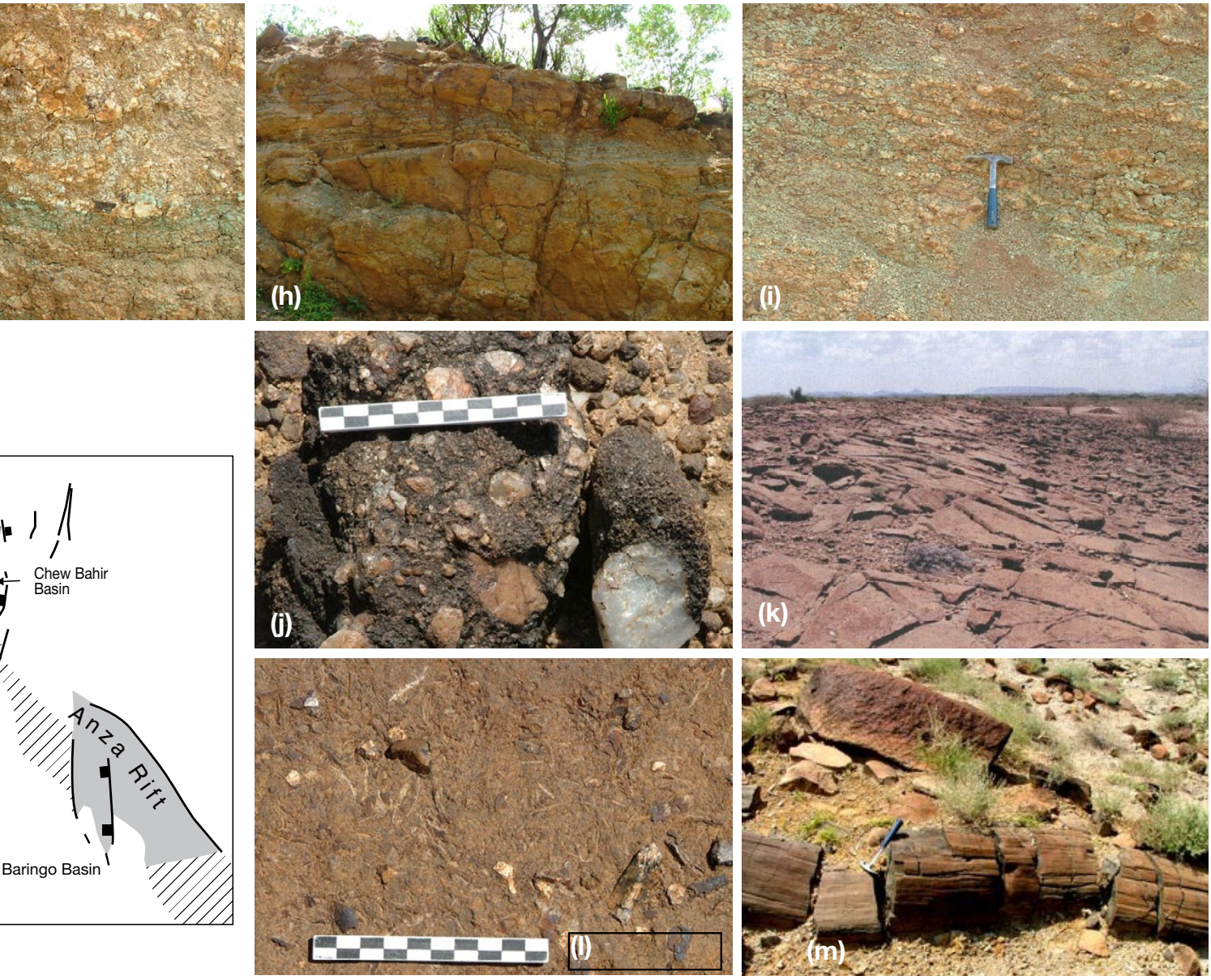

Lokone Sandstone *is currently (December 2014) the most prolific reservoir unit in Kenya. It is composed of (j) quartz–rich matrix-supported conglomerates (lithofacies Gmm with cobbles > 10cm) to very course massive sands (lithofacies Sm) (Morley et al., 199b; Tiercelin et al., 2004). (k) Intercalated within these are laterally extensive gastropod-rich mudstone to siltstone beds (lithofacies Fm) that are indicative of a shallow lacustrine depositional environment. (l) Related to these gastropod beds are 'bone-beds' which grade into the former and are also noted in silty to fine-grained, massive sandstone beds (lithofacies Sm) and which could represent deposition in a lacustrine (shoreline) depositional environment, Further from the palaeoshoreline, the supposition of a vegetated lacustrine environment is noted in form of (m) fossilized tree trunks.*

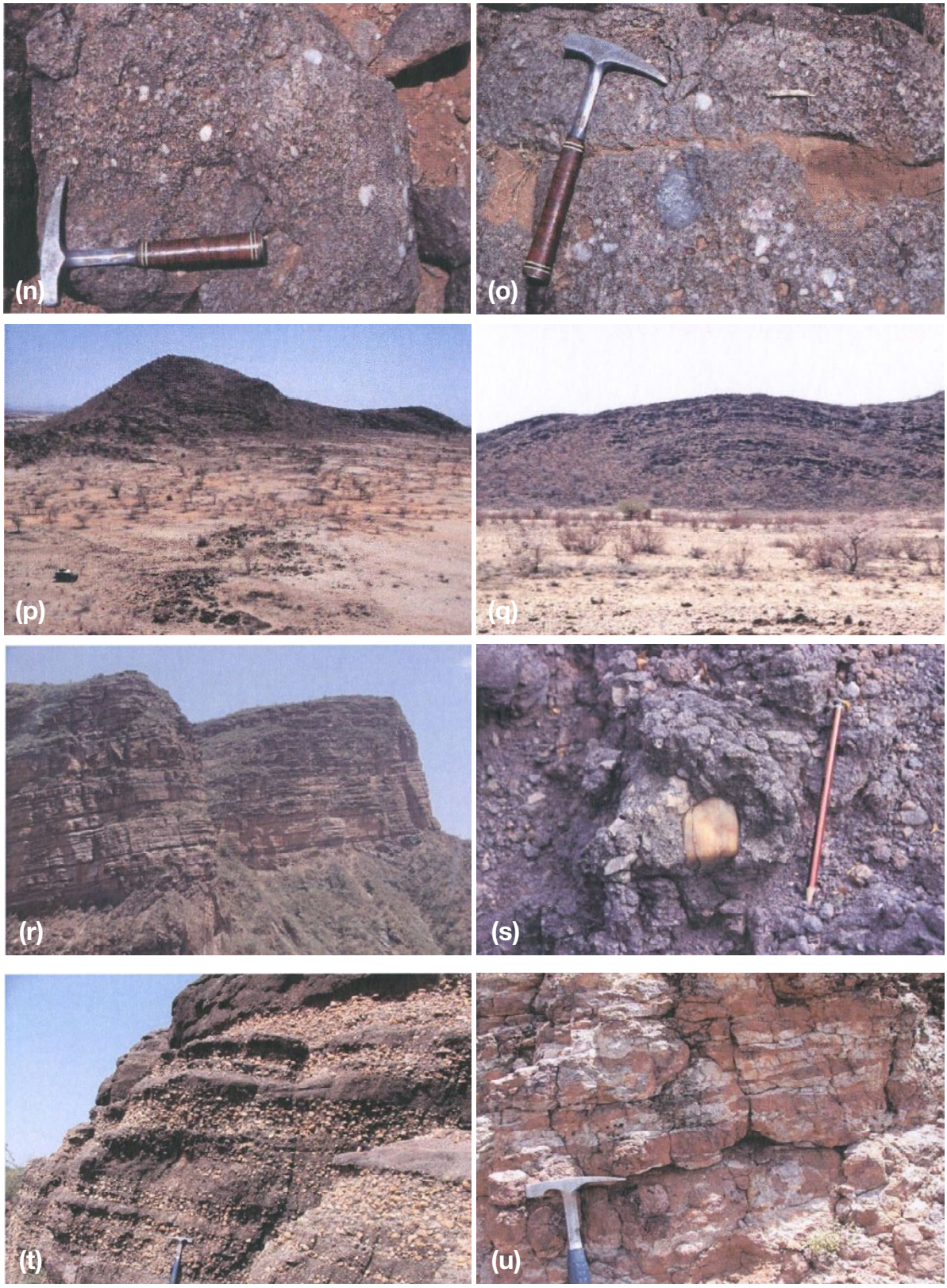

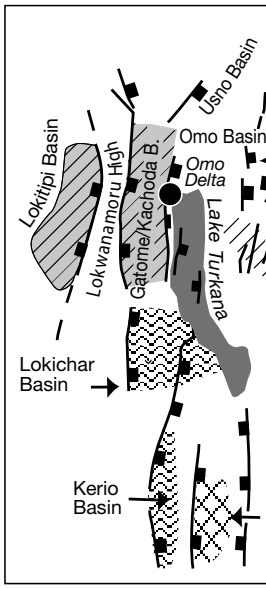

Fig. 58. *(a) the Kimwarer Formation outcrop showing horizontally bedded metric thick, beige coloured sandstones. The Lower Kimwarer Formation comThe Muruanachok Sandstone comprises of a is a series of fining upward channel sequences with (n) massive coarse arkosic pebbly sandstones and (o) very coarse to granular sandstones representing (lithofacies Sm) interbedded with grey-purple siltstone and shales, (Thuo, 2009). The outcrop itself (p and q) is 350m though the sediments that comprise the entire section must be much thicker as the top and base of the formation have not been established. On outcrop, the Muruanachok Sandstone outcrop shows a faint anticlinal attitude (Thuo, 2009).*
The Lapur Sandstone is an (r) impressive sedimentary sequence immature arkosic sandstones that overlie the Precambrian Basement. The major lithologies that comprise this formation are (s) Pebbly sandstones which is the dominant lithology (lithofacies Sm) and clast (lithofacies Gcm) to (t) matrix supported conglomerates (lithofacies Gmm) (Miall, 1996) which represent distal alluvial fan depositional environments (Thuo, 2009). (u) Within the Lapur Sandstone, there are various intervals that are indicative of sub-aerial exposure and which are represented by different palaeosol lithofacies.

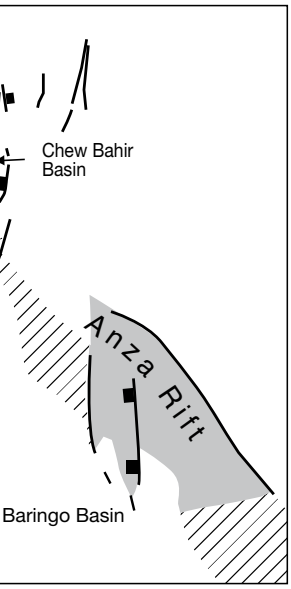

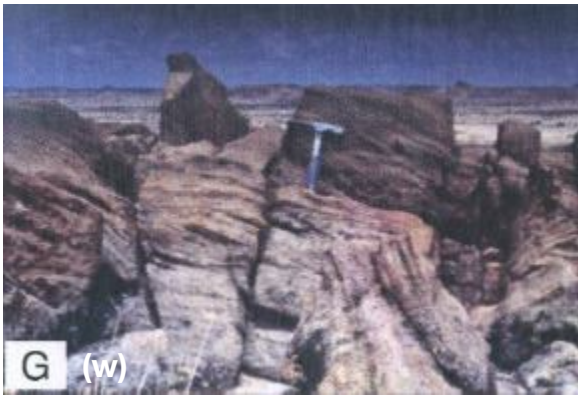

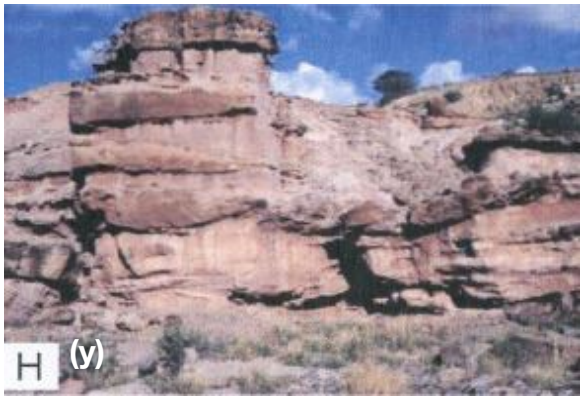

Mount Porr Sandstone is considered to be the lateral equivalent of the Loriu Sandstone (Wescott et al., 1993). It is a mainly (v) arkosic, coarse to medium grained, buff brown to purple, siliciclastic formation made-up of quartz and metamorphic rock fragments that are >5cm in diameter. These are typified by predominantly massive beds (lithofacies Sm) that are locally intercalated with low angle cross bedded sandstones (lithofacies Slp) representing a braided fluvial depositional environment. (w, x and y) Different aspects of the Mount Porr.
The Loriu Sandstone on outcrop, is an entirely fluvial deposited sandstone composed of (z) massive, metric thick, multi-coloured sandstone (lithofacies Sm) with few massive mudstone intervals. (a1) However more fine grained to mudstone lithologies could exist within the Loriu Sandstone and are obscured from view by the thick talus cover. (a2) Matrix-supported conglomerates (lithofacies Gmm) with cobbles > 10cm in diameter comprising of fractured quartz grains and metamorphic rock fragments are common in the Loriu Sandstone representing non-tractional deposition by high strength viscous plastic debri flows (Miall, 1996). (a3) The Loriu Sandstone is heavily intruded by fine-grained, porphyritic basaltic dykes.

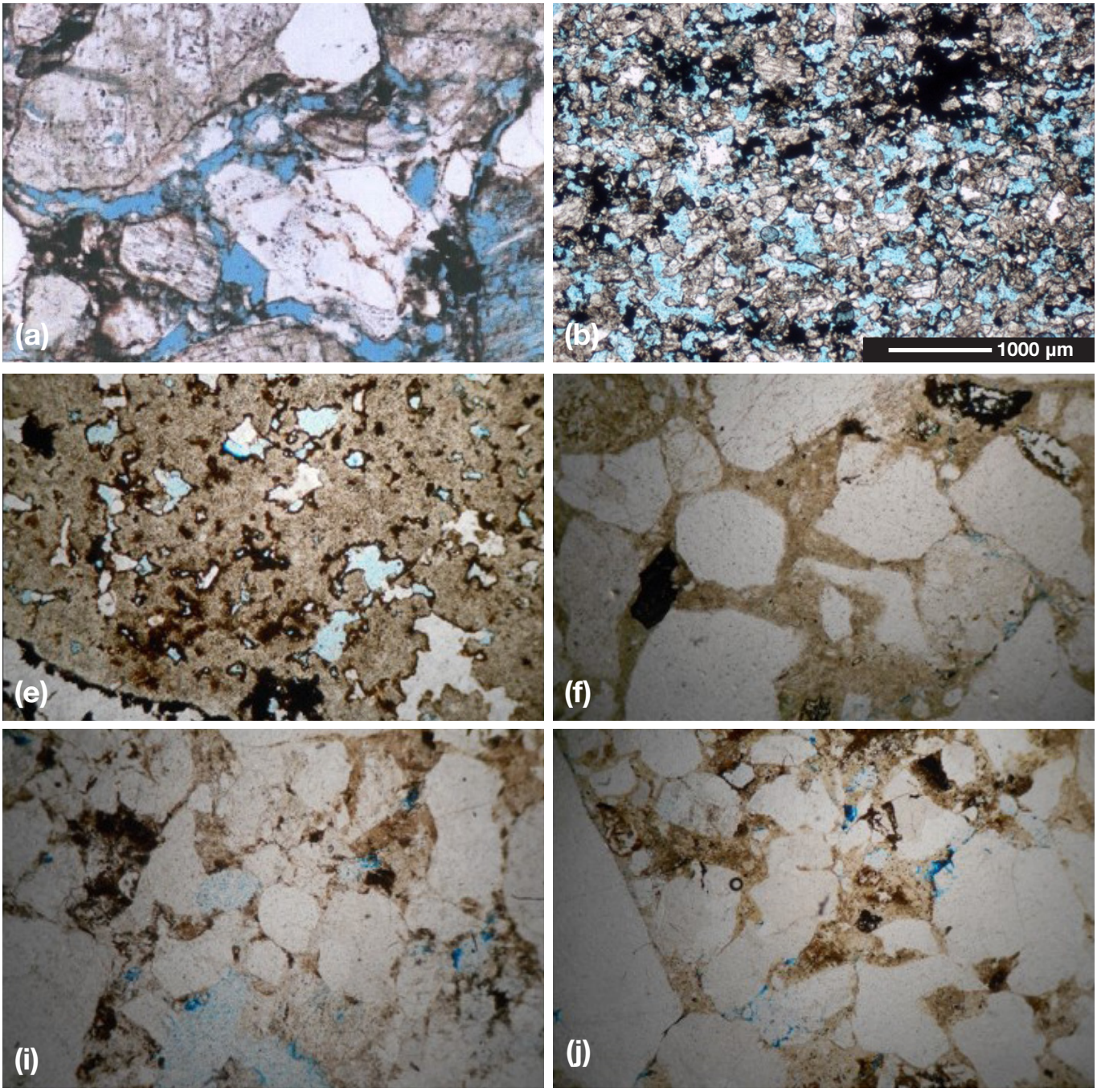

Fig. 59. The Kimwarer Formation: *Petrographic micrographs of selected samples from the Kimwarer Formation. (a) Sample (49/11) – Medium grained, poorly sorted, feldspathic arenite. Detrital component comprises of quartz and feldspar, with common detrital clays and scattered quartz cement and local hematite. Porosity is good (20% - visual estimate) and permeability is moderate. (b) Sample (KIM 5) Very fine grained, moderately well sorted, feldspathic arenite, comprising of monocrystalline quartz, feldspars (dominantly plagioclase) and detrital mud. Authigenic component comprises of hematite, siderite and calcite. Primary porosity is good and limited secondary porosity is noted. (c) Sample (02/11) - Medium grained poorly sorted feldspathic arenite. Detrital component comprises of monocrystalline and polycrystalline quartz, alkali and plagioclase feldspar. Mudclasts and lithic fragments are sparsely present. Authigenic component comprises of abundant hematite, feldspar and quartz overgrowths. Porosity is negligible owing to compaction and quartz and feldspar overgrowths. (d) Sample (KIMW 28/11) medium grained, very poorly sorted argillaceous sandstone. Detrital component comprises of monocrystalline and rare polycrystalline quartz, plagioclase feldspar. The authigenic component comprises of calcite cement and sparse hematite cement. Porosity is negligible due to downgrade by detrital clays, hematite and calcite pore occlusion.*

Kamego Formation: *(e) Sample (KAM 25) Cherty? tuffaceous mudstone with good secondary solution porosity (Sp, mainly vugs). Pore filling megaquartz & hematite are common. (f) Sample (KAM 23) Light greyish tuffaceous mudstone mostly with replacement silica & hematite. Very poor reservoir potential. (g) Sample (KAM 28) Feldspathic wacke with clays (Cl) intermixed with siderite & hematite. The main detrital*

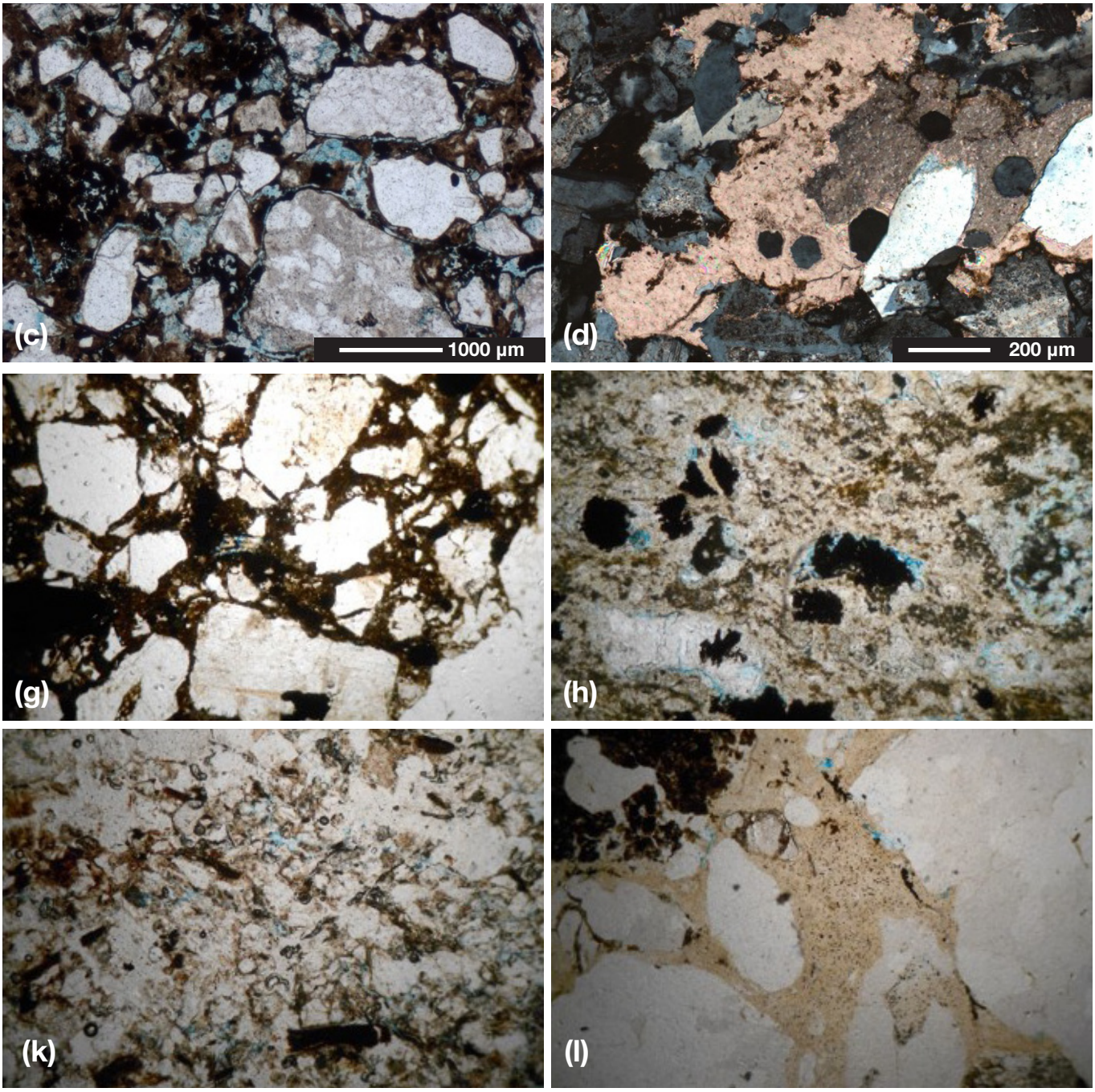

component is composed of monocrystalline quartz and feldspar. The main authigenic mineral and pore occluding mineral is pore filling hematite. Very poor reservoir potential. (h) Sample (KAM 18) Feldspathic wacke to paraconglomerate with metamorphic rock fragment granules/ pebbles and isolated secondary pores. Main pore occluding agent is detrital mud and pore filling and grain replacive calcite cement. Porosity is poor and predominantly secondary and associated with feldspar dissolution.

Loriu Sandstone: *(i) Sample (01/12/42) Wacke to microconglomerate comprised of polycrystalline quartz and sparse monocrystalline quartz, both alkali and plagioclase feldspar and abundant clays. Main authigenic mineral is grain replacive to pore filling brownish carbonate cement. Porosity is very poor and is secondary - mainly associated with the dissolution of feldspars and fracturing of detrital quartz grains. (j) Sample (01/12/12) Argillaceous poorly sorted sublithic-subfeldspathic arenite. The main detrital components are polycrystalline and sparse monocrystalline quartz, with plagioclase feldspar. Porosity is mainly confined to isolated secondary dissolution pores attributable to the dissolution of feldspars. Porosity is poor overall. (k) Sample (01/12/11) - Wacke (quartz-rich overall) with cryptocrystalline matrix. Main detrital component is quartz, metamorphic rock fragments, sparse feldspars and detrital clays. The authigenic components are mainly pore filling calcite (and siderite). Porosity is negligible. (l) Sample (02/12/08) Fine grained, micaceous lithic arenite. Detrital component is polycrystalline quartz, metamorphic rock fragments and detrital clays. The authigenic component comprises mainly of kaolinite clays and siderite. Porosity is poor and is concentrated to thin open fractures.*

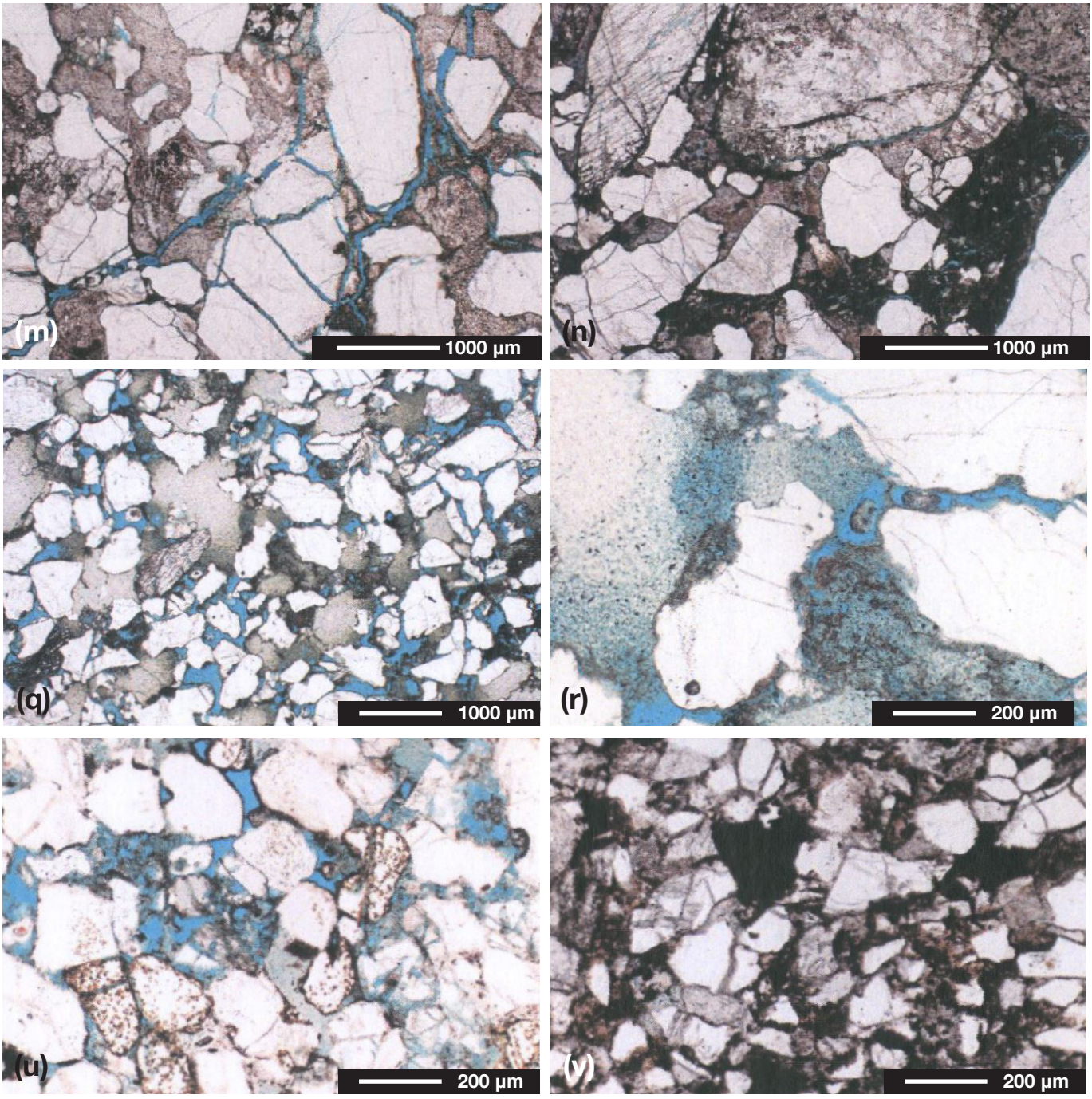

Lapur Sandstone: *(a) Coarse grained poorly sorted subfeldspathic arenite that is cemented by calcite/dolomite. Artificial pores are common. Porosity is moderate to good. (b) Polymictic paraconglomerate with common pore filling calcite/dolomite. Microporosity is locally noted. (c) Medium grained, moderately well sorted subfeldspathic-sublithic arenite with pore-filling clays and calcite. Porosity/permeability is moderate to good. (d) Coarse grained, moderately sorted subfeldspathic arenite with common pore filling kaolinite. Porosity is good (mainly secondary pores and micropores) (Core Laboratories, 2011).* **Mount Porr Sandstone:** *(q and r) Moderately sorted, medium grained feldspathic arenite with common pore filling kaolinite. Porosity is good to very good: secondary pore and micropores, the latter being concentrated within*

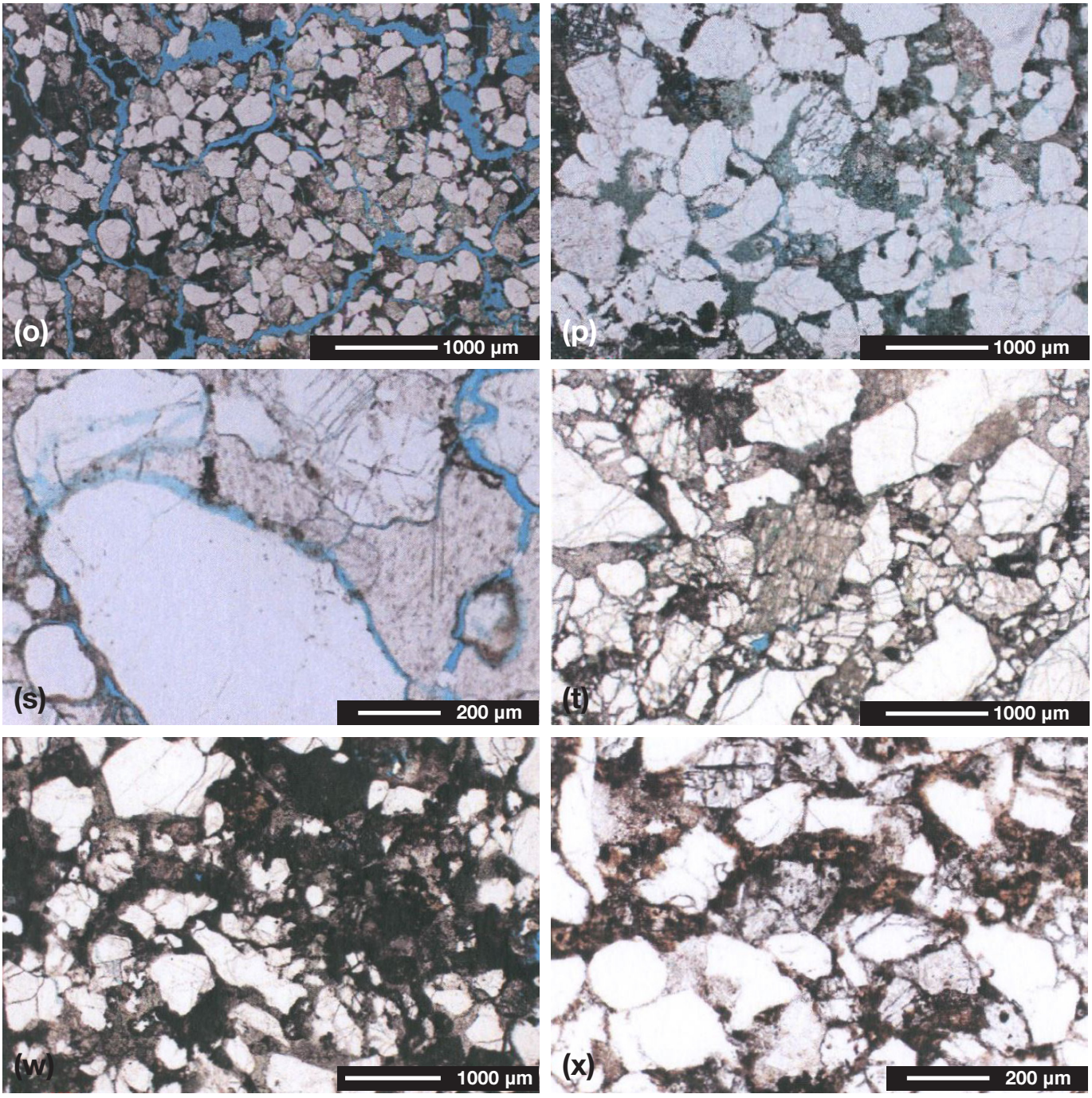

dissolved grains and between coarse kaolinite booklets. (s) Coarse grained poorly sorted feldspathic arenite with poor to moderate porosity. Porosity is occluded by pore filling and locally grain replacive calcite cement. (t) Poorly sorted feldspathic arenite with abundant pore filling calcite, poor to locally moderate porosity. (Core Laboratories, 2011). **Lokone Sandstone:** *(u) Fine grained, moderately well sorted feldspthic arenite with common pore filling kaolinite. Porosity is moderate to locally good. (v) Moderately well sorted calcite/dolomite cemented feldspathic arenite. Porosity is negligible. (w) Fine grained, well sorted lithic-rich feldspathic arenite with common calcite and clays. Porosity and permeability is poor. (x) Medium grained poorly sorted clayey lithic-rich feldspathic arenite with poor porosity overall. (Core Laboratories, 2011).*

References

• Adams, A.E, Mackenzie, W.S, Guilford, C., 1984. Atlas of sedimentary rock under the microscope, p. 104.
• Abeinomugisha, D., Kasande, R., 2012. Tectonic control on hydrocarbon accumulation in the intracontinental • Albertine Graben of the East African Rift System. In: Gao, D. (Ed.), Tectonics and Sedimentation: Implications for Petroleum systems, American Association of Petroleum Geologists Memoir 100, p. 209-228.
• Africa Oil Corporation, 2011. Hunting for Elephants in East Africa's Rift Basins. Accessed 24th February 2014, http://www.africaoilcorp.com/i/pdf/AOI-Hunting-Elephants-October-2011.pdf
• Africa Oil Corporation, 2014. String of pearls-Well summary. Accessed 15th August 2014, http://www.africaoilcorp.com/i/pdf/AOI-well-summary.pdf
• Arambourg, C., 1933a. Découverte d'un gisement de Mammifères burdigaliens dans le Bassin du lac Rodolphe (Afrique Orientale). Comptes Rendus Société géologique de France 14, 221-222.
• Arambourg, C., 1933b. Les formations prétertiaires de la bordure occidentale du lac Rodolphe (Afrique Orientale). Comptes Rendus de l'Académie des Sciences, Paris 197, 1663-1665.
• Arambourg, C., Wolff, R.G., 1969. Nouvelles données paléontologiques sur l'âge des grès du Lubur (Turkana Grits) à l'Ouest du lac Rodolphe. Comptes Rendus Société géologique de France 6, 190-192.
Athmer, W., Luthi, S.M., 2011. The effect of relay ramps on sediment routes and deposition: A review. Sedimentary Geology 242(1-4), 1-17.
• Baker, B.H., 1965. An Outline of the Geology of the Kenya Rift Valley: UMC/UNESCO Seminar Nairobi, April 1965. II. Report on the geology and geophysics of the East African Rift System: University College, Nairobi, 1-19.
• Baker, B.H., Wohlenberg, J., 1971. Structure and Evolution of the Kenya Rift Valley. Nature 229, 538-542.
• Baker, B.H., Williams, L.A.J., Miller, J.A., Fitch, F.J., 1971. Sequence and geochronology of the Kenya Rift volcanics. Tectonophysics 11, 191-215.
• Baker, B., Mitchell, J.G., and Williams, L.A.J., 1988. Stratigraphy, Geochronology and Volcano-Tectonic evolution of the Kedong-Naivasha-Kinangop Region, Gregory Rift Valley, Kenya. Journal of the Geological Society 145 (1), 107-116. doi:10.1144/gsjgs.145.1.0107.
• Berger, P., 1989. Rainfall and agro-climatology of the Laikipia Plateau, Kenya. African Studies Series A7, Institute of Geography, University of Bern, Switzerland.
• Behrensmeyer, A.K., Deino, A.L., Hill, A., Kingston, J.D., Saunders, J.J., 2002. Geology and geochronology of the middle Miocene Kipsaramon site complex, Muruyur Beds, Tugen Hills, Kenya. Journal of Human Evolution 42(1-2), 11-38.
• Beydoun, Z.R., Sikander, A.H., 1992. The Red Sea-Gulf of Aden: Re-assessment of hydrocarbon potential. Marine and Petroleum Geology 9, 474-485.
• Binks, R.M., Fairhead, J.D., 1991. A plate tectonic setting for Mesozoic rifts of West and Central Africa. In: Ziegler, P.A. (Ed.), Geodynamics of Rifting, Volume II. Case History Studies on Rifts: North and South America and Africa. Tectonophysics 213, 141-151.
• Bishop, W.W., Chapman, G.R., 1970. Early Pliocene sediments and fossils from the northern Kenya Rift. Nature 226, 914-918.
• Bishop, W.W., Hill, A., Miller, J.A. 1971. Succession of Cainozoic vertebrate assemblages fron the northern Kenya, Rift Valley. Nature 233, 389-394.
• Bishop, W.W., Pickford, M.H.L., 1975. Geology, fauna and palaeoenvironment of the Ngorora Formation, Kenya Rift Valley. Nature 254, 185-192.

References

• Boschetto, H.B., Brown, F.H., McDougall, I.M., 1992. Stratigraphy of the Lothidok Range, Northern Kenya, and K-Ar ages of its Miocene primates. Journal of Human Evolution 22, 47-71.

• Bosworth, W., Lambiase, J., Keisler, R., 1986. A New Look at Gregory's Rift: The Structural Style of Continental Rifting. Eos 67, 29, 577-583.

• Browne, S.E., Fairhead, J.D., Mohamed, I.I., 1985. Gravity study of the White Nile Rift, Sudan, and its regional tectonic setting. Tectonophysics 113, 123-137.

• Burke, K., MacGregor, D.S., Cameron, N.R., 2003. Africa's petroleum systems: four tectonic 'aces' in the past 600 million years. In: Arthur, T.J., MacGregor, D.S., Cameron, N.R. (Eds.), Petroleum geology of Africa: new themes and developing technologies. Geological Society, London, Special Publication 207, 21-60.

• Burgess, C.F., 1985. The structural and stratigraphic evolution of Lake Tanganyika: a case study of continental rifting. Thesis, Duke University, Durham, 46 pp.

• Burgess, C.F., Rosendahl, B.R., Sander, S., Burgess, C.A., Lambiase, J., Derksen, S., Meader, N., 1988. The structural and stratigraphic evolution of Lake Tanganyika: A case study of continental rifting. In: Manspeizer, W. (Ed.), Rifting and the Opening of the Atlantic Ocean, Elsevier, Amsterdam, p. 861-881.

• Chapman, G.R., 1971. The geological evolution of the northern Kamasia Hills, Baringo District, Kenya. Ph.D. dissertation, University of London, London, United Kingdom.

• Chapman, G.R., Brook, M., 1978. Chronostratigraphy of the Baringo Basin, Kenya. Geological Society (London) Special Publication 6, 207-223.

• Chapman, G.R., Lippard, S.J., Martyn, J.E., 1978. The stratigraphy and structure of the Kamasia Range, Kenya Rift Valley. Journal of the Geological Society of London 135, 265-281. doi:10.1144/gsjgs.135.3.0265

• Cohen, A.S., 1989. Facies relationships and sedimentation in large rift lakes and implications for hydrocarbon exploration: Examples from lakes Turkana and Tanganyika. Palaeogeography, Palaeoclimatology, Palaecology 70, 65-80.

• Cohen, K.M., Finney, S., Gibbard, P.L., 2013. International Chronostratigraphic Chart. International Commission on Stratigraphy.

• Collier, R.E., Gawthorpe, R.L., 1995. Neotectonics, drainage and sedimentation in central Greece: insights into coastal reservoir geometries in syn-rift sequences. Geological Society of London Special Publication 80, 165-181.

• Collinson, J.D., 1996. Alluvial sediments. In: Reading, H.G. (Ed.), Sedimentary environments: processes, facies and stratigraphy (3rd edition). Blackwell, Oxford. p. 688.

• Corti, G., 2011. Evolution and characteristics of continental rifting: Analog modeling-inspired view and comparison with examples from the East African Rift System. Tectonophysics 522-523, 1-33.

• Coulter, G.W., 1963. Hydrological changes in relation to biological production in southern Lake Tanganyika. Limnology Oceanography 8, 463-477.

• Daoudi, L., Potdevin, J.-L., 2002. Effets thermique et hydrothermal de la coulée de basalte triasico-liasique sur les argiles du bassin d'Argana (Maroc). Comptes Rendus Géosciences 334, 463-468.

• Deino, A.L., Hill, A., 2002. 40Ar/39Ar of the Chemeron Formation strata encompassing the site of hominid KNM-BC 1, Tugen Hills, Kenya. Journal of Human Evolution 42, 141-151.

• Demaison, G.J., Moore, G.T., 1980. Anoxic environments and oil source bed genesis. Organic Geochemistry 2, 9-31.

• Desprès, A., 2008. Evolution tectono-sédimentaire des bassins de rift Crétacé-Paléogène du Nord du Kenya. Master 2, Université de Rennes 1, France, 37 p.

• Dodson, R.G., 1963. Geology of the South Horr area. Geological Survey of Kenya, Report No. 60, p. 53.

• Dodson, R.G., 1971. Geology of the area south of Lodwar. Geological Survey of Kenya, Report No. 87, p. 36.

References

• Dou, L., Xiao, K., Cheng, D., Shi, B., Li, Z., 2006. Petroleum geology of the Melut Basin and the Great Palogue Field, Sudan. Marine and Petroleum Geology 24, 129-144.

• Ducrocq, S., Boisserie, J.R., Tiercelin, J.-J., Delmer, C., Garcia, G., Kyalo, M.F., Leakey, M.G., Marivaux, L., Otero, O., Peigné, S., Tassy, P., Lihoreau, F., 2010. New Oligocene vertebrate localities from Northern Kenya (Turkana Basin). Journal of Vertebrate Paleontology 30(1), 293-299.

• Ducrocq, S., Manthi, F.K., Lihoreau, F., 2011. First record of a parapithecid primate from the Oligocene of Kenya. Journal of Human Evolution 61, 327-331.

Dunkelman, T.J., Karson, J.A., Rosendahl, B.R., 1988. Structural style of the Turkana Rift, Kenya. Geology 16, 258-261.

• Dunkelman, T.J., Rosendahl, B.R., Karson, J.A., 1989. Structure and stratigraphy of the Turkana rift from seismic reflection data. Journal of African Earth Sciences 8, 489-510. doi:10.1016/S0899-5362(89)80041-7.

• Ebinger, C.J., Crow, M.J., Rosendahl, B.R., Livingstone, D.A., Le Fournier, J., 1984. Structural evolution of Lake Malawi, Africa. Nature 308, 627-629.

• Ebinger, C.J., Rosendahl, B.R., Reynolds, D.J., 1987. Tectonic model of the Malawi rift, Africa. Tectonophysics 141, 215-235.

• Ego, J.K., 1994, Sedimentology and diagenesis of Neogene sediments in the central Kenya Rift Valley. M.Sc. unpublished thesis, University of Saskatchewan, Saskatoon, Saskatchewan, Canada, 148 p.

• Fairhead, J.D., Mitchell, J.G., Williams L.A.J., 1972. New K/Ar Determinations on Rift Volcanics of S. Kenya and their bearing on age of rift faulting. Nature Physical Science (London) 238(83), 66-69.

• Fuchs, V.E., 1935. The Lake Rudolf rift valley expedition, 1934. Geographical Journal 86, 114-142.

• Fuchs, V.E., 1939. The geological history of the Lake Rudolf basin, Kenya Colony. Philosophical Transactions of the Royal Society London 229, 219–274.

• Gao, Dengliang, 2012. Dynamic interplay among tectonics, sedimentation and petroleum systems: An introduction and overview. In: Gao, D. (Ed.), Tectonics and Sedimentation: Implications for Petroleum Systems, American Association of Petroleum Geologists Memoir 100, 1-14.

• Gawthorpe, R.L., Hurst, J.M., 1993. Transfer zones in extensional basins: their structural style and influence on drainage development and stratigraphy. Journal of the Geological Society, London 150, 1137-1152.

• Gawthorpe, R.L., Fraser, A.J., Collier, R.E., 1994. Sequence stratigraphy in active extensional basins: implications for the interpretation of ancient basin-fills. Marine and Petroleum Geology 11, 6, 642-658.

• Gawthorpe, R.L., Leeder, M.R., 2000. Tectono-sedimentary evolution of active extensional basins. Basin Research 12, 195-218.

• Gregory, J.W., 1921. The Rift Valleys and Geology of East Africa. Seeley Service, London, p 479.

• Guiraud, R., Bosworth, W., Thierry, J., Delplanque, A., 2005. Phanerozoic geological evolution of Northern and central Africa: An overview. Journal of African Earth Sciences 43, 83-143.

• Hanes, J.A., York, D., Hall, C.M., 1985. An 40Ar/39Ar geochronological and electron microprobe investigation of an Archean pyroxenite and its bearing on ancient atmospheric compositions. Canadian Journal of Earth Sciences 22(7), 947-958.

• Hautot, S., Tarits, P., Whaler, K., Le Gall, B., Tiercelin, J.-J., Le Turdu, C., 2000. Deep structure of the Baringo Rift Basin (central Kenya) from three-dimensional magneto-telluric imaging: Implications for rift evolution. Journal of Geophysical Research 105, B10, 23,493-23,518. doi:10.1029/2000JB900213.

• Herbert, C., 2013. Rift Basins of the Turkana Region, Kenya (EARS). East Africa's New Frontier? Proceedings of the 6th East Africa Petroleum Conference and Exhibition, Arusha, Tanzania. 6th-8th March, 2013.

Herbin, J.P., 1979. Sédimentation de rift : géochimie organique des sédiments récents du lac Bogoria. Rapport Institut Français du Pétrole 26881.

References

• Hetzel, R., Strecker, M.R., 1994. Late Mozambique Belt structures in western Kenya and their influence of the Cenozoic Kenya Rift. Journal of Structural Geology 16, 189-201.

• Hill, A., 1999, The Baringo Basin, Kenya: From Bill Bishop to BPRP. In: Andrews, P., Banham, P., (Eds.), Late Cenozoic environments and hominid evolution: A tribute to Bill Bishop, Geological Society (London), p. 85-97.

• Hill, A., Curtis, G., Drake, R., 1986. Sedimentary stratigraphy of the Tugen Hills, Baringo, Kenya. In: Sedimentation in the African Rifts. In: Frostick, L.E., Renaut, R.W., Reid I. and Tiercelin, J.-J. (Eds.). Geological Society of London Special Publication 25, 285-295.

• Hubbert, M.K., 1965. National Academy of Sciences Report on Energy Resources. REPLY, American Association of Petroleum Geologists, 49, 1720-1727.

• Huc, A. Y., Le Fournier, J., Vandenbroucke, M., Bessereau, G., 1990. Northern Lake Tanganyika - An Example of Organic Sedimentation in an Anoxic Rift Lake. Lacustrine Basin Exploration: Case Studies and Modern Analogs A133, 169-208.

• Jones, G.P., 1965. Red beds in Eastern Nigeria. Sedimentology 5, 235 – 247.

• Joubert, P., 1966. Geology of the Loperot area. Geological Survey of Kenya Report 74, p. 52.

• Kalisa, K.F., 2013. Developments in Uganda's emerging oil and gas sector. Proceedings of the 6th East Africa Petroleum Conference and Exhibition. Arusha, Tanzania.

• Karp, T., Scholz, C.A., McGlue, M., 2012. Structure and stratigraphy of the Lake Albert Rift, East Africa: Observations from seismic reflection and gravity data. In: Baganz, O.W., Bartov, Y., Bohacs, K. and Nummedal, D. (Eds.), Lacustrine sandstone reservoirs and hydrocarbon systems, American Association of Petroleum Geologists Memoir 95, 299-318.

• Katz, B.J., 1995. A survey of rift basin source rocks. In: Lambiase, J.J. (Ed.), Hydrocarbon Habitat in Rift Basins, Geological Society Special Publication 80, 213-242.

• Kelts, K., 1988. Environments of deposition of lacustrine petroleum source rocks: An introduction. In: Fleet, A.J., Kelts, K., Talbot, M.R. (Eds.), Lacustrine Petroleum Source Rocks, Geological Society Special Publication 40, 3-26

• King, B.C., Chapman, G.R., 1972. Volcanism of the Kenya Rift Valley. Philosophical Transactions of the Royal Society A271, 185-208.

• KRISP Working Party, 1991. Large-scale variation in lithospheric structure along and across the Kenya Rift. Nature 354, 223-227.

• Kerio Valley Development Authority, 2010. Environmental Impact Assessment Project Report of the proposed rehabilitation of arror irrigation project. p 110.

• Lambiase, J.J., Bosworth, W., 1995. Structural controls on sedimentation in continental rifts. In: Lambiase, J.J. (Ed.), Hydrocarbon Habitat in Rift Basins, Geological Society Special Publication 80, 117-144.

• Leakey, M., Grossman, A., Gutiérrez, M., Fleagle, J.G., 2011. Faunal change in the Turkana Basin during the Late Oligocene and Miocene. Evolutionary Anthropology: Issues, News, and Reviews 20, 238-253.

• Le Turdu, C., Coussement, C., Tiercelin, J.-J., Renaut, R.W., Rolet, J., Richert, J.-P., Coquelet, D., 1995. Rift basin structure and depositional patterns interpreted using a 3D remote sensing approach: the Baringo and Bogoria Basins, Central Kenya Rift, East Africa. Bull. Cent. Rech. Explor.-Prod. ElfAquitaine 19 (1), 1–37.

• Le Turdu, C., Tiercelin, J.-J., Richert, J.-P., Rolet, J., Renaut, R.W., Lezzar, K. E., Coussement, C., Xavier, J. P., 1999. Influence of pre-existing oblique discontinuities on the geometry and evolution of extensional fault patterns: Evidence from the Kenya Rift using SPOT imagery. In: Morley, C.K. (Ed.), Geoscience of Rift Systems - Evolution of East Africa. AAPG Studies in Geology 44, 173-191.

• Leeder, M.R., Gawthorpe, R.L., 1987. Sedimentary models for extensional tilt-block/half-graben basins. In: Coward, M.P., Dewer, J. F., Hancock, P.L. (Eds.), Continental Extensional Tectonics, Geological Society Special Publication 28, 139-152.

References

• Leeder, M.R., Jackson, J.A., 1993. The interaction between normal faulting and drainage in active extensional basins with examples from the western United States and central Greece. Basin Research 5, 79-102.

• Leeder, M.R., Mack, G.H., Salyards, S.L., 1996. Axial-transverse fluvial interactions in half-graben: Plio-Pleistocene Palomas basin, southern Rio Grande Rift, New Mexico, USA. Basin Research 12, 225-241.

• Le Maître, R.W., Streckeisen, A., Zanettin, B., Le Bas, M.J., Bonin, B., Batemann, P., Bellieni, G., Dudek, A., Efremova, S., Keller, J., Lameyre, J., Sabine, P.A., Schmid, R., Sorensen, H., Woolley, A.R., 2002. Igneous Rocks. A classification and glossary of terms. Recommendations of the International union of Geological Sciences Subcommission on the Systematics of Igneous Rocks. 2nd Edition. Cambridge University Press, p. 236.

• Lezzar, K. E., 1997. Évolution du Bassin Nord du Lac Tanganyika, Rift Est-Africain, depuis le Miocène Supérieur. Analyse de la cinématique du rifting et des processus sédimentaires à partir de données de sismique réflexion, imagerie satellitaire et carottages. Thèse de Doctorat Nouveau Régime, Université de Bretagne Occidentale, Brest, p. 300.

• Lezzar, K. E., Tiercelin, J.-J., De Batist, M., Cohen, A.S., Bandora, T., Van Rensbergen, P., Le Turdu, C., Wafula, M., Klerkx, J., 1996. New seismic stratigraphy and Late Tertiary history of the North Tanganyika Basin, East African Rift system, deduced from multifold reflection and high-resolution seismic data and piston core evidence. Basin Research 8, 1-28.

• Lippard, S.J., 1972. The Stratigraphy and Structure of the Elgeyo Escarpment, Southern Kamasia Hills and Adjoining Areas, Rift Valley Province, Kenya. PhD Thesis, University of London.

• Lippard, S.J., 1973. The petrology of phonolites from the Kenya Rift. Lithos 6, 217-234. doi:10.1016/0024-4937(73)90083-2.

• Lo, C.H., Onstott, T.C., 1989. 39Ar recoil artifacts in chloritized biotite. Geochimica et Cosmochimica Acta 53, 2697-2711.

• Lowe, D.R., 1979. Sediment gravity flows: their classification and some problems of application to natural flows and deposits: Society of Sedimentary Geology Special Publication, 27, 75-82.

• Lowe, D.R., 1982. Sediment gravity flows: II. Depositional models with special reference to the deposits of high-density turbidity currents. Journal of Sedimentary Petrology 52, 279-297.

• Maguire, P.K.H., Swain, C.J., Masotti, R., Khan, M.A., 1994. A crustal and uppermost mantle cross sectional model of the Kenya Rift from seismic and gravity data, Tectonophysics 236, 217-249.

• Mann, P., Gahagan, L., Gordon, M.B., 2003. Tectonic setting of the world's giant oil and gas fields, In: Halbouty, M.T. (Ed.), Giant oil and gas fields of the decade 1990-1999, American Association of Petroleum Geologists Memoir 78, 15-105.

• Marivaux, L., Lihoreau, F., Manthi, F.K., Ducrocq, S. 2012. A new basal phiomorph (Rodentia, Hystricognathi) from the late Oligocene of Lokone (Turkana Basin, Kenya). Journal Vertebrate Paleontology. 32(3), 646 - 657.

• Mark, D.F., Stuart, F.M., De Podesta, M., 2011. New high-precision measurements of the isotopic composition of atmospheric argon. Geochimica Cosmochimica Acta 75, 7494-7501.

• Miall, A.D., 1988. Reservoir heterogeneities in fluvial sandstones: lessons from outcrop studies. American Association of Petroleum Geologists Bulletin 72, 682-697.

• Miall, A.D. 1996. The Geology of Fluvial Deposits. Sedimentary Facies, Basin Analysis, and Petroleum Geology. Berlin, Heidelberg, New York, London, Paris, Tokyo, Hong Kong: Springer-Verlag. p. 600.

• Morad, S., 1998. Carbonate cementation in sandstones: distribution patterns and geochemical evolution. International Association of Sedimentologists Special Publication 26, 1-26.

• Morano, S., Tiercelin, J.-J., Thuo, P., Muia, G., Pulman, A., Comfort, G., 2011. Combining outcrop data with sub-

surface data to better understand the petroleum system of the Kenya segment of the Eastern arm of the East Africa Rift System. 10th PESGB/HGS Conference on African E & P, London, 7-8 September 2011. Abstract Volume, 42.
• Morley, C.K., 1995. Developments in the structural geology of rifts over the last decade and their impact on hydrocarbon exploration. In: Lambiase, J.J. (Ed.), Hydrocarbon Habitat in Rift Basins, Geological Society Special Publication 80, 1-32.
• Morley, C.K., Ngenoh, D.K., Ego, J.K., 1999. Introduction to the East African Rift System. In: Morley, C.K., (Ed.), Geoscience of Rift Systems-Evolution of East Africa, American Association of Petroleum Geologists Studies in Geology No. 44, 1-18.
• Mugisha, F., 1994. Processing and interpretation of seismic and gravity data from the Kerio and northern Malawi Rifts, Africa. Masters thesis, University of Leeds, p. 161.
• Mugisha, F., Ebinger, C.J., Strecker, M., Pope, D., 1997. Two-stage rifting in the Kenya rift: implications for half-graben models. Tectonophysics 278, 63-81.
• Muia, G., Tiercelin, J.-J., 2013. Palaeogeographical reconstruction of successive rift lake environments in the northern and central segments of the Kenya Rift from Paleogene to middle-upper Miocene: To the search of potential source and reservoir rocks. The 6th East African Petroleum Conference & Exhibition, East African Region – The Emerging Destination For Investment and Future Supply of Oil and Gas for Sustainable Development. Arusha International Conference Center, Arusha, Tanzania, 6th-8th February, 2013.
• Murray-Hughes, R., 1933. Notes on the Geological Succession, Tectonics and Economic Geology of the Western Half of the Kenya Colony. Report Geological Survey of Kenya 3, 8 p.
• National Oil Corporation of Kenya., 2010. The geology of the Central Kenya Rift. Internal report, p. 42.
• Neumaier, M., Tiercelin, J.-J., Nalpas, T., Castillo, J.M., 2014. Basin analysis and petroleum systems modelling of the Lokichar Basin (Kenya). AAPG International Conference and Exhibition: The spirit between continents: Energy Geosciences in a changing world, Turquie (2014).
• Neves, M.A., Morales, N., Saad, A.R., 2005. Facies analysis of tertiary alluvial fan deposits in the Jundiaí region, São Paulo, southeastern Brazil. Journal of South American Earth Sciences 19, 513-524.
• Nichols, G., 2009. Sedimentology and Stratigraphy, 2nd ed., Wiley-Blackwell, West Sussex, UK. p. 411.
• OceanGrove Geoscience Limited., 2006. A guide to petroleum geochemistry - Training guides in petroleum geochemistry. Reference Manual.
• O'Connor, P.M., Sertich, J.J.W., Manthi, F.K., 2011. A pterodactyloid pterosaur from the Upper Cretaceous Lapurr sandstone, West Turkana, Kenya. Anais da Academia Brasileira de Ciências 83(1), 309-315.
• Ochan, A., Amusgut, C., 2012. Reservoir cjaracterisation for field development, Albertine Graben, East African Rift. American Association of Petroleum Geologists, International Conference and Exhibition, Milan, Italy, 23rd – 26th, 2011.
• Paul, M., Lisa, G., Mark, B.G., 2003. Tectonic setting of the world giant oil and gas fields. In: Halbouty, M.T. (Ed.), Giant Oil and Gas Fields of the Decade 1990-1999. American Association of Petroleum Geology Memoir 78, 107-122.
• Peacock, D.C.P., Sanderson, D.J., 1991. Displacements, segment linkage and relay ramps in normal fault zones. Journal of Structural Geology 13, 721-733.
• Perrodon, A., 1976. Logique des bassins sédimentaires. Comptes Rendus Académie des Sciences, Paris 283, 1265-1268.
• Petroleum Exploration and Production Department, 2008. The petroleum potential of the Albertine Graben. Ministry of Energy and Mineral Development, Republic of Uganda.

References

• Petroleum Exploration and Production Department, 2011. Petroleum exploration and investment opportunities in the Albertine Graben-Uganda. Ministry of Energy and Mineral Development, Republic of Uganda, p 17.
• Petroleum Exploration and Production Department, 2014. Petroleum discoveries in the Albertine Graben. Ministry of Energy and Mineral Development, Republic of Uganda.
• Pettijohn, F.J., 1975, Sedimentary Rocks, 3rd Edition: New York, Harper & Row, p. 628.
• Pettijohn, F.J., Potter, P.E., Siever, R., 1987. Sand and Sandstone, New York, Springer Verlag, p. 553.
• Pickford, M.H., 1978. Geology, paleoenvironment and vertebrate faunas of the mid-Miocene Ngorora Formation, Kenya. In: Bishop, W.W. (Ed.), Geological background to fossil man, Geological Society of London Special Publication 6, 237–262.
• Postma, G., 1990. Depositional architecture and facies of river and fan deltas: a synthesis. In: Colella, A., Prior, D.B., (Eds.), Coarse-grained Deltas. International Association Sedimentologists Special Publication 10, 13-28.
Ramberg, I.B., Neumann, E.R., 1984. Physical characteristics and evolutionary trends of continental rifts. Tectonics, 7, 165-216.
• Rasmussen, D.T., Gutierrez, M., 2009. A mammalian fauna from the late Oligocene of northwestern Kenya. Palaeontographica 288(1-3), 1-52.
• Renaut, R.W., Tiercelin, J.-J., 1994. Lake Bogoria, Kenya Rift Valley: A sedimentological overview. In: Renaut, R.W., Last, W.M. (Eds.), Sedimentology and geochemistry of modern and ancient saline lakes. Society of Sedimentary Geology 50, 101-123.
• Renaut, R.W., Ego, J.K., Tiercelin, J.J., Le Turdu, C., Owen, R.B., 1999. Saline, alkaline paleolakes of the Tugen Hills - Kerio Valley region, Kenya Rift Valley. In: Andrews, P., Banham, P. (Eds.), Late Cenozoic Environments and Hominid Evolution: A tribute to Bill Bishop. Geological Society of London, 41-58.
• Renaut, R.W., Jones, B., 2000. Microbial precipitates around continental hot springs and geysers. In: Riding, R.E., Awramik, S.M. (Eds.), Microbial Sediments. Springer, Berlin, 187-195.
• Renne, P.R., Mundil, R., Balco, G., Min, K., Ludwi, R.L., 2011. Joint determination of 40K decay constants and 40Ar∗/40K for the Fish Canyon sanidine standard, and improved accuracy for 40Ar/39Ar geochronology. Geochimica Cosmochimica Acta 74, 5349–5367.
• Renne, P.R., Balco, G., Ludwig, R.L., Mundil, R., Min, K., 2011. Response to the comment by W.H. Schwarz et al. on «Joint determination of 40K decay constants and 40Ar∗/40K for the Fish Canyon sanidine standard, and improved accuracy for 40Ar/39Ar geochronology» by P.R. Renne et al. (2010). Geochimica Cosmochimica Acta 75, 5097-5100.
• Riaroh, D., Okoth, W., 1994. The geothermal fields of the Kenya Rift. Tectonophysics 236, 117-130.
• Roddick, J.C., Cliff, R.A., Rex, D.C., 1980. The evolution of excess argon in Alpine biotites. A 40Ar-39Ar analysis. Earth Planetary Science Letters 48, 185-208.
• Rose, F.R., Curd, S.R., 2005. 'Rift' development and new play concepts in the Albert Graben. The 2nd East African Petroleum Conference – "Energy for Sustainable Development. Imperial Resort Beach Hotel, Entebbe, Uganda, 2nd-4th March, 2005.
• Rosendahl, B.R., 1987. Architecture of continental rifts with special reference to East Africa. Annual Reviews. Earth and Planetary Sciences 15, 445-503.
• Rosendahl, B.R., Kilembe, E., Kaczmarick, K., 1992. Comparison of the Tanganyika, Malawi, Rukwa and Turkana Rift zones from analyses of seismic reflection data. In: Ziegler, P.A. (Ed.), Geodynamics of rifting, volume II: Case history studies on rifts-North and South America and Africa. Tectonophysics 213, 235-256.
• Rosendahl, B.R., Livingstone, D.A., 1983. Rift lakes of East Africa. New Seismic Data and Implications for Future Research. Episodes 1983, 1, 14-19.
• Rosendahl, B.R., Reynolds, D.J., Lorber, P.M., Burgess, C.F., McGill, J., Scott, D., Lambiase, J.J., Derksen,

References

S.J., 1988. Structural expressions of rifting: lessons from Lake Tanganyika, Africa. In: Frostick, L.E., Renaut, R.W., Reid, I., Tiercelin, J.-J. (Eds.), Sedimentation in the African Rifts, Geological Society of London Special Publication 25, 29-43.

• Rowntree, K.M., 1988. Rainfall characteristics, rainfall reliability and the definition of drought: Baringo District, Kenya. South African Geographical Journal 71(2), 74-80.

• Ruffet, G., Féraud, G., Amouric, M., 1991. Comparison of 40Ar/39Ar conventional and laser dating of biotites fram the North Trégor Batholith. Geochimica et Cosmochimica Acta 55, 1675–1688.

• Ruffet, G., Féraud, G., Ballèvre, M., Kiénast, J.R., 1995. Plateau ages and excess argon on phengites: a 40Ar/39Ar laser probe study of alpine micas (Sesia zone, Western Alps, northern Italy). Chemical Geology 121, 327-343.

• Savage, R.J.G., Williamson, P.G., 1978. The early history of the Turkana Depression. In: Bishop, W.W. (Ed.), Geological background to fossil man, Geological Society (London) Special Publication, 375-394.

• Scholz, C.A., Rosendahl, B.R., 1988. Low Lake Stands in Lakes Malawi and Tanganyika, East Africa, Delineated with Multifold Seismic Data. Science 240, 1645-1648.

• Scholz, C.A., Rosendahl, B.R., Scott, D.L., 1990. Development of coarse-grained facies in lacustrine rift basins: Examples from East Africa. Geology 18, 140-144.

• Scholz, C.A., King, J.W., Ellis, G.S., Swart, P.K., Stager, J.C., Colman, S.M., 2003. Paleolimnology of Lake Tanganyika, East Africa, over the past 100 kyr. Journal of Paleolimnology 30, 139-150.

• Sellwood, B.W., Price, G.D., 1993. Sedimentary facies as indicators of Mesozoic paleoclimates. Philosophical transactions of the Royal Society of London B341, 225-233.

• Selley, R. C., 1978. Porosity gradients in North Sea oil-bearing sandstones. Journal of the Geological Society of London 135, 119 – 135.

• Sertich, J.J.W., Sampson, S.D., Loewen, M.A., Gathogo, P.N., Brown, F.H., 2005. Dinosaurs of Kenya's rift: fossil preservation in the Turkana Grits of northern Kenya. Journal of Vertebrate Paleontology 25 (3), 114A.

• Sertich, J.J.W., Manthi, F.K., Sampson, S.D., Loewen, M.A., Getty, M., 2006. Rift valley dinosaurs: a new Late Cretaceous vertebrate fauna from Kenya. Journal of Vertebrate Paleontology 26, Supplement 3, 124 A.

• Shackleton, R.M., 1946. Geology of the country between Nanyuki and Maralal. Geological Survey of Kenya, Report No. 11, p. 54.

• Shackleton, R.M., 1951. A contribution to the geology of the Kavirondo Rift Valley. Journal of the Geological Society of London 106, 345-392.

• Simiyu, S.M., Keller, G.R., 1998. Upper crustal structure in the vicinity of Lake Magadi in the Kenya Rift Valley region. Journal of African Earth Sciences 27(3), 359-371.

• Surdam, R.C., Eugster H.P., 1976. Mineral reactions in the sedimentary deposits of the Lake Magadi region, Kenya. Geological Society of America Bulletin 87, 1739-1752.

• Talbot, M.R., Morley, C.K., Tiercelin, J.-J., Le Hérissé, A., Potdevin, J.L., Le Gall, B., 2004. Hydrocarbon potential of the Meso-Cenozoic Turkana depression, northern Kenya. II: Source rocks: quality, maturation, depositional environments and structural control. Marine and Petroleum Geology 21, 63-78.

• Tarits, C., Renaut, R.W., Tiercelin, J.-J., Le Hérissé, A., Cotton, J., Cabon, J.Y., 2006. Geochemical evidence of hydrothermal recharge in Lake Baringo, central Kenya Rift Valley. Hydrological Processes 20, 2027-2055.

• Thuo, P., 2009. Stratigraphic, petrographic and diagenetic evaluation of Cretaceous/Paleogene potential reservoir sandstones of Western Turkana, Kenya. Implications on the petroleum potential of Northwestern Kenya. Thèse de l'Université de Bretagne Occidentale, Brest, France, 139 p.

• Thuo, P., Muia, G., Tiercelin, J.-J., 2011. Examples of sedimentation in the rift lakes of Eastern Africa - Tectonic versus Climatic controls: A comparison between the Eocene-mid Miocene Lake Lokichar and the mid Miocene-Present Lake Turkana in Northern Kenya. Consequences on hydrocarbon prospects. 5th International Congress of Limnogeology, Konstanz, august 30-September 3, 2011.

References

• Tissot, B.P., Welte, D.H., 1978. Petroleum formation and occurrence. Springer, New York, p. 538.

• Tiercelin, J.-J., Thouin, C., Kalala Tshibangu, Mondeguer, A., 1989. Discovery of sublacustrine hydrothermal activity and associated massive sulfides and hydrocarbons in the north Tanganyika trough, East African Rift. Geology 17, 1053-1056.

• Tiercelin, J.-J., Mondeguer, A., 1991. The geology of the Tanganyika Trough, East African Rift. In: Coulter, G.W. (Ed.), Lake Tanganyika and its Life, British Museum Natural History Publications and Oxford University Press, 7-48.

• Tiercelin, J.-J., Boulègue, J., Simoneit, B.R., 1993. Hydrocarbons, Sulphides, and Carbonate Deposits Related to Sub-lacustrine Hydrothermal Seeps in the North Tanganyika Trough, East African Rift. In: Parnell, J., Kucha, H., Landais, P. (Eds.), Bitumens in Ore Deposits, Society for Applied to Mineral Deposits 9, 96-113.

• Tiercelin, J.-J., Potdevin, J.L., Morley, C.K., Talbot, M.R., Bellon, H., Rio, A., Le Gall, B., Vétel, W., 2004. Hydrocarbon potential of the Meso-Cenozoic Turkana Depression, northern Kenya. I. Reservoirs: depositional environments, diagenetic characteristics, and source rock-reservoir relationships. Marine and Petroleum Geology 21, 41-62.

• Tiercelin, J.-J., Cohen, A.S., Soreghan, M.J., Lezzar, K.-E., 1994. Pleistocene-Modern Deposits of the Lake Tanganyika Rift Basin, East Africa: An Example of Lacustrine Source Rocks and Reservoirs. In: Lacustrine Reservoirs and Depositional Systems, Society for sedimentary Geology Core Workshop 19, 37-59.

• Tiercelin, J.-J., Thuo, P., Potdevin, J. L., Nalpas, T., 2012a. Hydrocarbon Prospectivity in Mesozoic and Early-Middle Cenozoic Rift Basins of Central and Northern Kenya, Eastern Africa. In: Gao, D. (Ed.), Tectonics and Sedimentation: Implications for Petroleum Systems, American Association of Petroleum Geologists Memoir 100, 1-29.

• Tiercelin, J.-J., Potdevin J. L., Thuo, P., Abdelfettah, Y., Schuster, M., Bourqin, S., Bellon, H., Clement, J. P., Guillou, H., Nalpas, T., Riffet, G., 2012b. Stratigraphy, sedimentology and diagenetic evolution of the Lapur Sandstone in northern Kenya: Implications for oil exploration of the Meso-Cenozoic Turkana depression, Journal of African Earth Sciences 71, 43 – 79.

• Tiercelin, J.-J., Soreghan, M., Cohen, A.S., Lezzar, K.-E., Bouroullec, J.-L., 1992. Sedimentation in large rift lakes: examples from the Middle Pleistocene-Modern deposits of the Tanganyika trough, East African Rift System. Bulletin des centres de recherches Exploration-Production Elf-Aquitaine 16 (1), 83-111.

• Tiercelin, J.-J., Le Fournier, J., Herbin, J.P., Richert, J.P., 1980. Continental rifts: modern sedimentation, tectonic and volcanic control. Example from the Bogoria-Baringo graben, Gregory Rift, Kenya. In: Geodynamic evolution of the Afro-Arabic Rift System. Roma, Accademia Nazionale dei Lincei, Atti dei convegni Lincei 47, 143-164.

• Tiercelin, J.-J., Périnet, G., Le Fournier, J., Bieda, S., Robert, P., 1982. Lacs du rift est-africain, exemples de transition eaux douces-eaux salées: le lac Bogoria, Rift Gregory, Kenya. Mémoire Société géologique de France, N.S., 144, 217-230.

• Tiercelin J.-J., Vincens A. (coordonnateurs), Barton, C.E., Carbonel, P., Casanova, J., Delibrias, G., Gasse, F., Grosdidier, E., Herbin, J.P., Huc, A.Y., Jardiné, S., Le Fournier, J., Meliäres, F., Owen, R.B., Page, P., Palacios, C., Paquet, H., Peniguel, G., Peypouquet, J.P., Raynaud, J.F., Renaut, R.W., De Reneville, P., Richert, J.P., Riff, R., Robert, P., Seyve, C., Vandenbroucke, M., Vidal, G., 1987. Le demi-graben de Baringo-Bogoria, Rift Gregory, Kenya. 30.000 ans d'histoire hydrologique et sédimentaire. Bulletin des centres de recherches Exploration-Production Elf-Aquitaine 11, 2, 249-540.

• Tissot, B.P., Welte, D.H., 1978. Petroleum formation and occurrence. Springer, New York, p. 538.

• Tobin, R.C., 1997. Porosity prediction in frontier basins: a systematic approach to estimating subsurface reservoir quality from outcrop samples. In: Reservoir Quality Predication in Sandstones and Carbonates, J.A. Kupecz, J. Gluyas and S. Bloch (eds.), American Association of Petroleum Geologists Memoir, 69, 1-18.

References

• Tomasso, M., Underhill, R.A., Hodgkinson, A., Young, M.J., 2008. Structural styles and depositional architecture in the Triassic of the Ninian and Alwyn North fields: Implications for basin development and prospectivity in the northern North Sea. Marine and Petroleum Geology 25, 588-605.

• Tritlla, J., Partida, G. E., Levresse, G., Banks, D., Pironon, J., 2004. Fluorite deposits at Encantada-Buenavista, Mexico: products of Mississippi Valley type processes [Ore Geol. Rev. 23 (2003), 107–124]—a reply. Ore Geology Reviews 25, 329 – 332.

• Turner, G., 1971. 40Ar-39Ar ages from lunar Maria. Earth Planetary Science Letters 11, 169-191.

• Vincens, A., Tiercelin, J.-J., Buchet, G., 2006. New Oligocene-early Miocene microflora from the southwestern Turkana Basin. Palaeoenvironmental implications in the northern Kenya Rift. Palaeogeography, Palaeoclimatology, Palaeoecology 239, 470-486.

• Walsh, J., 1969. Mineral and thermal waters of Kenya. Mineral and thermal waters of the world. Oversea countries Report of the International Geological Congress 19, 105-110.

• Walsh, J., Dodson, R.G., 1969. Geology of Northern Turkana. Geological Survey of Kenya, Report No. 82, p. 42.

• Wayland, E.J., 1925. Oil in Uganda. Geological Survey of Uganda Memoir 1, p. 66. (unpublished).

• Wescott, W.A., Morley, C.K., Karanja, F.M., 1993. Geology of the Turkana Grits in the Lariu Range and Mt Porr areas, southern Lake Turkana, Northwestern Kenya. Journal of African Earth Sciences 16, 425-435.

• Wescott, W.A., Wigger, S.T., Stone, D.M., Morley, C.K., 1999. Geology and geophysics of the Lotikipi Plain. In: Morley, C.K. (Ed.), Geoscience of Rift Systems – Evolution of East Africa. American Association of Petroleum Geologists Studies in Geology 44, 55-65.

• Williamson, P.G., Savage, R.J.G., 1986. Early sedimentation in the Turkana Basin, northern Kenya. In: Frostick, L.E., Renaut, R.W., Reid, I., Tiercelin, J.-J. (Eds.), Sedimentation in the African Rifts. Geological Society London, Special Publication 25, 267-283.

• Wohlenberg, J., 1975. The structure of the lithosphere beneath the East African Rift zones from interpretation of Bouguer anomalies. In: Pilger, A., Rosler, A. (Eds.), Afar Depression of Ethiopia, 2. Schweizerbart, Stuttgart, 125-130.

Appendix

Appendix 1

Kimwarer, Kamego and Loriu Formations: description of thin sections from the representative volcanic and intrusive samples used in this work. Rock names are derived from the total alkali versus silica (TAS) diagram (Le Maître et al., 2002) using available chemical analyses (Appendix 2). When indicated, formation names are from Chapman et al. (1978) and Chapman and Brook (1978) and were interpreted from the location of the sample using the geological map by Walsh (1969). Three samples from Magadi, which are not discussed in this work, are also described.

Appendix 2

Kimwarer, Kamego and Loriu Formations: geochemical data from the volcanic and intrusive samples used in this work. Trace element compositions of representive rocks from Unit1, Unit 2 and Unit 3 along the Kimwarer section (see Table 4 for major element contents). Major and trace elements of the samples from Kamego and Loriu, and three samples from Magadi, which are not discussed in this work.

Appendix 3

Kimwarer, Kamego and Loriu Formations: GPS coordinates of the volcanic and intrusive samples studied in this work. Also shown, three samples from Magadi, which are not discussed in this work.

Appendix 4

Kimwarer, Kamego and Loriu Formations: geochronological 39Ar/40Ar results from the volcanic and intrusive samples used in this work. The appendix successively includes: (i) the isotopic ratio and decay constant values used for age calculations; (ii) the data from each step-heating experiments carried out on whole-rock fragments (WR) or sanidine grains (data from the Magadi samples, which are not discussed in this work, are also shown); (iii) the plots showing the age-spectra obtained from step-heating experiments versus cumulative 39Ar gas released for the volcanic samples from Kamego (and Magadi) and for the intrusive sample from Loriu; (iv) 36Ar/40Ar versus 39Ar/40Ar isochrone diagrams with ellipses showing the correlated errors for the Kimwarer samples KALW 11-11 (step heating experiment z1696) and TUM 05-11 (step heating experiment z1702).

Appendix 1

Unit #	Formation	Rock name (analyse/thin section ID)	**Field ID Sample Nb**	Description
Unit 3 (Kimwarer section)	Uasin Gishu Phonolites (lower member)	Phonolite massive lava flow (KEN 18)	**TUM01/11**	Texture is porphyritic (phenocryst poor <10 vol%), microlitic to trachytic and fluidal. Main phenocrysts are euhedral sanidine (up to 0.5cm), aegerine-augite, biotite and rare opaque minerals. Groundmass is predominantly composed of weathered sanidine-anorthoclase microlites, clinopyroxene and opaque mineral microcrysts. Euhedral feldspathoid microphenocrysts (noseane?) are present. Clay minerals form the main secondary phases.
		Phonolite massive lava flow (KEN 19)	**TUM02/11**	Texture is porphyritic to glomeroporphyritic (phenocryst up to ~10 vol%), microlytic to trachytic and fluidal. Main phenocrysts are euhedral sanidine (up to 1cm), aegerine-augite containing apatite needlelike and opaque mineral inclusions and minor opaque minerals. Groundmass is predominantly composed of sanidine-anorthoclase microlites and weathered clinopyroxene and opaque mineral microcrysts. Euhedral feldspathoid microphenocrysts (nepheline?) are present. Clay minerals form the main secondary phases. Cross-cutting veins are also present.
	Chof Phonolites	Phonolite massive lava flow (KEN 20)	**TUM03/11**	Texture is porphyritic (phenocrysts, up to 3cm in size represent about 25 vol% and locally up to 50 vol% of the rock) and amygdaloidal with a microlytic groundmass. Main phenocrysts are euhedral sanidine and corroded nepheline that may embay portions of the groundmass (including amygdules). The groundmass is mainly composed of weathered plagioclase and/or sanidine-anorthoclase microlites and glass. Apatite and opaque mineral microcrsysts are the main accessory phases. Carbonate and zeolite fill the amygdules.
		Phonolite massive lava flow (KEN 21)	**TUM04/11**	Texture is porphyritic (phenocrysts, up to 1cm in size represent about 25 vol% of the rock) and vesicular to amygdaloidal with a microlitic groundmass. Main phenocrysts are euhedral and locally elongate weathered sanidine and corroded nepheline (the phenocrysts embay portions of the groundmass). Carbonate and zeolite fill the amygdules. The groundmass is mainly composed of weathered plagioclase and/or sanidine microlites and glass. Apatite and opaque mineral microcrsysts are the main accessory phases..
		Phonolite massive lava flow (KEN 22)	**TUM05/11**	Texture is porphyritic (phenocrysts, up to 1cm in size represent about 40 vol% of the rock)) and amygdaloidal with a microlytic groundmass. Main phenocrysts are euhedral and locally elongate weathered sanidine and nepheline. Carbonate (calcite?)/zeolite filled amygdules are also noted. The phenocrysts embay portions of the groundmass (corrosion gulf?) The groundmass is mainly composed of weathered plagioclase and/or sanidine-anorthoclase microlites and glass. Euhedral to subhedral apatite and opaque mineral microcrsysts are the main accessory phases
	Elgeyo Basalts	Tephrite massive lava flow (KEN 23)	**TUM06/11**	Texture is porphyritic , locally glomeroporphyritic (phenocrysts are >1mm), and amygdaloidal with a microcristalline groundmass. Ultramafic rock. Main phenocrysts are euhedral-subhedral zoned clinopyroxene and rare subhedral olivine pseudomorphs and opaque minerals. The olivine pseudomorphs are rimmed by Fe hydroxides-clay (iddingsite) and filled by greenish clays-chlorite (serpentine?). Amygdules are filled by carbonates and rimmed by zeolites although zeolites can also fill the amygdules. Apatite needles are common in the amygdules. The groundmass is composed of weathered volcanic glass, weathered clinoyroxene, plagioclase microcrysts or micro-oikocrysts and opaque mineral microcrysts. Opaque minerals also form inclusions in the outer rims of the plagioclase and clinopyroxenes phenocrysts. The pinkish color of the outer clinopyroxene rims suggests Ti-rich augite.
		Tephritic breccia. Tuff or brecciated top/base of massive lava flow (KEN 24)	**TUM07/11**	The rock is made of ultramafic angular clasts up to 5mm in size and clinopyroxene clasts within a matrix of ash and carbonate forming a complex network of veins. Texture of the clasts is porphyritic to glomeroporphyritic (phenocryst agglomerates up to 2 mm in size), sometimes amygdaloidal (amygdules >3mm) with a microcrystalline groundmass. Main phenocrysts are zoned clinopyroxenes (Ti-rich ? augite), rare olivine pseudomorphs, nepheline (?) and opaque minerals. The amygdules are filled by carbonates (calcite?) and rimmed by iron hydroxides. The mesostasis is composed of weathered volcanic glass, opaque mineral, plagioclase and clinopyroxene microcrysts. Sample 24A represents a larger clast (block?)or the inner part of a massive flow.

Unit 2 (Kimwarer section)	Elgeyo Basalts	Tephritic dyke (KEN 26)	**KALW 02/11**	Texture is porphyritic to glomeroporphyritic, amygdoloidal, and microcrystalline. Ultramafic rock. Main phenocrysts are euhedral to subhedral zoned clinopyroxenes (Ti-rich ? augite), euhedral olivine pseudomorphs that are filled by chlorite and carbonates, and opaque minerals. The amygdules are filled by chlorite and carbonates and needlelike apatite crystals. The mesostasis is microcrystalline, made of opaque mineral, plagioclase (?) and clinopyroxene microcrysts.
		Tephrite massive lava flow (KEN 25)	**KALW 01/11**	Texture is porphyritic to glomeroporphyritic, and microcrystalline. Ultramafic rock. Main phenocrysts are euhedral to subhedral , zoned, colourless to pinkish clinopyroxenes (Ti-rich ? augite) with opaque mineral inclusions, euhedral olivine pseudomorphs that are filled by chlorite, carbonates, opaque minerals, hydroxides and clays. The microcrystalline mesostasis is composed of opaque minerals, plagioclase (often forming sub-poikilitic micro-oikocrysts with apatite inclusions)and clinoyroxene microcrysts.
		Tephrite massive lava flow (KEN 44)	**KALW 03/11**	Texture is porphyritic to glomeroporphyritic and microcrystalline with amygdules filled by carbonates, chlorite, clays and zeolite (?). Main phenocrysts are zoned,colourless to pinkish clinopyroxenes (Ti-rich ? augite), opaque minerals and subhedral olivine pseudomorphs. Apatite needles occur within the groundmass feldspar microcrysts. The microcrystalline groundmass is predominantly composed of clinopyroxene and opaque mineral microcrysts. A cryptocrystalline groudmass often embays groups of clinopyroxene phenocrysts. Plagioclase microcrysts are rare. Feldspathoid microcrysts are possibly present. Apatite. Scattered greenish clay minerals form the main secondary phases in the groundmass.
		Tephrite massive lava flow (KEN 27)	**KALW 04/11**	same texture and mineralogy as sample KEN 44
		Basanite massive lava flow (KEN 28)	**KALW 05/11**	Texture is porphyritic to glomeroporphyritic, amygdaloidal and microcrystalline. Phenocrysts include abundant euhedral to subhedral olivine pseudomorphs that are filled by chlorite, and carbonates, and abundant subhedral clinopyroxene and opaque minerals. Larger (up to a few mm in size) colorless to greenish clinopyroxene phenocrysts or phenocryst cores suggest aegyrine-augite compositions and smaller pinkish grouped clinopyroxene phenocrysts or phenocryst rims suggest Ti-augite compositions. The amygdules are filled by carbonates, zeolites and analcite (?) and contains needlelike apatite crystals. The microcrystalline mesostasis is composed opaque minerals, plagioclase and clinopyroxene microcrysts.
		Basanite massive lava flow (KEN 29)	**KALW 06/11**	same texture and mineralogy as sample KEN 28 with a few plagioclase microlites and weathered subhedral feldpsathoids (noseane?) microphenocrysts in the groundmass.
		Tephrite massive lava flow (KEN 30)	**KALW 07/11**	Texture is porphyritic to glomeroporphyritic, amygdoloidal, and microcrystalline to cryptocrystalline. Phenocrysts include euhedral zoned clinopyroxenes (<1mm long aegyrine-augite to Ti-augite compositions), euhedral olivine pseudomorphs that are filled by carbonates and low grade hydrothermal minerals, and opaque minerals. The amygdules are filled by carbonates. The mesostasis is weathered and composed of opaque mineral, plagioclase (often forming sub-poikilitic micro-oikocrysts) and clinopyroxene microcrysts.
		Picrobasalt massive lava flow (KEN 31)	**KALW 08/11**	Texture is porphyritic to glomeroporphyritic, amygdoloidal, and micro/cyptocrystalline. Main phenocrysts are euhedral zoned clinopyroxenes (<1mm long), euhedral olivine pseudomorphs that are filled by greenish to brownish clays, chlorite, carbonates and opaque minerals (>3mm). The rare amygdules are filled by carbonates and analcite (?). The mesostasis is weathered and composed of opaque mineral and clinopyroxene microcrysts. Plagioclase often forms sub-poikilitic micro-oikocrysts. Apatite is common in the plagioclase microcrysts.
		Tephrite or basalt massive lava flow (KEN 32)	**KALW 09/11**	Texture highly vesicular to amygdoloidal, porphyritic and micro to cyptocrystalline. Main rare phenocrysts are clinopyroxenes. The amygdules are filled or partly filled by zeolites, analcite?, brownish clays, iron hydroxide minerals and carbonates. The mesostasis is composed of weathered glass, opaque minerals and pyroxenes microcrysts.
		Tephrite or picrobasalt massive lava flow (KEN 33)	**KALW 10/11**	same texture and mineralogy as samples KEN 30/31
		Basalt massive lava flow (KEN 34)	**KALW 11/11**	same texture and mineralogy as samples KEN 30/31/33 with more abundant plagioclase micro-oikocrysts.

Unit 1(Kimwarer section)	Elgeyo Basalts	Trachybasalt or alkaline basalt Volcaniclast (KEN 35)	**KALW 23/11**	Texture is porphyritic, vesicular to amygdaloidal and microlitic. Main phenocrysts include euhedral plagioclase and clinopyroxene (augite / aegyrine augite) and opaque minerals. Sparse pseudomorphs of olivine are also noted and are infilled by clays. Abundant amygdules are rimmed by calcite and filled by low grade hydrothermal minerals e.g. zeolites and/or clays. The groundmass is composed of dark volcanic glass and plagioclase microlites.
		Trachybasalt or alkaline basalt Volcaniclast (KEN 35A)	**KALW 23/11**	same texture and mineralogy as sample KEN 35 with more abundant and larger amygdules
		Trachybasalt or alkaline basalt Volcaniclast (KEN 35B)	**KALW 23/11**	Idem sample KEN 35A
		Trachybasalt or alkaline basalt Volcaniclast (KEN 35C)	**KALW 23/11**	Idem sample KEN 35
		Trachybasalt or alkaline basalt Volcaniclast (KEN 35D)	**KALW 23/11**	Idem sample KEN 35
		Trachybasalt or basalt Volcaniclast (KEN 35E)	**KALW 23α/11**	Texture is porphyritic to glomeroporphyritic, fluidal and microlitic. Main phenocrysts are plagioclase (>1 cm in length) and clinopyroxene (augite). Opaque minerals often form microphenocrysts. Amygdules are absent. The groundmass is composed of dark volcanic glass and abundant plagioclase microlites.
		(KEN 36)	**Breccia**	Breccia containing rock fragments similar to KEN35C.
		Trachybasalt massive lava flow (KEN 37)	**KALW 24/11**	same texture and mineralogy as sample KEN 39.
		KEN 38	**Breccia**	
		Trachybasalt Volcaniclast from massive lava flow (KEN 39)	**KALW 26/11**	Texture is porphyritic to glomeroporphyritic, amygdaloidal, fluidal and microlitic. Main phenocrysts are zoned and often grouped clinopyroxene (augite >3mm in size), abundant scattered and often highly weathered plagioclase (>6mm in lenght), and rare opaque minerals. Sparse euhedral pseudomorphs of olivine are also noted and are infilled by green clays and chlorite. Amygdules (up to 3mm in diameter) are filled by carbonate (calcite) and other low grade hydrothermal minerals e.g. zeolites. Apatite inclusions in feldspars and groundmass. The groundmass is composed of weathered volcanic glass and abundant plagioclase and clinopyroxene microlites and opaque mineral microcrysts.

LORIU		Tephrite Dyke (K7)	**Loriu dyke**	Texture is porphyritic to glomeroporphyritic (phenocrysts are <.5mm), with a microlitic to microcystaline groundmass. Main phenocrysts are euhedral-subhedral zoned clinopyroxene, euhedral olivine phenocrysts and pseudomorphs, and opaque minerals. Olivine pseudomorphs are filled by greenish to brownish clays-chlorite assemblage. The groundmass is composed of plagioclase microlites and opaque mineral clinopyroxenes and olivine microcrysts. Apatite occurs as a common accessory phase. The pinkish color of the clinopyroxene rims suggests Ti-rich augite. A few enclaves of microgabbro are present.
KAMEGO		Phonolite Lava flow (K1)	**KAM (V) 30**	Porphyritic, phenocryst poor (a few vol%) with a fluidal and microlitic groundmass, phenocrsysts are small <0.3mm in size; phenocrysts are weathered clinopyroxene (augite?) and sanidine-anorthoclase with tiny spongy rims, most of the microlites are sanidine with few plagioclase. Microphenocryst of weathered feldspathoid are rare.
		Phonolite Lava flow (K2)	**KAM V2**	Porphyritic, phenocryst poor (a few vol percent), with a microlitic groundmass, Phenocrsysts are large .<1cm in length, mostly sanidine-anorthoclase with sometimes spongy rims. Greenish clinopyroxene phenocrysts to microphenocrysts– Aegirine-augite composition- are present; weathered to fresh feldspathoids (nepheline?) microphenocrysts, sanidine-anorthoclase and a few plagioclase microlites in the groundmass with opaque mineral microcrysts and abundant weathered volcanic glass

MAGADI		Basalt Lava flow (K3)	**KIR(V)2/13a**	Porphyritic, phenocryst poor (a few vol %) texture with a microlitic to trachytic groundmass, phenocrsysts are small .<0.5 cm in size; phenocrysts are partially resorbed plagioclase and euhedral plagioclase microcrysts, rare augite. Enclaves of trachytic rocks, microgabbro and quartz or microcline xenocrysts rimed by opaque minerals are common. The groudmass is composed of plagioclase microlites. Opaque minerals, olivine and clinopyroxene (augite) microcrysts are present. Carbonates and opaque minerals amygdules or pseudomorhs.
		Basalt Lava flow (K5)	**KIR(V)2/13b**	same as K3 and K4 with amygdules filled with clay minerals and carbonates
		Trachyte Lava flow (K6)	**KIR(V)1/13**	Porphyritic and trachytic texture; phenocrysts: sanidine-anorthoclase<1cm in length, aegerine-augite and rare opaque mineral. Groundmass composed by almost joined sanidine –anorhtoclase microlites, a few opaque mineral microcrsysts and rare flakes of orange-yellowish volcanic glass

Appendix 2

Table: trace element compositions

	Unit	Unit 1	Unit 2								Unit 3					
		Lava block	Lava flows							Dyke	Lava flows					
	Sample Nb	KEN 39	KEN 34	KEN 31	KEN 30	KEN 28	KEN 27	KEN 44	KEN 25	KEN 26	KEN 23	KEN 22	KEN 21	KEN 20	KEN 19	KEN 18
	Rock name	Tephrite / Trachybasalt	Basalt	Picrobasalt	Tephrite	Basanite	Tephrite	Tephrite	Tephrite	Tephrite	Tephrite	Phonolite	Phonolite	Phonolite	Phonolite	Phonolite
ppm	d.l. (ppm)															
As	1.20	< d.l.	< d.l.	< d.l.	< d.l.	< d.l.	< d.l.	< d.l.	< d.l.	< d.l.	< d.l.	< d.l.	1.87	< d.l.	2.106	< d.l.
Ba	1.50	1364	529.5	561.4	572.5	674.9	647.6	616.5	805.6	472.2	377.9	966.2	982.6	848.8	295.4	40
Be	1.00	2.601	2.208	2.151	2.827	2.868	2.464	2.309	2.41	2.35	2.359	6.284	6.232	6.498	6.925	8.533
Bi	0.10	< d.l.	< d.l.	< d.l.	< d.l.	< d.l.	< d.l.	< d.l.	< d.l.	< d.l.	< d.l.	< d.l.	< d.l.	< d.l.	< d.l.	< d.l.
Cd	0.15	0.233	0.247	0.225	0.243	0.211	0.214	0.22	0.222	0.221	0.21	0.367	0.352	0.381	0.403	0.512
Co	0.40	37.17	52.3	58.76	49.65	47.89	56.84	55.53	55.26	56.54	62.28	2.37	2.357	2.375	1.271	2.011
Cr	5.00	30.76	354.8	361.5	122	201.3	88.27	78.66	364.9	489.8	161	< d.l.	< d.l.	< d.l.	< d.l.	< d.l.
Cs	0.15	0.237	0.522	0.279	0.742	0.371	0.422	0.453	0.274	0.319	0.253	1.181	1.265	1.549	1.558	1.538
Cu	5.00	135.9	157.1	215.3	212.6	147.2	220	197.8	201.8	214.6	271.7	< d.l.	< d.l.	< d.l.	< d.l.	< d.l.
Ga	0.20	23.77	19.65	20.3	20.98	21.04	21.32	20.4	18.97	19.54	22.59	26.71	26.64	25.42	29.32	32.65
Ge	0.10	1.191	1.308	1.312	1.211	1.207	1.33	1.291	1.38	1.362	1.312	0.864	0.859	0.773	1.109	1.365
Hf	0.04	6.615	6.944	7.518	7.673	7.4	7.508	7.2	6.738	6.568	7.87	12.22	12.18	11.57	12.09	15.04
In	0.10	< d.l.	< d.l.	0.081	< d.l.	< d.l.	< d.l.	0.081	< d.l.	< d.l.	0.09	< d.l.	< d.l.	< d.l.	< d.l.	< d.l.
Mo	0.35	1.721	1.357	1.756	1.883	2.075	1.391	1.378	1.772	1.885	1.507	< d.l.	2.385	< d.l.	5.305	< d.l.
Nb	0.06	80.5	73.97	77.93	107.3	108.7	89.28	86.01	82.35	83.69	67.1	211.1	207.2	202	186.4	221.9
Ni	4.50	35.92	110.2	160.4	79.23	84.55	87.95	83.03	138.2	168.2	67.23	< d.l.	< d.l.	< d.l.	< d.l.	< d.l.
Pb	1.40	4.2983	5.1908	3.7787	4.8556	4.2651	4.5849	4.4558	3.7641	3.9159	3.953	8.9041	8.5909	8.4901	15.5001	20.2865
Rb	0.35	72.4	8.49	11.24	11.66	15.13	15.41	13.19	13.87	9.72	18.88	105.7	96.29	110.3	131.7	179
Sc	1.00	13.79	32.61	30.48	24.09	25.56	30.71	29.85	33.19	33.49	23.33	< d.l.	< d.l.	< d.l.	1.21	< d.l.
Sb	0.20	< d.l.	< d.l.	< d.l.	< d.l.	< d.l.	< d.l.	< d.l.	< d.l.	< d.l.	< d.l.	< d.l.	0.435	< d.l.	0.263	< d.l.
Sn	0.40	7.219	1.997	2.019	2.294	2.16	2.242	2.101	2.176	2.116	1.997	2.76	2.48	2.515	3.428	4.217
Sr	1.20	2507	747.6	1135	721.3	879	751.9	675.8	1541	1035	747.3	834.5	1351	899.5	115.9	74.83
Ta	0.02	5.903	5.643	5.9	7.904	7.735	6.514	6.376	6.057	6.002	5.182	14.9	14.45	14.21	12.93	15.09
Th	0.02	7.772	6.495	6.432	9.062	9.204	7.189	6.725	6.846	6.909	5.637	20.32	19.71	19.56	17.44	24.86
U	0.04	2.102	1.279	1.3	1.796	2.759	1.417	1.285	1.909	1.445	1.151	4.853	4.495	4.282	3.722	0.764
V	0.60	219.5	314.7	356.4	295	300.6	374.9	352	308	295.3	409.4	5.834	5.598	5.282	2.357	< d.l.
W	0.30	0.502	0.537	0.434	0.923	1.57	0.804	0.681	0.952	1.061	0.605	0.323	0.897	< d.l.	2.673	0.557
Y	0.40	29.39	23.1	24.54	26.83	26.07	25.61	23.86	27.24	23.01	30.24	37.65	38.37	38.28	46.5	44.73
Zn	11.00	136	132.2	141.2	144.7	136.7	145.7	137	126.8	127	163.3	131.3	126.9	127.7	175.6	190.2
Zr	1.30	310.4	293	315.4	349.2	346.3	322	310.9	295.3	291.7	315	600.5	622.8	590.5	593	717.8
La	0.05	82.29	54.07	56.13	88.54	85.74	62.39	58.94	67.84	57.54	55.36	159.2	154.9	154.1	134.9	135
Ce	0.1	157.8	131.7	138.6	172.7	166.1	149.6	146.4	135.4	134.6	136.3	280.1	270.7	269.5	232.7	213.4
Pr	0.01	17.56	15.39	16.31	19.6	18.73	17.56	16.88	15.81	15.6	16.78	27.64	26.55	26.74	22.51	21.33
Nd	0.03	63.05	58.46	62.96	73.13	68.6	65.55	63.71	59.61	58.63	66.86	88.22	84.87	85.8	68.81	62.93
Sm	0.01	10.86	10.67	11.55	12.76	11.9	11.74	11.44	10.56	10.37	12.64	12.7	12.35	12.4	10.34	9.219
Eu	0.004	3.201	3.174	3.486	3.787	3.572	3.548	3.422	3.2	3.174	3.873	3.384	3.342	3.268	2.439	1.509
Gd	0.02	8.192	8.378	9.053	9.798	9.233	9.31	8.914	8.39	8.23	10.52	8.865	8.861	8.74	7.878	6.999
Tb	0.006	1.12	1.138	1.222	1.317	1.271	1.264	1.212	1.15	1.119	1.448	1.355	1.318	1.319	1.328	1.2
Dy	0.007	5.949	5.962	6.405	6.868	6.529	6.488	6.318	5.838	5.726	7.548	7.243	7.247	7.219	7.946	7.441
Ho	0.001	1.032	1.015	1.087	1.164	1.112	1.091	1.054	0.988	0.977	1.286	1.331	1.339	1.349	1.595	1.56
Er	0.003	2.703	2.601	2.707	2.943	2.809	2.72	2.631	2.473	2.449	3.228	3.693	3.717	3.731	4.746	4.755
Tm	0.005	0.367	0.339	0.348	0.383	0.369	0.354	0.338	0.328	0.32	0.421	0.549	0.553	0.558	0.749	0.802
Yb	0.003	2.345	2.141	2.15	2.394	2.233	2.156	2.104	1.983	1.955	2.576	3.681	3.67	3.727	5.169	5.871
Lu	0.001	0.349	0.303	0.306	0.34	0.321	0.304	0.303	0.283	0.28	0.367	0.549	0.554	0.561	0.804	0.913
Σ REE		356.82	295.34	312.31	395.72	378.52	334.08	323.67	313.85	300.97	319.21	598.51	579.97	579.01	501.91	472.93
Eu/Eu*		1.05	1.04	1.05	1.05	1.05	1.05	1.05	1.05	1.06	1.04	0.99	0.99	0.97	0.83	0.58
(La)N		261.24	171.65	178.19	281.08	272.19	198.06	187.11	215.37	182.67	175.75	505.40	491.75	489.21	428.25	428.57
(Yb)N		11.27	10.29	10.34	11.51	10.74	10.37	10.12	9.53	9.40	12.38	17.70	17.64	17.92	24.85	28.23
(La/Yb)N		23.17	16.68	17.24	24.42	25.35	19.11	18.50	22.59	19.43	14.19	28.56	27.87	27.30	17.23	15.18
(La/Sm)N		4.62	3.09	2.96	4.23	4.39	3.24	3.14	3.92	3.38	2.67	7.64	7.64	7.57	7.95	8.93
(Nd/Sm)N		1.87	1.76	1.75	1.84	1.85	1.80	1.79	1.82	1.82	1.70	2.23	2.21	2.23	2.14	2.20
(Gd/Yb)N		2.81	3.14	3.38	3.29	3.32	3.47	3.40	3.40	3.38	3.28	1.93	1.94	1.88	1.22	0.96

d.l. detection limit; Eu*: calculated Eu content; ( )N: chondrite normalized

Major and trace elements compositions of the volcanic rocks from the Loriu, Kamego & Magadi sections

Section		**Loriu**	**Kamego**		**Magadi**		
Sample name		LORIU DYKE	KAM (V) 30	KAM V2	KIR(V)2/13a	KIR(V)2/13b	KIR(V)1/13
		K7	K1	K2	K3	K5	K6
Rock name		Téphrite	Phonolite	Phonolite	Basalte	Basalte	Trachyte
wt%							
SiO_2		43,90	55,40	54,67	46,46	46,41	60,71
Al_2O_3		14,72	18,36	18,85	13,03	12,96	15,04
Fe_2O_3*		13,17	6,38	6,06	15,15	15,28	5,51
MnO		0,21	0,36	0,35	0,22	0,22	0,23
MgO		5,08	0,24	0,40	4,64	4,71	0,68
CaO		9,59	1,13	1,15	8,87	8,75	1,16
Na_2O		4,45	5,94	7,57	3,37	3,35	6,07
K_2O		1,60	6,34	5,68	1,22	1,23	5,06
TiO_2		3,12	0,29	0,52	3,64	3,64	0,94
P_2O_5		0,74	< d.l.	0,05	0,72	0,72	0,18
PF		2,81	4,55	3,83	1,85	1,67	3,17
Total		99,36	98,97	99,12	99,15	98,93	98,75
ppm	d.l. (ppm)						
As	1,20	1,62	< d.l.	2,11	< d.l.	< d.l.	< d.l.
Ba	1,50	592,10	98,05	24,14	539,60	550,80	111,20
Be	1,00	2,28	10,58	7,93	1,29	1,35	3,25
Bi	0,10	< d.l.	< d.l.	< d.l.	< d.l.	< d.l.	< d.l.
Cd	0,15	0,32	1,10	0,79	0,21	0,25	0,43
Ce	0,1	135,40	338,50	362,60	82,92	84,11	174,10
Co	0,40	42,23	1,03	1,14	43,48	43,50	0,63
Cr	5,00	79,33	< d.l.	< d.l.	11,31	11,42	4,05
Cs	0,15	0,36	2,19	1,14	< d.l.	< d.l.	0,20
Cu	5,00	144,50	5,99	< d.l.	59,18	59,00	< d.l.
Dy	0,007	6,34	10,23	8,85	6,45	6,46	8,90
Er	0,003	2,97	4,51	3,25	3,05	3,04	4,62
Eu	0,004	3,14	0,97	2,14	3,21	3,17	3,57
Ga	0,20	22,93	38,43	34,31	23,07	22,93	31,27
Gd	0,02	8,29	12,62	11,73	7,86	7,88	10,04
Ge	0,10	1,40	2,44	1,90	1,49	1,42	1,60
Hf	0,04	6,08	21,16	18,80	4,43	4,45	9,74
Ho	0,001	1,20	1,78	1,46	1,24	1,24	1,76
In	0,10	0,12	0,10	0,10	0,13	0,13	0,11
La	0,05	67,49	209,30	210,20	38,92	39,29	89,59
Lu	0,001	0,36	1,03	0,44	0,37	0,37	0,64
Mo	0,35	2,56	0,60	5,91	1,22	1,18	0,66
Nb	0,06	90,00	321,30	291,20	33,07	33,44	104,80
Nd	0,03	56,63	103,10	104,30	42,79	43,06	70,69
Ni	4,50	63,19	5,76	< d.l.	23,63	23,42	< d.l.
Pb	1,40	4,79	19,97	18,15	3,69	3,53	8,13
Pr	0,01	15,22	34,00	34,22	10,37	10,47	19,52
Rb	0,35	38,78	215,50	147,20	20,14	18,77	47,91
Sb	0,20	17,70	< d.l.	1,09	26,53	26,63	8,42
Sc	1,00	< d.l.	0,44	0,32	< d.l.	< d.l.	< d.l.
Sm	0,01	10,22	15,95	15,50	8,94	9,01	12,67
Sn	0,40	2,63	7,37	5,84	1,82	1,85	3,76
Sr	1,20	779,70	119,40	75,48	669,50	668,40	13,81
Ta	0,02	6,59	22,68	21,96	2,66	2,68	7,15
Tb	0,006	1,14	1,87	1,67	1,11	1,12	1,51
Th	0,02	7,80	15,30	11,33	3,98	4,02	9,42
Tm	0,005	0,39	0,73	0,40	0,40	0,40	0,64
U	0,04	2,03	0,43	0,61	0,98	0,99	2,66
V	0,60	261,40	< d.l.	< d.l.	312,10	310,10	2,15
W	0,30	0,66	2,19	1,57	0,29	0,27	0,31
Y	0,40	30,68	47,04	38,31	31,24	31,38	45,60
Yb	0,003	2,47	6,18	2,65	2,52	2,52	4,20
Zn	11,00	134,70	221,60	206,70	151,80	152,80	170,10
Zr	1,30	273,60	923,40	701,80	161,20	162,60	431,30

Fe_2O_3*: total iron; d.l.: detection limit

Appendix 3

GPS coordinates for the Volcanic samples collected

Basin	Formation	Sample number	Longitude	Latitude
North Kerio Basin	Loriu Sandstone	Loriu 1	02° 42’ 50.34” N	36° 25’ 46.80” E
Baringo Basin	Kamego Formation	KAM (V) 2	00° 45’ 11.40” N	35° 50’ 38.80” E
		KAM V 30	00° 45’ 03.70” N	35° 51’ 04.80” E
Kerio Basin	Chof Phonolites	TUM 1	00° 19’ 12.53” N	35° 34’ 49.14” E
		TUM 2	00° 19’ 12.53” N	35° 34’ 53.28” E
		TUM 3	00° 19’ 15.19” N	35° 35’ 01.04” E
		TUM 4	00° 18’ 57.53” N	35° 34’ 50.08” E
		TUM 5	00° 19’ 09.76” N	35° 35’ 03.36” E
		TUM 6	00° 18’ 13.95” N	35° 35’ 28.30” E
		TUM 7	00° 18’ 06.18” N	35° 35’ 28.30” E
	Elgeyo Formation	KALW 01/11	00° 16’ 28.38” N	35° 37’ 17.42” E
		KALW 04/11	00° 16’ 28.98” N	35° 37’ 17.74” E
		KALW 11/11	00° 16’ 31.06” N	35° 37’ 18.99” E
		KALW 23/11	00° 16’ 59.04” N	35° 37’ 32.84” E
		KALW 26/11	00° 16’ 57.95” N	35° 37’ 34.28” E

Appendix 4

Parameters used for ^{39}Ar-^{40}Ar age calculations: isotopic ratios measured on K, Ca and Cl pure salts, atmosphere (Atm) and decay constants (λ). References: (1) Lee et al. (2006); (1') Mark et al. (2011); (2) Renne et al. (2011); (3) York, D., Personnal Communication - McMaster reactor.

Isotopic interference ratios	References	Value		Error	
$(^{36}Ar/^{37}Ar)_{Ca}$		0.000279	±	3	%
$(^{39}Ar/^{37}Ar)_{Ca}$		0.000706	±	4	%
$(^{38}Ar/^{37}Ar)_{Ca}$		0.00003	±	100	%
$(^{40}Ar/^{37}Ar)_{Ca}$		0.002	±	100	%
$(^{40}Ar/^{39}Ar)_{K}$		0.00085	±	4	%
$(^{38}A/3^{9}Ar)_{K}$		0.011	±	91	%
$(^{36}Cli/^{38}Cl)$	(3)	316	±	5	%
$(^{40}Ar/^{36}Ar)_{Atm}$	(1) and (1')	298.56	±	0.104	%
$(^{38}Ar/^{36}Ar)_{Atm}$	(1) and (1')	0.1885	±	0.159	%
Decay constants					
λ^{40}	(2)	5.5305×10^{-10}	±	1.34×10^{-12}	y^{-1}
λ^{39}		2.58×10^{-03}			y^{-1}
λ^{37}		1.98×10^{-02}			d^{-1}
λ^{36}_{Cl}		2.26×10^{-06}			y^{-1}

									Mass Discrimination (1+e)	
Experiment	Title	Nb of steps	J parameter	error J					Mass Discrimin:	Err Discrimination
z1695	KEN39_WR	9	6,91E-03	1,88E-05					1,009688	1,33E-03
Laser power	40Ar	Error 40Ar	39Ar	Error 39Ar	38Ar	Error 38Ar	37Ar	Error 37Ar	36Ar	Error 36Ar
350	3745,753482	2,19486	35,071703	0,101218	2,896438	0,079002	0,15945	0,027307	12,586717	0,027461
420	5260,781244	2,562635	125,804616	0,183507	5,061469	0,158842	0,475173	0,032285	17,80185	0,097095
500	7022,6969	2,79198	685,7489	0,515858	13,0367	0,162006	1,1734	0,033804	21,3768	0,093633
570	5031,7603	2,329882	791,138	0,429569	12,3572	0,166255	0,8908	0,029846	14,1249	0,027002
650	4230,6859	1,985491	876,7525	0,83389	12,3247	0,130942	0,679	0,036283	10,8821	0,061273
750	4492,6634	2,286016	1441,2626	0,706724	18,5659	0,195994	1,1957	0,025962	9,4627	0,080189
900	9174,9356	1,820681	2814,684	0,645246	37,4556	0,123128	4,3712	0,061225	20,1835	0,047795
1100	51668,7594	18,321794	5319,6318	3,046079	94,0785	0,270167	13,5215	0,117423	156,3499	0,229983
fusion	32078,896	9,301174	4989,5557	2,19221	77,3273	0,392184	9,8295	0,081863	89,6343	0,185898

	KEN39_WR				
	40Ar*/39ArK	Error 40Ar*/39A	Apparent age (M	Error Age (My)	Delay to irradiation (day)
350	3,855583	0,599592	47,53263	7,297645	285,427778
420	1,269122	0,312118	15,784443	3,865438	285,447917
500	1,336454	0,063159	16,618038	0,784091	285,477778
570	1,268546	0,030583	15,777313	0,383063	288,197917
650	1,288419	0,028985	16,023391	0,363606	288,218056
750	1,260561	0,019979	15,678428	0,253936	288,238194
900	1,246886	0,013472	15,509068	0,176173	288,257639
1100	1,342762	0,048073	16,696116	0,598102	288,338194
fusion	1,32712	0,030947	16,502506	0,387761	288,357639

Experiment	Title	Nb of steps	J parameter	error J					Mass Discrimin:	Err Discrimination
z1696	KEN34_WR	12	6,91E-03	1,88E-05					1,009688	1,33E-03
Laser power	40Ar	Error 40Ar	39Ar	Error 39Ar	38Ar	Error 38Ar	37Ar	Error 37Ar	36Ar	Error 36Ar
350	7757,15049	4,182152	46,376381	0,093344	5,75111	0,082113	0,797043	0,020578	26,504778	0,045226
420	1901,483944	1,657387	21,790635	0,084078	1,531068	0,044706	0,240767	0,020463	6,45934	0,047267
500	4228,789292	1,814087	184,26247	0,153651	5,055583	0,09108	1,379658	0,02877	13,566722	0,04547
570	2167,328546	0,789869	272,395799	0,370688	4,43796	0,118358	0,689431	0,027801	5,987181	0,037791
640	1019,918358	0,757049	316,911224	0,405454	4,22028	0,080916	0,558016	0,024757	1,870988	0,012434
700	992,52928	1,010112	364,766055	0,372498	4,705101	0,065712	0,758758	0,038619	1,645639	0,019937
760	913,633557	0,647648	349,323305	0,386587	4,401161	0,065129	0,620232	0,023131	1,454898	0,018192
820	924,357096	0,672303	357,417883	0,268078	4,536693	0,103072	0,661941	0,023888	1,483023	0,039181
900	1482,048287	1,30347	607,333344	0,211289	7,709004	0,052511	1,587648	0,041976	2,214501	0,025656
1000	1354,147787	0,65105	582,505044	0,411161	7,347604	0,166653	3,356248	0,043467	2,137501	0,056278
1150	1469,062387	1,801508	657,959444	0,504239	8,446004	0,121478	7,639448	0,022293	2,560701	0,038158
fusion	4233,501387	1,476174	1533,481744	0,818032	20,650204	0,286259	45,671048	0,100012	11,462901	0,037964

	KEN34_WR				
	40Ar*/39ArK	Error 40Ar*/39A	Apparent age (M	Error Age (My)	Delay to irradiation (day)
350	3,564408	0,924692	43,980414	11,273037	288,407639
420	2,409924	0,780242	29,852304	9,586302	288,438194
500	2,001843	0,13509	24,831845	1,666723	288,468056
570	1,718291	0,053809	21,335188	0,668725	288,507639
640	1,577462	0,01625	19,596024	0,21309	288,527778
700	1,487238	0,018566	18,480925	0,239213	288,557639
760	1,473574	0,017458	18,31199	0,225936	288,577778
820	1,450581	0,032907	18,027677	0,4122	288,607639
900	1,468855	0,014584	18,253641	0,192206	289,197917
1000	1,424969	0,02899	17,71093	0,364317	289,218056
1150	1,415432	0,018439	17,592961	0,23692	289,238194
fusion	1,368404	0,01287	17,011174	0,170892	289,268056

Experiment	Title	Nb of steps	J parameter	error J				Mass Discrimin	Err Discrimination		
z1697	KEN31_WR	10	6,91E-03	1,88E-05				1,009688	1,33E-03		
Laser power	40Ar	Error 40Ar	39Ar	Error 39Ar	38Ar	Error 38Ar	37Ar	Error 37Ar	36Ar	Error 36Ar	
350	12228,83274	2,721982	64,039272	0,132108	8,9385	0,146384	0,390684	0,029448	41,818005	0,126183	
400	70,103817	0,192141	0,225449	0,033216	0,070853	0,018052	0,014905	0,022394	0,24248	0,016143	
500	2815,57093	1,509185	170,051408	0,11415	3,747915	0,060824	0,847109	0,033497	8,373464	0,020271	
560	693,265793	0,487531	59,808251	0,061617	1,039512	0,045478	0,241574	0,023662	2,064397	0,033421	
620	292,359062	0,223074	33,527982	0,106484	0,51508	0,02805	0,067886	0,021606	0,857022	0,014735	
720	987,302562	0,660021	204,370082	0,134283	2,88178	0,035783	0,347986	0,028506	2,412722	0,022032	
820	901,842562	0,623177	236,190482	0,342234	3,02508	0,092639	0,437986	0,021875	1,988222	0,013573	
920	1158,591662	0,744845	360,118882	0,244728	4,59808	0,078233	1,095986	0,022504	2,342222	0,019273	
1100	1898,241371	1,21224	616,567695	0,598008	8,301882	0,072278	8,657716	0,04353	4,296351	0,037336	
fusion	5786,127271	1,993376	483,278695	0,447577	9,986082	0,071907	36,217816	0,180718	20,836451	0,011992	

	KEN31_WR				
	40Ar*/39ArK	Error 40Ar*/39	Apparent age (I	Error Age (My)	Delay to irradiation (day)
350	3,575917	1,151226	44,114841	14,031321	289,307639
400	3,752872	21,272179	46,270173	258,942937	289,327778
500	2,558662	0,085816	31,674484	1,059369	289,347917
560	1,791517	0,171341	22,235866	2,115163	289,377778
620	1,4387	0,134838	17,878366	1,668617	289,438194
720	1,49351	0,037308	18,555989	0,466087	289,457639
820	1,457355	0,022544	18,109029	0,286444	289,477778
920	1,435834	0,019568	17,842916	0,250563	289,497917
1100	1,440947	0,021102	17,906143	0,26897	289,538194
fusion	1,486635	0,062501	18,471003	0,77553	289,557639

Experiment	Title	Nb of steps	J parameter	error J				Mass Discrimin	Err Discrimination		
z1699	KEN30_WR	12	6,91E-03	1,88E-05				1,009688	1,32E-03		
Laser power	40Ar	Error 40Ar	39Ar	Error 39Ar	38Ar	Error 38Ar	37Ar	Error 37Ar	36Ar	Error 36Ar	
350	2275,284635	1,524215	2,347208	0,025877	1,542687	0,034449	0,066776	0,019614	7,887563	0,036405	
420	155,851516	0,270736	0,060256	0,016794	0,068377	0,027882	0,000001	0,018571	0,483477	0,019388	
500	76683,57094	28,272316	166,534708	0,258277	52,267587	0,346479	3,034976	0,051369	260,010863	0,281939	
560	22443,02993	7,879576	410,205108	0,194999	19,559887	0,154003	3,053176	0,070408	74,459663	0,128386	
600	3413,272159	1,691283	168,352636	0,29578	3,714157	0,105372	0,457664	0,02803	10,611675	0,026739	
660	3297,036802	1,423849	290,067802	0,23891	5,003843	0,131376	1,06871	0,032115	9,866524	0,06004	
720	904,38679	0,50553	143,359549	0,142928	2,04915	0,056972	0,498424	0,024713	2,440865	0,024355	
800	1118,967614	0,610051	135,779667	0,168735	2,063375	0,050075	0,338174	0,024708	3,234385	0,031993	
900	1481,91805	0,888562	187,015074	0,226742	3,004746	0,120941	0,922619	0,027506	4,264626	0,049527	
1000	2597,39485	1,548671	245,089174	0,127894	4,401046	0,050844	2,577119	0,041238	7,987826	0,083422	
1200	5953,95505	1,831298	460,637174	0,388182	9,156746	0,129697	14,301519	0,029179	19,615526	0,118308	
fusion	4596,44875	2,160221	492,299374	0,311475	8,796646	0,133082	41,449019	0,073852	17,348226	0,017776	

	KEN30_WR				
	40Ar*/39ArK	Error 40Ar*/39	Apparent age (I	Error Age (My)	Delay to irradiation (day)
350	4,923351	6,877175	60,454399	83,049707	290,307639
420	283,919816	125,714324	1962,54062	530,200768	290,338194
500	12,614132	2,451277	151,02224	28,160705	290,347917
560	2,787016	0,294079	34,469978	3,604907	290,368056
600	2,255855	0,109323	27,95104	1,347981	290,407639
660	1,703055	0,080637	21,141474	0,998162	290,438194
720	1,517965	0,056721	18,855732	0,704272	290,457639
800	1,473151	0,078364	18,301867	0,970952	290,477778
900	1,511574	0,085093	18,776751	1,053773	290,518056
1000	1,517322	0,111226	18,847787	1,376157	290,538194
1200	1,502595	0,098575	18,665789	1,220134	290,568056
fusion	1,386692	0,049349	17,232833	0,613584	290,588194

Experiment	Title	Nb of steps	J parameter	error J			Mass Discrimin	Err Discrimination		
z1700	KEN28_WR	11	6,91E-03	1,88E-05			1,009688	1,33E-03		
Laser power	40Ar	Error 40Ar	39Ar	Error 39Ar	38Ar	Error 38Ar	37Ar	Error 37Ar	36Ar	Error 36Ar
350	9673,357584	4,947487	427,098908	0,50062	11,329662	0,185277	1,144311	0,037394	32,018569	0,096361
400	424,476747	0,184078	20,751282	0,051467	0,553833	0,024781	0,065075	0,031474	1,31793	0,019501
470	6802,909624	3,374641	1403,731018	0,672499	19,146235	0,286809	2,445383	0,02281	13,754158	0,045855
510	3102,087224	1,660201	815,031218	0,632806	9,888435	0,112094	0,702683	0,030807	4,231158	0,034406
550	1810,221834	1,509565	471,430447	0,40499	6,333867	0,141051	0,585799	0,030348	3,426587	0,027286
620	1215,754492	1,011712	433,577305	0,331604	5,706873	0,032478	0,560561	0,035593	2,095328	0,012949
700	1025,314385	0,543944	449,717524	0,352464	5,534357	0,092762	0,484171	0,022393	1,32368	0,022302
820	1753,85807	0,795254	906,951112	1,052503	10,897667	0,126937	1,172571	0,038882	1,603926	0,030002
950	2079,6339	1,398948	1137,4722	0,892829	14,2455	0,15385	7,5432	0,06861	2,3684	0,015838
1050	1553,257637	0,886112	794,274623	0,72629	10,33113	0,157496	7,425676	0,061655	2,265402	0,0156
fusion	7890,6685	2,668297	3402,8221	1,595252	43,7484	0,320572	79,0263	0,278254	18,4368	0,042186

	KEN28_WR				
	40Ar*/39ArK	Error 40Ar*/39	Apparent age (M	Error Age (My)	Delay to irradiation (day)
350	1,19379	0,133151	14,843413	1,649695	291,188194
400	2,312653	0,292764	28,645435	3,599221	291,218056
470	2,092786	0,020124	25,94151	0,265056	291,227778
510	2,354773	0,016724	29,162966	0,231235	291,257639
550	1,797655	0,02182	22,305623	0,281079	291,297917
620	1,460145	0,013138	18,138674	0,175326	291,318056
700	1,473105	0,015917	18,298859	0,207712	291,338194
820	1,470076	0,010944	18,261415	0,150741	291,357639
950	1,413499	0,00659	17,56202	0,103616	291,407639
1050	1,39047	0,008348	17,277261	0,120921	291,427778
fusion	1,379125	0,009016	17,136952	0,127806	291,457639

Experiment	Title	Nb of steps	J parameter	error J			Mass Discrimin	Err Discrimination		
z1702	KEN22_Sanidin	11	6,94E-03	1,89E-05			1,010298	1,33E-03		
Laser power	40Ar	Error 40Ar	39Ar	Error 39Ar	38Ar	Error 38Ar	37Ar	Error 37Ar	36Ar	Error 36Ar
350	2091,545817	1,941741	218,225408	0,243693	4,224289	0,101635	0,226562	0,03402	6,644796	0,049024
400	21,652459	0,159155	7,969701	0,029991	0,102787	0,027638	0,000001	0,025302	0,009094	0,011534
490	1754,9154	1,279698	1118,2946	0,750773	13,4639	0,149349	0,6429	0,030265	1,1295	0,019039
510	555,228496	0,248066	410,36423	0,378092	4,961206	0,109501	0,158869	0,022785	0,102062	0,012224
560	1280,8451	1,370802	944,2265	0,677647	11,5447	0,15074	0,3766	0,032259	0,262	0,018321
610	808,7456	0,586476	574,9524	0,552803	6,837	0,115683	0,2457	0,0208	0,2455	0,026753
670	968,6419	0,678477	674,4997	0,485545	8,0642	0,19171	0,2757	0,027382	0,338	0,028174
671	1183,603	1,070268	868,427	0,716134	10,5993	0,087143	0,4118	0,025447	0,2648	0,019059
680	1606,9467	1,50439	1205,69	0,944147	14,3257	0,120047	0,5452	0,012342	0,2348	0,014106
800	1226,8304	0,98763	923,48	0,656256	11,1602	0,151696	0,4162	0,020652	0,1491	0,012728
fusion	6385,9868	2,820167	4852,89	2,11201	58,5079	0,49046	2,1376	0,049866	0,4887	0,025015

	KEN22_Sanidine				
	40Ar*/39ArK	Error 40Ar*/39	Apparent age (M	Error Age (My)	Delay to irradiation (day)
350	0,893719	0,081009	11,18121	1,011193	292,197917
400	2,409196	0,427447	29,984525	5,277206	292,218056
490	1,305134	0,006319	16,305222	0,098537	292,238194
510	1,302059	0,009232	16,266976	0,129228	292,268056
560	1,297608	0,006523	16,21161	0,100372	292,307639
610	1,30566	0,013881	16,311758	0,182592	292,327778
670	1,313465	0,012558	16,408829	0,167242	292,347917
671	1,298181	0,007138	16,218742	0,106658	292,368056
680	1,29901	0,004568	16,229053	0,082025	292,418056
800	1,304276	0,004982	16,294546	0,085835	292,438194
fusion	1,308881	0,003037	16,351812	0,070562	292,457639

Experiment	Title	Nb of steps	J parameter	error J				Mass Discrimin	Err Discrimination		
z1705	KEN23_WR	9	6,93E-03	1,88E-05				1,009688	1,32E-03		
Laser power	40Ar	Error 40Ar	39Ar	Error 39Ar	38Ar	Error 38Ar	37Ar	Error 37Ar	36Ar	Error 36Ar	
350	7847,558761	1,903357	67,095285	0,133463	6,243988	0,096527	0,255738	0,024858	26,748921	0,137798	
420	50,270624	0,225962	0,046409	0,022227	0,002767	0,01832	0,042223	0,023878	0,182457	0,015857	
500	11780,21241	4,76046	582,167222	0,332373	13,961784	0,13836	1,614924	0,040534	36,249393	0,100025	
550	2837,111764	1,168122	315,277726	0,438156	4,924783	0,115032	1,05612	0,03199	7,419619	0,042344	
590	1049,887077	1,085949	177,472953	0,224712	2,557797	0,038068	0,95224	0,039284	2,769711	0,022291	
660	1607,868337	1,388278	180,149791	0,242759	3,093892	0,061888	0,91554	0,031807	4,72455	0,028378	
750	2631,160539	2,103841	261,91397	0,411125	4,550206	0,11287	1,043282	0,017234	7,889898	0,082513	
900	1551,124939	0,779599	283,24267	0,304474	4,538406	0,098979	3,135182	0,050844	4,482498	0,026259	
fusion	2718,629639	1,977423	370,46667	0,353195	6,752406	0,024868	27,428782	0,108414	10,566898	0,048675	

	KEN23_WR				
	40Ar*/39ArK	Error 40Ar*/39	Apparent age (I	Error Age (My)	Delay to irradiation (day)
350	2,578615	0,851948	32,014058	10,484669	295,407639
420	-26,712747	128,540017	-370,00254	1975,700242	295,427778
500	2,447405	0,109836	30,398678	1,357356	295,518056
550	2,351915	0,055053	29,222152	0,686808	295,547917
590	1,596807	0,045248	19,89143	0,565226	295,568056
660	1,547713	0,062344	19,283121	0,77581	295,588194
750	1,518539	0,103204	18,921528	1,281112	296,197917
900	1,257116	0,036934	15,678187	0,462184	296,218056
fusion	1,278962	0,054819	15,949439	0,683097	296,238194

Experiment	Title	Nb of steps	J parameter	error J				Mass Discrimin	Err Discrimination		
z1706	KEN26_WR	8	6,91E-03	1,88E-05				1,009688	1,32E-03		
Laser power	40Ar	Error 40Ar	39Ar	Error 39Ar	38Ar	Error 38Ar	37Ar	Error 37Ar	36Ar	Error 36Ar	
350	9776,696329	2,974958	114,987482	0,311679	8,06891	0,103177	1,144977	0,033555	33,376772	0,037989	
420	2320,943586	1,071548	90,572603	0,088084	2,578702	0,079517	0,607175	0,026306	7,510903	0,079251	
500	2704,969741	1,674714	382,725605	0,435484	5,716213	0,078235	1,601356	0,028906	7,103944	0,032933	
570	1956,874177	1,171125	322,782362	0,567967	4,561649	0,074423	0,651079	0,018555	5,102295	0,046186	
650	1545,131729	0,748714	372,901199	0,326098	5,072397	0,092479	0,653298	0,024033	3,620308	0,054151	
750	1403,956329	0,910974	463,054199	0,360754	5,839797	0,06988	0,759898	0,026687	2,645208	0,021473	
900	2361,408829	1,158257	1063,524699	0,58803	13,239997	0,134524	3,806398	0,052555	3,380308	0,018615	
fusion	8204,342929	2,959841	2557,853999	1,47813	35,446097	0,189848	57,782198	0,127946	21,887108	0,082094	

	KEN26_WR				
	40Ar*/39ArK	Error 40Ar*/39	Apparent age (I	Error Age (My)	Delay to irradiation (day)
350	1,952772	0,454396	24,250229	5,605881	296,288194
420	2,014469	0,284563	25,011126	3,509914	296,307639
500	1,870513	0,039567	23,23524	0,495623	296,327778
570	1,591609	0,049131	19,789628	0,611815	296,347917
650	1,415486	0,045276	17,610384	0,564214	296,397917
750	1,448707	0,017302	18,021651	0,224003	296,407639
900	1,42075	0,008496	17,675561	0,12334	296,438194
fusion	1,411477	0,015733	17,560755	0,205036	296,457639

Experiment	Title	Nb of steps	J parameter	error J			Mass Discrimin	Err Discrimination		
z1707	KEN25_WR	8	6,90E-03	1,88E-05			1,009688	1,32E-03		
Laser power	40Ar	Error 40Ar	39Ar	Error 39Ar	38Ar	Error 38Ar	37Ar	Error 37Ar	36Ar	Error 36Ar
350	40272,28576	9,680014	139,386661	0,149482	28,252734	0,233742	1,716187	0,03607	137,276274	0,123942
400	3721,205666	1,607245	23,650723	0,071301	2,762037	0,087419	0,236728	0,021116	12,679756	0,076983
480	13107,77736	4,213905	491,744685	0,287519	14,233043	0,157888	2,040456	0,034242	43,212555	0,060131
540	1234,129407	1,548634	330,360445	0,708591	4,256969	0,111969	0,373405	0,021584	2,592031	0,053248
600	1019,311911	0,483682	280,75594	0,171206	3,391418	0,092432	0,4619	0,031709	2,100045	0,021067
700	1393,371756	1,507057	270,194115	0,645763	3,671989	0,066566	0,554832	0,032545	3,488839	0,03967
850	1121,641256	0,733734	276,727215	0,342995	3,755689	0,060475	0,967232	0,039748	2,583839	0,010457
fusion	5631,959056	1,335814	1210,940415	0,631869	18,010389	0,244388	59,063832	0,102262	20,160739	0,079733

	KEN25_WR				
	40Ar*/39ArK	Error 40Ar*/39	Apparent age (I	Error Age (My)	Delay to irradiation (day)
350	6,46055	1,530739	78,881696	18,290302	296,507639
400	3,669486	1,2529	45,224882	15,250832	296,527778
480	1,545955	0,139998	19,191332	1,730149	296,547917
540	1,525604	0,049071	18,940012	0,609942	296,568056
600	1,541134	0,025775	19,131803	0,325831	297,188194
700	1,518993	0,048224	18,85837	0,599537	297,207639
850	1,484331	0,019978	18,430219	0,255771	297,227778
fusion	1,305941	0,029216	16,22514	0,366162	297,247917

Experiment	Title	Nb of steps	J parameter	error J			Mass Discrimin	Err Discrimination		
z1708	KEN27_WR	8	6,90E-03	1,88E-05			1,009688	1,32E-03		
Laser power	40Ar	Error 40Ar	39Ar	Error 39Ar	38Ar	Error 38Ar	37Ar	Error 37Ar	36Ar	Error 36Ar
350	1457,901587	1,080832	11,202544	0,040366	1,055396	0,03547	0,04139	0,022903	4,971696	0,024814
420	4999,562216	1,240039	133,937937	0,161392	4,637763	0,069164	0,325572	0,020722	16,677965	0,080178
490	6662,830488	2,775486	681,571354	0,544321	11,380912	0,12138	0,970872	0,036596	18,660129	0,085102
550	2589,417116	1,42889	283,995237	0,406101	4,803063	0,104172	0,404172	0,026252	7,519165	0,043586
630	2286,940839	1,127625	156,912172	0,191068	3,241146	0,158721	0,35518	0,028278	7,034502	0,046071
750	1245,190932	0,68433	189,250781	0,178763	2,897095	0,077124	0,514126	0,030264	3,377374	0,027549
900	1757,055564	1,083753	274,409967	0,446357	4,3556	0,091402	2,119477	0,045146	4,953852	0,026941
fusion	8127,799839	5,441722	861,895672	0,829397	16,796246	0,163371	59,63928	0,236793	30,574702	0,08679

	KEN27_WR				
	40Ar*/39ArK	Error 40Ar*/39	Apparent age (I	Error Age (My)	Delay to irradiation (day)
350	2,79595	0,940525	34,570233	11,519236	297,297917
420	1,644308	0,258242	20,410849	3,188404	297,318056
490	1,968029	0,057172	24,4022	0,709718	297,338194
550	1,566	0,061559	19,444013	0,763538	297,357639
630	1,777383	0,110664	22,052681	1,367069	297,407639
750	1,544656	0,051481	19,180399	0,639698	297,427778
900	1,455463	0,040875	18,07839	0,50946	297,447917
fusion	1,284339	0,057803	15,962202	0,717601	297,468056

Experiment	Title	Nb of steps	J parameter	error J			Mass Discrimin	Err Discrimination		
z1709	KEN22_WR	10	6,94E-03	1,89E-05			1,009688	1,32E-03		
Laser power	40Ar	Error 40Ar	39Ar	Error 39Ar	38Ar	Error 38Ar	37Ar	Error 37Ar	36Ar	Error 36Ar
400	22840,01476	7,923569	355,481191	0,234534	21,072651	0,267866	0,982976	0,028679	78,551515	0,155112
450	15616,96546	5,103883	704,660991	0,373935	21,231751	0,230493	1,088376	0,029138	52,129515	0,052232
490	3956,782942	1,861919	1123,336979	0,754452	15,063859	0,114129	0,8803	0,039098	8,699807	0,029819
540	2958,879562	1,25922	1692,360425	0,753789	20,145081	0,191247	1,386206	0,030917	2,862458	0,025726
600	4394,076662	1,259919	2651,480525	1,217117	32,291981	0,177091	0,890206	0,03258	3,582258	0,041051
670	3058,155862	1,173663	1854,185225	1,336007	22,619381	0,175696	0,271706	0,031515	2,438058	0,032374
750	3927,718278	1,746447	2405,251456	1,068621	29,464635	0,134226	0,28033	0,028781	3,205285	0,010381
850	4950,251946	0,9724	3204,105741	1,820404	38,346615	0,220691	0,556732	0,029914	3,432454	0,044423
1000	5346,968715	1,845209	3348,465019	1,913675	40,654485	0,135995	1,020844	0,029379	4,269409	0,037088
fusion	10404,51365	2,467664	6225,039363	2,031111	76,294204	0,443011	2,579928	0,025907	9,949536	0,07131

	KEN22_WR				
	40Ar*/39ArK	Error 40Ar*/39	Apparent age (M	Error Age (My)	Delay to irradiation (day)
400	0,868407	0,360257	10,865482	4,494181	297,547917
450	0,966168	0,115728	12,084588	1,443348	297,577778
490	1,330654	0,015708	16,62258	0,204507	298,197917
540	1,296098	0,006404	16,192834	0,099135	298,218056
600	1,28828	0,006126	16,095597	0,096173	298,238194
670	1,285107	0,006597	16,056129	0,100797	298,268056
750	1,262609	0,004359	15,77626	0,079048	298,307639
850	1,251259	0,00551	15,635055	0,089151	298,338194
1000	1,248527	0,005168	15,601055	0,085846	298,357639
fusion	1,233399	0,005507	15,412835	0,088619	298,368056

Experiment	Title	Nb of steps	J parameter	error J			Mass Discrimin	Err Discrimination		
z1710	KEN44_WR	7	6,90E-03	1,88E-05			1,009688	1,32E-03		
Laser power	40Ar	Error 40Ar	39Ar	Error 39Ar	38Ar	Error 38Ar	37Ar	Error 37Ar	36Ar	Error 36Ar
350	29943,32658	9,909293	116,216414	0,135684	20,835047	0,179769	0,587721	0,028488	101,744113	0,113492
400	4400,518371	1,799611	54,985658	0,08813	3,664769	0,088282	0,14037	0,021883	14,656646	0,069971
470	5405,886779	2,175753	271,399555	0,188564	6,421768	0,055252	0,478013	0,037183	16,581768	0,052812
550	1940,656636	1,200882	110,498712	0,104945	2,471868	0,055366	0,203039	0,021362	6,077661	0,026829
700	1891,138326	1,236212	159,674684	0,215544	2,946103	0,060716	0,41682	0,033181	5,840922	0,044557
900	1721,903726	1,161678	238,175884	0,189841	3,888503	0,110691	1,75462	0,042766	5,085322	0,054696
450	5802,830026	1,311993	742,272884	0,639185	13,319803	0,188729	35,45242	0,118952	20,555022	0,085145

	KEN44_WR				
	40Ar*/39ArK	Error 40Ar*/39	Apparent age (M	Error Age (My)	Delay to irradiation (day)
350	6,393544	1,371239	78,091234	16,394297	298,418056
400	3,57241	0,552044	44,048758	6,726499	298,438194
470	2,440634	0,111554	30,209452	1,373709	298,457639
550	1,832913	0,111613	22,734326	1,378202	298,477778
700	1,425276	0,099531	17,702909	1,231898	298,568056
900	1,327727	0,074876	16,496793	0,928037	298,577778
450	1,309134	0,051514	16,266813	0,639976	298,597917

Experiment	Title	Nb of steps	J parameter	error J				Mass Discrimin	Err Discrimination		
z1720	KEN21_sanidin	13	6,95E-03	1,89E-05				1,008789	1,32E-03		
Laser power	40Ar	Error 40Ar	39Ar	Error 39Ar	38Ar	Error 38Ar	37Ar	Error 37Ar	36Ar	Error 36Ar	
300	32,500602	0,133918	0,488319	0,030839	0,076343	0,010025	0,000001	0,031333	0,109651	0,014761	
360	225,590202	0,311249	5,867119	0,044856	0,274843	0,014462	0,014174	0,029428	0,760651	0,01986	
500	479,423298	0,428869	36,693666	0,026136	0,891945	0,049559	0,074625	0,026609	1,617154	0,023625	
550	2287,903864	0,856188	424,239013	0,565064	6,29484	0,15189	0,118494	0,020156	6,017833	0,040908	
570	773,596143	0,362452	100,691908	0,126794	1,558317	0,030587	0,007871	0,02542	2,304881	0,017878	
600	376,515343	0,240214	78,138008	0,083471	1,138417	0,04336	0,038771	0,027321	0,963681	0,014186	
650	3638,072843	1,097884	173,661108	0,244166	4,548017	0,087972	0,028271	0,022754	11,885281	0,07952	
700	5713,719836	1,926294	306,99823	0,363107	7,395256	0,118805	0,073648	0,024285	18,506729	0,088638	
770	2156,388436	1,914416	362,08933	0,697724	5,681256	0,135108	0,054748	0,030997	5,883629	0,041042	
870	771,915636	0,603743	426,20013	0,419272	5,235856	0,100454	0,042648	0,028722	0,744729	0,015306	
890	2456,250436	1,724005	550,08973	0,418374	8,372956	0,117216	0,089148	0,022825	6,064429	0,050194	
950	2073,9215	0,56115	1014,8416	0,463757	12,9241	0,169326	0,1311	0,020787	2,6086	0,027262	
fusion	6734,0785	4,738378	4132,0489	2,032981	51,5483	0,316641	0,6531	0,03441	4,6356	0,050658	

	KEN21_sanidine				
	40Ar*/39ArK	Error 40Ar*/39	Apparent age (M	Error Age (My)	Delay to irradiation (day)
300	1,858778	9,164658	23,221736	113,762061	313,207639
360	1,184731	1,024811	14,835279	12,780369	313,227778
500	0,44594	0,201197	5,59839	2,522025	313,257639
550	1,323429	0,036568	16,564133	0,459587	313,297917
570	1,094061	0,063933	13,704201	0,799357	313,318056
600	1,291456	0,058376	16,165749	0,729839	313,338194
650	1,235455	0,169924	15,467743	2,119099	313,357639
700	1,252115	0,125523	15,675427	1,565695	313,488194
770	1,28557	0,042728	16,092401	0,535705	313,507639
870	1,319579	0,011928	16,516167	0,160349	313,527778
890	1,30204	0,032523	16,297631	0,409594	313,547917
950	1,315968	0,009844	16,471184	0,136558	313,588194
fusion	1,320868	0,00543	16,532236	0,090595	313,607639

Experiment	Title	Nb of steps	J parameter	error J				Mass Discrimin	Err Discrimination		
z1721	KEN20_Sanidin	10	6,97E-03	1,89E-05				1,008789	1,32E-03		
Laser power	40Ar	Error 40Ar	39Ar	Error 39Ar	38Ar	Error 38Ar	37Ar	Error 37Ar	36Ar	Error 36Ar	
300	84,953234	0,196184	4,31742	0,042653	0,092395	0,022306	0,03411	0,014641	0,278227	0,017522	
370	316,905016	0,354978	19,649568	0,058083	0,477651	0,022655	0,069901	0,023468	1,092297	0,015174	
500	1380,241725	0,277794	324,936407	0,362779	4,633192	0,056234	0,252264	0,024763	3,400833	0,031908	
550	1161,212064	0,922282	800,325381	0,492412	10,091062	0,161302	0,225369	0,025136	0,522331	0,011786	
620	1416,686464	0,955753	1077,464481	0,552988	13,349662	0,115522	0,264569	0,034633	0,179331	0,014798	
700	1252,347564	0,829496	952,906681	0,872119	11,774662	0,106757	0,322269	0,019994	0,159931	0,014658	
710	957,554054	0,57695	736,883862	0,621039	8,633007	0,068892	0,233145	0,026983	0,089614	0,014084	
770	1509,819674	0,860581	1162,515286	0,724912	14,118944	0,172213	0,407481	0,028872	0,133232	0,013162	
850	1030,491213	0,319498	793,624212	0,574926	9,588348	0,140861	0,260918	0,023824	0,086946	0,023852	
fusion	3656,128618	1,404721	2833,591028	0,968135	34,467125	0,140014	0,842508	0,035166	0,247092	0,016777	

	KEN20_Sanidine				
	40Ar*/39ArK	Error 40Ar*/39	Apparent age (M	Error Age (My)	Delay to irradiation (day)
300	1,446973	1,195232	18,137147	14,906932	316,197917
370	0,256021	0,245738	3,222377	3,090228	316,227778
500	1,271759	0,033666	15,950579	0,424382	316,257639
550	1,282738	0,005688	16,087662	0,092102	316,338194
620	1,285254	0,005102	16,119076	0,086666	316,357639
700	1,288248	0,005465	16,156459	0,090136	316,388194
710	1,285741	0,006463	16,125156	0,099834	316,427778
770	1,288616	0,00445	16,161051	0,080981	316,447917
850	1,288844	0,009244	16,163901	0,129588	316,468056
fusion	1,285757	0,003195	16,125354	0,071038	316,488194

Experiment	Title	Nb of steps	J parameter	error J				Mass Discrimin	Err Discrimination		
z1722	KEN19_Sanidin	10	6,98E-03	1,90E-05				1,008789	1,32E-03		
Laser power	40Ar	Error 40Ar	39Ar	Error 39Ar	38Ar	Error 38Ar	37Ar	Error 37Ar	36Ar	Error 36Ar	
370	184,447158	0,242082	5,508343	0,042812	0,182946	0,031176	0,000001	0,025467	0,580873	0,020144	
370	184,447158	0,242082	5,508343	0,042812	0,182946	0,031176	0,000001	0,025467	0,580873	0,020144	
430	244,92594	0,370303	52,546522	0,176635	0,697026	0,033649	0,012705	0,013916	0,591863	0,018313	
500	412,320011	0,651291	260,764091	0,271374	3,310402	0,10406	0,016897	0,026886	0,408866	0,016583	
570	582,416539	0,274186	422,675743	0,273741	5,301771	0,074098	0,054352	0,026199	0,352796	0,014671	
670	499,955786	0,24765	401,212242	0,43767	5,02246	0,102455	0,036368	0,026835	0,145985	0,015684	
790	397,206108	0,400405	313,502684	0,493221	3,908236	0,058046	0,046073	0,026737	0,140907	0,013162	
930	679,535716	0,295581	533,926935	0,241698	6,290759	0,137366	0,054223	0,038837	0,235958	0,021492	
1000	1102,425413	0,784049	609,496244	0,537941	7,767183	0,113419	0,079746	0,023011	1,421817	0,039685	
fusion	3221,344516	1,151271	2518,351035	1,638629	30,898559	0,136969	0,234823	0,026813	1,176358	0,016341	

	KEN19_Sanidine				
	40Ar*/39ArK	Error 40Ar*/39	Apparent age (M	Error Age (My)	Delay to irradiation (day)
370	3,107621	1,094152	38,804217	13,517604	316,557639
370	3,107621	1,094152	38,804217	13,517604	316,557639
430	1,433377	0,103919	18,001811	1,300296	316,577778
500	1,13896	0,019673	14,318816	0,251825	317,188194
570	1,149908	0,010992	14,455908	0,147379	317,218056
670	1,152185	0,012119	14,484418	0,160675	317,238194
790	1,150824	0,013247	14,467379	0,174057	317,257639
930	1,156654	0,012465	14,540372	0,164826	317,297917
1000	1,148981	0,019779	14,4443	0,253193	317,327778
fusion	1,155551	0,003582	14,526569	0,069405	317,347917

Experiment	Title	Nb of steps	J parameter	error J				Mass Discrimin	Err Discrimination		
z1723	KEN18_Sanidin	12	6,99E-03	1,90E-05				1,008789	1,32E-03		
Laser power	40Ar	Error 40Ar	39Ar	Error 39Ar	38Ar	Error 38Ar	37Ar	Error 37Ar	36Ar	Error 36Ar	
350	1978,071184	1,3627	17,808083	0,094795	1,564338	0,07437	0,00199	0,019115	6,798341	0,020538	
400	180,973876	0,292914	2,640051	0,058185	0,163957	0,030447	0,030689	0,023417	0,642665	0,016954	
500	1890,218899	1,421359	80,997891	0,252719	2,358897	0,080153	0,262615	0,027397	6,226367	0,054572	
570	388,367448	0,184967	289,017819	0,287683	3,380742	0,060422	0,380389	0,033067	0,34205	0,016256	
750	1722,210663	1,053204	1451,832051	0,692337	17,563995	0,148489	0,140048	0,0326	0,656558	0,014808	
750	2505,293795	1,079896	2286,583564	0,932779	27,902472	0,149681	0,117738	0,02618	0,288328	0,019225	
850	3382,677794	1,501313	3097,780992	1,627632	37,036009	0,201413	0,165989	0,026949	0,384736	0,01079	
950	3138,658674	2,081239	2706,797326	1,695551	32,765208	0,10849	0,170436	0,029478	0,934424	0,017289	
1000	6206,948715	1,253938	5672,761139	2,529976	69,040031	0,383278	0,33138	0,034422	0,736182	0,013243	
1200	4696,416281	1,635344	4365,423399	1,861046	52,590772	0,158103	0,20006	0,02286	0,277708	0,013835	
1250	3944,172289	0,897498	3668,659404	1,369067	43,916713	0,25057	0,203159	0,021564	0,211405	0,015098	
fusion	7428,609121	1,630852	6913,154063	1,96374	83,018671	0,311898	0,398088	0,031032	0,335018	0,020046	

	KEN18_Sanidine				
	40Ar*/39ArK	Error 40Ar*/39	Apparent age (M	Error Age (My)	Delay to irradiation (day)
350	1,045576	0,676698	13,174217	8,495518	317,388194
400	-1,129685	1,949171	-14,34271	24,845538	317,418056
500	1,328699	0,22982	16,725094	2,880184	317,438194
570	1,066395	0,017488	13,435559	0,224921	317,477778
750	1,066456	0,004269	13,436331	0,072615	317,497917
750	1,067957	0,003543	13,455165	0,066221	317,518056
850	1,06485	0,002761	13,416161	0,059961	317,538194
950	1,069179	0,003436	13,470512	0,065367	317,568056
1000	1,065699	0,002596	13,426825	0,058818	317,588194
1200	1,065874	0,002626	13,429024	0,059033	318,197917
1250	1,067299	0,002709	13,446903	0,05967	318,218056
fusion	1,069523	0,002547	13,474828	0,058621	318,238194

Experiment	Title	Nb of steps	J parameter	error J			Mass Discrimin	Err Discrimination		
z1819	KENYA_1_WR	12	2,27E-03	6,17E-06			1,008709	1,32E-03		
Laser power	40Ar	Error 40Ar	39Ar	Error 39Ar	38Ar	Error 38Ar	37Ar	Error 37Ar	36Ar	Error 36Ar
300	18944,90787	7,282562	199,705244	0,074303	15,008556	0,154413	13,683328	0,067973	65,527205	0,101061
350	8520,000953	6,085715	347,118221	0,244663	10,128035	0,112126	11,894463	0,136352	27,123596	0,068032
400	1706,471895	1,279913	180,321757	0,160229	2,801386	0,062933	3,002803	0,053999	4,16119	0,038312
460	727,071874	0,272019	96,51709	0,074268	1,36605	0,059236	1,414242	0,044686	1,490292	0,017742
540	920,541402	0,503192	153,428654	0,163355	2,02312	0,040673	1,85372	0,035046	1,351616	0,021745
620	584,610917	0,627919	105,462168	0,287999	1,442162	0,050893	1,035191	0,062192	0,622206	0,017722
720	1259,323242	0,565214	235,580867	0,357769	2,964119	0,068501	3,103253	0,038997	0,910681	0,022421
800	1533,442892	1,377771	299,356657	0,348167	3,792504	0,033429	4,353888	0,062572	0,899918	0,025203
880	1326,456606	0,873905	275,811169	0,456067	3,378416	0,053132	5,095627	0,073574	0,584806	0,026461
1000	1123,165016	0,647217	241,586384	0,359069	2,939587	0,075433	12,060944	0,097897	0,406429	0,021407
1200	2711,999206	1,460718	555,467169	0,423579	7,126916	0,200012	42,900827	0,134858	1,418106	0,032995
fusion	7046,809016	4,581245	1572,253454	1,207488	20,492025	0,201182	27,490792	0,097319	1,705025	0,030201

	KENYA_1_WR				
	40Ar*/39ArK	Error 40Ar*/39	Apparent age (I	Error Age (My)	Delay to irradiation (day)
300	0,256913	0,522109	1,0535	2,14034	43,804167
350	2,03433	0,135403	8,325215	0,553678	43,823611
400	2,834873	0,073359	11,590842	0,301955	43,84375
460	3,108351	0,060256	12,705083	0,249763	43,863889
540	3,490065	0,045234	14,259162	0,191286	43,913889
620	3,875447	0,052281	15,826823	0,22027	43,934028
720	4,268265	0,030745	17,423334	0,140116	43,954167
800	4,293472	0,027379	17,525736	0,128258	43,973611
880	4,236069	0,030239	17,292537	0,138079	44,023611
1000	4,208289	0,02784	17,179671	0,12929	44,04375
1200	4,195861	0,020065	17,129173	0,102685	44,063889
fusion	4,207063	0,010066	17,174687	0,074775	44,09375

Experiment	Title	Nb of steps	J parameter	error J			Mass Discrimin	Err Discrimination		
z1821	KENYA_1_Sanic	10	2,27E-03	6,17E-06			1,008709	1,32E-03		
Laser power	40Ar	Error 40Ar	39Ar	Error 39Ar	38Ar	Error 38Ar	37Ar	Error 37Ar	36Ar	Error 36Ar
300	620,550339	0,501025	2,588491	0,033231	0,489843	0,040489	0,673165	0,027965	2,193366	0,033479
400	352,569466	0,405323	24,52827	0,057243	0,515921	0,018149	2,470355	0,035926	0,833419	0,023144
500	343,332037	0,512144	49,875919	0,105772	0,766074	0,048378	2,251703	0,037933	0,366239	0,02238
570	566,523353	0,880457	110,002071	0,151166	1,378351	0,039075	0,903788	0,029995	0,126289	0,012717
600	360,693209	0,381248	67,6296	0,128928	0,906208	0,046235	0,312115	0,031854	0,118538	0,013161
660	521,444957	0,511598	100,866573	0,235004	1,257178	0,063556	0,637577	0,045871	0,14255	0,020355
840	781,99016	0,606395	151,301058	0,199455	1,906204	0,088031	0,511117	0,031793	0,196056	0,025717
900	2422,293496	0,799134	448,87492	0,492789	5,915253	0,075445	1,144514	0,026649	0,923306	0,030215
910	828,432498	0,904445	151,151723	0,149411	1,901665	0,054617	0,28902	0,038119	0,349608	0,025979
fusion	4228,318057	1,719676	818,111657	0,585495	10,601246	0,141252	1,772247	0,033756	0,955215	0,03119

	KENYA_1_Sanidine				
	40Ar*/39ArK	Error 40Ar*/39	Apparent age (I	Error Age (My)	Delay to irradiation (day)
300	-4,612704	3,981051	-19,020076	16,502307	44,19375
400	4,634068	0,281139	18,908784	1,143255	44,804167
500	4,814801	0,13246	19,642256	0,542196	44,823611
570	4,860437	0,036136	19,82741	0,163435	44,84375
600	4,868654	0,058333	19,860748	0,247469	44,863889
660	4,802622	0,060551	19,592837	0,255852	44,904167
840	4,834945	0,050685	19,723987	0,217838	45,134028
900	4,84329	0,022456	19,757843	0,116115	45,163889
910	4,853831	0,051528	19,800612	0,221151	45,184028
fusion	4,871936	0,014354	19,874062	0,092918	45,204167

Appendix

Experiment	Title	Nb of steps	J parameter	error J				Mass Discrimin	Err Discrimination		
z1822	KENYA_2_WR	13	2,27E-03	6,17E-06				1,008709	1,32E-03		
Laser power	40Ar	Error 40Ar	39Ar	Error 39Ar	38Ar	Error 38Ar	37Ar	Error 37Ar	36Ar	Error 36Ar	
300	5546,975981	3,233354	37,38712	0,116191	4,330155	0,084189	3,772859	0,040544	19,211855	0,098622	
400	17724,06481	12,124202	697,553812	0,588296	20,8411	0,219314	34,779072	0,079514	55,91995	0,157591	
450	1232,278171	0,627333	243,051273	0,222554	3,190323	0,05977	4,429546	0,073023	1,082927	0,014277	
520	902,005272	0,841825	192,090457	0,188392	2,463238	0,04434	4,535423	0,071527	0,611015	0,014379	
580	1221,559801	0,836828	269,304612	0,306366	3,420944	0,089115	3,27271	0,053937	0,710995	0,017658	
700	1853,601566	1,826896	413,065043	0,359412	5,030916	0,102923	3,040982	0,067105	1,045289	0,029165	
800	1633,204066	0,710419	380,102843	0,288489	4,689216	0,086284	3,198582	0,037914	0,659089	0,013149	
950	2497,410256	1,216804	601,57669	0,450631	7,584404	0,088838	9,452973	0,075691	0,834038	0,026117	
1100	2417,386692	0,982078	577,165227	0,314793	7,192731	0,128072	15,32201	0,079476	0,761036	0,01898	
1300	1361,628752	0,874802	319,891888	0,29451	4,250467	0,066589	10,466639	0,067324	0,538881	0,018826	
1500	896,634356	1,015066	206,306637	0,386913	2,640166	0,081696	14,861147	0,102265	0,389294	0,026767	
1900	2321,234592	1,548387	539,099327	0,549996	6,666231	0,069591	30,43181	0,14668	0,920036	0,030259	
fusion	3043,470292	1,231022	714,183927	0,504767	9,004331	0,127285	18,47991	0,080444	0,967036	0,020681	

	KENYA_2_WR				
	40Ar*/39ArK	Error 40Ar*/39	Apparent age (M	Error Age (My)	Delay to irradiation (day)
300	0,201319	1,099107	0,826022	4,508654	45,804167
400	2,31975	0,142295	9,495232	0,581948	45,823611
450	3,81995	0,021195	15,609423	0,103321	45,854167
520	3,814306	0,024572	15,586457	0,114997	45,873611
580	3,808062	0,02175	15,561056	0,105119	45,904167
700	3,789949	0,02302	15,487352	0,109369	45,934028
800	3,829534	0,013102	15,648419	0,078078	45,954167
950	3,78562	0,014879	15,469741	0,082741	45,973611
1100	3,844872	0,012169	15,710821	0,075708	46,013889
1300	3,808479	0,019221	15,562749	0,096621	46,034028
1500	3,848225	0,039526	15,72446	0,170721	46,054167
1900	3,856692	0,018659	15,758909	0,0952	46,084028
fusion	3,908132	0,011524	15,968172	0,07474	46,104167

Experiment	Title	Nb of steps	J parameter	error J				Mass Discrimin	Err Discrimination		
z1823	KENYA_2_Sanic	12	2,27E-03	6,17E-06				1,008709	1,32E-03		
Laser power	40Ar	Error 40Ar	39Ar	Error 39Ar	38Ar	Error 38Ar	37Ar	Error 37Ar	36Ar	Error 36Ar	
300	1606,043693	0,745017	21,163834	0,071062	1,322209	0,060435	0,7637	0,030213	5,247934	0,015893	
400	366,86414	0,338472	68,210768	0,099981	0,939697	0,03865	1,321716	0,034967	0,33367	0,021039	
500	770,488863	1,262384	168,924288	0,37793	2,203109	0,066541	2,199015	0,036091	0,13318	0,013131	
560	772,676644	0,853674	176,970259	0,297938	2,320741	0,063825	0,861318	0,025713	0,096492	0,018012	
650	601,48438	0,545095	138,487944	0,127674	1,72712	0,038313	0,610035	0,029753	0,107891	0,018709	
740	1250,273756	0,792052	289,503574	0,306076	3,877402	0,089963	1,221944	0,055541	0,313708	0,014799	
750	1626,478091	0,875716	376,905485	0,337488	4,85457	0,11486	1,257584	0,041186	0,331112	0,014587	
760	1866,812924	1,098113	428,245372	0,267172	5,534144	0,073061	1,474024	0,030916	0,214562	0,01771	
770	369,012825	0,365804	83,67659	0,260141	1,135276	0,056775	0,246721	0,024497	0,073052	0,010992	
800	519,073771	0,562849	117,939013	0,124428	1,546333	0,07668	0,30893	0,023627	0,05578	0,013218	
980	360,034291	0,326477	80,321851	0,213884	1,085209	0,045527	0,260652	0,032769	0,028511	0,009971	
fusion	716,280057	0,709618	161,598772	0,218801	2,112319	0,08772	0,469453	0,022065	0,103391	0,012812	

	KENYA_2_Sanidine				
	40Ar*/39ArK	Error 40Ar*/39	Apparent age (M	Error Age (My)	Delay to irradiation (day)
300	4,422051	0,442622	18,057534	1,799665	46,154167
400	4,00433	0,090917	16,359456	0,374539	46,173611
500	4,372141	0,02667	17,854728	0,126411	46,19375
560	4,244475	0,031488	17,335863	0,14274	46,804167
650	4,153257	0,04022	16,965042	0,174822	46,823611
740	4,03993	0,017174	16,504235	0,092179	46,84375
750	4,09601	0,013801	16,73228	0,082878	46,863889
760	4,250039	0,014084	17,35848	0,085322	46,904167
770	4,192973	0,041173	17,126505	0,178641	46,923611
800	4,300374	0,033857	17,563068	0,151763	46,954167
980	4,416705	0,038708	18,035812	0,170462	46,973611
fusion	4,283432	0,025062	17,49421	0,120174	46,99375

Experiment	Title	Nb of steps	J parameter	error J			Mass Discrimin	Err Discrimination		
z1824	KENYA_2_Sanic	10	2,27E-03	6,17E-06			1,008709	1,32E-03		
Laser power	40Ar	Error 40Ar	39Ar	Error 39Ar	38Ar	Error 38Ar	37Ar	Error 37Ar	36Ar	Error 36Ar
300	178,147542	0,438373	5,667559	0,051035	0,153971	0,030768	1,392408	0,035538	0,509391	0,01366
400	428,322174	0,389248	89,850877	0,231576	1,192262	0,054303	4,697989	0,037642	0,138881	0,01498
500	1131,164051	0,640863	254,57431	0,252662	3,10587	0,128513	2,02899	0,036769	0,057766	0,018749
550	1009,978055	0,445838	226,929831	0,211066	2,793641	0,06444	1,261309	0,047517	0,076734	0,020826
600	1329,21353	0,83332	299,149677	0,531294	3,828182	0,093483	1,348279	0,032265	0,048063	0,018347
650	1211,898878	0,60017	273,58751	0,31478	3,618975	0,105014	1,470741	0,02695	0,043323	0,018347
720	2294,589998	0,883913	518,437994	0,310728	6,83441	0,163026	4,167914	0,033829	0,117987	0,020488
760	893,093086	0,472056	202,511299	0,237041	2,447863	0,052106	0,826848	0,038792	0,013709	0,021298
800	1211,980962	0,542445	273,44826	0,16045	3,291118	0,079859	1,081777	0,023554	0,056219	0,018513
fusion	2048,980248	1,626253	461,938232	0,248655	5,642604	0,075755	1,583895	0,036544	0,066106	0,022392

	KENYA_2_Sanidine				
	40Ar*/39ArK	Error 40Ar*/39	Apparent age (I	Error Age (My)	Delay to irradiation (day)
300	5,612862	0,721845	22,889567	2,926358	47,034028
400	4,368019	0,05061	17,837979	0,215694	47,063889
500	4,415554	0,022844	18,031137	0,113725	47,084028
550	4,390016	0,027786	17,927366	0,130447	47,113889
600	4,434039	0,020605	18,106243	0,106597	47,14375
650	4,421147	0,021151	18,053863	0,108235	47,173611
720	4,397869	0,013386	17,959274	0,0851	47,19375
760	4,427469	0,031663	18,079547	0,144542	47,213889
800	4,40964	0,020865	18,007107	0,107211	47,804167
fusion	4,431132	0,015913	18,094431	0,092349	47,823611

Experiment	Title	Nb of steps	J parameter	error J			Mass Discrimin	Err Discrimination		
z1825	KENYA_3_WR	9	2,27E-03	6,18E-06			1,008709	1,32E-03		
Laser power	40Ar	Error 40Ar	39Ar	Error 39Ar	38Ar	Error 38Ar	37Ar	Error 37Ar	36Ar	Error 36Ar
300	785,470576	0,581947	8,70632	0,051828	0,652433	0,023687	3,924954	0,045406	2,738056	0,024091
400	451,761709	0,374264	21,207682	0,062858	0,579023	0,03744	17,946992	0,109327	1,544581	0,026233
470	251,731543	0,43614	36,68773	0,086592	0,62426	0,043225	23,711484	0,118168	0,811963	0,018895
550	466,804615	0,444498	52,853775	0,112055	1,003371	0,051208	35,536536	0,190612	1,481411	0,033985
650	606,157712	0,409966	188,177331	0,221413	2,672745	0,091353	112,658688	0,185734	1,789892	0,029616
750	385,917647	0,411924	255,23254	0,294342	3,256447	0,082827	120,157372	0,255645	0,972486	0,011714
950	472,718238	0,395695	550,98532	0,512876	6,690485	0,088172	238,852391	0,442414	0,86979	0,02227
1200	239,58043	0,380336	269,505259	0,336108	3,362015	0,066566	98,583511	0,070555	0,407716	0,012203
fusion	609,370835	0,384346	681,992456	0,493247	9,70981	0,192721	1834,794431	1,021844	2,423263	0,03497

	KENYA_3_WR				
	40Ar*/39ArK	Error 40Ar*/39	Apparent age (I	Error Age (My)	Delay to irradiation (day)
300	-0,383098	0,938931	-1,573748	3,858767	47,863889
400	0,48004	0,377362	1,97005	1,54784	47,884028
470	0,619574	0,15422	2,542285	0,632433	47,904167
550	0,897865	0,192356	3,683029	0,788353	47,934028
650	0,608635	0,048201	2,497432	0,19786	47,963889
750	0,515874	0,014786	2,117022	0,061132	47,984028
950	0,497367	0,012103	2,04112	0,050197	48,013889
1200	0,533447	0,013544	2,189098	0,056118	48,034028
fusion	0,43885	0,01547	1,801094	0,063798	48,063889

Experiment	Title	Nb of steps	J parameter	error J				Mass Discrimin	Err Discrimination		
z1827	KENYA_5_WR	9	2,27E-03	6,18E-06				1,008709	1,32E-03		
Laser power	40Ar	Error 40Ar	39Ar	Error 39Ar	38Ar	Error 38Ar	37Ar	Error 37Ar	36Ar	Error 36Ar	
300	1953,180389	0,880316	13,736734	0,024738	1,461217	0,044533	4,393947	0,069137	6,74267	0,03066	
400	675,934164	0,540541	55,744294	0,15322	1,133954	0,073199	28,791725	0,093241	2,24213	0,049485	
500	143,759064	0,224021	48,421594	0,062925	0,678354	0,041005	26,423325	0,089105	0,48033	0,018744	
600	274,887164	0,245266	71,139894	0,09299	0,962454	0,05818	44,604625	0,17521	0,85563	0,021409	
750	390,888236	0,186214	326,998162	0,284342	4,291503	0,111414	164,399048	0,271578	0,881469	0,030696	
900	225,389422	0,106518	250,336536	0,297749	3,047358	0,095124	89,021465	0,187044	0,425727	0,020359	
1100	135,045736	0,103473	135,424162	0,223346	1,754903	0,041797	53,447248	0,075531	0,271969	0,018469	
1400	99,303715	0,209137	117,66377	0,210389	1,567744	0,062864	318,007443	0,292654	0,382139	0,018084	
fusion	98,551036	0,148656	118,618262	0,205926	1,605903	0,067476	388,617748	0,520466	0,438869	0,032491	

	KENYA_5_WR				
	40Ar*/39ArK	Error 40Ar*/39	Apparent age (M	Error Age (My)	Delay to irradiation (day)
300	0,713996	0,992635	2,930971	4,071502	50,823611
400	0,646432	0,265834	2,653821	1,09058	50,834028
500	0,230758	0,113766	0,947789	0,467159	50,863889
600	0,539122	0,089617	2,21355	0,367816	50,884028
750	0,533918	0,027682	2,192194	0,11387	50,934028
900	0,492602	0,023859	2,022653	0,098189	50,954167
1100	0,509673	0,039849	2,092705	0,163705	50,973611
1400	0,514979	0,045092	2,114479	0,185199	50,99375
fusion	0,499731	0,080246	2,051905	0,329391	51,013889

Experiment	Title	Nb of steps	J parameter	error J				Mass Discrimin	Err Discrimination		
z1830	KENYA_6_WR	11	2,28E-03	6,19E-06				1,008709	1,32E-03		
Laser power	40Ar	Error 40Ar	39Ar	Error 39Ar	38Ar	Error 38Ar	37Ar	Error 37Ar	36Ar	Error 36Ar	
300	4511,452766	3,515008	32,208479	0,090337	3,384714	0,031532	2,365647	0,048021	15,550481	0,09715	
400	1521,560752	1,135085	206,159789	0,418832	3,344066	0,118284	5,058441	0,055438	4,456902	0,05055	
500	808,311329	0,838919	496,448274	0,460035	6,505849	0,051133	8,236371	0,052849	1,323325	0,027622	
570	842,669773	0,792318	694,484463	0,727475	8,796233	0,135771	9,876729	0,057011	0,823031	0,032312	
650	1032,322604	0,71155	966,352822	1,352422	12,149149	0,156158	12,317578	0,065324	0,667497	0,032782	
750	1163,283294	1,040461	1166,663574	0,592593	15,500464	0,252801	14,367186	0,037847	0,504511	0,027308	
900	2230,808811	1,897132	2341,499519	1,329142	29,572876	0,296754	32,26221	0,071627	0,678429	0,030366	
1100	2640,090304	1,465104	2897,858022	1,857789	37,262249	0,291771	51,358378	0,184425	0,463397	0,026334	
1300	2515,403237	1,024363	2750,062758	1,169386	35,350511	0,209668	65,946087	0,09751	0,537297	0,037278	
1500	1173,784417	0,933412	1249,885515	0,644876	16,025487	0,17014	56,715951	0,160062	0,360969	0,034972	
fusion	1343,829637	0,902463	1459,063758	1,221652	18,659911	0,056846	100,300387	0,371848	0,382797	0,032344	

	KENYA_6_WR				
	40Ar*/39ArK	Error 40Ar*/39	Apparent age (M	Error Age (My)	Delay to irradiation (day)
300	0,863628	1,150201	3,548787	4,721742	51,89375
400	1,160613	0,079394	4,767536	0,32617	51,904167
500	0,869698	0,017096	3,573705	0,071382	51,923611
570	0,881374	0,013928	3,621634	0,058686	51,94375
650	0,878468	0,010211	3,609705	0,043941	51,984028
750	0,881743	0,007119	3,623151	0,032079	52,004167
900	0,878811	0,00421	3,611112	0,02174	52,023611
1100	0,875458	0,003088	3,597348	0,018258	52,054167
1300	0,870245	0,004232	3,575951	0,021736	52,09375
1500	0,872672	0,008334	3,585911	0,036631	52,113889
fusion	0,867524	0,00669	3,564778	0,030391	52,134028

Experiment	Title	Nb of steps	J parameter	error J			Mass Discrimin	Err Discrimination		
z1831	KENYA_6_sanid	11	2,28E-03	6,19E-06			1,008709	1,32E-03		
Laser power	40Ar	Error 40Ar	39Ar	Error 39Ar	38Ar	Error 38Ar	37Ar	Error 37Ar	36Ar	Error 36Ar
300	1001,745057	0,745811	0,936804	0,04452	0,602444	0,035064	0,080323	0,030804	3,466467	0,039438
400	130,099605	0,174234	5,65736	0,053495	0,198306	0,030176	0,132462	0,038108	0,395773	0,017385
500	64,5477	0,238731	15,9595	0,05272	0,2182	0,039924	0,2217	0,029314	0,2089	0,012587
650	165,5657	0,205158	122,4132	0,182501	1,6286	0,048573	1,1842	0,064263	0,2081	0,016479
700	87,7095	0,151591	84,3942	0,123093	1,0396	0,052513	0,713	0,039125	0,0547	0,030056
800	172,3139	0,271803	179,5381	0,212616	2,3725	0,095567	1,622	0,041434	0,0639	0,013909
950	191,984505	0,122199	201,219483	0,331034	2,593675	0,058929	1,932595	0,023335	0,136159	0,017862
1050	1211,091405	1,444867	1242,073583	0,515671	15,807875	0,102765	14,430195	0,122736	0,521859	0,021749
1060	1403,849505	0,968731	1408,444183	1,130115	17,862175	0,140323	12,915195	0,074852	0,694059	0,023745
1061	1012,921633	0,324966	1086,672376	0,488494	13,726078	0,09862	8,694938	0,078862	0,299799	0,024093
fusion	3130,263076	1,505023	3266,22102	1,573992	40,825665	0,35497	28,899279	0,08566	1,161083	0,025513

	KENYA_6_sanidine				
	40Ar*/39ArK	Error 40Ar*/39	Apparent age (M	Error Age (My)	Delay to irradiation (day)
300	2,277533	13,502275	9,343752	55,251233	52,184028
400	2,851138	0,901323	11,689421	3,683674	52,204167
500	0,274454	0,230728	1,128531	0,948447	52,804167
650	0,87096	0,039382	3,578884	0,162195	52,823611
700	0,860657	0,103609	3,536592	0,425528	52,84375
800	0,865617	0,022666	3,556952	0,093949	52,873611
950	0,766764	0,025932	3,151101	0,1071	52,913889
1050	0,862953	0,005534	3,546015	0,026148	52,934028
1060	0,863119	0,005347	3,546698	0,025489	52,954167
1061	0,860771	0,006654	3,537057	0,030216	53,013889
fusion	0,864283	0,002901	3,551475	0,017608	53,023611

Experiment	Title	Nb of steps	J parameter	error J			Mass Discrimin	Err Discrimination		
z1832	KENYA_7_WR	9	2,28E-03	6,19E-06			1,008709	1,32E-03		
Laser power	40Ar	Error 40Ar	39Ar	Error 39Ar	38Ar	Error 38Ar	37Ar	Error 37Ar	36Ar	Error 36Ar
300	43575,74613	16,212385	96,49647	0,244917	30,233928	0,331877	99,332605	0,119687	149,482215	0,237558
370	10123,34414	5,295177	166,862549	0,208966	8,272393	0,054638	83,361353	0,082583	32,533215	0,107614
450	3566,633079	3,211956	242,966842	0,55146	4,473604	0,066874	89,932505	0,142745	8,586171	0,039042
530	3095,273934	0,867836	299,10547	0,41966	5,081628	0,123913	145,994705	0,185269	6,162615	0,047736
600	2387,414295	0,68701	223,536649	0,360223	3,738965	0,059813	78,410988	0,114027	4,810332	0,030402
680	3666,398164	3,214375	363,774	0,315317	5,729312	0,054128	72,604472	0,155458	7,00868	0,050731
800	1878,4745	0,775756	230,0767	0,213398	3,4485	0,113101	36,8412	0,210869	2,9328	0,046213
1000	1432,3796	1,020366	202,5994	0,232988	3,0586	0,03356	58,4222	0,176022	1,8582	0,047722
fusion	7837,0519	3,628441	933,7213	0,625642	15,1022	0,116145	1824,8888	1,489679	14,5256	0,092525

	KENYA_7_WR				
	40Ar*/39ArK	Error 40Ar*/39	Apparent age (M	Error Age (My)	Delay to irradiation (day)
300	5,148496	2,482722	21,067232	10,10043	53,073611
370	4,601877	0,357851	18,84212	1,459208	53,104167
450	4,615319	0,077627	18,896875	0,32359	53,123611
530	4,561618	0,05978	18,678134	0,252848	53,14375
600	4,596544	0,055806	18,8204	0,237429	53,184028
680	4,608335	0,054608	18,868427	0,232807	53,204167
800	4,564736	0,063885	18,690836	0,269003	53,804167
1000	4,532307	0,071669	18,558729	0,299698	53,823611
fusion	4,420421	0,040432	18,102869	0,177473	53,84375

Experiment	Title	Nb of steps	J parameter	error J			Mass Discrimin	Err Discrimination		
z1834	KENYA_7_WR	11	2,28E-03	6,19E-06			1,008709	1,32E-03		
Laser power	40Ar	Error 40Ar	39Ar	Error 39Ar	38Ar	Error 38Ar	37Ar	Error 37Ar	36Ar	Error 36Ar
300	11190,41775	3,419479	35,604318	0,120203	8,177923	0,149537	34,029307	0,131474	38,095003	0,084581
400	12853,26428	5,80747	128,095679	0,173193	10,010388	0,126199	74,596257	0,176233	42,136308	0,10204
460	6324,287339	5,03262	304,20233	0,33274	6,65089	0,115426	86,307445	0,202172	16,62624	0,055111
530	3825,903702	2,872451	350,964152	0,41518	5,644648	0,091897	85,119972	0,116425	7,776324	0,039357
600	3858,551621	1,74364	461,056514	0,569704	6,816912	0,142263	126,06189	0,232918	6,119406	0,057484
680	4417,488339	2,198782	527,609659	0,602739	7,829734	0,124011	132,411431	0,376037	6,79753	0,028111
800	5232,51571	1,459915	637,623571	0,654672	9,463018	0,134146	106,117584	0,225795	7,939754	0,04865
950	4956,304908	2,418542	727,677037	0,426463	9,968627	0,161004	102,622282	0,128154	5,755114	0,046054
1150	2056,342452	1,36338	329,844756	0,362381	4,477632	0,101687	84,8246	0,250259	2,115919	0,035749
1400	5079,354183	1,732076	678,710215	0,601364	10,477568	0,097086	769,787783	0,725261	8,156454	0,058512
fusion	12045,15232	5,729345	1434,091073	1,087883	22,913165	0,250278	3197,081552	2,49767	23,005956	0,079818

	KENYA_7_WR				
	40Ar*/39ArK	Error 40Ar*/39	Apparent age (M	Error Age (My)	Delay to irradiation (day)
300	6,042008	1,781056	24,698284	7,231586	54,904167
400	5,674789	0,560309	23,206774	2,27828	54,923611
460	5,141458	0,105492	21,038379	0,435952	54,94375
530	4,609548	0,052204	18,873169	0,223473	54,963889
600	4,647545	0,045179	19,027929	0,19663	55,004167
680	4,716823	0,030791	19,310059	0,143775	-3,976389
800	4,695147	0,033812	19,221788	0,154479	55,04375
950	4,602997	0,026055	18,846487	0,126407	55,054167
1150	4,485086	0,03568	18,366158	0,160035	55,09375
1400	4,337259	0,034344	17,763779	0,154217	55,113889
fusion	4,397335	0,032886	18,008604	0,149217	57,804167

Experiment	Title	Nb of steps	J parameter	error J			Mass Discrimin	Err Discrimination		
z1835	KENYA_1_WR	11	2,27E-03	6,17E-06			1,008709	1,32E-03		
Laser power	40Ar	Error 40Ar	39Ar	Error 39Ar	38Ar	Error 38Ar	37Ar	Error 37Ar	36Ar	Error 36Ar
300	12580,96488	3,355136	156,47631	0,124357	10,543524	0,137474	8,684684	0,041762	43,202033	0,105339
370	6012,335107	4,2582	626,100509	0,559597	11,024683	0,215768	14,274104	0,131695	15,388219	0,11041
460	707,797698	0,484892	154,698366	0,260545	2,043323	0,073362	4,471454	0,042074	0,843404	0,02634
550	894,264338	0,768516	183,244299	0,276087	2,422459	0,088406	2,118882	0,063377	0,965699	0,027496
620	445,417717	0,323727	90,98048	0,074036	1,270266	0,037781	0,714194	0,035837	0,296397	0,014601
730	1548,439166	1,048233	304,177536	0,226044	3,887518	0,06218	3,525173	0,062422	0,903666	0,02682
800	1069,018714	0,330673	219,624772	0,303371	2,847899	0,083731	2,894157	0,051084	0,533151	0,018738
900	1715,152814	1,025807	363,679372	0,330333	4,780199	0,125429	10,393957	0,080038	0,720151	0,026664
1200	2484,973909	0,654927	528,74665	0,35421	6,886383	0,098794	32,780596	0,108768	0,919931	0,028687
1400	1714,424756	0,789798	373,998708	0,372601	4,865045	0,0997	14,875516	0,094696	0,466939	0,029525
fusion	5913,37838	3,281191	1327,161633	0,840503	17,121947	0,137589	15,079934	0,085426	0,960876	0,016848

	KENYA_1_WR				
	40Ar*/39ArK	Error 40Ar*/39	Apparent age (M	Error Age (My)	Delay to irradiation (day)
300	0,804582	0,464883	3,297226	1,903419	57,873611
370	2,541765	0,065864	10,395862	0,271277	57,904167
460	3,035525	0,051357	12,408432	0,214054	57,923611
550	3,390876	0,045856	13,855462	0,193374	57,94375
620	3,990667	0,048006	16,295254	0,203986	57,984028
730	4,271598	0,027957	17,436877	0,130144	58,004167
800	4,205085	0,027128	17,166653	0,126742	58,023611
900	4,186987	0,023427	17,093117	0,113763	58,04375
1200	4,250006	0,018029	17,349158	0,096762	58,084028
1400	4,269809	0,024601	17,429609	0,118421	58,104167
fusion	4,284679	0,008493	17,490016	0,072482	58,123611

Experiment	Title	Nb of steps	J parameter	error J				Mass Discrimin	Err Discrimination		
z1836	KENYA_1_sanid	11	2,27E-03	6,17E-06				1,008709	1,32E-03		
Laser power	40Ar	Error 40Ar	39Ar	Error 39Ar	38Ar	Error 38Ar	37Ar	Error 37Ar	36Ar	Error 36Ar	
300	373,005738	0,356518	0,952175	0,032892	0,237793	0,04976	0,225744	0,022184	1,285948	0,030988	
400	356,516615	0,389829	15,0999	0,04503	0,357198	0,036591	1,590309	0,031209	0,97753	0,018949	
470	208,581274	0,216394	17,485697	0,072318	0,353986	0,060777	0,491574	0,038806	0,423846	0,021022	
560	415,1155	0,38683	43,7115	0,102944	0,8104	0,038652	0,8846	0,036583	0,6574	0,048812	
650	508,2255	0,34284	93,3326	0,134955	1,2014	0,05918	0,5663	0,036583	0,2007	0,034779	
730	544,705134	0,389751	99,431451	0,226593	1,262119	0,065952	0,376787	0,031264	0,201738	0,026543	
800	379,2265	0,279466	72,3772	0,282382	0,8956	0,072591	0,1806	0,02846	0,0746	0,036842	
900	947,418624	0,537004	164,860742	0,273045	2,142652	0,050137	0,225935	0,035364	0,505136	0,037278	
1000	2730,553339	1,659211	471,632263	0,349158	6,273268	0,100046	0,801272	0,036359	1,636052	0,026933	
1200	2101,836324	1,36332	382,708342	0,236277	4,947952	0,102175	0,481835	0,02884	0,845536	0,029761	
fusion	2725,466424	2,090182	481,975642	0,388793	6,259352	0,141011	0,650035	0,039985	1,328636	0,026099	

	KENYA_1_sanidine				
	40Ar*/39ArK	Error 40Ar*/39	Apparent age (M	Error Age (My)	Delay to irradiation (day)
300	2,359409	9,697216	9,652009	39,564252	58,163889
400	5,010504	0,380962	20,436142	1,54686	58,184028
470	4,986547	0,353108	20,338976	1,434092	58,204167
560	5,207421	0,326429	21,234598	1,325569	58,804167
650	4,866164	0,109075	19,850646	0,44839	58,823611
730	4,934009	0,079111	20,125874	0,329175	58,84375
800	4,983305	0,149554	20,325828	0,611087	58,863889
900	4,903189	0,06725	20,000849	0,282373	58,904167
1000	4,828708	0,020871	19,69868	0,111003	58,934028
1200	4,89478	0,025076	19,966739	0,125059	58,954167
fusion	4,899792	0,019879	19,98707	0,108654	58,973611

Experiment	Title	Nb of steps	J parameter	error J		
z1837	KENYA_3_WR	8	2,27E-03	6,18E-06		
Laser power	40Ar	Error 40Ar	39Ar	Error 39Ar	38Ar	Error 38Ar
300	119,381346	0,24115	2,918412	0,019926	0,070724	0,0377
400	73,725513	0,323897	11,340839	0,066168	0,28273	0,0378
500	47,553159	0,413138	13,243812	0,033566	0,22706	0,0425
650	226,232242	0,303603	164,890609	0,185152	2,019708	0,0547
750	85,117198	0,191886	122,416101	0,242853	1,52721	0,0460
1000	213,69486	0,227804	326,235942	0,307682	3,966931	0,0995
1300	51,583098	0,129939	64,741531	0,156173	0,974291	0,0449
fusion	246,203198	0,329218	325,911531	0,263488	4,694991	0,1038

	KENYA_3_WR				
	40Ar*/39ArK	Error 40Ar*/39	Apparent age (M	Error Age (My)	Delay to irradiation (day)
300	5,518276	2,72694	22,518141	11,058975	59,013889
400	1,17639	0,636722	4,824012	2,607577	59,034028
500	0,763392	0,39336	3,131901	1,612445	59,054167
650	0,548854	0,040329	2,252281	0,165598	59,073611
750	0,540593	0,06241	2,218405	0,25608	59,123611
1000	0,506325	0,021404	2,077861	0,088113	59,14375
1300	0,39845	0,101231	1,63536	0,415336	59,163889
fusion	0,456715	0,038529	1,874374	0,15819	59,184028

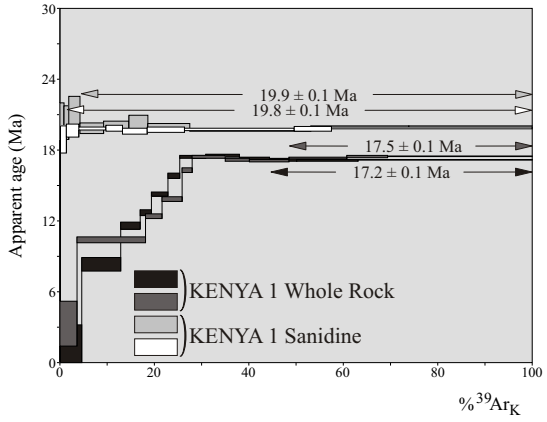
Apparent age (Ma)
19.9 ± 0.1 Ma
19.8 ± 0.1 Ma
17.5 ± 0.1 Ma
17.2 ± 0.1 Ma
KENYA 1 Whole Rock
KENYA 1 Sanidine
%39ArK

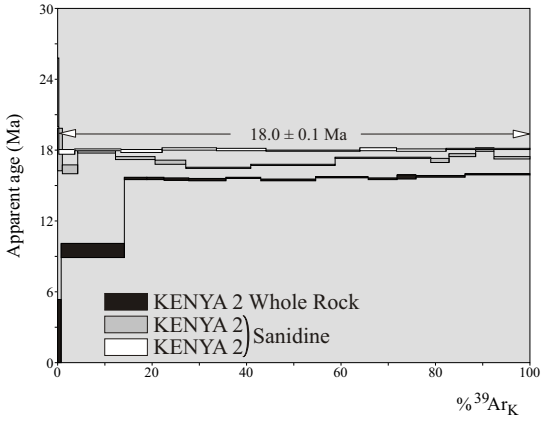
Apparent age (Ma)
18.0 ± 0.1 Ma
KENYA 2 Whole Rock
KENYA 2
KENYA 2
Sanidine
%39ArK

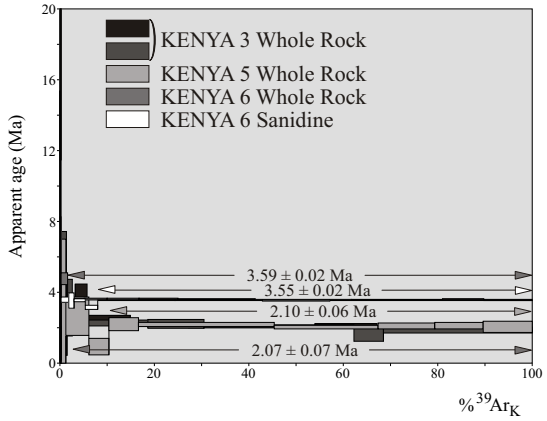
Apparent age (Ma)
KENYA 3 Whole Rock
KENYA 5 Whole Rock
KENYA 6 Whole Rock
KENYA 6 Sanidine
3.59 ± 0.02 Ma
3.55 ± 0.02 Ma
2.10 ± 0.06 Ma
2.07 ± 0.07 Ma
%39ArK

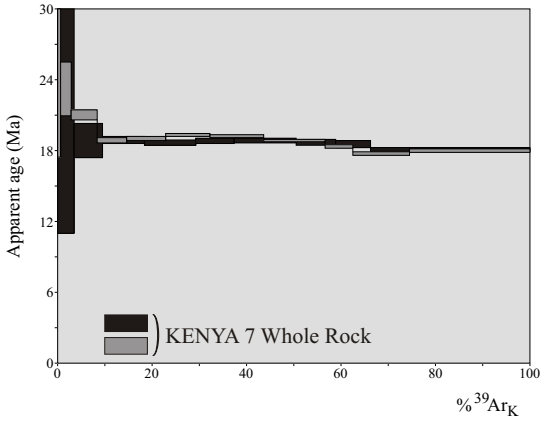
Apparent age (Ma)
KENYA 7 Whole Rock
%39ArK

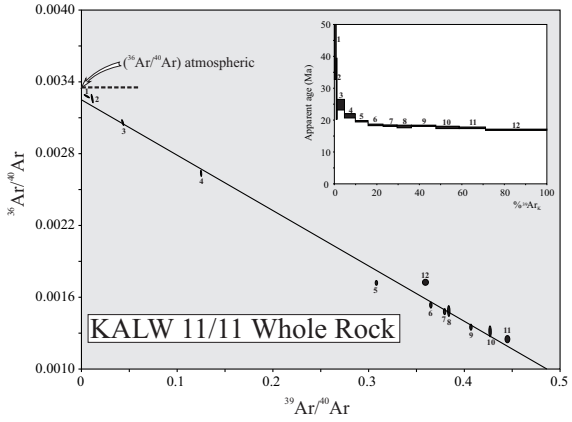
(36Ar/40Ar) atmospheric
Apparent age (Ma)
%39ArK
KALW 11/11 Whole Rock
36Ar/40Ar
39Ar/40Ar

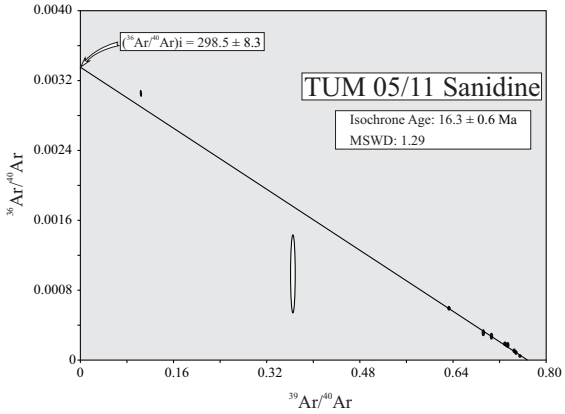
(36Ar/40Ar)i = 298.5 ± 8.3
TUM 05/11 Sanidine
Isochrone Age: 16.3 ± 0.6 Ma
MSWD: 1.29
36Ar/40Ar
39Ar/40Ar

References

VU :

Le Directeur de Thèse
TIERCELIN Jean-Jacques

VU :

Le Responsable de l'École Doctorale

VU pour autorisation de soutenance

Rennes, le

Le Président de l'Université de Rennes 1

Guy CATHELINEAU

VU après soutenance pour autorisation de publication :

Le Président de Jury,
(Nom et Prénom)